THE UNIVERSITY of EDINBURGH

Title	Submillimetre polarimetry of blazars
Author	Nartallo Garcia, Ramon.
Qualification	PhD
Year	1995

Digitisation Notes:

- Page 119 appears twice in original

Submillimetre Polarimetry of Blazars

Ramón Nartallo García

B. Sc. (Edin.), M. Sc. (London)

Thesis presented for the degree of
Doctor of Philosophy

University of Edinburgh

1995

Abstract

The magnetic field is a major contributor to the physics of many types of astronomical objects. Polarimetry is a powerful tool for probing directly into the magnetic field to estimate its degree of ordering and orientation. This knowledge is often essential in order to constrain theoretical models in astrophysics. The advent of submillimetre polarimetry has opened a new window through which polarised emission produced by dust grains or the synchrotron mechanism can be investigated. This has immediate applications to the study of star forming regions and radio-loud extragalactic sources. The work presented in this thesis covers several aspects of doing polarimetry in the submillimetre with the James Clerk Maxwell Telescope (JCMT), and its application to an on-going observing programme dedicated to monitoring the polarisation of highly variable extragalactic sources, which include BL Lac Objects and a subset of Quasars, often referred to collectively as Blazars. The more instrumental parts of this project are concerned with the development of data reduction algorithms and their implementation in a new common user software package for the analysis of JCMT polarimetry data, the optimisation of data acquisition techniques in the currently available observing mode and the development of a new (potentially more efficient) observing mode, including numerical simulations, extensive laboratory experiments and telescope tests. The Blazar monitoring programme consists of a series of observing runs during which polarimetry and multi-frequency photometry have been done on a sample of sources. The observations allow two different types of study to be carried out: one in terms of the variability of individual sources and the other in terms of the overall properties derived for the two classes of object. While variability observations are used to distinguish between and place constraints on theoretical models that deal with the energy production and transport mechanisms, the comparison between BL Lac Objects and Quasars investigates whether they are likely to have different parent populations, or if their properties can be accounted for within a single unifying theory.

Declaration

This thesis is submitted in accordance with the regulations for the degree of Doctor of Philosophy. I declare that the work described herein is my own and that this thesis has been composed by myself. All sources of information have been specifically acknowledged.

September, 1995

Acknowledgements

During the course of my Ph. D. I have received help, guidance and kindness from a number of people whom I would like to thank. First of all is my supervisor Walter Gear for suggesting an exciting project to work on, providing guidance throughout and for introducing me to the world of professional astronomy. I would like to thank him especially for his faith in my ability to carry out the work, his encouragement, suggestions and fair and constructive criticism. Special thanks are also due to Sye Murray for his effective role as my unofficial supervisor. His unfailing help and support in carrying out most of the technical work described in this thesis, and his numerous comments and suggestions in all aspects of the project, earned him my appreciation. Much of the work presented in this thesis follows on from his own work. I am also grateful to Walter and Sye for their companionship during the observing trips. I would also like to thank my university supervisor John Cooke, for his encouragement, proof reading of the manuscript and his help in all academic matters.

I have been a student at the now Institute for Astronomy for the best part of the last ten years and I would like to express my gratitude to all members of staff, to whom I owe most of my scientific education, for their help and for always making me feel at home. It is their example that encouraged me to pursue a career in Astronomy. I would also like to thank my fellow students for providing the atmosphere and the staff at the ROE for providing and supporting the facilities. I am grateful to Peter Ade and his group at the Astrophysics Laboratory at QMW, for allowing me use of their facilities and their help in setting up and carrying out the laboratory experiments. I gratefully acknowledge the receipt of a postgraduate scholarship from the Spanish Ministry of Education and Science and I thank the staff at the Servicio de F. P. U. (Becas en el Extranjero) for their excellent support and competence in dealing with all financial matters. I also thank the JCMT development fund for the financial assistance provided to cover the trips to QMW.

Finally, I would like to thank my family for their love and support during these years. Most of all, I thank my wife Yamuna for being the light at the end of the tunnel and for giving me a wonderful baby, the best prize of all. Without her love, understanding and extreme patience it would not have been worthwhile, and it is to Yamuna that I dedicate this thesis.

Table of Contents

1. Introduction

2. Submillimetre Polarimetry with the JCMT

4. Variability of Blazars: Observations

5. Variability of Blazars: Analysis

7. Summary and Future Prospects

List of Figures

Chapter 1

Chapter 2

Chapter 3

Chapter 4

Chapter 5

Chapter 6

List of Tables

Chapter 2

Chapter 3

Chapter 4

Chapter 5

List of Symbols

c	speed of light
e	electronic charge
f	normalised flux density
k	Boltzman's constant
k	propagation vector of electromagnetic wave
m_e	electron mass
q	normalised Stokes Q parameter
s	power law index (§ 1)
u	normalised Stokes U parameter
v	velocity of electron
B	magnetic field vector
B	magnetic field strength
$B_\perp$	magnetic field component perpendicular to the VLBI jet
$B_\parallel$	magnetic field component parallel to the VLBI jet
$D(\theta)$	predicted power as a function of waveplate position
E	electric field vector
E	electron energy
F	flux density
I	total intensity, 1st Stokes parameter
I_u	unpolarised intensity
I_p	polarised intensity
$I(\nu)$	intensity as a function of frequency
Jy	Jansky
P	percentage linear polarisation
Q	2nd Stokes parameter
R	radius of shocked emitting region
$S(\theta)$	power measured as a function of waveplate position

T_b	brightness temperature
T_e	effective temperature
U	3rd Stokes parameter
V	4th Stokes parameter
α	spectral index
χ	polarisation position angle
χ_{VLA}	polarisation position angle measured with the VLA
$\chi_{Optical}$	polarisation position angle measured at optical wavelengths
χ_{Core}	polarisation position angle measured at radio wavelengths near the AGN core
χ_{Jet}	polarisation position angle measured at radio wavelengths in the VLBI jet
δ	absolute difference between $\mid \theta_{VLBI} - \chi \mid$
ε	elevation
ϕ	jet opening half-angle
γ	Lorentz factor
ν	frequency
ν_g	electron gyrofrequency
μ_o	permeability of free space
θ	waveplate position (§ 1 and § 2)
θ	viewing angle (§ 6)
θ_c	critical viewing angle
θ_{VLBI}	position angle of the VLBI jet
ρ	parallactic angle
σ	signal to noise ratio
σ_P	uncertainty in percentage of linear polarisation
σ_T	Thomson Cross-section
σ_χ	uncertainty in position angle
Γ	Lorentz factor
Π	percentage polarisation
Π_e	degree of ellipticity

List of Abbreviations

AC	Alternating Current
ADC	Analogue to Digital Converter
AGN	Active Galactic Nucleus
ATF	Angle Track False
ATT	Angle Track True
BL Lac	BL Lac Object
CPU	Central Processing Unit
CS	Continuous Spinning polarimetry mode
CSO	Caltech Submillimetre Observatory
DC	Direct Current
DVM	Digital Volt Meter
FFT	Fast Fourier Transform
GSD	UKT14 standard format for raw data files
HPQ	Highly Polarised Quasar
IP	Instrumental Polarisation
JCMT	James Clerk Maxwell Telescope
K-S	Kolmogorov-Smirnov Test
LIA	Lock-in-Amplifier
LPQ	Low Polarisation Quasar
NRAO	National Radio Astronomy Observatory
OMC	Orion Molecular Cloud
QMW	Queen Mary and Westfield College, University of London
PC	Personal Computer
PSD	Phase Sensitive Detector
SCUBA	Submillimetre Common User Bolometer Array
SI	Step and Integrate polarimetry mode
SVD	Singular Value Decomposition
VLA	Very Long Array
VLBI	Very Long Baseline Interferometry

Chapter 1

Introduction

Polarimetry is a powerful probe into the physics of astronomical sources that produce polarised emission and their environments. In the submillimetre, there are two possible origins for this type of emission: non-thermal synchrotron radiation from relativistic electrons gyrating in a magnetic field and thermal emission produced by aligned dust grains. Submillimetre polarimetry has only become available fairly recently and there is a lot of scope for new and interesting science to emerge from this type of measurement, as it can yield essential information for the study of areas as diverse as extragalactic radio sources, star formation or the structure of the galaxy.

1.1 Outline of the Work Presented in this Thesis

There are two main aspects to the work presented in this thesis: one is eminently instrumental, primarily concerned with furthering the development of the techniques required to measure the polarisation of astronomical sources in the submillimetre, and the other is observational, where the subject of study is the submillimetre polarisation of Blazars. The breakdown of the thesis into chapters is as follows:

- The remainder of Chapter 1 is an introduction to the basic physics required to understand how to carry out polarisation measurements of astronomical sources in general. The physics responsible for the origin of the submillimetre polarised emission in Blazars and a brief review of what has been learnt about these sources from measurements of their polarisation carried out at other frequencies are also introduced.

- In Chapter 2 various modes of observation to carry out polarisation measurements with the JCMT[1] are discussed. The development and software implementation of the data reduction techniques needed to convert the raw observations into meaningful physical parameters are also described.

- In Chapter 3 an account is given of preliminary investigations on a new data acquisition mode, so far not implemented in any sub/millimetre polarimeter, but which could prove to be the most efficient way of measuring polarisation. It includes computer simulations and tests carried out both in the laboratory and at the telescope.

- In Chapter 4 the details on a monitoring campaign of the polarisation of a sample of Blazars carried out at 800 and 1100 μm with the JCMT between 1991 and 1994 are given. A literature search carried out for VLBI observations of the sources concerned is also outlined.

- In Chapter 5 graphical and statistical analysis performed on the Blazars' polarisation database obtained at 1100 μm, are described in terms of polarisation properties and source type.

- In Chapter 6 possible physical mechanisms responsible for the origin and characteristics of the polarised emission in Blazars and its extreme variability (as inferred from the submillimetre data) are discussed. The results obtained are compared with what is observed at other frequencies and their implications on the nature of the sources that make up the Blazar category are highlighted.

- In Chapter 7 the main results obtained with respect to the instrumental techniques in submillimetre polarimetry and their application to the study of Blazars are summarised. The future prospects of these two areas of research are discussed.

1.2 Measuring Polarisation in the Submillimetre

The development of polarimetry in the submillimetre has borrowed heavily from the techniques used at other frequencies. This is true not only where the hardware is concerned

[1] James Clerk Maxwell Telescope at Mauna Kea, Hawaii.

but also of the methods utilised to reduce and understand the data. In this section, the properties of polarised light and how these can be given a suitable mathematical treatment are outlined and the method of measuring polarisation using a rotating half-waveplate and a fixed analyser is presented. In particular, the polarimetry set up at the JCMT is described.

1.2.1 Historical Review

The state of submillimetre polarimetry before the commissioning of the Aberdeen/QMW Polarimeter at the JCMT is reviewed in Murray (1991). The first real detections of astronomical polarised emission in the submillimetre were obtained at 270 μm by Hildebrand *et al.* (1984) from NASA's Kuiper Airborne Observatory, although other groups had been able to get upper limit measurements in the far-infrared from balloon observations (Cudlip *et al.* 1982). A millimetre polarimeter was used on the NRAO 12-metre telescope (Clemens *et al.* 1990) operating between 3 and 1.3 mm, but has now been decommissioned. The JCMT polarimeter has been available to the common user since 1990, although its optimisation in terms of modes of observation and especially data reduction techniques, has come about as a result of the work described in Chapter 2 of this thesis. At present, an array polarimeter is being operated at 450 μm at the CSO on Mauna Kea, Hawaii (Schleuning *et al.* 1995).

1.2.2 The Nature of Polarised Light

Light can be described as a transverse electromagnetic wave, characterised by the evolution with time of its electric field vector **E** and its propagation vector **k** in the direction of motion. A beam of light results from the superposition of a number of waves moving through the same region of space. Polarisation occurs when the electric field vector resultant from a superposition of waves of the same frequency moving together has a preferred orientation. The most general case is that of elliptical polarisation where the tip of the resultant **E** vector traces out an ellipse in a fixed space perpendicular to **k**. Circular and linear polarisation states are special cases of elliptical polarisation. Circular polarisation occurs when the magnitude of the resultant **E** vector is constant but its orientation rotates through 2π as the wave advances one wavelength. Right and Left circular polarisation distinguishes between the two senses of rotation of **E**. Linear polarisation arises when the magnitude of the **E** vector oscillates along a fixed orientation as the wave advances by one wavelength along its direction of motion. Figure 1.1 illustrates elliptical, circular and linear polarisation.

Figure 1.1 **Representation of Elliptical, Circular and Linear Polarisation**

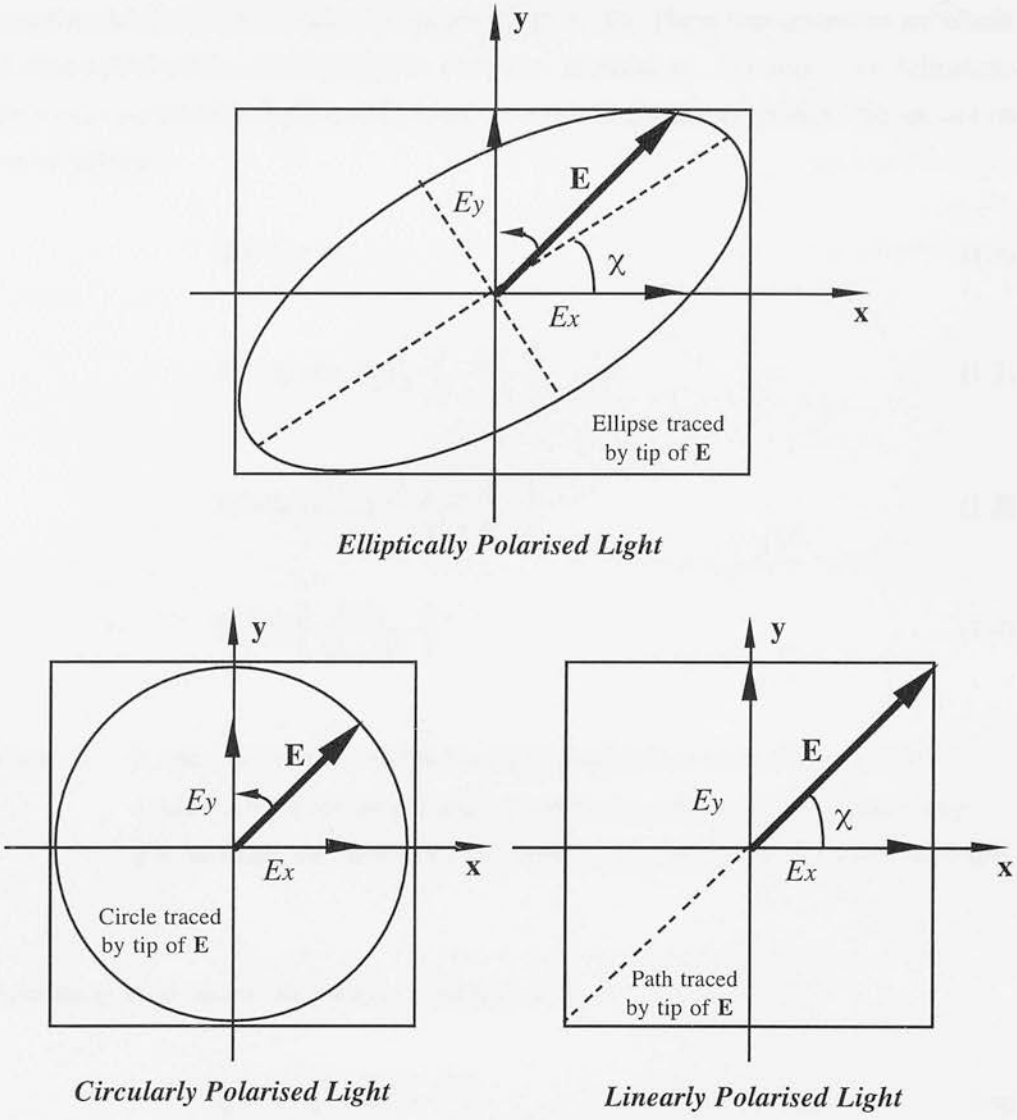

1.2.3 Mathematical Treatment of Polarisation: Stokes Parameters

Maxwell's equations can be solved for electromagnetic waves describing polarised light and characterise the changes in the properties of such waves as they encounter various optical components. However, this treatment becomes mathematically cumbersome, difficult to follow and the properties of such waves impossible to measure experimentally. An alternative treatment introduces the Stokes vector, to completely describe the state of polarisation of a beam of light, and Mueller matrices to describe the properties of an optical

system. Matrix calculus can be used to follow the interactions between a beam of light with one or more optical systems (e.g. Hecht 1987, see also Murray 1991 for relevant examples). Any state of polarisation can be fully described in terms of a Stokes vector whose components are the four Stokes parameters: *(I, Q, U, V)*. These four quantities are functions of observables of the electromagnetic wave (i.e. intensities). The following definitions of the Stokes parameters apply to elliptically polarised light and from them the special cases can be inferred.

$$I = I_u + I_p \tag{1.1}$$

$$Q = I_p \cos(2\chi)\left(\frac{a^2 - b^2}{a^2 + b^2}\right) \tag{1.2}$$

$$U = I_p \sin(2\chi)\left(\frac{a^2 - b^2}{a^2 + b^2}\right) \tag{1.3}$$

$$V = I_p\left(\frac{2ab}{a^2 + b^2}\right) \tag{1.4}$$

where I_u and I_p are the unpolarised and polarised components of the intensity
a and b are the semimajor and semiminor axes of the ellipse respectively
χ is the angle the semimajor axis makes with some given reference direction

From these expressions, the polarised component is

$$I_p = \sqrt{\left(Q^2 + U^2 + V^2\right)} \tag{1.5}$$

The degree of polarisation Π in terms of Stokes parameters is

$$\Pi = \frac{I_p}{I} = \frac{\sqrt{\left(Q^2 + U^2 + V^2\right)}}{I} \tag{1.6}$$

For linearly polarised light $b = 0$ and hence $V = 0$. For circular polarisation $a = b$ and hence $Q = U = 0$ and $V = I_p$. From this, the Stokes V parameter is clearly identified as describing the circular component of polarisation, while Q and U deal with the linear component and I is the total intensity.

The degree of linear polarisation P and the degree of ellipticity Π_e are given by

$$P = \frac{\sqrt{(Q^2 + U^2)}}{I} \tag{1.7}$$

$$\Pi_e = \frac{V}{I} \tag{1.8}$$

Finally, the orientation of the position angle χ in the linear polarisation case can also be expressed in terms of Stokes parameters,

$$\chi = \frac{1}{2} \arctan\left(\frac{U}{Q}\right) \tag{1.9}$$

The normalised Stokes parameters q and u are often used and these are obtained by dividing Q and U by I respectively. For the linearly polarised case,

$$\begin{aligned} q &= \frac{I_p}{I} \cos(2\chi) \\ u &= \frac{I_p}{I} \sin(2\chi) \end{aligned} \tag{1.10}$$

Optical systems can be devised to measure the Stokes parameters directly, from which P and χ can be obtained to fully describe linearly polarised radiation.

1.2.4 The Rotating Half-Waveplate and Analyser Polarimeter

a) The JCMT Polarimeter

The polarimeter used throughout this work is the Aberdeen/QMW Polarimeter[2] placed in front of the bolometer receiver UKT14 (Duncan *et al.* 1990) at the East Nasmyth focus of the JCMT. It consists of a rotatable half-waveplate followed by a fixed analyser. The details of the selection of the materials and manufacture of the polarimeter are documented in Murray (1991) and Murray *et al.* (1992). Figure 1.2 illustrates the polarimetry set-up at the telescope. The main components of the polarimeter are:

[2] Its prototype was also used in laboratory experiments.

1) The Half-Waveplate

A half-waveplate is a retarder that changes the state of polarisation of the incident light in a controlled and well understood fashion. It exploits the birefringent properties of quartz: different refractive indices along two orthogonal directions define the optic *fast* and *slow* axes. The waveplate is optimised to introduce a phase shift of a half-wavelength between the **E** vector components of a beam of light travelling along each of the waveplate's axes. The waveplates currently available are not achromatic, and a different one has to be used for each of the three frequencies at which the polarimeter works: 450, 800 and 1100 μm.

2) The Analyser

The analyser is a free standing wire-grid polariser with parallel conducting wires. The conduction electrons in the wires are driven by the parallel component of **E** which is thus mostly absorbed, whereas the perpendicular component of **E** goes through with hardly any loss. The net effect of a wire-grid polariser is the selection of the polarised component perpendicular to the direction of the wires. The transmission of this type of polariser is exactly *50 %*, i.e. it cuts the incident power by a factor 1/2.

Figure 1.2 Schematic of the Polarimetry Set-Up at the JCMT

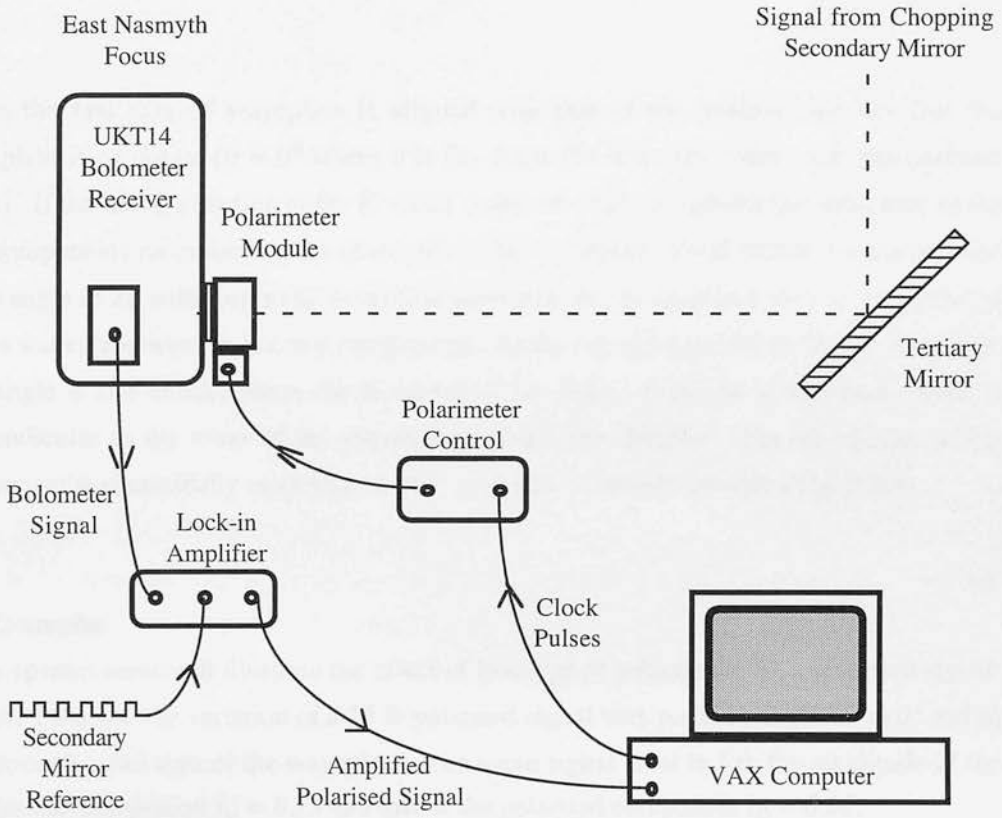

b) How it Works

The principle behind this type of polarimeter is to position the waveplate at known orientations of its fast axis relative to a prescribed reference direction, which is provided by the transmission axis of the analyser. Figure 1.3 illustrates the effect of a half-waveplate and analyser on a totally polarised signal.

Figure 1.3 Schematic of Polariser, Half-Waveplate and Analyser

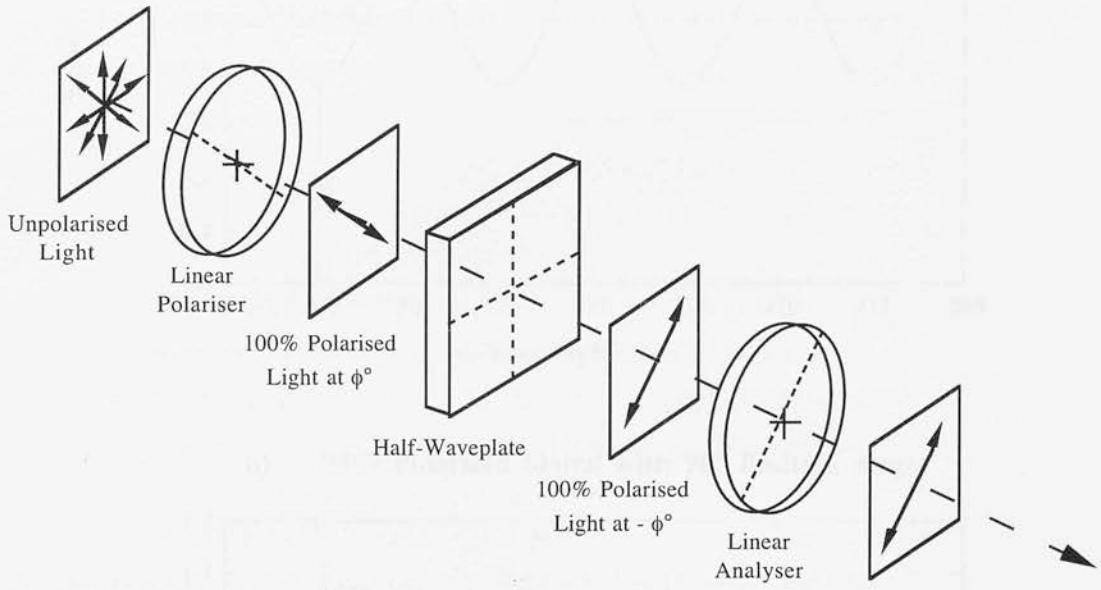

When the fast axis of waveplate is aligned with that of the analyser we say that the waveplate is *at datum* ($\theta = 0°$ where θ is the angle the fast axis makes with the analyser wires). If the initial direction of the **E** vector makes an angle ϕ with the fast axis, then as the two components recombine at the other side of the waveplate, the **E** vector has been turned by an angle of 2ϕ with respect to its original direction, due to the phase shift of π introduced by the waveplate between the two components. As the waveplate position rotates, it changes this angle ϕ and hence rotates the **E** vector of the light. Only the component which is perpendicular to the wires of the analyser can reach the detector. The magnitude of this component is sinusoidally modulated as the waveplate is rotated through a full cycle.

c) Examples

Some special cases will illustrate the effect of this type of polarimeter on a polarised signal. Figures 1.4 show the variation of a *25 %* polarised signal with position angles at a) $0°$ and b) $90°$ through a full turn of the waveplate. The mean signal level is *1.0*, the amplitude of the unpolarised component $I_u = 0.75$ and that of the polarised component $I_p = 0.25$.

Figures 1.4 Examples

a) 25% Polarised Signal with 0° Position Angle

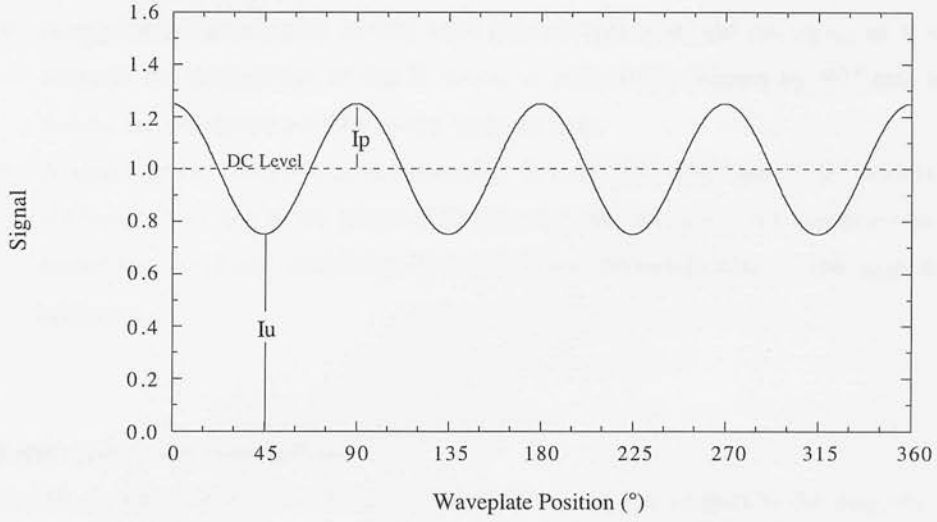

b) 25% Polarised Signal with 90° Position Angle

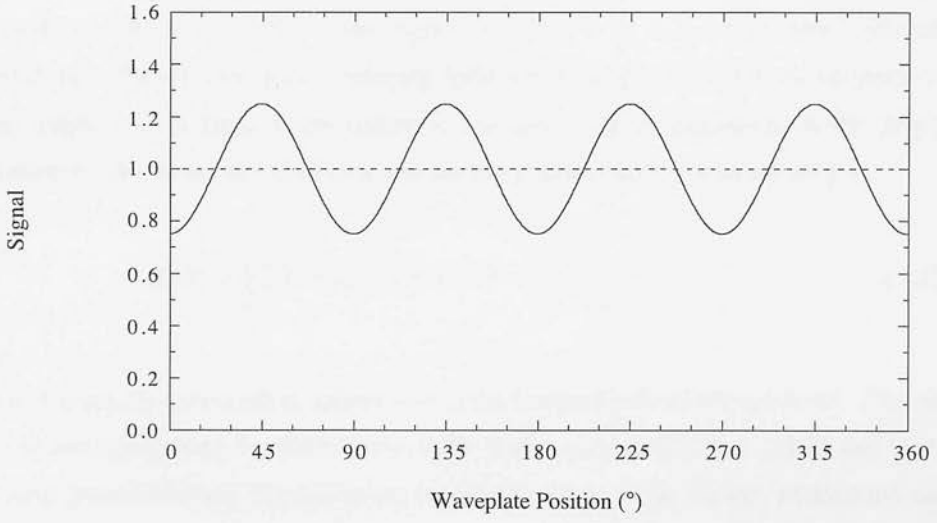

1) Electric Field Aligned with the Analyser

- A maximum in intensity is achieved at waveplate positions $\theta = 0°$ and $180°$ (**E** vector aligned with the plate's fast axis) and $\theta = 90°$ and $270°$ (**E** vector perpendicular to fast axis). This is because at these positions the waveplate introduces no phase shift between the electric field components, and hence the **E** vector maintains its orientation aligned with the axis of the analyser after crossing the waveplate.

- A minimum in intensity occurs at odd multiples of $\theta = 45°$ because the orientation of the electric field is effectively rotated by $90°$ and hence leaves the waveplate perpendicular to the axis of the analyser.

2) Electric Field Perpendicular to the Analyser

- A maximum in intensity occurs with the waveplate at odd multiples of $\theta = 45°$ because the orientation of the **E** vector is effectively rotated by $90°$ and hence leaves the waveplate parallel to the analyser axis.
- A minimum in intensity is achieved for $\theta = 0, 90°, 180°$ and $270°$ because the waveplate introduces no phase shift between the electric field components, and hence the **E** vector maintains its orientation perpendicular to the axis of the analyser.

d) Mathematical Representation

Whatever the orientation χ of the initial polarisation vector with respect to the analyser axis, the combined effect of a rotating half-waveplate and a fixed analyser on a polarised signal is a $cos(4\theta)$ modulation (i.e. a sinusoidal variation with four maxima and four minima). The first maximum occurs when $\theta = \chi/2$ (subsequent maxima are $90°$ apart). The intensity of the signal oscillates about the mean signal level $I\ (= I_u + I_p)$, the amplitude of the oscillation I_p is the amount of the incoming light which is polarised and whose phase is the position angle χ. The ratio of the polarised and mean signal amplitudes is the degree of polarisation P. A mathematical description for the polarimeter's output signal S is:

$$S(\theta) = \frac{1}{2}\left[I_u + I_p\left[1 + \cos(4\theta - 2\chi)\right]\right] \qquad (1.11)$$

The actual intensity measured is halved due to the transmission of the analyser. Expanding the cosine term and using the definitions of the Stokes parameters (1.1), (1.2) and (1.3) for the linearly polarised case, an expression for $S(\theta)$ in terms of the Stokes parameters can be obtained:

$$S(\theta) = \frac{1}{2}\left[I_u + I_p + I_p\left[\cos(4\theta)\cos(2\chi) + \sin(4\theta)\sin(2\chi)\right]\right] \qquad (1.12)$$

$$S(\theta) = \frac{1}{2}\left[I + Q\cos(4\theta) + U\sin(4\theta)\right] \qquad (1.13)$$

Expression (1.13) shows that the variation in the output signal from the polarimeter as the waveplate rotates can be fully characterised in terms of the Stokes parameters I, Q and U.

1.3 Blazars: Polarised Emission and Variability

In the past, every time a distinctive feature was observed to be shared by a few objects a new term was invented to classify them. This has led to the current zoo of names applicable to highly variable extragalactic radio sources such as BL Lac Objects, Highly Polarised Quasars, Optically Violently Variables, Superluminal Sources and finally Blazars. Burbridge & Hewitt (1992) have reviewed the various terminologies associated with these sources and provide a list of 215 objects, most of which could be classified as Blazars. From time to time, voices are raised to banish the Blazar category, on the grounds that it groups together objects that are quite distinct and which originate from different parent populations. Discrepant voices, however, proclaim the equality of all Blazars (and other extragalactic radio sources) in the so-called unifying theories. In this section, the basic characteristics a Blazar must have are described, the origin of their polarised radiation is introduced and the convenience of observing them at millimetre and submillimetre wavelengths justified. The canonical model for Blazar activity and some suggestions about the origin of their extreme variability are briefly presented.

1.3.1 Description of a Blazar

The term *Blazar* is used to describe a subset of extragalactic sources which are compact and radio-loud and whose main characteristics are: a large amplitude variability on short timescales (at all wavelengths from radio to x-rays), flat-spectrum radio emission, steep optical-infrared spectra and substantially polarised continuum emission (e.g. Angel & Stockman 1980). There are two main types of sources included in this category, namely BL Lac Objects and Highly Polarised Quasars (HPQs), traditionally distinguished by the lack of strong emission lines in the BL Lacs when observed at optical wavelengths. All of these sources have a compact radio core and jets (usually single-sided) which extend into the kiloparsec scale. The cores are 'point-like' and mostly unresolved even in high frequency VLBI radio observations. Blandford & Rees (1978) first suggested that these jets lie close to our line of sight and hence any emission (of synchrotron origin) is highly beamed towards us. They usually have a number of 'knots' or radio components which originate from the nucleus of the AGN at epochs of great activity and which evolve as they travel along the jet at superluminal speeds. In some sources stationary knots have been observed, perhaps associated with bends in the jets.

1.3.2 Origin of the Radiation

The bulk of the emitted flux is due to synchrotron radiation (hence non-thermal) displaying a spectral index which is flat over the radio frequencies and becomes steep in the infrared and optical parts of the spectrum. The synchrotron origin of the emission betrays the presence of magnetic fields around which the relativistic electrons gyrate. A full exposition of the theory of synchrotron radiation can be found in e.g. Pacholczyk (1970) but an alternative more pedestrian approach is given in e.g. Longair (1981) or Begelman, Blandford & Rees (1984), who also review the major physical processes at play in extragalactic sources.

a) Synchrotron Radiation

The canonical model of synchrotron emission for extended radio sources considers a power-law distribution of electron energies E with an isotropic distribution of velocities (or pitch angles), immersed in a uniform magnetic field $\boldsymbol{B}$,

$$N(E)\,dE \propto E^{-s}\,dE \tag{1.14}$$

where $N(E)\,dE$ refers to the number of electrons per unit volume. The energy of an ultrarelativistic electron is

$$E = \gamma m_e c^2 \tag{1.15}$$

where γ $\left(= (1 - v^2/c^2)^{-1/2}\right)$ is the Lorentz factor and v is the electron velocity. Relativistic electrons radiate high harmonics of the non-relativistic gyrofrequency ν_g $(= eB/2\pi m_e c)$. The radiation is mostly emitted at characteristic frequency ν_c and Doppler beamed (with angular width γ^{-1}) towards an observer lying in the electron's orbital plane (see Figure 1.5 a)) in time interval $\delta t_{em} \sim \nu_g^{-1}$. The observer sees a pulse of duration $\delta t_{obs} \sim \gamma^{-2} \delta t_{em}$. Therefore,

$$\nu_c \approx \gamma^2 \nu_g \tag{1.16}$$

The energy losses of an electron due to synchrotron radiation are given by

$$\left(-\frac{dE}{dt}\right) = \frac{4}{3}\,\sigma_T\,c\,\left(\frac{E}{m_e c^2}\right)^2 \frac{B^2}{2\mu_o} \tag{1.17}$$

where σ_T is the Thomson cross section.

Figure 1.5 Synchrotron Radiation from an Electron Accelerated in a Magnetic Field

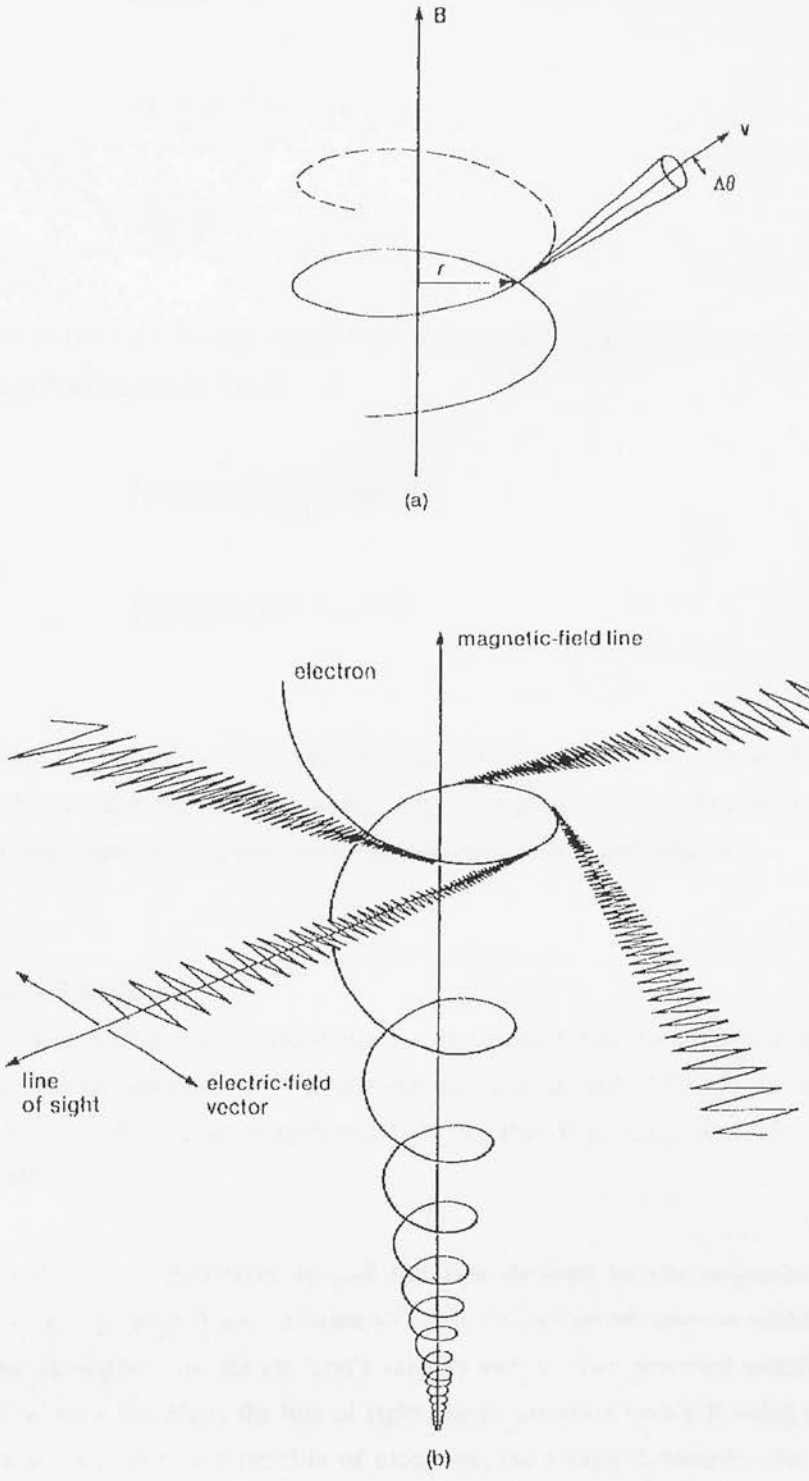

Figure a) shows the angular cone into which most of the radiation is beamed. Figure b) illustrates the polatisation plane of the electric field. (Taken from Bowers & Deeming 1984).

From the above expressions the following dependencies can be established:

$$E \propto B^{-1/2} \nu^{1/2} \tag{1.18}$$

$$dE \propto B^{-1/2} \nu^{-1/2} d\nu \tag{1.19}$$

$$-\frac{dE}{dt} \propto B \nu \tag{1.20}$$

If $I(\nu)\, d\nu$ denotes the energy radiated in the frequency range ν to $\nu + d\nu$ due to electrons with energies in the range E to $E + dE$,

$$I(\nu)\, d\nu = \left(-\frac{dE}{dt} \right) N(E)\, dE \tag{1.21}$$

therefore,

$$I(\nu)\, d\nu \propto B^{(s+1)/2} \nu^{-(s-1)/2} \tag{1.22}$$

The emitted spectrum is a power-law of spectral index $\alpha = -(s-1)/2$ (as shown by equation (1.22) and it is a function of the magnetic field strength (B) and electron energy distribution (s). This holds true for frequencies at which the radiation is optically thin.

b) Polarised Emission

Synchrotron radiation from a single electron is naturally linearly polarised (see Figure 1.5 b)). This can be visualised by considering the cone described by the electron's velocity vector **v** as it spirals around the magnetic field line **B** as Figure 1.6 illustrates (adapted from Longair 1981).

The velocity vector precesses around the axis defined by the magnetic field at the gyrofrequency ν_g. Significant radiation will only be seen by an observer whose line of sight lies within an angle γ^{-1} of the electron's velocity vector. The observed radiation is linearly polarised when **v** lies along the line of sight, the polarisation vector **E** being parallel to the direction $\mathbf{v} \times \mathbf{B}$. For an ensemble of electrons, the emission seen by the observer has contributions from all the electrons with velocity vectors within angular distance γ^{-1} of the line of sight. These contributions will be elliptically polarised in opposite senses on either side of the velocity cone, but given the isotropic distribution of velocities, the polarised components parallel to the projection of **B** cancel out and the resultant polarisation is linear.

Figure 1.6 **Velocity Cone of Relativistic Electron in a Magnetic Field**

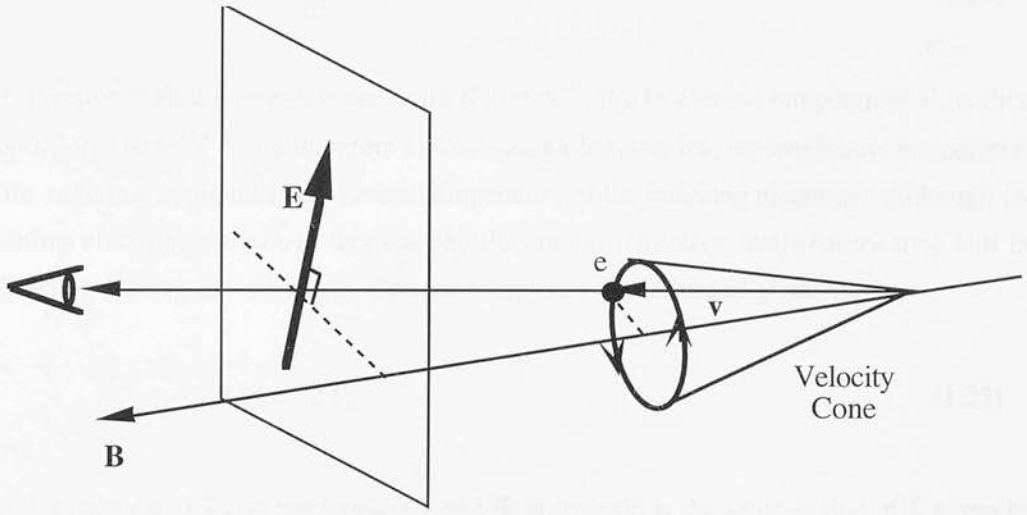

The full theoretical treatment (e.g. Pacholczyk 1970) shows that for a power-law distribution of electrons, such as given by equation (1.14), the degree of linear polarisation of an optically thin homogeneous source in a uniform magnetic field is given by

$$P = \frac{I_{max} - I_{min}}{I_{max} + I_{min}} = \frac{s + 1}{s + \frac{7}{3}} \qquad (1.23)$$

Thus, for typical values of $s = 2.5$ equation (1.23) gives a theoretical maximum linear percentage polarisation of $\sim 72\ \%$. The orientation of the polarisation vector is perpendicular to the projection of the magnetic field onto the plane of the sky. Any disordering of the magnetic field lines will, of course, lower the degree of linear polarisation. Polarimetric observations of extragalactic sources can therefore yield information about the degree of ordering and orientation of the magnetic field.

c) Sub/millimetre Emission

In order to understand the importance of observing compact extragalactic sources at submillimetre wavelengths, one has to consider what happens to the radiation as the energy density of synchrotron emission becomes very large within the emitting volume. Self-absorption effects become important (the electrons absorb as well as emit energy) and the emission resembles that of a black-body at a given temperature.

In the Rayleigh-Jeans limit,

$$I(\nu) = \frac{2\nu^2 k}{c^2} T_b \tag{1.24}$$

For a source with a power-law spectrum $I(\nu) \propto \nu^{-\alpha}$, the brightness temperature T_b is then proportional to $\nu^{-(2+\alpha)}$ and therefore at low enough frequencies, the brightness temperature of the radiation approaches the kinetic temperature of the radiating electrons. Although the emitting electrons are not in thermal equilibrium, an *effective temperature* may still be defined by relating the relativistic electron energy to temperature as given by

$$\gamma m_e c^2 = 3kT_e \tag{1.25}$$

The dependence of T_e on the frequency and field strength is the same as that of E given by equation (1.18).

$$T_e \propto B^{-1/2} \nu^{1/2} \tag{1.26}$$

Therefore, in the optically thick case when $T_b \approx T_e$ the radiation spectrum is approximated by the following dependence

$$I(\nu) \propto B^{-1/2} \nu^{5/2} \tag{1.27}$$

which is independent of the electron energy distribution. Figure 1.7 shows the spectrum of a homogeneous synchrotron source including self-absorption.

The turnover frequency ν_m is at the boundary between the optically thin and optically thick regimes at which the flux output is a maximum. In the case of compact radio sources, this occurs in the millimetre and submillimetre part of the spectrum. This emission arises from the innermost regions at the base of the radio jets, i.e. the unresolved VLBI core when observed at centimetre wavelengths. Since the emission comes from the most compact regions, any activity will be seen first at these wavelengths before evolving into the lower radio frequencies (Gear 1988). This also implies that the variability of Blazars is best monitored in the sub/millimetre where the most energetic stages of Blazar flares occur, spending most of the available energy budget. A further advantage of observing the polarisation of Blazars at these wavelengths is that the emission is optically thin and Faraday rotation is not important, unlike at the longer radio wavelengths.

Figure 1.7 Spectrum of Synchrotron Radiation

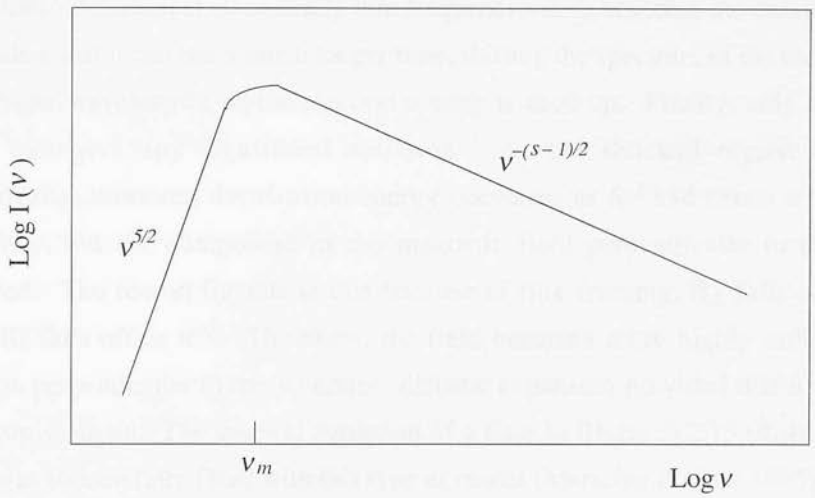

1.3.3 Blazar Variability

a) Modelling Blazar Activity

Models have been proposed in recent years to explain the extreme activity of these sources and deal with the observed evolution of flares. The most successful models consider the creation of shocks in the jets due to a disturbance such as an injection of relativistic particles from the nucleus. This type of model was first proposed by Blandford & Königl (1979) and developed further by Marscher & Gear (1985) using newly acquired infrared - submillimetre data to test its predictions. Hughes, Aller & Aller (1985) and (1989a) have also proposed a similar model based on centimetre waveband polarisation observations.

1) The Shock-in-Jet Model

The emission of a Blazar flares as a shock travels at relativistic speed down the jet (which lies close to the line of sight), compressing the material present, energising the emitting particles and perpendicularising the magnetic field with respect to the direction of the flow (further details are given in § 6.2). The evolution of the flare is characterised in terms of the dominant energy loss mechanism. In the early stages, the photon energy density is very high and Inverse Compton Scattering is the dominant loss mechanism. During this process, relativistic electrons lose energy by colliding with photons, scattering them to much higher frequencies (many extragalactic sources are *x*-ray emitters). The dependence of Compton losses on the size of the shocked

emitting region is $R^{-3.9}$ (Gear 1988) where R is the radius, i.e. much stronger than for synchrotron losses $\propto B^2 \propto R^{-2}$ (equation (1.17)), resulting in a rapid decrease of the amount of energy dissipated by Compton scattering as the emitting region expands. Synchrotron radiation at all optically thin frequencies then becomes the dominant loss mechanism and it can last a much longer time, shifting the spectrum of the emission to ever longer wavelengths as the electron energy is used up. Finally, only adiabatic losses can give any significant emission. As the shocked region expands adiabatically, however, the electron energy decreases as R^{-1} and hence reduces its emissivity, but the component of the magnetic field perpendicular to the jet is enhanced. The reason for this is that because of flux-freezing, $B_{\perp}$ falls off as R^{-1} while $B_{\parallel}$ falls off as R^{-2}. Therefore, the field becomes more highly ordered in a direction perpendicular to the jet under adiabatic expansion provided that it does not re-isotropise again. The spectral evolution of a flare in Blazar 3C273 (Robson *et al.* 1983) was successfully fitted with this type of model (Marscher & Gear 1985).

2) *Alternative Models*

Alternative models have been proposed but which cannot be applied convincingly to a large group of objects to explain all of their observed properties. For example, short-lived, randomly oriented sub-components brightening up at a rate of several per day (Moore *et al.* 1982), or the superposition of sub-components on an underlying steady component (Brindle *et al.* 1985) were fitted to observations of BL Lacertae. Other models proposed include the possibility that the variable emission is due to hot spots orbiting around an accretion disk (e.g. see Begelman, Blanford & Rees 1984), or a collection of supernova explosions (Telervich *et al.* 1992). Other physical mechanisms suggested to explain certain features in the observed activity of Blazars are discussed by Burbridge & Hewitt (1992) (and references therein) and include relativistic expansion of the source, gravitational microlensing by a foreground object and coherent radiation mechanisms.

b) Rapid Variability

In studies of variability, the frequency with which observations are made is of the utmost importance since one can impose a variability timescale by undersampling (Gear 1988) which might lead to erroneous conclusions about the physical processes taking place in these sources. This is illustrated by the fact that the optical emission from some Blazars (especially the BL Lacs) has been measured to change between observations only days apart (e.g. Wills 1989). Rapid variability is observed at all wavelengths and, besides the origin of the strongly variable emission, theoretical models also seek to explain what causes it (e.g. Wiita *et al.* 1992, Miller *et al.* 1992). If the short period variability is due to the same

processes responsible for the origin of the radiation, it may constitute evidence that the emitting region is very compact indeed. However, other physical mechanisms may conspire to enhance the variability of these already very variable sources: this is where gravitational microlensing becomes an attractive proposition (Ostriker & Vietri 1985 and Ostriker 1989). Although this process may apply to a handful of sources, it is ruled out by other evidence which shows that the emitting regions involved would have to be exceptionally compact (Gear 1991). Another possibility is the 'Christmas tree' model (Björnsson 1992), where small subcomponents turn on at random within a given magnetic field structure. Perhaps, a more likely explanation is provided by considering the relativistic effects associated with the 'swinging' of jets and their close alignment with our line of sight (see Gopal-Krishna & Wiita 1992 and Chapter 6).

1.4 Optical and Radio Polarisation of Blazars

An important result that can be obtained from polarisation measurements of Blazars is the degree of ordering of the magnetic field and its orientation with respect to the structural radio jet. This knowledge helps to develop and constrain theoretical models for the energy production and transport mechanisms in these sources. It has also been used to compare the behaviour of the two types of objects within the Blazar category. The polarisation of extragalactic radio sources has been reviewed by Saikia & Salter (1988); an excellent review of what has been learnt about the magnetic fields in extragalactic radio sources from this type of study is given in Perley (1987) and a theoretical interpretation of the implications of these observations to the evolution of the magnetic fields is given in Königl (1987). In this section, polarimetric studies of Blazars carried out at optical-infrared and centimetre wavelengths are reviewed. These will be compared to the results derived from the database obtained with the JCMT at 1.1 mm in Chapter 6.

1.4.1 Optical - Infrared

The optical and infrared polarisation of active extragalactic objects was first reviewed by Angel & Stockman (1980). These sources can exhibit very high levels of polarisation in the visible (more than *20 %* polarisation is not uncommon, see for example Rusk 1990). The polarised flux as well as the intensity are both extremely variable, with variability timescales of days and even hours often reported in OJ287 and BL Lacertae (e.g. Moore *et al.* 1982 and

Holmes *et al.* 1984). Mead *et al.* (1990) carried out a multi-frequency polarisation study of 44 Blazars and candidate Blazars observed in the optical and near-infrared. Most of the sources were observed at 2 or 3 different epochs. The results from their database are discussed in Ballard *et al.* (1990) and can be summarised as follows:

- The spectrum of the radiation is best understood in terms of the shock-in-jet model (see § 1.3.3), i.e. a synchrotron component is the most likely origin of the emission, but significant spectral curvature is found. The spectral behaviour is inconsistent with particle acceleration at relativistic shocks unless the observations were made in the region of a high-frequency cut-off or the source is inhomogeneous.
- Frequency dependence is a common feature of the polarisation behaviour of these sources, with the polarisation and spectral index generally increasing towards the higher frequencies in the BL Lac Objects. However, the frequency dependence of the polarisation position angle is not common and no evidence was found to relate frequency dependence to high levels of polarisation.
- The variability observed did not comply with any characteristic pattern, although it was present in all sources.
- The superposition of the emission from a steady-state lowly polarised component and a more highly polarised shocked component best explains the observations.

1.4.2 Radio

There are two important databases of radio polarisation observations of Blazars on parsec scales: one based on single dish observations carried out by Aller, Aller and Hughes at the University of Michigan, and VLBI polarimetry pioneered by the group at Brandeis University led by Wardle and Roberts. This technique has opened up a new window with its high resolution capability of probing deep into the milliarcsecond regions, where the most intense activity takes place. These observations are well fitted by synchrotron relativistic shock models, as indicated by the results of e.g. Hughes, Aller & Aller (1985, 1989a, 1992).

a) Kiloparsec Scale

The kiloparsec scale magnetic field configuration in extragalactic sources is reviewed in for example Perley (1987). Most of these results are directly applicable to Blazars. Polarimetric observations of jets on kiloparsec scales indicate that high luminosity sources with one-sided jets always have longitudinal magnetic fields throughout the full length of the jet. This is true of all quasars including the compact-core objects. In contrast, low

luminosity sources have two-sided symmetric jets and perpendicular magnetic fields. Some have bright one-sided inner jets where the field is often aligned. The transition from aligned to transverse field may be associated with the emissivity of the jet (Bridle 1984). In the case of bent jets, strong shear and compression at the bend aligns the magnetic field. Shock processes are believed to be responsible for the sudden changes in magnetic field configuration seen for example on bright knots, amplifying the transverse component of the magnetic field (due to flux-freezing) and enhancing the emissivity.

b) Parsec Scale

Milliarcsecond scale radio observations probe closer to the cores of compact radio sources. Available data seems to indicate that the polarisation properties of Active Galaxies and Quasars may be different from those of BL Lac Objects, as illustrated by Figure 1.8 adapted from Rusk (1988). This is a histogram of the orientation of the radio polarisation vector measured with the VLA, with respect to the VLBI structural axis[3].

Figure 1.8 VLBI Jet Orientation – VLA Polarisation Position Angle

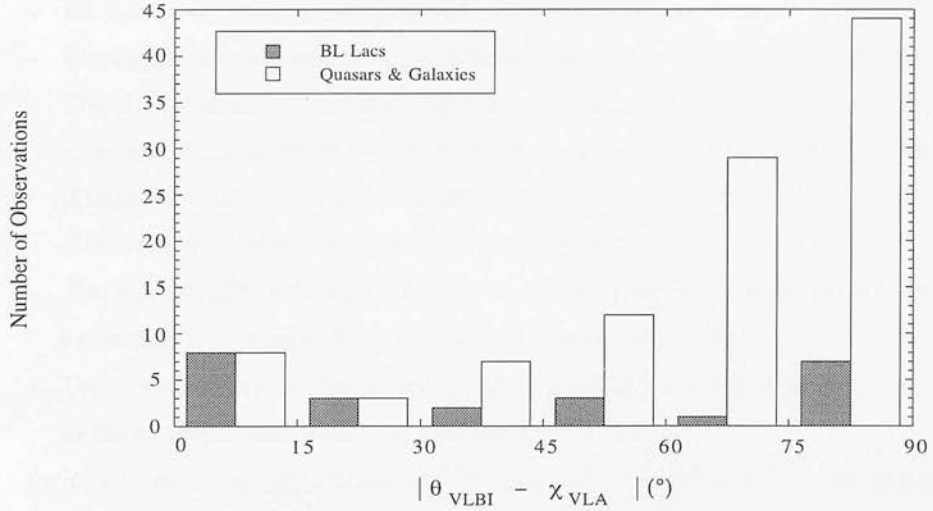

The University of Michigan group have been monitoring the polarisation behaviour of a sample of Blazars for almost 30 years (e.g. Aller, Aller & Hughes 1992). Using a different source sample, they find a similar distribution of $|\theta_{VLBI} - \chi_{VLA}|$ to that shown in Figure 1.8 but with a less pronounced peak near $0°$. The most striking feature in these datasets is the scarcity of points between $15°$ and $60°$. The Brandeis group VLBI polarisation observations

---

[3] $|\theta_{VLBI} - \chi_{VLA}| = 0°$ if the magnetic field is perpendicular and $90°$ if it is aligned with the jet.

are presented in numerous papers but the bulk of their database can be found in Cawthorne *et al.* (1993a) and is discussed in Cawthorne *et al.* (1993b); additional data on a group of BL Lac Objects is given in Gabuzda *et al.* (1994b). The polarised emission from the main VLBI components and the compact cores has been measured at 5 GHz and a significant number of sources have been observed at a number of epochs. Differences between the radio polarisation properties of VLBI jets and cores were first reported in a paper by Roberts *et al.* (1990).

The main results that have come out of the VLBI polarisation database can be summarised as follows:

- Significant polarisation has been detected in *~75 %* of the Blazars observed. In a few instances, the level of polarisation measured in the jets approach the theoretical limit for synchrotron radiation in a uniform field (see § 1.3.2), indicating that significant scales of the magnetic field structure are being resolved.
- BL Lac Objects and Quasars seem to differ in terms of their level of polarisation and inferred orientation of the magnetic field, both in the cores and further out in the jets. The main trends seem to be:
  - BL Lacs have more highly polarised cores than Quasars.
  - The degree of polarisation in Quasars increases with distance from the core.
  - The distribution of position angle in the cores of BL Lacs is bimodal, i.e. the magnetic field tends to be either parallel or perpendicular to the structural axis (Gabuzda *et al.* 1994b and Gabuzda 1994) and not random as previously thought (Gabuzda *et al.* 1992 and Cawthorne *et al.* 1993b).
  - The most highly polarised VLBI cores of BL Lacs (with degrees of polarisation exceeding *5 %*) tend to have perpendicular magnetic fields.
  - The preferred orientation of the magnetic field in the jet tends to be perpendicular to the structural axis in BL Lacs but parallel in Quasars.
- Swings in position angle of up to *60°* have been observed in the core polarisation vector of some BL Lacs which may be associated with the emergence of a new VLBI component (Gabuzda 1994). This view is supported by the fact that a higher polarisation is observed when the position angle is parallel to the jet (i.e. perpendicular magnetic field). This is believed to be caused by an accelerating relativistic shock. In the quiescent state the polarisation would be low and the magnetic field parallel.
- The distribution of speeds of the VLBI components are typically lower in BL Lacs than in Quasars.

Figures 1.9 VLBI Core and Jet Polarisation in relation to the Structural Axis

a) VLBI Jet Orientation - VLBI Core Polarisation Position Angle

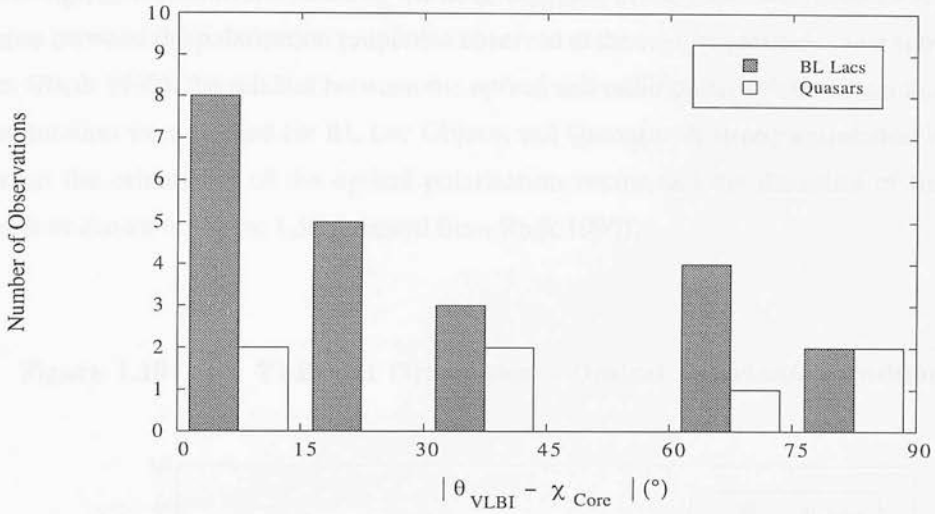

b) VLBI Jet Orientation - VLBI Jet Polarisation Position Angle

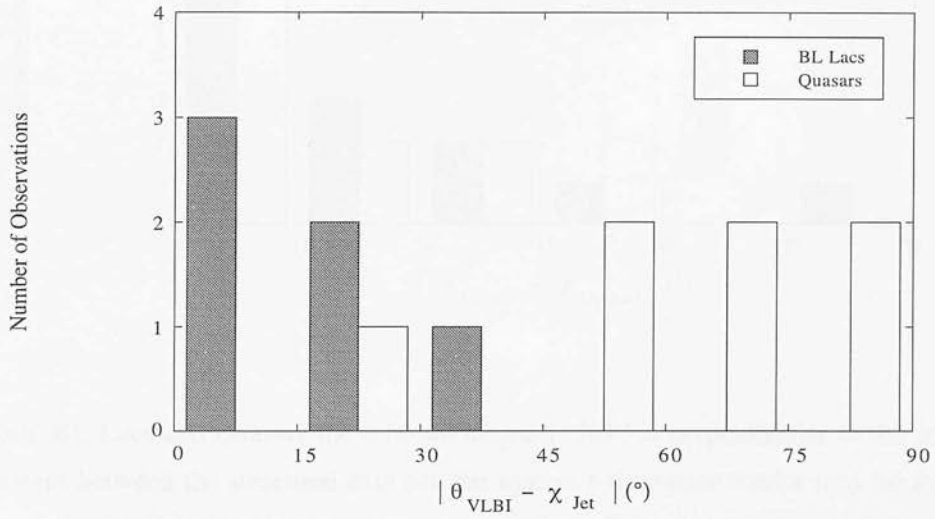

Figures 1.9 illustrate the relation between the structural VLBI jet position angle and the position angle determined from the measurements of a) the core and b) the milliarsecond jet (adapted from Cawthorne *et al.* 1993b and Gabuzda *et al.* 1994b). The histograms clearly show that the data available at the moment is somewhat scarce and probably not statistically significant, therefore the results derived from it must be considered only as preliminary. The techniques employed in VLBI polarimetry are fairly recent and good North-South and East-West coverage is not always available, so selection effects may be affecting the data sample.

1.4.3 The Optical – Radio Link

A database of optical and VLA polarisation measurements on many compact radio sources was compiled from the literature by Rusk & Seaquist (1985) and was used to study the relation between the polarisation properties observed at the two frequencies. In a subsequent paper (Rusk 1990), the relation between the optical and radio polarisation vectors and VLBI jet orientation were studied for BL Lac Objects and Quasars. A strong correlation is found between the orientation of the optical polarisation vector and the direction of the jet in Blazars as shown in Figure 1.10 (adapted from Rusk 1990).

Figure 1.10 VLBI Jet Orientation - Optical Polarisation Position Angle

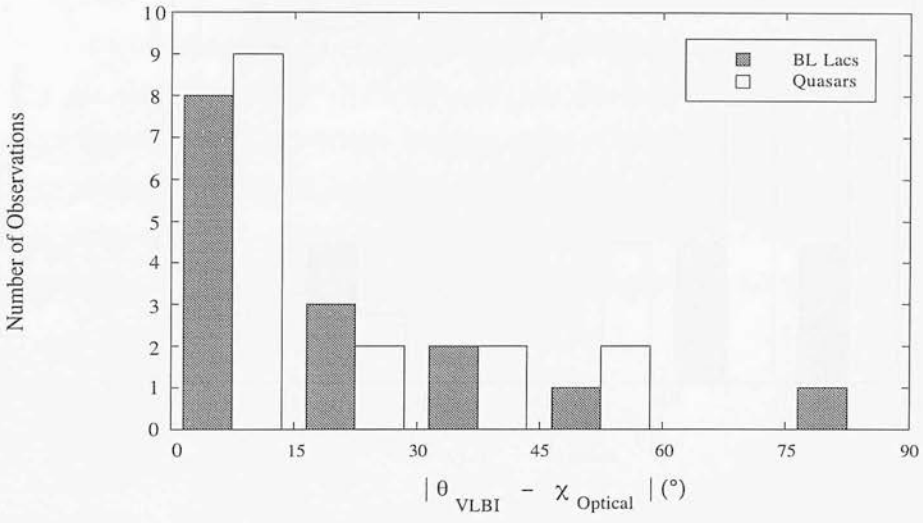

In both, BL Lacs and Quasars the inferred magnetic field is perpendicular to the jet. The alignment between the structural axis and the optical polarisation vector may be evidence that significant curvature between the parsec scale radio emitting region and the region responsible for the optical emission (closer to the core) is rare. In BL Lac Objects, both the radio and optical polarisation vectors lie mainly parallel to the structural axis (see preceding graphs). Impey *et al.* (1991) find the same result for Highly Polarised Quasars but this alignment is not shown on low polarisation objects. These results suggest that the optical and radio emissions may originate in the same region and that the same mechanism is responsible for the radiation. The correlation between the optical and radio variability seen in at least one source, OJ287 (Rusk 1990) supports this scenario. More recently, optical and VLBI polarisation measurements have been compared for five strongly polarised sources

(Gabuzda & Sitko 1994) and evidence was found of a link between the position angles determined in the two wavebands, again indicating that the optical and radio emission regions may coincide spatially.

However, Figure 1.11 (adapted from Rusk 1990) plots the difference in position angle measured in the radio (corrected for Faraday rotation) and the optical for BL Lac Objects and High and Low (optical) Polarisation Quasars (of the LPQs, only the core-dominated objects have been selected). It shows that in the BL Lacs there is a tendency for the optical and radio polarisation vectors to be aligned, whereas in the Quasars they tend to be orthogonal.

Figure 1.11 Difference between VLA & Optical Polarisation Position Angles

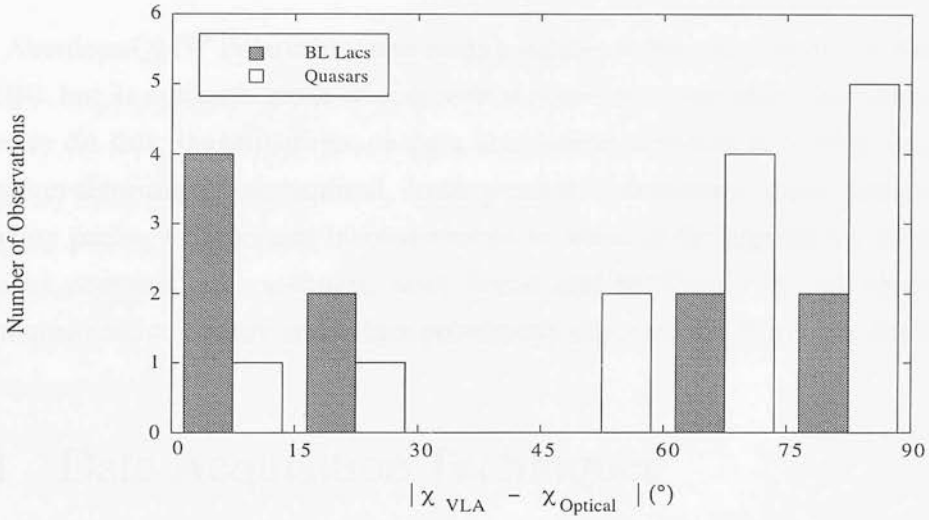

Although there are a number of possible sources of contamination in this plot (like variability at both frequencies or optical measurements of LPQs being affected by foreground interstellar polarisation), it may constitute evidence that Quasars and BL Lacs have different magnetic field morphologies further out in the jets, or that the radio emission in Quasars is affected by physical processes that can lead to a $90°$ rotation of the position angle measured at radio frequencies (perhaps synchrotron self-absorption) which do not affect the optically thin emission in the visible part of the spectrum.

Chapter 2

Submillimetre Polarimetry at the JCMT

The Aberdeen/QMW Polarimeter was made available to the common user at the JCMT in 1990, but its optimum mode of operation was still not completely characterised. In order to do this, investigations on data acquisition schemes and, especially, data reduction algorithms were required. In the process of developing a new data reduction software package, important inconsistencies in some of the algorithms used in the original common user software were found and rectified. In this chapter the techniques used to acquire and reduce polarimetry data with the JCMT are described.

2.1 Data Acquisition Techniques

Acquiring polarimetric data with the JCMT is no more than a sophisticated way of doing photometry with a polarimeter in front of the detector (see Figure 1.2). As in photometry, the contribution from the thermal sky background has to be removed during acquisition. This is achieved by *chopping* with the secondary mirror ON and OFF the source and *nodding* the telescope[1]. There are two possible modes of observation with the polarimeter itself: *Step and Integrate* (SI) and *Continuous Spinning* (CS). The names of the different modes refer to the way in which the waveplate is operated. Doing polarimetry at the JCMT also involves other factors that affect the position angle of the polarisation: a reflection at each mirror, a rotation due to the alt-azimuth mounting of the telescope and a further rotation due to the tertiary mirror, which is used to divert the image to the East Nasmyth focus where UKT14 is located (Murray 1991). These effects may be corrected for during data acquisition or later in

[1] Further details on these techniques are given in § 4.2.2.

software as part of the analysis. In this section the various modes of observation are described and an account of how they have been implemented at the telescope is given.

2.1.1 The Step and Integrate Mode of Observation

In the SI mode the waveplate is sequentially driven to a number of equally spaced positions (corresponding to points on the curve represented by equation (1.13)) where photometric measurements are made. This involves a nod-pair at each position while the secondary mirror is kept constantly chopping. If the positions of the waveplate are carefully chosen, the Stokes parameters can be measured directly, otherwise they can be obtained by fitting the data points mathematically. There are various ways of implementing the SI mode of observation, by selecting different schemes of moving the waveplate and the telescope during data acquisition. Each scheme has different data reduction requirements.

a) Beam Switching Schemes

Different beam switching schemes have different efficiencies, that is the ratio of the amount of time spent integrating on the source to the total amount of time employed to carry out the observation. The efficiency of a beam switching scheme in the SI mode is constrained by the following factors:

- *Dead time of the instrument*
  For each nod-pair, of the order of 2 seconds have to be allowed for the waveplate to be moved to the next integrating position and settle, and some 4 seconds have to be allowed for the telescope to switch beams and settle, making it at least 6 seconds per nod-pair during which the detector cannot integrate on the source.
- *Integration time at each waveplate position per beam switch*
  The longer the integration time the greater the efficiency. However, very long integrations compromise the ability of the switching scheme to subtract the background offset correctly.
- *Total time taken to acquire a polarisation measurement*
  If the time needed to obtain an estimate of the Stokes parameters is very long it can be affected by changes in the sky, and consistent repeatable measurements will be impossible to achieve.

The accuracy of a polarisation measurement cannot be improved by increasing the integration time indefinitely, because the sky may have changed significantly during the

observation. The only feasible procedure is to carry out the observation repeatedly and average the Stokes parameters measured until the required signal to noise ratio is achieved. The success of this approach will depend on the stability of the atmospheric conditions, the brightness of the source and its polarisation level. All these aspects must be taken into account when choosing the most appropriate beam switching scheme.

1) $Q - U$

In this scheme the integrations are carried out at specific waveplate positions that enable the Stokes parameters to be measured directly, with no extra mathematical manipulation. The Q and U parameters are obtained from measurements taken at positions $0°, 22.5°, 45°$ and $67.5°$. Q is obtained from the subtraction of the $0°$ and $45°$ positions and U by subtracting the $22.5°$ and $67.5°$ positions. The Stokes I parameter can be obtained by averaging all four measurements. In this scheme only four positions of the waveplate are needed and, in fact, each quadrant of the waveplate can be used in turn, to obtain four estimates of the Stokes parameters as it is rotated through a whole $360°$ cycle. There are various ways of actually implementing this scheme in order to optimise the number of nods and waveplate moves. The merits of this scheme and analysis procedure are discussed in § 2.3.2.

2) 10 Waveplate Positions

As the waveplate is rotated through $360°$ a photometric measurement (nod-pair) is taken at 10 evenly spaced positions, that is every $36°$. This was the scheme adopted during the commissioning runs and has remained the most widely used for no other good reason. The origin of this scheme has to do with using a Fourier Transform of the data points to obtain the spectral components (more than 8 points are needed to obtain the fourth harmonic of the frequency). The data points can also be fitted by a least squares method.

3) 16 Waveplate Positions

Photometric measurements are carried out at 16 equispaced waveplate positions in a full cycle, i.e. every $22.5°$. The symmetry involved allows the Stokes parameters to be estimated by subtraction of the positions that correspond to Q and U as in *1)* or the data can be fitted by a least squares method (which also allows the data to be de-spiked). One or two estimates of the Stokes parameters can be obtained from a full waveplate cycle by fitting 16 or 2×8 points respectively. The 8-point approach allows to obtain an estimate of the Stokes parameters faster than the 10 waveplate positions scheme and this may be more efficient; the 16-point approach takes twice as long to get an estimate but allows for the removal of a greater number of spikes.

In practice, the optimum beam switching scheme is dependent on the sky conditions and the type of source being observed. Under certain conditions it may be advantageous to obtain the Stokes parameters as fast as possible, even with low signal to noise, but overall it is better to take longer to get an estimate of higher signal to noise which can be de-spiked. A comparison between the performance of the different schemes will be discussed in § 2.3.

b) Angle Tracking Modes

As the source is tracked on the sky during an observation, the polarisation signal is smeared out due to the varying rotation suffered by the position angle of the polarisation vector. This implies that very long integrations on a source are not feasible. The amount of rotation varies with parallactic angle and elevation of the source, being at its worst near the zenith. The rotations suffered by the position angle due to the telescope can be corrected for during data acquisition or at a later stage in software. In fact, both alternatives have their merits (discussed in more detail in § 2.2) and both observing modes have been implemented.

1) Angle Track False (ATF)

The waveplate is driven to the position required by the beam switching scheme in use and a normal photometric measurement is made. This mode of observation is compulsory for measurements of instrumental polarisation (IP)[2] but it can also be used for observing astronomical sources. In addition, the polarisation vector from astronomical sources also suffers the rotation due to the alt-azimuth mounting. Data acquired in this mode have to be corrected for the rotations in software and the IP must be subtracted as part of the data reduction.

2) Angle Track True (ATT)

The amount of rotation suffered by the position angle can be calculated at the time of observation from the position of the source on the sky. The waveplate can then be driven to a position away from its current *nominal* position (as defined by the beam switching scheme adopted), such that the effects of the rotations are cancelled out. Data acquired in ATT mode still have to be corrected in software for an IP which itself has been unnecessarily 'de-rotated' by the action of the waveplate.

---

[2] The main contribution to the IP comes from optical elements forward of the tertiary mirror and hence its position angle suffers a rotation due to it (Murray 1991) but it is not affected by the position of the unpolarised source on the sky.

c) Observation Data Files

More than one revolution of the waveplate can be included in a single observation. The source position recorded in the data file is that at the middle of the observation; if this changes significantly during the integration (like for example when the source is near transit) the corrections for the rotations may be affected. This effect together with the switching scheme adopted and the integration time chosen, limits the number of waveplate revolutions per observation. For example, in the most recent observing runs of the Blazars monitoring programme a 16 position switching scheme has been used, with 8 seconds integration time in each beam at each waveplate position. Each observation comprises 2 full revolutions of the waveplate, which can be analysed in cycles of 4, 8 or 16 points, thus providing 8, 4 or 2 estimates of the Stokes parameters per observation respectively.

2.1.2 The Continuous Spinning Mode of Observation

In the CS mode the waveplate is rotated continuously while the detector is integrating and the secondary mirror chops between the source and the background. This produces modulations in the signal at four times the waveplate rotation rate (i.e. the polarisation signal) and at the chopping frequency (the total power signal). All polarised components, from both the source and the background[3] are modulated. This polarised background has to be measured and subtracted. A nod-pair is completed by carrying out a few seconds integration (between 10 – 20 seconds) with the source in each beam and subtracting them. One clear advantage of this mode of observation over the SI mode is its potentially greater efficiency, since the detector only stops integrating while the telescope is nodding. The CS mode is currently under development and the details of its implementation, both in the laboratory and at the telescope, are the subject of Chapter 3.

2.2 Data Reduction Techniques

A new software package has been developed to reduce polarimetry data acquired with the JCMT. In the process, problems which affected the original data reduction code were identified and corrected and new algorithms implemented. This new code is now

[3] The background may also be partly polarised, even if it is only due to the instrumental polarisation present in the system.

available to the common user at the JCMT. Although the algorithms employed were originally developed to deal with observations acquired in the SI mode (the only one so far implemented at telescope) most are also relevant for the reduction of CS data . In this section the whole approach to the reduction of polarimetry data is reviewed. The algorithms adopted are explained and justified, and the convenience of their use (or otherwise) is discussed. Later in this chapter the performance of this analytical tool will be assessed by using it to reduce real astronomical datasets.

2.2.1 Estimating the Stokes Parameters

The observation is initially recorded on a GSD file (the standard for UKT14). This can be reduced to a series of photometric measurements and their uncertainties at each waveplate position by running a JCMT programme called *'extract_integs'*. The output file also contains a header with all the relevant information about the source's position at the time of observation. This is used to calculate the parallactic angle and the elevation of the source. The Stokes parameters I, Q and U and their uncertainties can be measured directly from the photometric measurements at *specific* waveplate positions, or can be obtained from the fit to a number of data points obtained at *known* waveplate positions. Different fitting procedures can be applied depending on the data acquisition mode employed.

a) Fitting the Raw Data

A mathematical model representing the output signal from an ideal rotating half-waveplate and analyser polarimeter is defined by equation (1.13). This model can be fitted to a number of photometric points measured at known waveplate positions in order to estimate the Stokes parameters.

1) Fast Fourier Transform

If $S(\theta)$ in equation (1.13) is expressed in terms of its Fourier components, Q and U correspond to the cosine and sine coefficients of the fourth harmonic respectively. The Stokes parameters can then be obtained from any number of points greater than 8. Other harmonics may be present and will yield information on instrumental effects (Murray 1991). The main disadvantage of this technique is the inability to exclude spiked measurements from the fit, since the data points must be equally spaced. Because of the need for more than 8 data points, the common practice has been to use a 10-point beam switching scheme, which limits

the analysis methods available for reducing the data. Using this scheme to fit polarimetry data, whole observations may have to be discarded if affected by spikes due to changing weather conditions or electronic glitches, with the consequent waste of telescope time and perhaps still recoverable data.

2) *Least Squares Method*

A least squares method for fitting the data can be useful where the FFT fails because it does not require as many as 8 points, and these need not be equally spaced. This facilitates the removal of spiked data points and hence the observations can be optimised. The optimum data acquisition mode is with a 16 position switching scheme which can be fitted in terms of a full 16-point cycle or two 8-point half-cycles.

i) Fitting a Polarisation Model to the Raw Data

The model represented by equation (1.13) can be fitted to n data points by minimising Δ^2 (the square of the sum of the differences between the measured and predicted values) with respect to each of the Stokes parameters. These differences can be weighted by the uncertainties in the measurements. Hence,

$$\Delta^2 = \sum_{i=1}^{n} \left[\frac{S(\theta_i) - D(\theta_i)}{\sigma_i} \right]^2 \qquad (2.1)$$

where i labels each waveplate position
$S(\theta_i)$ is defined by equation (1.12) for each waveplate position
$D(\theta_i)$ is the photometric measurement made at position θ_i
σ_i is the uncertainty in measurement $D(\theta_i)$

The Stokes vector *(I, Q, U)* wanted is such that

$$\begin{bmatrix} \frac{\partial \Delta^2}{\partial I} \\ \frac{\partial \Delta^2}{\partial Q} \\ \frac{\partial \Delta^2}{\partial U} \end{bmatrix} = \sum_{i=1}^{n} \left[\frac{S(\theta_i) - D(\theta_i)}{\sigma_i^2} \right] \begin{bmatrix} 1 \\ \cos(4\theta_i) \\ \sin(4\theta_i) \end{bmatrix} = \begin{bmatrix} 0 \\ 0 \\ 0 \end{bmatrix} \qquad (2.2)$$

A Singular Value Decomposition (SVD) method (e.g. Press *et al.* 1992) was adopted to solve equations (2.2). It yields not only the best estimate for the

Stokes vector, but also the uncorrelated uncertainties of each parameter. The *number of degrees of freedom* of the fit is $n - p$, where $p = 3$ is the number of parameters to be determined. In principle, the number of data points required must be at least equal to the minimum number of degrees of freedom; in practice it is found that a fit to less than 5 data points does not provide consistent estimates.

ii) De-spiking Procedure

The following procedure was developed to check for spikes in the raw data and remove them:

- A fit to the data would be accepted as soon as its Δ^2 has an *acceptable* value, which a commonly used 'rule of thumb' says that it should be of the order of the number of degrees of freedom (Press *et al.* 1992).
- Firstly, all n points acquired in a whole waveplate cycle are used to find a fit, which is accepted if it yields a good enough Δ^2 or refused otherwise.
- Upon refusal of a n-point fit, all n possible combinations of any $n-1$ points are fitted in turn, and their corresponding Δ^2 worked out. The combination of $n-1$ points fitted with the lowest Δ^2 is selected, thus removing one point in the process. Now the constraints on the acceptance of a $(n-1)$-point fit are harder because the acceptable Δ^2 is lower (one degree of freedom has been lost).
- If the $(n-1)$-point fit is still not good enough, all $n-1$ possible combinations of any $n-2$ points are fitted in turn and again, the fit with the lowest Δ^2 is selected, thus removing a second point. This procedure can be applied until a fit of acceptable Δ^2 is obtained, as long as at least 5 points are retained. If by the time only 5 points remain (one degree of freedom) the value of Δ^2 for the fit is significantly greater than 1, that whole cycle must be rejected.

The efficiency of this procedure can be examined graphically by looking at the quality of the fit before and after de-spiking the raw data. It has been observed that the point that seems to be most out of line with the others is consistently removed. The advantage of removing spiked points in this way resides in that it is done purely on a statistical basis and not subject to bias by an observer hand-picking bad points. Checks were carried out to compare the performance of the FFT and Least Squares methods (without de-spiking) and the estimates of the Stokes parameters derived were identical to the last decimal place in each case. This test was done on both, good and spiked observations.

3) Examples

Figures 2.1 show SVD fits to the normalised polarised component of an observation of Blazar 3C279 acquired in February 1994 using the 16-positions switching scheme. Figure a) corresponds to the 8 points covering the second half-cycle of the waveplate and figures b) and c) show the fits to the data from the first half-cycle before and after de-spiking respectively. The degree of polarisation can be read directly from the plot and the position angle is twice the phase shift of the cosine curve along the x-axis.

In figure a) the data is clearly not affected by spikes and the Δ^2 of the fit was accepted. In contrast, the Δ^2 of the fit to the first half-cycle depicted in b) was too large and was rejected for the 8-point fit and all possible 7-point fits. The fit accepted was the 6-point fit with lowest Δ^2 shown in figure c).

Comparing the data points in b) and c) it can seen that the spiked integrations occurred at waveplate positions $0°$ and $22.5°$ and that the de-spiking algorithm was able to pick them successfully. The polarisation parameters estimated from the three fits are given in Table 2.1.

Table 2.1 Statistics of the Fits in Figures 2.1

Fit	P (%)	χ (°)	Δ^2	Freedom	Points
a)	13.17 ± 0.76	41.64 ± 1.64	5.245	5	8
b)	30.09 ± 1.00	59.84 ± 0.90	>>100	5	8
c)	15.88 ± 0.97	34.96 ± 1.74	3.244	3	6

The polarisation parameters shown above have not been corrected for instrumental polarisation. The position angle is not affected by rotations since the data was acquired with ATT. The fits shown on figures a) and c) (and the parameters derived from them) are comparable and can be averaged together with confidence. However, without de-spiking (in the case of b)) the first half-cycle of the waveplate would have to be rejected. These examples also illustrate how spikes can occur in observations of the brightest and most highly polarised sources even under good sky conditions.

Figures 2.1 Examples of Fits to Spiked and De-spiked Data

a) 8-point fit to non-spiked data

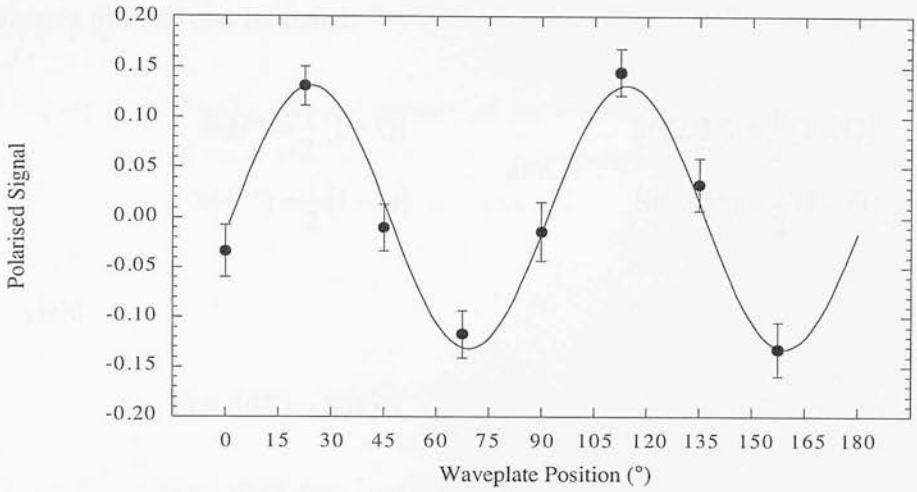

b) 8-point fit to spiked data

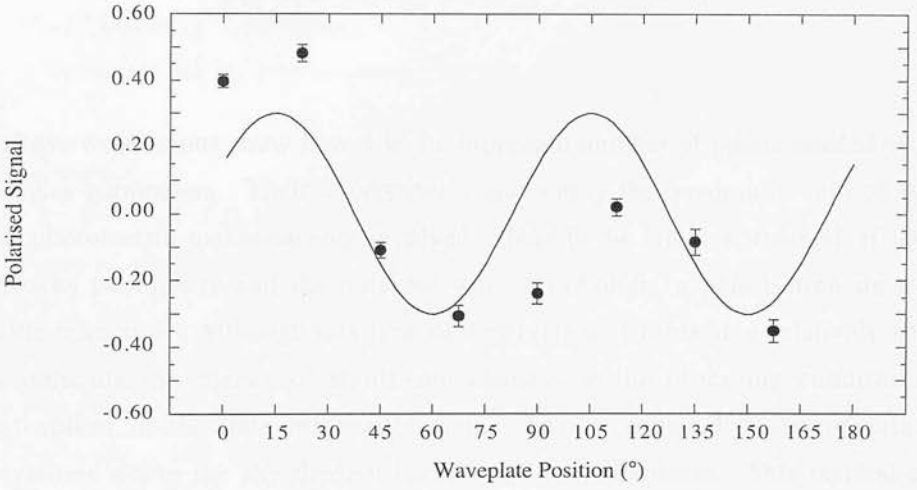

c) 6-point fit to de-spiked data

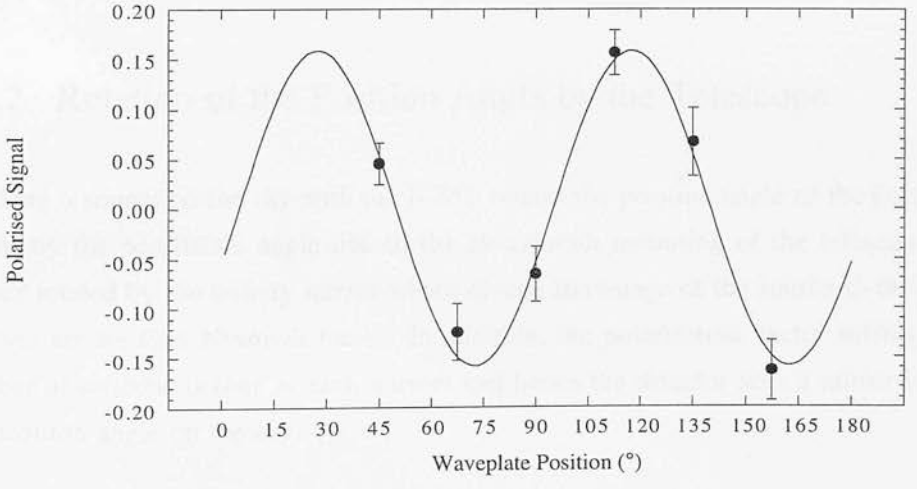

b) Measuring the Stokes Parameters Directly

By inspection of equation (1.13) the waveplate positions needed to estimate the Stokes parameters directly can be found:

$$S(0°) = \frac{1}{2}[I + Q] \qquad S(22.5°) = \frac{1}{2}[I + Q]$$

and

$$S(45°) = \frac{1}{2}[I - Q] \qquad S(67.5°) = \frac{1}{2}[I - Q]$$

yield

$$Q = S(0°) - S(45°)$$

$$U = S(22.5°) - S(67.5°)$$

$$I = \frac{1}{2}[S(0°) + S(22.5°) + S(45°) + S(67.5°)]$$

The above expressions show how 4 is the minimum number of points needed to estimate the Stokes parameters. Their uncertainties are simply the quadrature sum of the errors of the photometric measurements involved. This is the simplest method of measuring the Stokes parameters and the quickest way of obtaining a polarisation measurement with the telescope. Although this type of observation is made in a relatively short time (thus reducing the chance of significant changes in the observing conditions taking place) spikes in the data may still occur. This is especially true of faint object observations where the sky thermal background may dominate. This method does not allow the removal of single spikes and affected observations have to be discarded.

2.2.2 Rotation of the Position Angle by the Telescope

Tracking a source on the sky with the JCMT rotates the position angle of the polarisation vector by the parallactic angle due to the alt-azimuth mounting of the telescope. It is further rotated by the tertiary mirror which diverts the image of the source to the UKT14 receiver on the East Nasmyth focus. In addition, the polarisation vector suffers an odd number of reflections (one at each mirror) and hence the detector sees a mirror image of the position angle on the sky.

The intensity measured by the detector (given by equation (1.11)) can be written as:

$$S(\theta) = \frac{1}{2}\left[I + I_p \cos(4\theta' - 2\chi')\right] \qquad (2.3)$$

where θ is the *nominal* position of the waveplate
θ' is the true position of the waveplate
χ' is the position angle measured

a) Angle Track False

In ATF mode the integration is carried out at the *nominal* position of the waveplate θ and the data needs to be compensated for rotations during its analysis. In this observation mode $\theta' = \theta$ and the true position angle on the sky χ is obtained by applying the following corrections on the measured position angle χ':

1) Odd Number of Reflections
χ' is *multiplied* by (–1) to correct for this effect.

2) Elevation
The elevation ε is *subtracted* from χ' to correct for tertiary mirror rotation for all types of observations (polarised sources and IP measurements).

3) Parallactic Angle
The parallactic angle ρ is *added* to χ' to correct for the rotation due to alt-azimuth mounting, only for observations of polarised sources (it does not affect IP measurements).

Therefore, the relation between χ and χ' and is given by

$$\chi = -\chi' - \varepsilon + \rho \qquad (2.4)$$

b) Angle Track True

In ATT mode the integration is carried out at waveplate position θ' such that the data is compensated for rotations during acquisition, where

$$\theta' = \theta + \frac{\rho - \varepsilon}{2} \qquad (2.5)$$

Then equation (2.3) becomes

$$S(\theta) = \frac{1}{2}\left[I + I_p \cos(4\theta + 2\rho - 2\varepsilon - 2\chi')\right]$$

$$S(\theta) = \frac{1}{2}\left[I + I_p \cos(4\theta - 2(\chi' + \varepsilon - \rho))\right]$$

using equation (2.4)

$$S(\theta) = \frac{1}{2}\left[I + I_p \cos(4\theta - 2(-\chi))\right] \qquad (2.6)$$

Equation (2.6) shows that analysis of ATT data yields the true position angle directly but with its sign reversed and hence it must be compensated for the odd number of reflections only.

c) Note: Compensating for Reflections

The net effect of seeing the mirror image of the true position angle of the polarisation vector at the detector's focal plane (due to the odd number of reflections), is to reverse the sign of the Stokes *U* parameter as determined from the analysis of the data[4]. Since this affects both ATF and ATT measurements, it is corrected for in practice by changing the sign of *U* estimated from the raw data. This problem could be overcome at the telescope by changing the sense of rotation of the waveplate.

2.2.3 Characterising the Instrumental Polarisation

During the commissioning runs of the polarimeter it was established that the main source of instrumental polarisation was the wind blind that covers the entrance of the JCMT dome (Murray 1991). This has been confirmed by the changes observed in the measured values of the IP every time this membrane is replaced or tensed up. In this section, the method for characterising the IP is briefly presented (see also Murray 1991 for a detailed account) and new observations are shown to illustrate it.

---

[4] See equations (1.11) – (1.13) and the definitions of *Q* and *U* equations (1.2) and (1.3).

a) Magnitude of the IP

The IP is determined by observing the planets (considered to be unpolarised sources) in ATF mode. The IP at 800 μm is of the order of a factor 3 smaller than the IP at 1100 μm (roughly *0.50 %* compared to *1.65 %*). At 1100 μm, two different estimates of the degree of instrumental polarisation result from observing different planets: a lower value is obtained if measured on planets that subtend a larger angle than the beam size (e.g. Jupiter and Saturn) and a higher value is measured if the angular size of the planet fits within the telescope beam (e.g. Mars and Uranus). All observations from planets of similar angular size can be averaged to obtain an estimate of the IP with good signal to noise. Which estimate of the IP to use will depend on the type of source being observed. If the source is extended then the IP measured on the large planets should be used, the higher value from the smaller planets is more relevant for 'point-like' objects (see § 4.2.3 for further details and examples).

Figure 2.2 Mars Observations at 1100 μm

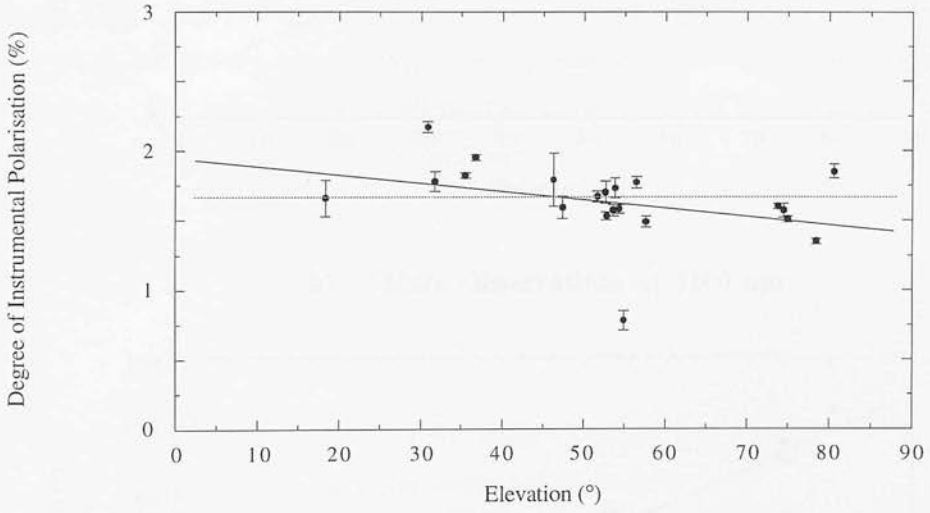

The degree of instrumental polarisation is not expected to be strongly dependent on the elevation of the unpolarised source. Figure 2.2 shows IP observations made on Mars at 1100 μm in October of 1992 plotted against the elevation of the planet. The straight line with the small negative gradient corresponds to a linear fit to the data and the flat line to a weighted average. It can be seen that over the elevation range typical of most observations (*30° – 60°*), the dependence of the IP on the position of the planet on the sky is not very significant and it is well approximated by the mean IP level.

b) IP Position Angle

In contrast with the degree of instrumental polarisation, the zero elevation IP position angle is the same at the two frequencies used and for both, 'extended' and 'point-like' planets (roughly *175°*)[5]. The position angle of the IP tracks with elevation because it originates forward of the tertiary mirror and is therefore rotated by it, but it is otherwise independent of the position of the planet on the sky. Figures 2.3 show the variation of the measured IP position angle (corrected for reflections) with planet elevation.

Figures 2.3 Tracking of IP Position Angle with Source Elevation

a) Jupiter and Mars Observations at 800 μm

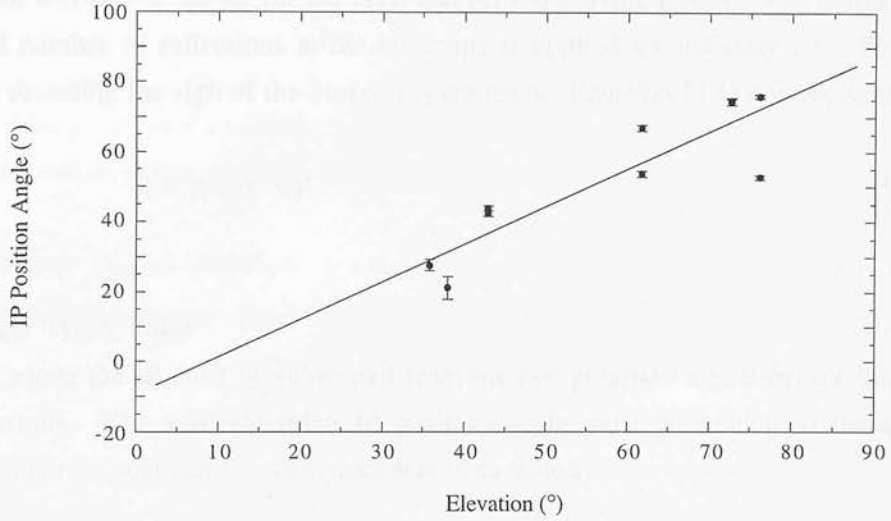

b) Mars Observations at 1100 μm

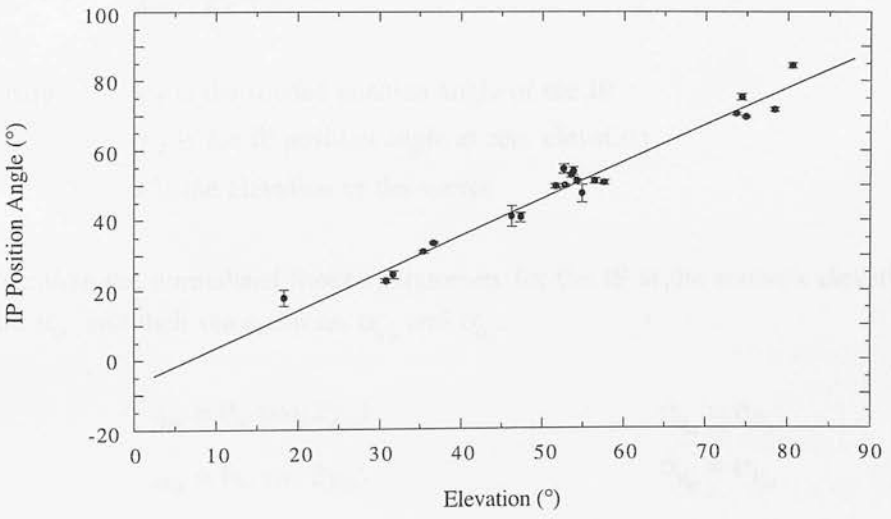

[5] The IP position angle is usually defined at zero elevation. It is obtained by extrapolating a series of measurements acquired with the unpolarised source at various elevations.

The data plotted in figure a) correspond to observations of Mars and Jupiter at 800 μm obtained in January 1992 and those in b) are observations of Mars at 1100 μm acquired in October 1992. A straight line has been fitted to both sets of data with identical results.

2.2.4 Correcting Source Observations for Rotations and IP

The corrections to the raw signal are applied to the normalised Stokes parameters estimated from each individual cycle before they are averaged together. In this section the way in which the corrections for rotations and IP have been implemented in the data reduction software is shown for the ATF and ATT observing modes. The correction for the odd number of reflections at the telescope is applied immediately after fitting the data by reversing the sign of the Stokes U parameter. Equation (2.4) now becomes,

$$\chi = \chi' - \varepsilon + \rho \qquad (2.7)$$

a) Angle Track False

In ATF mode the IP must be subtracted from the raw polarised signal *before* correcting for rotations. The zero elevation IP position angle must be rotated to the source's elevation before subtraction. The procedure is as follows:

i) Rotate the IP position angle by the elevation of the source.

$$\chi'_{ip} = \chi_{ip} + \varepsilon$$

where χ'_{ip} is the rotated position angle of the IP
χ_{ip} is the IP position angle at zero elevation
ε is the elevation of the source

ii) Calculate the normalised Stokes parameters for the IP at the source's elevation: q'_{ip} and u'_{ip} and their uncertainties $\sigma_{q'_{ip}}$ and $\sigma_{u'_{ip}}$.

$$q'_{ip} = P_{ip} \cos(2\chi'_{ip}) \qquad \sigma_{q'_{ip}} = \sigma_{P_{ip}}$$

$$u'_{ip} = P_{ip} \sin(2\chi'_{ip}) \qquad \sigma_{u'_{ip}} = \sigma_{P_{ip}}$$

where P_{ip} is the degree of instrumental polarisation
$\sigma_{P_{ip}}$ is the uncertainty in P_{ip}

iii) Subtract the IP from the raw signal parameters q'_{raw} and u'_{raw} to get the Stokes parameters for the source alone q'_s and u'_s . Their uncertainties are added in quadrature.

$$q'_s = q'_{raw} - q'_{ip} \qquad \sigma_{q'_s} = \sqrt{\sigma^2_{q'_{raw}} + \sigma^2_{P_{ip}}}$$

$$u'_s = u'_{raw} - u'_{ip} \qquad \sigma_{u'_s} = \sqrt{\sigma^2_{u'_{raw}} + \sigma^2_{P_{ip}}}$$

iv) Calculate the position angle of the source χ'_s before the rotations are compensated for.

$$\chi'_s = \frac{1}{2}\,\mathrm{atan2}\left(\frac{u'_s}{q'_s}\right)$$

where *atan2* is a modified *arctan* function[6] that takes into account the individual signs of q'_s and u'_s giving χ'_s in the correct quadrant.

v) Correct χ'_s for elevation ε and parallactic angle ρ to find the true source polarisation position angle on the sky χ_s (equation (2.7)).

$$\chi_s = \chi'_s - \varepsilon + \rho$$

vi) Calculate the normalised Stokes parameters for the corrected source signal q_s and u_s and their uncertainties σ_{q_s} and σ_{u_s}.

$$q_s = P_s \cos(2\chi_s) \qquad \sigma_{q_s} = \sigma_{P_s}$$

$$u_s = P_s \sin(2\chi_s) \qquad \sigma_{u_s} = \sigma_{P_s}$$

where P_s is the degree of polarisation of the source

b) Angle Track True

Data acquired in ATT mode is compensated for rotations during acquisition and this affects both the polarised component from the source and that from the IP. Although the source component has been corrected properly, the IP component has been 'de-rotated' for parallactic angle unnecessarily. Hence, before subtracting the IP from the raw signal, the IP position angle has to be rotated by the parallactic angle to cancel it out.

---

6 The *atan2* function is supported in the 'C' and FORTRAN programming languages.

The procedure used is as follows:

i) Rotate the IP position angle χ_{ip} by the parallactic angle ρ.

$$\chi'_{ip} = \chi_{ip} + \rho$$

ii) Recalculate the rotated normalised Stokes parameters of the IP q'_{ip} and u'_{ip} and their uncertainties $\sigma_{q'_{ip}}$ and $\sigma_{u'_{ip}}$.

$$q'_{ip} = P_{ip} \cos(2\chi'_{ip}) \qquad \sigma_{q'_{ip}} = \sigma_{P_{ip}}$$

$$u'_{ip} = P_{ip} \sin(2\chi'_{ip}) \qquad \sigma_{u'_{ip}} = \sigma_{P_{ip}}$$

iii) Subtract the IP from the raw signal parameters q_{raw} and u_{raw} to get source parameters q_s and u_s. Their uncertainties are added in quadrature[7].

$$q_s = q_{raw} - q'_{ip} \qquad \sigma_{q_s} = \sqrt{\sigma^2_{q_{raw}} + \sigma^2_{q'_{ip}}}$$

$$u_s = u_{raw} - u'_{ip} \qquad \sigma_{u_s} = \sqrt{\sigma^2_{u_{raw}} + \sigma^2_{q'_{ip}}}$$

2.2.5 Averaging Observation Cycles

As discussed in § 2.1 the best signal to noise is not achieved by long individual scans but by averaging repeated scans. This is true of photometric measurements and also for the polarimetry. The Stokes parameters derived from a number of observations can be averaged and then used to estimate the polarisation properties of a source. The number of observations needed to achieve a given signal to noise will depend on the brightness of the source, its level of polarisation and the observing conditions. In this section the criteria adopted for averaging observations of the same source is presented.

a) Checking the Homogeneity of the Observations

As illustrated by Figure 2.1 b) fitting a polarisation model to a few data points does not guarantee a physically meaningful measurement. Even a de-spiked observation with an acceptable fit may be dominated by noise and result in Stokes parameters that do not truly represent the state of polarisation of the source. It is a reasonable assumption to expect a series of repeated measurements of the same object (carried out in the same way

---

[7] In the original analysis procedures (employed to reduce the data given in Appendix B) the uncertainties in the IP Stokes parameters were simply added to those of the source (in both ATF and ATT modes), rather than added in quadrature. However, this has not had any effect on the final result obtained because the Stokes parameters of the source always have much larger errors than those of the IP.

and within a short time scale) to be normally distributed around a mean value. This can be checked by performing a Kolmogorov-Smirnov (K-S) test on the data, where the distribution of each of the measured parameters is compared to a theoretical Gaussian distribution. This test has been implemented in the data reduction software and is carried out on the normalised Stokes parameters after the corrections for rotations and IP have been applied. It is also done on the mean signal level, though no corrections for airmass have been included and this must be used with care. The analytical procedure is as follows:

i) The estimates of each parameter are sorted in ascending order.

ii) The distributions of I, q and u are independently compared against a normal distribution and the four moments of each distribution: mean, standard deviation, skewness and kurtosis are estimated.

iii) The K-S test is performed to calculate the probability that the entries in each distribution are drawn from a unique population.

iv) The sorted measurements, the moments of the distributions and the K-S probabilities are printed on the computer screen. With this information the user must judge if all the estimates are consistent, or if the homogeneity of the measurements could be improved by removing entries that may lie too far from the mean.

v) Individual entries for any of the three parameters can be selected for removal, one at a time. This automatically removes the entries in the distributions of the other two parameters which correspond to the same observation. Then the whole procedure is repeated from the beginning and the improvements on the quality of the data (or otherwise) can thus be monitored.

vi) Once the distributions of the normalised Stokes parameters have been optimised they can be averaged.

The signal to noise achievable also depends on the spread in the values of q and u and this procedure may help to reduce that. However, the significance on this test of homogeneity depends on the number of cycles available. It is not very meaningful to try to match a very small sample of measurements to a normal distribution, but inspection of the actual values of the sorted Stokes parameters can be useful to remove bogus observations.

b) Finding the Mean of the Stokes Parameters

There are two options for averaging the Stokes parameters: an error weighted or a straight statistical average. The resulting uncertainties are the error weighted error and the standard error respectively. Which of the two methods is more appropriate depends on the quality and quantity of the data.

1) Error Weighted Mean

If the number of observations is sufficient and of similar quality, the error weighted average can improve the signal to noise because the error weighted error is normally lower than the standard error. However, if there is a significant spread in the *size* of the errors (or in the Stokes parameters themselves), those observations with larger values and/or smaller errors will be emphasised over the others. If the number of observations to be averaged is small and the measurements are not very consistent with each other, this averaging method is not adequate. For a reasonable number of observations however, the main advantage of this method is that the presence of a few inconsistent measurements have little effect on the result. This averaging method has been implemented as follows:

$$\text{Mean} = \frac{\sum_i \frac{D_i}{\sigma_i^2}}{\sum_i \sigma_i^2} \qquad \text{Error} = \frac{1}{\sqrt{\sum_i \sigma_i^2}} \tag{2.8}$$

where D_i is the value of the i^{th} measurement

σ_i is the uncertainty in D_i

2) Straight Mean

This is a more conservative approach which is recommended when the number of observations is small. It treats all measurements equally and estimates the uncertainty from the spread in the values and the number of observations. It will normally result in a lower signal to noise than the error weighted average and may fail to account for a bad estimate which was not removed in the previous part of the analysis. The mean and standard error are found using:

$$\text{Mean} = \frac{\sum_i D_i}{n} \qquad \text{Error} = \sqrt{\frac{\text{Variance}}{n}} \tag{2.9}$$

where n is the number of points

In practice, for observations where the photometry and the polarimetry are very good (i.e. highly polarised bright sources) the two methods yield similar signal to noise (see examples in § 2.3).

2.2.6 Calculating the Polarisation Parameters

The degree of linear polarisation and the position angle of the electric field vector can be estimated from the normalised Stokes parameters using modified versions of equations (1.7) and (1.9),

$$P_{obs} = \sqrt{q^2 + u^2} \tag{2.10}$$

$$\chi = \frac{1}{2}\,\mathrm{atan2}\left(\frac{u}{q}\right) \tag{2.11}$$

The uncertainties in these parameters are given by,

$$\sigma_p = \frac{\sqrt{(q\times\sigma_q)^2 + (u\times\sigma_u)^2}}{P_{obs}} \tag{2.12}$$

$$\sigma_\chi = \frac{1}{2}\frac{\sigma_p}{P_{obs}} \tag{2.13}$$

Expression (2.10) introduces a statistical bias since the noise in the Stokes parameters always translates into a positive percentage polarisation. The statistical behaviour of these parameters has been investigated (e.g. Clarke & Stewart 1986) and various methods to try to compensate for this effect have been developed. In radio astronomy the correction proposed by Wardle & Kronberg (1974) is usually adopted,

$$P = \sqrt{P_{obs}^2 - \sigma_p^2} \tag{2.14}$$

However, Simmons & Stewart (1985) have shown that some corrections are more appropriate than others, depending on the signal to noise available and the levels of polarisation involved. In general, the Wardle & Kronberg correction is best for signal to noise $P/\sigma_p \geq 0.7$. This has been implemented in the data reduction software since a lower signal to noise would be considered a non-detection. The uncertainty in the position angle is correctly approximated by equation (2.13) if $P/\sigma_p \geq 3$.

2.3 Tests on Astronomical Datasets

In this section astronomical datasets are used to test various aspects of the analysis discussed in § 2.2. In particular, the algorithms presented in § 2.2.4 to correct data for the rotations in the position angle introduced by the telescope and the subtraction of the IP need to be tested in the two observing modes ATF and ATT. Also the procedures for estimating and averaging the Stokes parameters are compared.

2.3.1 Correcting for Rotations and IP

a) Selection of Test Sources

1) Rotations Correction

Observations of Taurus A obtained during the polarimeter commissioning runs are ideal for testing the algorithm that corrects for the position angle rotations, because this source is very bright and its polarisation is high, with a fairly well known position angle. It was observed at 1100 μm (in both ATF and ATT modes) in September 1989 and June 1990. At radio and optical wavelengths its polarisation has been measured to be *13 %* and *21 %* respectively, at position angle *135°* (Murray 1991).

2) IP Subtraction

The polarised dust emission from OMC1 can be used to check the correctness of the IP subtraction algorithm. It is a bright object with low polarisation (of the order of the IP itself), so that failure to subtract the IP correctly would result in an inconsistent detection (see Table 2.3). Observations of this source at 1100 μm obtained in September 1989 and in August 1993 (in both ATF and ATT modes) are available. Its degree of polarisation lies between *1–2 %* at position angles between *16° (± 8)* in the infrared and *40° (±8)* at 1300 μm (Murray 1991).

b) Results

Both Taurus A and OMC1 are extended sources so the IP at 1100 μm to be used is that measured on planets such as Jupiter and Saturn. Tables 2.2 and 2.3 summarise the results from the ATF and ATT observations of these objects, with and without IP correction[8].

[8] The relevant IP values are given in Table 4.3 in Chapter 4.

From inspection of Table 2.2 it can be established that both modes of observation yield the same result, which agrees with the position angle measured at other wavelengths, thus proving that the rotations induced by the telescope have been properly accounted for.

Table 2.2 **Taurus A observations at 1100 μm**

		Without IP Subtraction		*IP Subtracted*	
Epoch	**Mode**	**P (%)**	**χ (°)**	**P (%)**	**χ (°)**
September 1989	ATF	23.68 ± 1.59	139.84 ± 1.91	24.32 ± 1.59	140.85 ± 1.87
June 1990	ATF	27.24 ± 2.82	137.87 ± 2.95	27.52 ± 2.83	139.18 ± 2.93
June 1990	ATT	25.46 ± 3.62	142.89 ± 4.03	26.18 ± 3.62	144.14 ± 3.92

Table 2.3 **OMC1 observations at 1100 μm**

		Without IP Subtraction		*IP Subtracted*	
Epoch	**Mode**	**P (%)**	**χ (°)**	**P (%)**	**χ (°)**
September 1989	ATF	1.95 ± 0.05	37.08 ± 0.68	1.24 ± 0.05	47.38 ± 1.17
August 1993	ATF	2.33 ± 0.06	26.42 ± 0.74	1.34 ± 0.07	46.01 ± 1.40
August 1993	ATT	1.10 ± 0.04	23.09 ± 0.94	1.38 ± 0.04	39.44 ± 0.84

From the results in Table 2.3 the importance of the IP correction becomes obvious. Without correcting for the IP the measurements are not consistent with each other. When the IP is subtracted they become consistent and the degree of polarisation of OMC1 turns out to be of the same order as the IP at 1100 μm. The fact that low levels of polarisation can be measured with good signal to noise in the presence of a comparable IP, is a strong indication that the algorithm for the subtraction of the IP have been correctly implemented.

2.3.2 Comparison of Data Analysis Schemes

a) Observations

Observations of extragalactic sources 3C279, 3C273 and OJ287 acquired at 1100 μm have been analysed in a number of ways to compare different data reduction schemes.

All three sources were acquired with a 16-positions switching scheme and were phase compensated during acquisition (ATT mode). The details are given in Table 2.4.

Table 2.4 Observations

Source	Epoch	Polarisation	Brightness	Flux (Jy)	Cycles
3C279	February 1994	high	bright	13.46 ± 0.49	8
3C273	May 1994	low	bright	11.34 ± 0.87	16
OJ287	May 1994	high	faint	1.33 ± 0.13	28

b) Analysis

The results of the analysis are shown in Table 2.5. The analysis procedures employed are listed below:

- The Stokes parameters have been obtained by direct estimation from the photometric measurements (4 points), by fitting every half-cycle of the waveplate (8 points) and by fitting full waveplate cycles (16 points). The 8 and 16-point estimates were de-spiked.
- The IP has been subtracted from the normalised Stokes parameters.
- A Kolmogorov-Smirnov test has been carried out and spurious estimates removed.
- The normalised Stokes parameters have been averaged with error weighting (*wgt*) and without it (*std*).
- The polarisation parameters have been calculated and the percentage polarisation corrected for bias.

Table 2.5 Three Source Polarisation Analysis

		3C279		*3C273*		*OJ287*	
NP	**Mean**	**P (%)**	**χ (°)**	**P (%)**	**χ (°)**	**P (%)**	**χ (°)**
4	std	14.81 ± 0.57	40.87 ± 1.09	0.14 ± 0.76	95.20 ± 28.2	3.30 ± 5.33	123.60 ± 24.4
4	wgt	15.19 ± 0.68	40.74 ± 1.28	1.36 ± 1.43	88.65 ± 93.0	57.18 ± 4.89	20.11 ± 2.44
8	std	14.69 ± 0.40	40.58 ± 0.78	2.44 ± 0.73	122.92 ± 8.18	19.42 ± 6.67	84.74 ± 9.31
8	wgt	14.78 ± 0.33	40.40 ± 0.63	2.16 ± 0.51	130.45 ± 6.60	13.17 ± 3.58	57.02 ± 7.51
16	std	15.01 ± 0.40	39.75 ± 0.76	1.56 ± 0.67	124.29 ± 11.3	10.04 ± 5.88	91.51 ± 14.5
16	wgt	14.99 ± 0.32	39.69 ± 0.62	1.85 ± 0.51	134.07 ± 7.62	7.47 ± 4.01	73.08 ± 13.6

c) Discussion

The results from the various analysis schemes are assessed below for each source in turn. The comparison can be done because the data have been optimised by de-spiking and/or removing bad estimates from the average. The performance of the two averaging algorithms is also compared.

- *3C279*

  This is a very bright and very highly polarised source. The number of full waveplate cycles acquired (8) is minimal, yet the signal to noise is very high. Whichever option is chosen to estimate and average the Stokes parameters, yields the same result in degree of polarisation and position angle (well within the errors) and to very similar signal to noise. This result confirms that all the approaches to data analysis are equally valid when the data is of the highest quality. It also shows that, under such ideal conditions, not a lot of data is required, since this measurement was obtained in less than 25 minutes of total telescope time.

- *3C273*

  This is also a very bright source but with low polarisation. The weather during the May 1994 run was not as good as in February (when the observations of 3C279 were taken) and this may play a part in the difficulty for obtaining a measurement. The 4-point estimates cannot be de-spiked and no detection at all is extracted from them. The 16-point de-spiked fits give a poorer result than the 8-point fits, probably because of changing sky conditions during the observations. All this indicates that changes in the sky background affect the performance of the various data acquisition and reduction schemes, and make the task of measuring low levels of polarisation even more difficult. The best signal to noise is obtained from the 8-point fits. The two averaging methods yield similar results but the error weighting seems to help in improving the signal to noise.

- *OJ287*

  This source was observed in similar sky conditions as 3C273 but presents the opposite characteristics, it is faint (just over 1 Jy) and highly polarised. The performances of the analysis schemes are similar to the case of 3C273. No detection at all can be obtained from the 4-point estimates; this is most likely due to the inability to remove the spikes in the data. Fitting the raw data points with de-spiking allows to obtain a measurement but only just, eventhough 28 waveplate cycles are available. Again 8-point estimates perform better than 16-point ones and in this case a clear advantage is obtained from error weighting the average.

d) Conclusions

1) Estimating the Stokes Parameters

Under ideal sky conditions and for easily observable sources, there is no appreciable difference between measuring the Stokes parameters from 4, 8 or 16 data points. When the sky background is unstable and/or the source is either lowly polarised or faint, 4-point estimates fail to yield a result. The better performance of the least squares fitting procedure is without doubt due to the possibility of de-spiking the observations. If the sky conditions are changing rapidly a quicker estimate (8 points) is better.

2) Error Weighted Mean

There is not much difference in the signal to noise achievable between using the standard and error weighted mean of the Stokes parameters, but a slight difference may be introduced in the actual values of the polarisation obtained. This is because those observations with smaller errors are emphasised if error weighting is applied. Also, if the number of observations is small, the standard error is always larger than the error weighted error and results in a lower signal to noise. On the whole, no problems have become apparent by using error weighted averages, unless very few and/or noisy observations are used to obtain upper limits on the polarisation (e.g. 4-point estimates of OJ287). Under these conditions a straight average is a more reliable approach.

Chapter 3

Development of the Continuous Spinning Mode

At present, polarimetry at the JCMT can only be done in the Step and Integrate (SI) mode. In this chapter the work carried out to develop the Continuous Spinning (CS) mode for the Aberdeen/QMW Polarimeter is reviewed. It includes a description of the principles behind this polarimetric method, the approach adopted to deal with the analysis of digitally recorded data and an account of the tests carried out in the laboratory and the telescope. The objective of this work is to reproduce in the CS mode, measurements carried out in SI and establish a comparison between the two methods.

3.1 Introduction

3.1.1 Basic Operational Principles

In the CS mode the waveplate is rotated continuously while the detector is integrating, making it potentially more efficient than the SI mode since it can achieve a higher integration to total time ratio. This is because the integration need not be stopped while the waveplate is moved to the next position and wait for the system to settle. As in the SI mode, the photometric signal is modulated by chopping ON and OFF the source at a selected rate. The rotation of the waveplate affects the polarised component alone, by modulating the signal at four times the waveplate's spinning rate (see § 1.2.4). However, if there is any instrumental polarisation in the system or the background signal has a small polarised component, the OFF source measurement too gets modulated by the action of the waveplate. Therefore, chopping ON and OFF the source is no longer sufficient to effectively remove

the background from the raw signal. This can only be done by making a measurement of the background itself, which must be temporally related to the source signal. Reference signals from the chopper and waveplate spinner module are needed in order to demodulate the receiver output. This can be done electronically using a Phase Sensitive Detector (PSD), or in software by digitising the raw and reference signals. The novelty of this work lies in the digital approach adopted to reduce the raw data.

3.1.2 Electronic versus Software Demodulation

There are two modulations in the signal to deal with: the photometric one due to the action of the chopper and that on the polarised component due to the action of the waveplate. Each modulation can be removed electronically by a combination of single and 2-phase Lock-In Amplifiers (LIAs), that phase the raw signal with the references from the chopper and waveplate driver. The output of the LIA is fed to a Digital Volt Meter (DVM) that converts the signal to a voltage, which can be input to a computer where the polarisation analysis is carried out. The alternative approach is to digitise the bolometer output and the reference signals from the chopper and waveplate driver using a multichannel Analogue to Digital Converter (ADC) to sample the signals at a suitable rate. This is driven from a microcomputer, where the digitised output is recorded. The signal can then be demodulated in software. Both these approaches were tried in the laboratory. However, the modulated background still needs to be subtracted from the source signal. In principle, the main difficulty involved is to make a measurement of the background which is temporally related to the source signal. In the analogue system, this requires a separate observation of the background alone to be carried out after the source observation and, in real observing conditions, these are hard to relate (as found from experiments carried out during the polarimeter commissioning runs at the telescope (Murray 1991)). The advantage of the digital approach is that the data is recorded in its raw state, without any electronic processing other than linear amplification, and different software methods for decoding the signal can be tried *off-line*. The only disadvantage of this technique is the amount of memory needed to store the data and CPU time required to reduce the observations.

3.1.3 Outline of the Work Carried out

In order to establish the viability of the software approach to demodulation of a digitally recorded signal, a computer programme was written to generate synthetic data, so that

different data reduction procedures could be tested. These techniques were then tried on real data acquired in the laboratory, which enabled further development and understanding of the techniques required. A brief test was also carried out at the JCMT. In the remainder of this chapter the techniques developed to acquire and reduce the data and the results of the laboratory and telescope tests are described.

3.2 Computer Simulation

Computer code was written to simulate data acquired in the CS mode in order to test the performance of different analysis procedures under varying conditions. In this section, the results obtained with the various data analysis schemes investigated are reviewed.

3.2.1 Generating Synthetic Data

The simulation programme generates a digitally sampled polarised signal as if modulated by a rotating waveplate. It is further modulated by 'chopping' ON and OFF the *source*. The two modulation frequencies and the sampling rate[1] can be selected. The two parts of the signal, corresponding to (*source+background*) and (*background*), are mixed with randomly generated Gaussian noise and a selectable level of instrumental polarisation. The mean source and background signal levels can be set independently, so that faint sources can be simulated against a much brighter background. The background signal can also be made to 'drift' with time and beam switching (equivalent to telescope nodding) has been implemented to counteract this effect.

An example of simulated CS data is illustrated by Figures 3.1. These show a 'one-second' integration plotted in units of unity source brightness, the background being 10 times brighter than the source. The source is *5 %* polarised with a position angle at *40°*. The chopping modulation frequency is 10 Hz and the polarisation modulation is 4 Hz, produced by spinning the waveplate at 1 Hz. Figure a) plots the idealised signal before any instrumental polarisation or sky noise is added. Figure b) contains two curves: the dotted line is the same as in a) (included here for reference) and the solid line is produced by the same base signal but mixed with an IP of *1.5 %* at position angle at *0°*, randomly generated Gaussian noise of the same amplitude as the source signal and a random background drift.

[1] The sampling rate in this case is the number of points *per second*. A second is defined by the choice of modulation frequencies.

3.4.2 Data Analysis Schemes

The data reduction software has to perform a similar function to the phase sensitive detector in the SI mode in order to remove the background[2] and also calculate the Stokes parameters. There are two different approaches depending which of these functions is carried out first.

Figures 3.1 Idealised 5 % Polarised Signal Sampled in CS Mode

a) Clean Source Signal

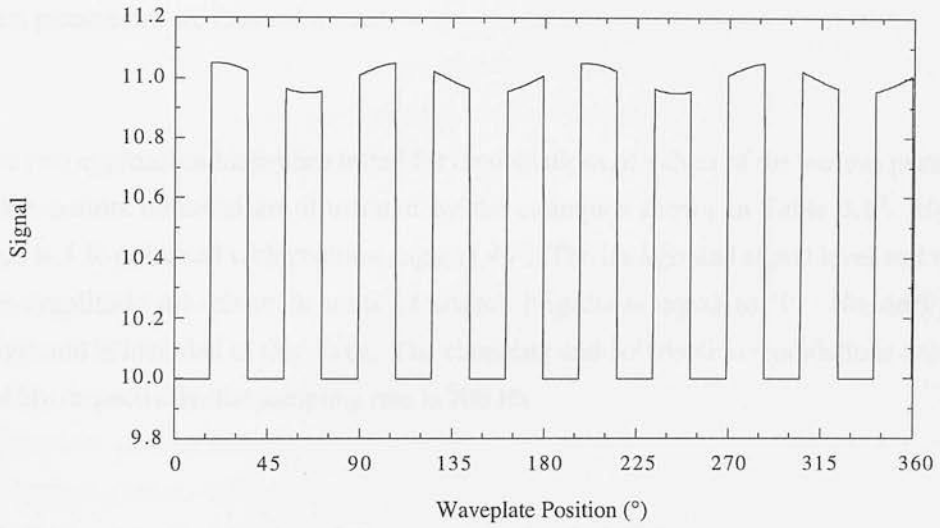

b) Source Signal with IP and Sky Noise

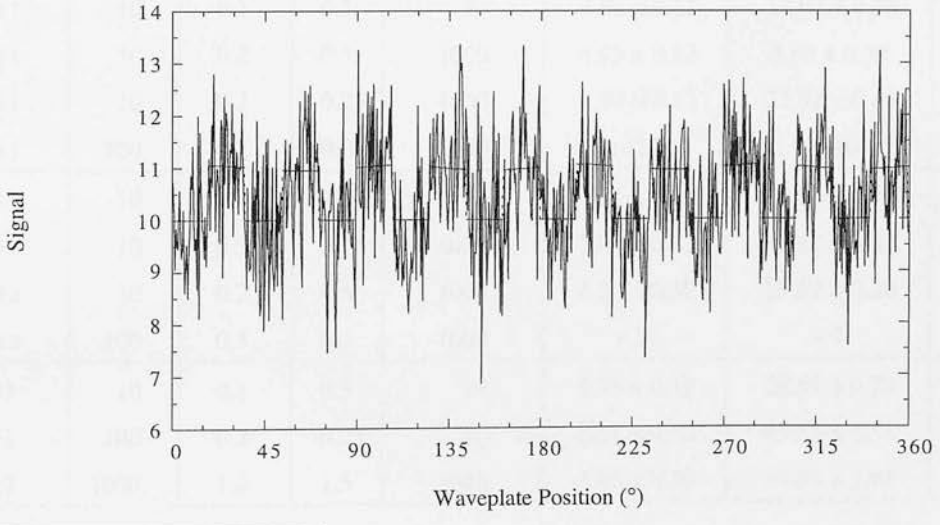

[2] The background can be estimated from the part of the signal acquired while chopping OFF the source.

a) Subtraction of the Background *before* Fitting the Data

For each chopper cycle the average of the background samples is subtracted from that of the source samples The resulting number is assigned to a waveplate position centred on the source samples and then the data is fitted to a polarisation model to estimate the Stokes parameters as done in the SI mode (see Chapter 2). Alternatively, the background is estimated from the chopper half-cycles immediately preceding and following the source signal.

b) Subtraction of the Background *after* Fitting the Data

The least squares fitting algorithm described in § 2.2 is independently applied to the source and background data samples acquired during a one-second integration. The resulting Stokes parameters are then subtracted.

These two approaches have been tested for combinations of values of the various parameters and the results obtained are illustrated by the examples shown in Table 3.1[3]. Here the source is *5 %* polarised with position angle at *40°*. The background signal level and the sky noise amplitude are given in units of source brightness equal to '1'. No drift in the background is included at this stage. The chopping and polarisation modulations are 10 Hz and 4 Hz respectively; the sampling rate is 200 Hz.

Table 3.1 Results from Different Data Analysis Schemes

Analysis Scheme	Sky Signal	Noise Level	IP (%)	Integration Time (sec)	Polarisation (%)	Position Angle (°)	OK
a) 1	10	0.1	0.3	30	4.02 ± 0.11	18.02 ± 0.76	×
a) 1	10	0.2	0.5	1000	4.93 ± 0.12	5.68 ± 0.72	×
a) 1	10	0.2	0.25	1000	4.10 ± 0.13	23.92 ± 0.88	×
a) 1	100	0.2	0.25	1000	> 24	~ 160	×
a) 2	10	0.1	0.3	30	5.51 ± 0.09	32.06 ± 0.49	×
a) 2	10	0.2	0.25	1000	5.65 ± 0.12	33.42 ± 0.63	×
a) 2	10	0.2	0.5	1000	6.34 ± 0.12	27.57 ± 0.56	×
a) 2	100	0.5	0.5	1000	> 24	~ 7	×
b)	10	0.1	0.3	10	5.25 ± 0.15	38.51 ± 0.79	√
b)	100	0.2	0.25	50	4.45 ± 0.52	41.55 ± 3.31	√
b)	1000	1.0	1.5	1000	4.96 ± 0.59	34.94 ± 3.41	√

[3] Analysis scheme a) has been labelled '1' if the background is estimated from a single chopper cycle and '2' when it is estimated from two half-cycles either side of the source signal.

The results in Table 3.1 clearly show that the most efficient way of removing the background from the source signal is to do it in terms of the Stokes parameters. For example, for the very noisy signal shown in Figure 3.1 b) this method yields a polarisation measurement of *4.96 % ± 0.59* at position angle *34.94 ± 3.41* after a 1000-seconds integration, while the other two algorithms fail to unscramble the data.

3.4.3 Examples

The computer code has been run extensively combining the various parameters so as to simulate sources of different brightness and polarisation levels, observed under different types of sky noise conditions and with high and low levels of instrumental polarisation. In the following examples, beam switching (nodding) is performed every 10 seconds. A sample of the results obtained are listed in Table 3.2. The amplitudes of the sky signal and noise level are given in units in which the source signal is equal to '1'; the sky drift is given as a percentage of the sky signal. Throughout the experiments the modulation frequencies used are 4 Hz and 10 Hz for the polarisation and chopping modulations respectively; a sampling rate of 200 Hz was used. The result of the same experiments with other (adequate) combinations of modulation frequencies yield very similar results. Within the scope of this simulation the actual choice of modulation frequencies does not appear to be a crucial factor.

The main conclusions from these tests are:

- Faint sources in a bright background should be detected in the CS mode.
- Subtraction of the modulated background can be done most efficiently by estimating the Stokes parameters of the source and background signals separately.
- In the absence of sky noise the signal from the source (no matter how faint) is always recoverable even with significant IP. As the sky worsens, faint sources become increasingly more difficult to detect, requiring ever longer integration times and achieving poorer signal to noise.
- Highly polarised sources are easily detected even in noisy conditions, but sources with low polarisation (of the order of the IP level) are always difficult to observe even for very bright sources

Table 3.2 Simulated CS Measurements with IP and Sky Noise

Source Polarisation	Sky Signal	Sky Drift	Noise Level	IP (%)	Integration Time (sec)	Polarisation (%)	Position Angle (°)
5 % @ 40°	10	0	0.0	1.0	20	5.00 ± 0.00	40.00 ± 0.00
5 % @ 40°	10	1	0.0	1.0	20	4.77 ± 0.13	39.72 ± 0.80
5 % @ 40°	10	1	0.0	1.0	100	5.00 ± 0.06	40.00 ± 0.36
5 % @ 40°	100	1	0.0	1.0	200	4.57 ± 0.41	39.48 ± 2.54
5 % @ 40°	1000	1	0.0	1.0	200	2.41 ± 1.25	34.96 ± 13.16
5 % @ 40°	1000	1	0.0	1.0	1000	4.08 ± 1.72	39.25 ± 11.13
5 % @ 40°	1	1	0.25	1.0	20	3.61 ± 1.05	40.97 ± 7.98
5 % @ 40°	1	1	0.25	1.0	200	4.57 ± 0.35	37.65 ± 2.17
5 % @ 40°	1	1	0.25	1.0	1000	4.98 ± 0.15	38.74 ± 0.86
5 % @ 40°	10	1	0.25	1.0	1000	4.98 ± 0.13	38.74 ± 0.77
5 % @ 40°	100	1	0.25	1.0	1000	4.92 ± 0.07	38.67 ± 0.39
5 % @ 40°	1000	1	0.25	1.0	1000	4.14 ± 1.55	38.00 ± 10.06
5 % @ 40°	1000	1	0.5	1.0	2000	3.97 ± 0.75	36.60 ± 5.31
5 % @ 40°	1000	1	0.5	1.0	3000	4.76 ± 0.96	38.41 ± 5.65
5 % @ 40°	1000	1	1.0	1.0	3000	5.01 ± 0.82	37.36 ± 4.66
5 % @ 40°	1000	1	1.0	1.5	3000	5.02 ± 0.82	37.16 ± 4.64
5 % @ 40°	2500	1	1.0	1.5	3000	4.16 ± 2.02	36.29 ± 12.53
5 % @ 40°	2500	1	1.0	1.5	10000	5.51 ± 1.97	38.50 ± 9.63
5 % @ 40°	5000	1	1.0	1.5	10000	3.87 ± 5.21	39.24 ± 23.01
1 % @ 40°	1	0.5	0.5	1.5	3000	1.22 ± 0.18	35.03 ± 4.20
1 % @ 40°	100	1	0.5	1.5	1000	1.01 ± 0.27	27.25 ± 7.46
1 % @ 40°	1000	1	0.5	1.5	1000	1.01 ± 0.26	23.65 ± 7.08
1 % @ 40°	1000	1	1.0	1.5	2000	1.44 ± 0.18	22.38 ± 3.61
1.5 % @ 40°	10	1	1.0	0.5	1000	1.54 ± 0.61	24.07 ± 10.55
1.5 % @ 40°	1000	1	1.0	0.5	2000	1.63± 0.08	29.28 ± 1.35
1.5 % @ 40°	1000	1	1.0	1.5	2000	1.77± 0.14	25.92 ± 2.26
2.5 % @ 40°	1000	1	1.0	1.5	3000	2.77± 0.29	34.80 ± 3.02
15 % @ 40°	1000	1	1.0	1.5	1000	12.45± 4.52	37.95 ± 9.78
15 % @ 40°	1000	1	1.0	1.5	3000	14.02 ± 3.01	39.00 ± 6.02

3.3 Laboratory Tests

The development of the CS data acquisition and analysis techniques hinges on the results obtained from experiments carried out using the JCMT prototype polarimeter module. These were done using the telescope simulator at the Astrophysics Laboratory, QMW, to measure different levels of polarisation with a bright source. In this section the basic experimental arrangement used is presented and the characteristics of the raw signal and its software treatment discussed. Finally, the results obtained from the various tests carried out with high and low level source signal are shown and compared with similar measurements made in the SI mode.

3.3.1 Experimental Set-Up

A schematic of the basic experimental set up arranged on an optical bench in the laboratory is shown on Figure 3.2. The main components are the following:

- A He-3 bolometer receiver system with a filter stack[4] optimised to detect the signal provided by a black-body source at 800 μm. A chopper wheel in front of the black-body makes the receiver alternate between seeing the source and the background.
- A sample of a partially polarising material (fluorogold) and a wire grid polariser can be placed on a rotatable sample holder in front of the black-body source, to provide partially and totally polarised light at various known position angles.
- The polarimeter module enclosing a half-waveplate[5], driven from pulses generated by a computer, is set up in the middle of a Gaussian beam telescope so that light travels parallel through the waveplate, improving the 'cleanliness' of the system and optimising the amount of signal available.
- An analyser wire grid is placed in front of the receiver window[6].
- An analogue-to-digital converter card (ADC) on the computer is used to sample and digitise the bolometer signal (amplified by a low noise amplifier) and the reference signals from the chopper and the polarisation modulation[7].

---

[4] The filter stack comprised an 800 μm bandpass filter, a standard 55 cm^{-1} waveband edge filter and an 18 cm^{-1} waveband polypropylene edge filter.
[5] The operation of a rotating half-waveplate polarimeter is described in § 1.2.
[6] The analyser is angled with respect to the window, to avoid any reflections from it bouncing off other surfaces in the system back into the detector.
[7] The polarisation modulation frequency is four times the waveplate's rotation frequency.

Figure 3.2 **Schematic of the Basic Experimental Arrangement**

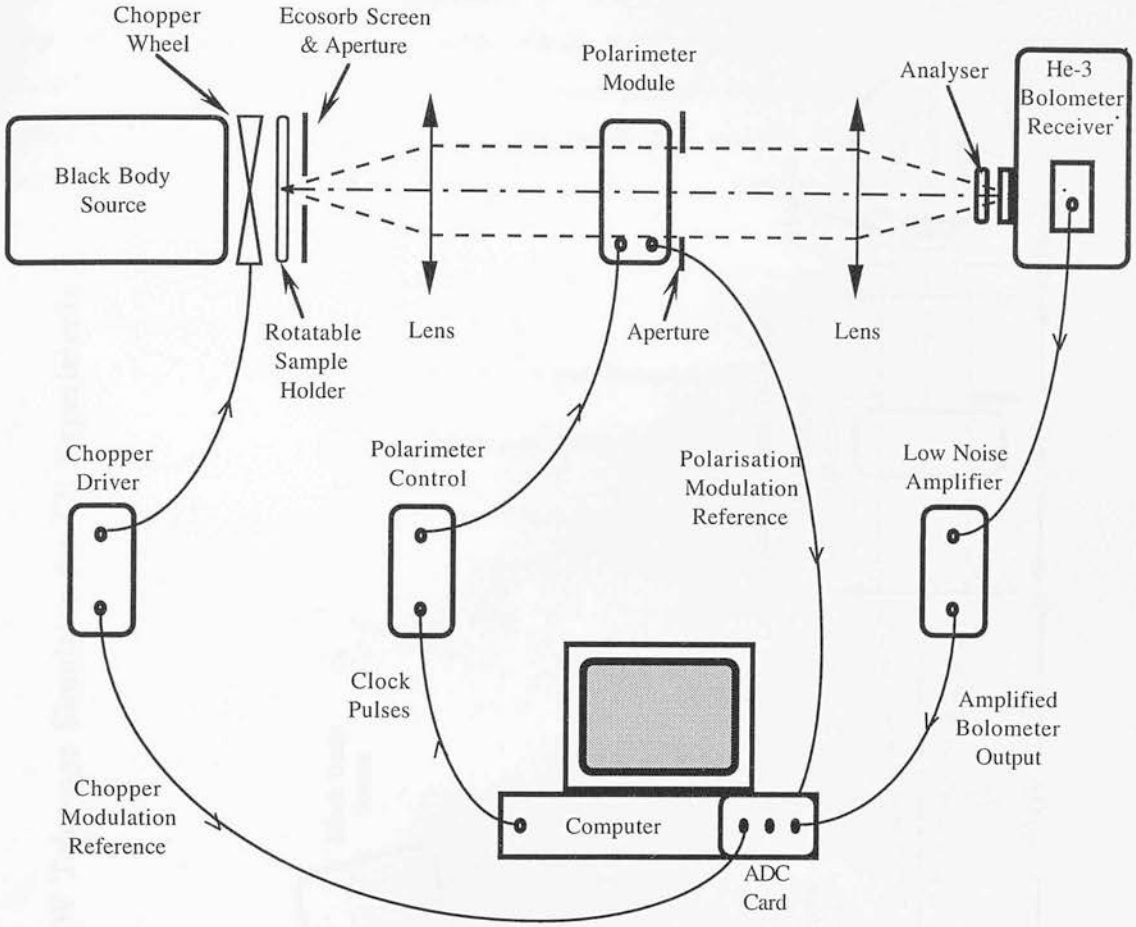

A set of experiments were carried out using the full telescope simulator arrangement, with its image plane coinciding with the object plane of the Gaussian beam telescope. Figure 3.3 shows the optical layout. Choppers '1' and '2' were tried independently to check whether there are any differences between chopping behind the source sample (*chopper 1*) or at the focal plane (*chopper 2*). However, the telescope simulator did not provide as clean a signal as the simpler basic arrangement, see for example the signals plotted in Figure 3.5 a) (obtained with the telescope simulator) and Figures 3.7 c) (obtained without it).

3.3.2 Characterisation of the Raw Signal

The detector output is affected by the response of the bolometer at the frequency of the modulations present in the raw signal, therefore the choice of adequate chopper and waveplate frequencies is of crucial importance.

Figure 3.3 Optical Layout of the QMW Telescope Simulator for CS Experiments

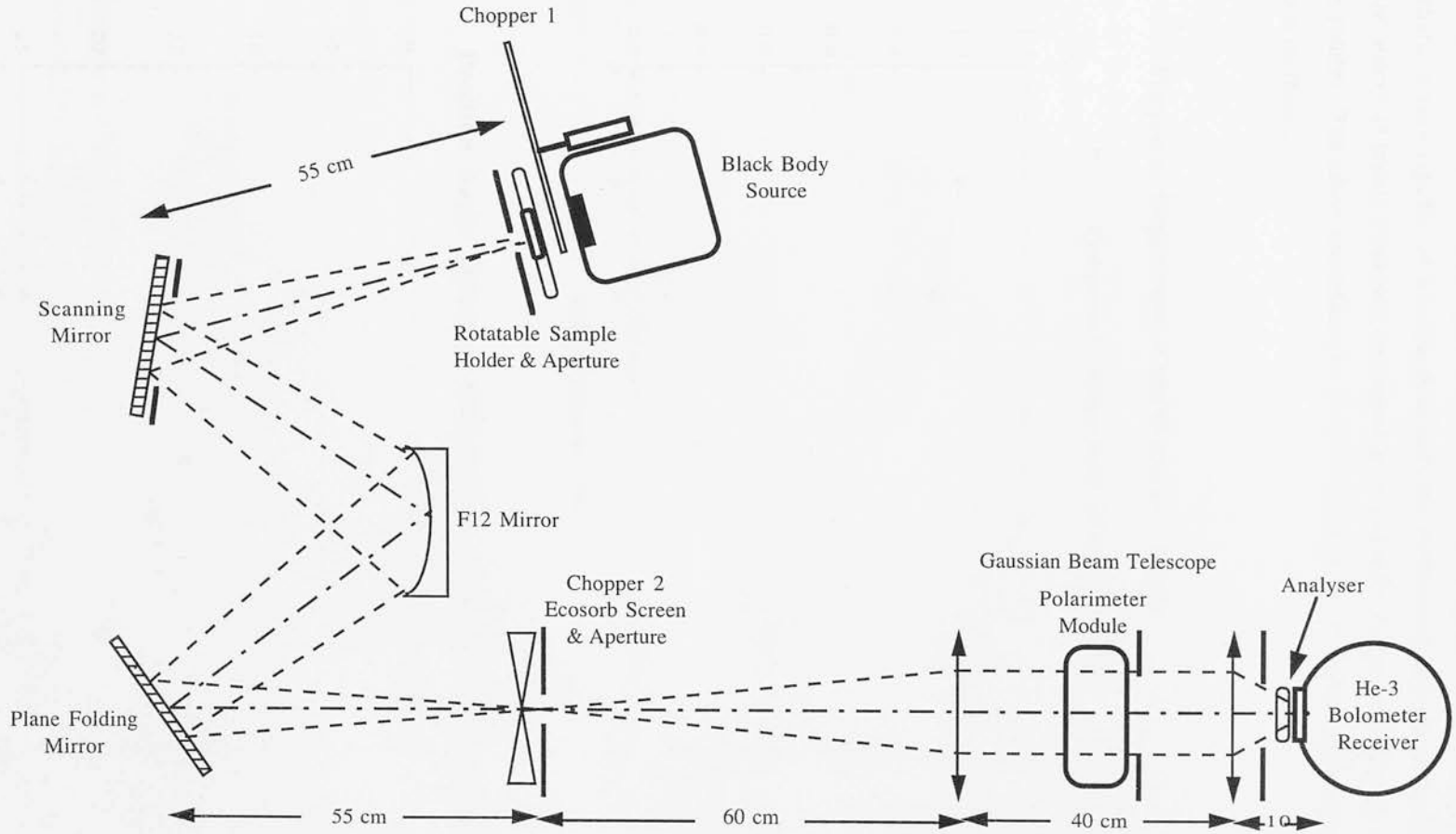

a) The Bolometer Frequency Response

The bolometer has a finite time-constant which means that its response drops when the signal level changes very rapidly, as it is the case with the modulation introduced by the chopper. If the source is highly polarised, the signal level can also change significantly as the waveplate rotates. Therefore, the efficiency of the detector rolls off as the frequency of the modulations increase.

Figures 3.4 Frequency Dependence of the Bolometer Output

a) Frequency Response of a Bolometer

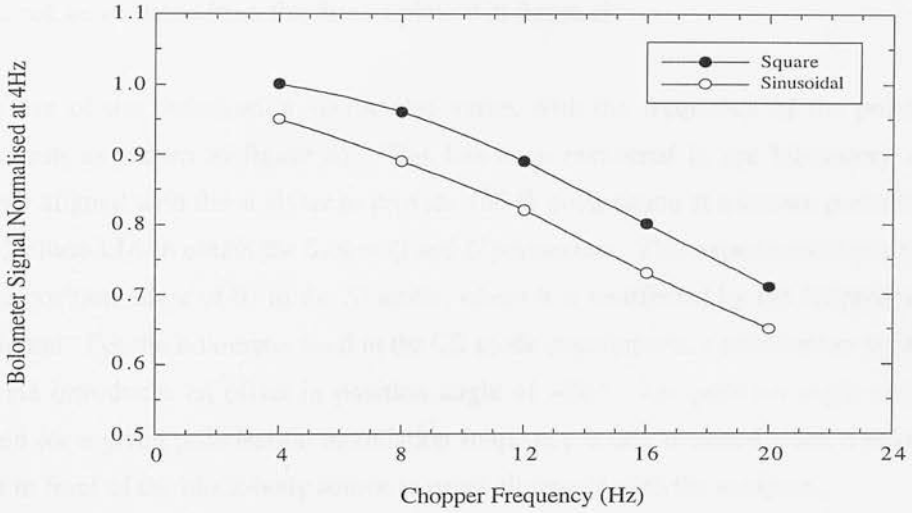

b) Position Angle Offset vs Polarisation Modulation Frequency

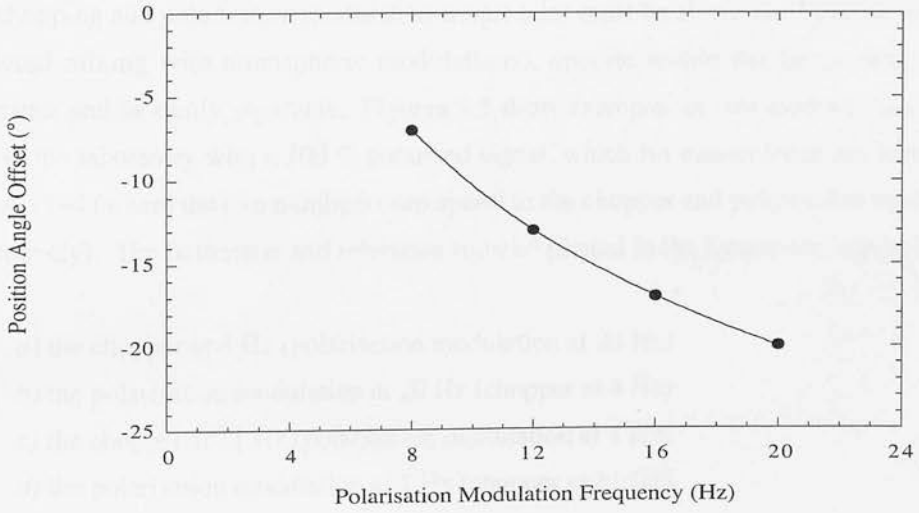

Figures 3.4 show the effects that increasing the modulation frequency of a signal has on the bolometer output. Figure a) illustrates the variation in the bolometer output with frequency for square wave (chopping) and sinusoidal (polarisation) modulated signals. Experiments carried out in the laboratory show that the overall shape of the frequency response curve is the same for both types of modulations, although the rms amplitude of the fundamental component at a given frequency is higher for a square wave modulated signal. This has important implications for the calibration of polarisation data: while the chopping modulation affects both components of the signal (polarised and unpolarised) equally, the polarisation modulation only affects the polarised component. This means that the polarised component could be underestimated relative to the unpolarised component and, unless it is calibrated, it would result in a lower degree of polarisation being measured. The calibration factors can be obtained from the dataset plotted in figure a).

The phase of the polarisation vector also varies with the frequency of the polarisation modulation as shown in figure b). This has been measured in the laboratory using a polariser aligned with the analyser to provide *100 %* polarisation at a known position angle, and a 2-phase LIA to obtain the Stokes Q and U parameters. This experimental arrangement gives a position angle of $0°$ in the SI mode, where it is unaffected by the frequency of the modulation. For the bolometer used in the CS mode experiments, a polarisation modulation of 20 Hz introduces an offset in position angle of $-20°$. The position angle correction required for a given polarisation modulation frequency is that obtained when a polariser is placed in front of the black-body source in exact alignment with the analyser.

b) The Choice of Modulation Frequencies

The chopping and polarisation modulation frequencies must be above the *1/f* noise spectrum (to avoid mixing with atmospheric modulations), operate within the linear range of the bolometer and be easily separable. Figures 3.5 show examples of two modulation schemes tried in the laboratory with a *100 %* polarised signal, which for convenience are labelled 4–20 and 11–4 (where the two numbers correspond to the chopper and polarisation modulation respectively). The bolometer and reference signals[8] plotted in the figures correspond to:

a) the chopper at 4 Hz (polarisation modulation at 20 Hz)
b) the polarisation modulation at 20 Hz (chopper at 4 Hz)
c) the chopper at 11 Hz (polarisation modulation at 4 Hz)
d) the polarisation modulation at 4 Hz (chopper at 11 Hz)

[8] The reference signals are superimposed on the bolometer signal, so that the effects of each modulation can be identified.

Figures 3.5 **Modulation Frequencies Effects on the Output Signal**

a) 4-20 Signal and Chopper Reference at 4 Hz

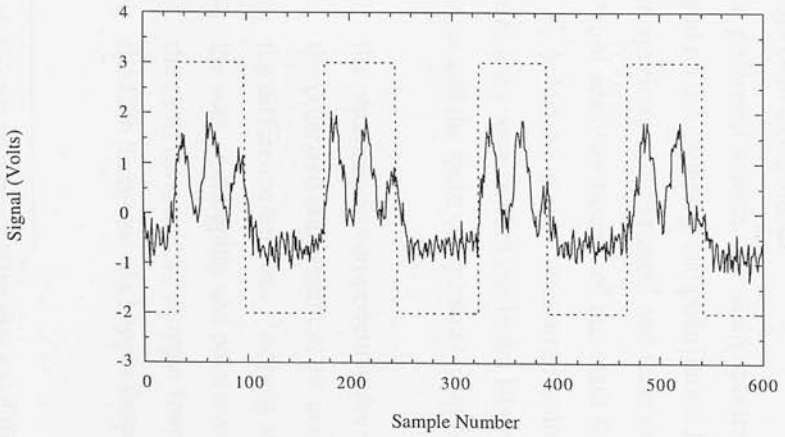

b) 4-20 Signal and Polarisation Modulation Reference at 20 Hz

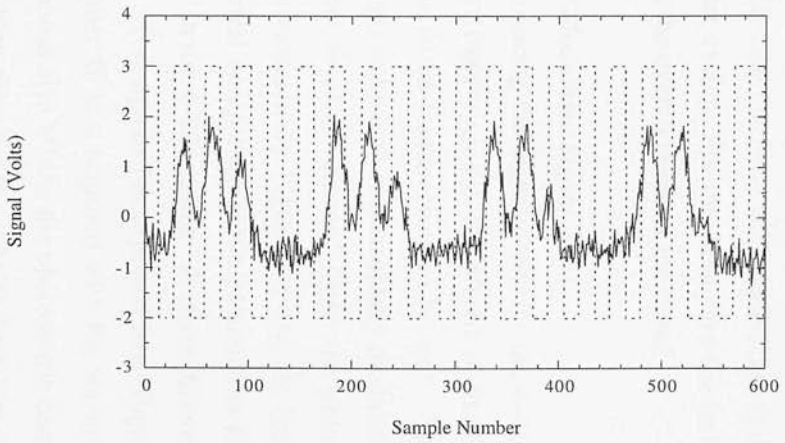

c) 11-4 Signal and Chopper Reference at 11 Hz

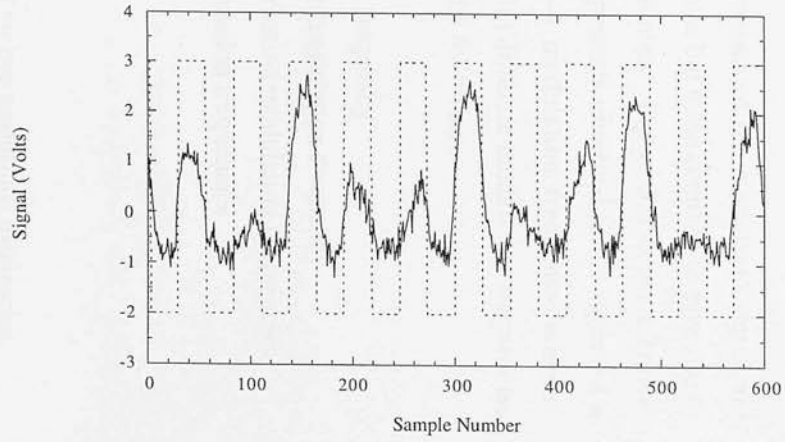

d) 11-4 Signal and Polarisation Modulation Reference at 4 Hz

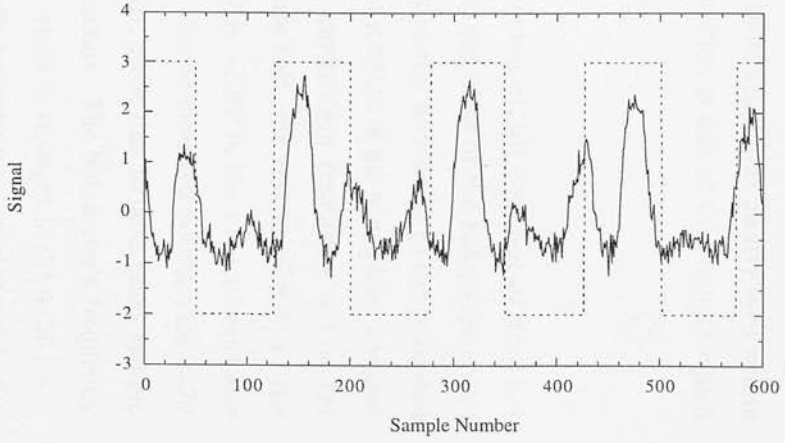

These plots graphically illustrate the effects of the two modulations on the bolometer signal. In the 4–20 case the faster modulation due to the waveplate rotation is clearly seen within the chopper cycles. For the 11–4 case the faster modulation is that of the chopper which dominates the overall shape of the signal.

1) *The Modulated Signal*

Comparing the signal curve for the 4–20 case (figures a), b)) with that of the 11–4 case (figures c), d)), the effects of the frequency response of the bolometer at the modulation frequencies can be seen. This is especially noticeable in the polarised component which is sinusoidally modulated by the rotation of the waveplate: a higher signal level is recorded when the polarisation modulation frequency is low (as demonstrated by Figure 3.4 a)). In these experiments, the rms amplitude of the spectral component at the polarisation frequency is $\sim 2.8V$ in the 11–4 scheme and $\sim 2V$ in the 4–20 scheme. A phase difference can also be observed between the 4–20 and 11–4 signals (as expected from Figure 3.4 b)), given that in both cases sample number '0' was acquired with the waveplate at datum. The bolometer's frequency response also affects the photometric component which is stronger in the 4–20 case. It is then essential to calibrate these two components accurately in order to obtain the correct estimate of the degree of polarisation and position angle.

2) *The Spectral Components*

For a polarised source, the main spectral components of the modulated signal are centred on the chopping and polarisation frequencies but these combine to give rise to other spurious components[9] and their own harmonics. Figure 3.6 shows a typical spectrum analyser trace[10] of the main four components observed in the signal of a *100 %* polarised source measured using a 11–4 modulation frequency scheme. Several tests were carried out in the laboratory with different modulation frequencies schemes and the main components identified are the following:

i) the photometric component at the chopper frequency
ii) the polarised component at the polarisation modulation frequency
iii) the difference between chopping and polarisation modulation frequencies
iv) the sum of chopping and polarisation modulation frequencies
v) the third harmonic of chopper frequency
vi) the fifth harmonic of chopper frequency

[9] The most significant ones occur at the sum and difference of the two modulation frequencies.
[10] The rms amplitude of the spectral components in mV is plotted against frequency.

Figure 3.6 Spectrum Analyser Trace for 11-4 Modulations

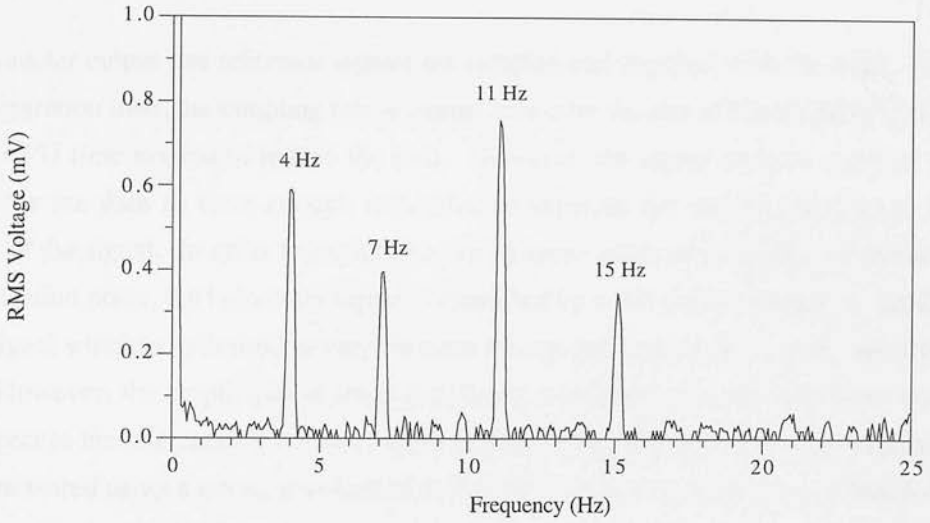

The order of the various components in the list above indicates their relative strengths for a *100 %* polarised signal. In the 11–4 scheme, for instance, the third and fifth harmonics of the chopper frequency lie at 33 Hz and 55 Hz and cannot interfere with the components of interest. The relative strengths of the spectral components centred at the sum and difference of the modulation frequencies illustrate the difficulties involved in choosing operable modulation frequencies. If any of these components coincide at the same frequency as (or are very close to) the main polarisation or photometric components, they may reinforce them possibly giving a wrong estimate of the polarisation. The chopping and waveplate rotation frequencies must be chosen so that this is avoided.

3) Example

At the telescope the secondary mirror acts as a chopper usually driven at a frequency of 7.8125 Hz. Considering polarisation modulation frequencies due to spinning the waveplate at 1, 2, 3, 4 and 5 Hz, the spectral components that arise can be investigated. For polarisation modulations at 4 Hz or 16 Hz there is a superposition of the *difference* component with the polarisation and chopping components respectively, while at 8 Hz the two components are inseparable. For polarisation modulation frequencies at 12 Hz and 20 Hz the various components are well separated. Examples of reduced data acquired in the laboratory with different schemes are given in § 3.3.5.

3.3.3 Sampling the Bolometer Output Signal

The bolometer output and reference signals are sampled and digitised with the ADC. For a given integration time, the sampling rate is compromised by the size of the resulting data file and the CPU time needed to reduce the data. However, the signal must be sampled fast enough for the data to have enough resolution to separate the source and background portions of the signal. In order to exploit the full dynamic range of the ADC and minimise the digitisation noise, the bolometer signal is amplified by a low noise amplifier to produce an AC signal which is optimised to vary between the top and bottom of the ADC sensitivity range. However, the amplification stage introduces a retardation in the bolometer signal with respect to the references from the chopper and waveplate rotator. This phase difference can be measured using a strong unpolarised source and comparing the peaks and troughs of the bolometer signal (ON-OFF the source) with the chopper reference. In the tests carried out in the laboratory, the phase shift introduced in the bolometer signal by the amplification process is $< 3°$.

Figures 3.7 are examples of digitised signals from strong laboratory sources sampled at 600 Hz with a) no polarisation (used to estimate the IP), b) lowly polarised (*~3 %*) and c) totally polarised. The high voltage part of the signal corresponds to the source signal and the low voltage samples are acquired while the chopper blocks the detector's view of the black-body source. These plots show how the *structure* in the source signal becomes more evident with increasing source polarisation. They also show that a number of samples have been acquired while the chopper was transiting between the ON and OFF-source positions. In the totally polarised case (Figure 3.7 c)) the background signal exhibits a significant amount of polarisation due to reflections in the system reaching the detector.

3.3.4 Data Analysis

a) Formatting the Raw Data

The first stage in the analysis of CS data is to format the digitised data. This involves converting the recorded digital numbers back to voltages in the range from *–5* to *+5* Volts and correcting for any phase difference between the three signals.

Figures 3.7 **Digitised Bolometer Output for One-second Integrations**

a) Unpolarised Source

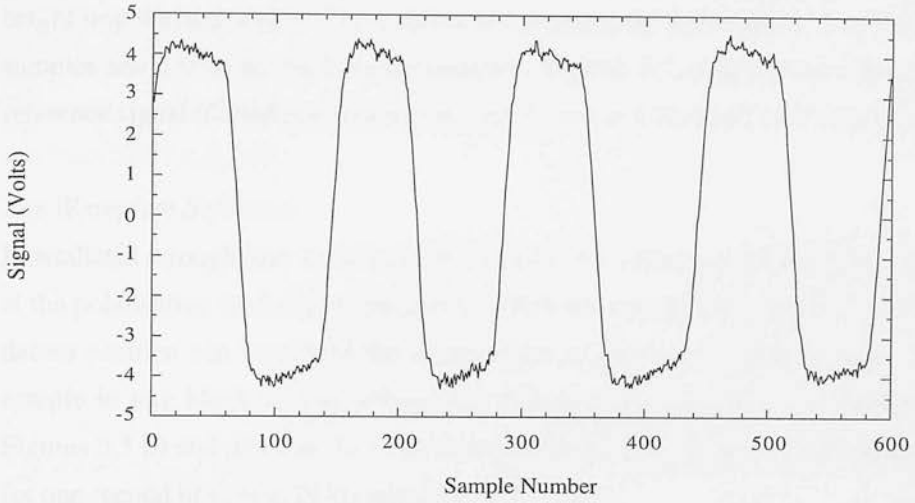

b) Partially Polarised Source

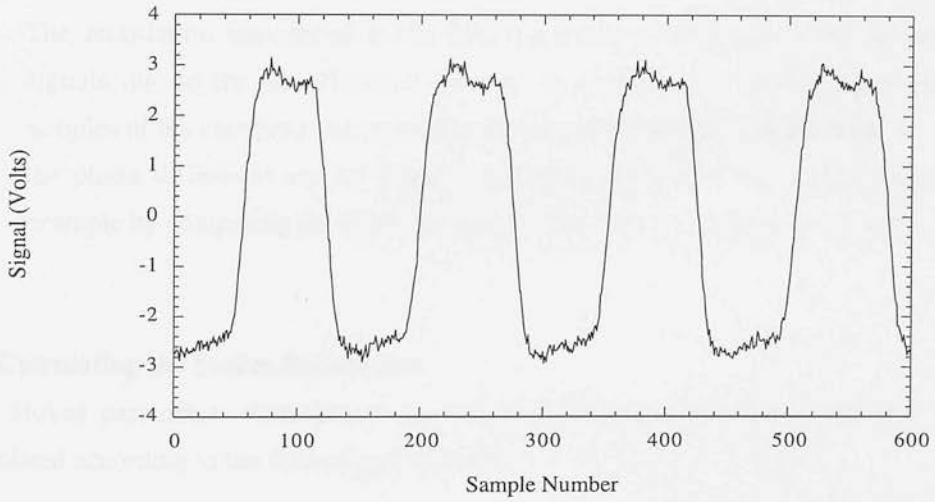

c) Totally Polarised Source

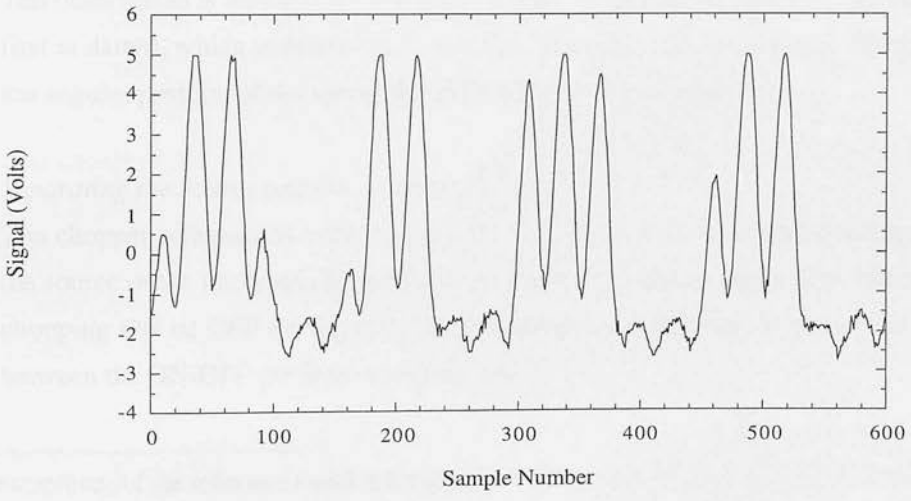

1) The Chopper Reference

It oscillates between HIGH and LOW voltage at the chopping rate. Whether HIGH voltage corresponds to the source or the background can be established by observing a bright unpolarised source. This signal is formatted by assigning a '1' to the source samples and a '0' to the background samples. Figures 3.5 a) and c) show the chopper reference signal (dotted line) for one second of data at 4 Hz and 11 Hz respectively[11].

2) The Waveplate Reference

It oscillates through *four* cycles of HIGH and LOW voltage per waveplate cycle, i.e. at the polarisation modulation frequency, which are formatted to 1's and 0's. The first datum position can be any of the rising edges of the reference signal (e.g. the first sample in any block of 1's), subsequent datums occur at every four rising edges. Figures 3.5 b) and d) show the polarisation modulation reference signal (dotted line) for one second of data at 20 Hz and 4 Hz respectively.

3) The Bolometer Signal

The retardation introduced in the bolometer output with respect to the reference signals due to the amplification process, is corrected by shifting backwards the samples of the chopping and polarisation references until they are all in phase. Again, the phase difference can be found by observing a bright unpolarised source (for example by comparing the signal in Figure 3.7 a) with its chopper reference).

b) Calculating the Stokes Parameters

The Stokes parameters that characterise the polarisation of the source signal only, are calculated according to the following procedure:

1) One-Second Data Blocks

The observation is divided into one-second data blocks starting when the waveplate is first at datum, which is determined from the waveplate reference signal. This allows the angular position of the waveplate to be known for each sample.

2) Separating the Source and Background Signals

The chopper reference is used to monitor when the bolometer output corresponds to the source or the background, by checking whether the data samples were taken while chopping ON or OFF the source. Samples acquired while the chopper is in transit between the ON-OFF positions are taken out.

---

[11] The amplitude of the reference signal in the plots is NOT varying between '1' and '0' for clarity.

3) Fitting the Source and Background Signals

The least squares method described in § 2.2 is used to fit the data and estimate the Stokes parameters for the two parts of the signal (*source+background*) and (*background*) separately. In contrast with the SI mode, the digitised samples have no known photometric errors associated with them and the fit to the polarimetric model is not weighted. The Δ^2 to be minimised with respect to the three Stokes parameters (cf. equation (2.13)) is now,

$$\Delta^2 = \sum_{i=1}^{n} \left[S(\theta_i) - D(\theta_i) \right]^2 \qquad (3.1)$$

4) Subtracting the Background

Since the background is observed simultaneously with the source signal, the two sets of Stokes parameters are temporally related and can be subtracted, thus removing the background. The Stokes *I* parameters derived for the source and background are also subtracted to give the peak to peak amplitude of the signal. This can be used to find the normalised *q* and *u* parameters which will be correct up to a calibration factor.

5) Examples

Figures 3.8 illustrate the above procedure applied to a signal recorded using a bright source in the laboratory. The points in figures a) and c) represent the raw signal sampled by the ADC, and the solid lines are the curves fitted to the source and background signals separately, for a totally polarised and a partially polarised (*~3 %*) source respectively. The Stokes parameters derived from the source and background data have been subtracted and calibrated for the frequency response of the bolometer. The resulting parameters, which correspond to the corrected source signal alone, have been used with equation (1.13) to generate the curves plotted in figures b) and d).

Figure a) clearly illustrates the validity of the fitting procedure. The fact that the background signal is significantly polarised does not affect the measurements because this is also the background superposed on the source signal. When the background and source signals are subtracted, the resulting curve (figure b)) is equivalent to a DC signal, with the polarised component varying sinusoidally about the mean signal level (as in the SI mode). In figure c), although the source is only *~3 %* polarised, the greater peak to peak amplitude in the source signal relative to the background can still be appreciated. The difference between the two fitted curves is shown in figure d)[12].

[12] In this particular example, the mean signal level determined from the data is $I=3.72$ Volts and the amplitude of the polarised component is $I_p=0.128$ Volts, giving a polarisation of roughly *3.4 %*.

Figures 3.8 **Fitted and Corrected Signals from Totally and Partially Polarised Laboratory Sources**

a) **Fit to the Signal from a Totally Polarised Source**

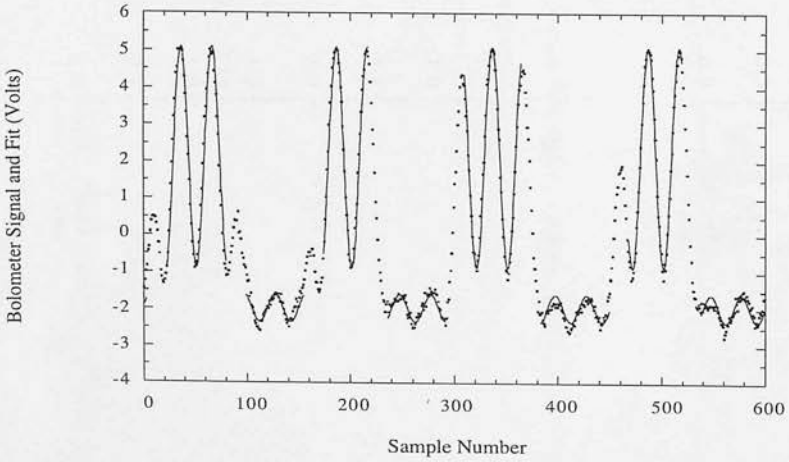

b) **Corrected Signal from a Totally Polarised Source**

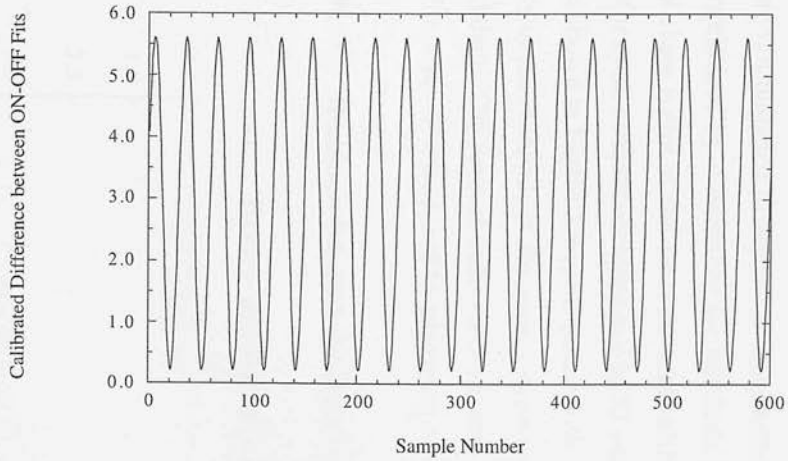

c) **Fit to the Signal from a Partially Polarised Source**

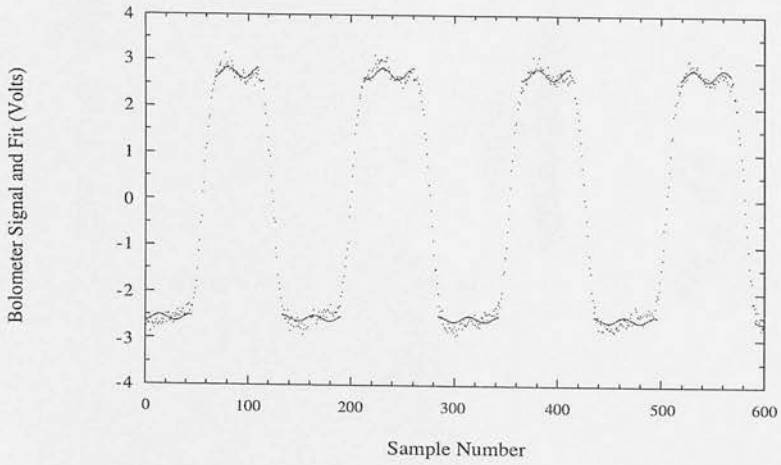

d) **Corrected Signal from a Partially Polarised Source**

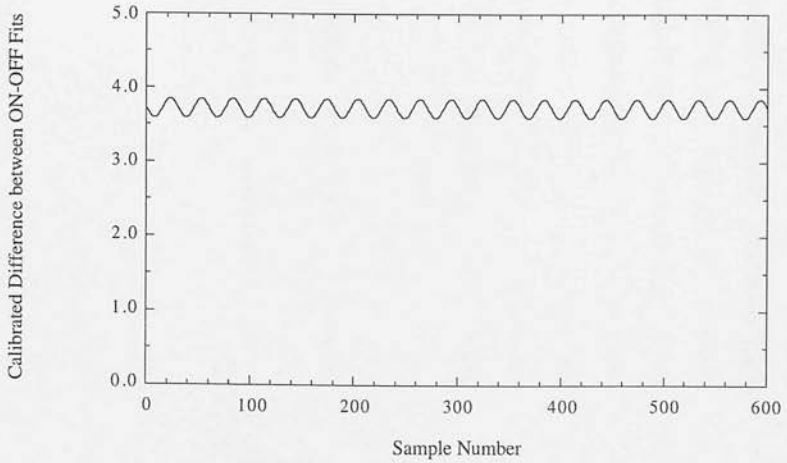

Note on the Fitting Procedure

The data samples acquired while the chopper is transiting between the ON-OFF source positions are not included in any of the fits plotted. The number of samples excluded from the fits is optimised by minimising the residuals between the raw signal and the fit itself. Figures 3.9 show a plot of the absolute value of the residuals between the measured signal and the fit for a) all samples included and b) 22 samples excluded at each chopper transition, for the data shown in Figure 3.8 c) (acquired with a sampling rate of 600 Hz). The solid line corresponds to the residuals in the source signal and the dotted line are the residuals in the background data. The vertical scales of both plots are matched to highlight the improvement in the quality of the fit introduced by removing the chopper transition samples.

Figures 3.9 Residuals between the Raw Signal and the Fitted Curve

a) Before Removing Chopper Transition Samples

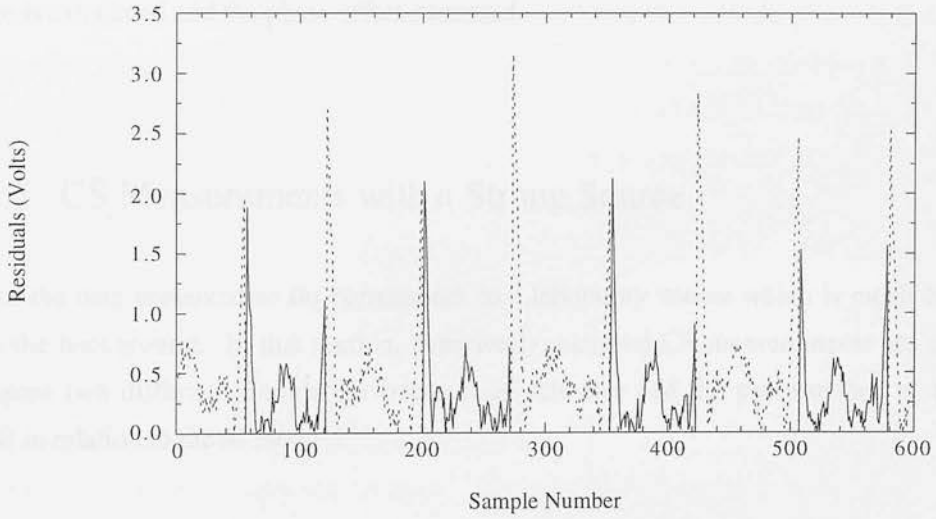

b) After Removing Chopper Transition Samples

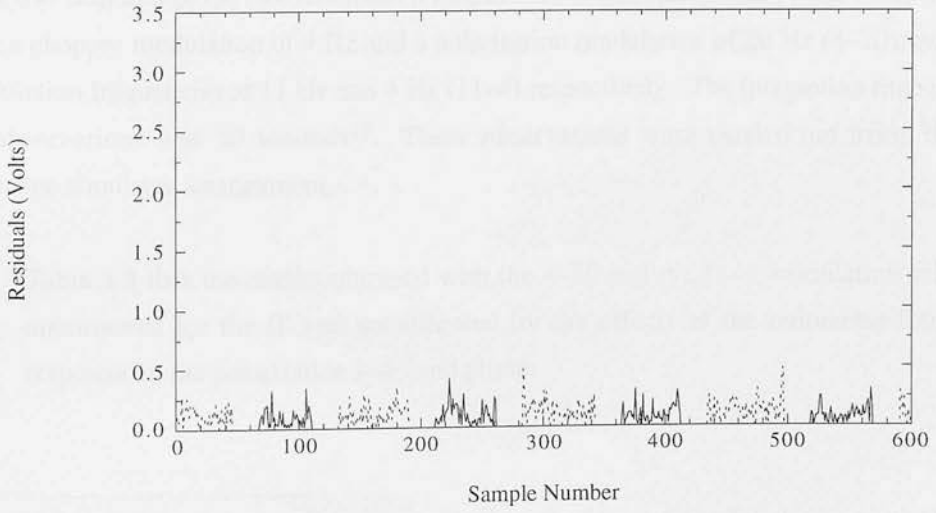

In Figure 3.9 a) a peak in the size of the residuals occurs at each transition of the chopper between the ON and OFF-source positions (where the fit is at its worst). Figure 3.9 b) shows the residuals between the fitted curve and the raw bolometer signal shown in Figure 3.8 c). The peak-to-peak amplitude of the signal is of the order of 6 Volts and the absolute size of the residuals between the fit and the raw signal is of only ≤ 0.25 Volts.

c) Estimating the Polarisation

The procedure described in § 2.2.5 is used to check the homogeneity of the values of the normalised Stokes parameters derived from the one-second integration data blocks before averaging them; their uncertainties are the statistical standard errors. The IP Stokes parameters are then subtracted. The degree of polarisation is calculated, corrected for bias and calibrated for the effects due to the frequency response of the bolometer. The position angle is calculated and the phase offset corrected.

3.3.5 CS Measurements with a Strong Source

All of the data presented so far corresponds to a laboratory source which is much brighter than the background. In this section, completely analysed CS measurements are used to compare two different modulation frequencies schemes and the performance of the CS mode in relation to the SI mode.

a) Comparison between Modulation Frequencies Schemes

Data was acquired in the two modulation frequencies schemes discussed earlier (see § 3.3.2) with a chopper modulation of 4 Hz and a polarisation modulation of 20 Hz (4–20), and with modulation frequencies at 11 Hz and 4 Hz (11–4) respectively. The integration time used in all observations was 30 seconds[13]. These observations were carried out using the full telescope simulator arrangement.

- Table 3.3 lists the results obtained with the 4–20 and the 11–4 modulation schemes, uncorrected for the IP and uncalibrated for the effects of the bolometer frequency response on the polarisation level and phase.

[13] Only 29 seconds' worth of data can be fitted because the data up to the first datum can not be used.

- Table 3.4 lists the results obtained with the 4–20 and the 11–4 modulation schemes, after IP subtraction and calibrated for the effects of the bolometer frequency response on the polarisation level and position angle. The polarisation level in the 11–4 data need not be calibrated for the bolometer response[14] but the phase does. After subtracting the IP the normalised Stokes parameters (in the 4–20 scheme) are multiplied by a constant which represents the drop in the bolometer frequency response as the polarisation modulation frequency is increased from 4 to 20 Hz, as estimated from the data plotted in Figure 3.4 a). The position angle measured with the wire grid at $0°$ is the correction applied to the position angles measured in all observations.

From the results in Table 3.4 it can be concluded that there is no difference between the two schemes. The small variation in position angle are due to the inaccuracy involved in repositioning the wire grid and fluorogold sample in the object plane before each observation was acquired. The variation in polarisation level with position angle in the fluorogold experiments is due to the sample having a wedged shape. The 11–4 scheme is perhaps more convenient to use because (at least for the bolometer used in the laboratory) it does not require the polarised component to be calibrated, and the correct degree of polarisation is obtained directly from the raw data. These results also show that the approach adopted for calibrating the data is adequate.

b) Comparison between the SI and CS Modes

Measurements in both modes are given in Table 3.5. The CS measurements were obtained with a chopper modulation of 4 Hz and a polarisation modulation of 20 Hz. Although the same optical arrangement was used to make the SI measurements, they were obtained on a different day and hence small differences in the positioning of the various components (especially the detector system) and other factors such as condensation building up on the cryostat window[15], have to be allowed for.

These tests show that the two modes of observation yield equivalent measurements, even if the consistency of the SI measurements is superior. This is probably due to the much longer integration times involved and therefore, the comparison to be made must take into account the amount of time taken in each mode to accomplish the measurements and the efficiency with which that time is used.

---

[14] This is because at 4 Hz the bolometer's response is not depressed.
[15] This decreases the level of signal reaching the detector.

Table 3.3 Uncalibrated Results from the Two Modulation Schemes

	Chopper: 4 Hz / Pol. Mod: 20 Hz		*Chopper: 11 Hz / Pol. Mod: 4 Hz*	
Observation	**P (%)**	**χ (°)**	**P (%)**	**χ (°)**
IP	0.67 ± 0.31	16.73 ± 12.17	1.03 ± 0.34	152.72 ± 8.92
Polariser @ 0°	62.52 ± 0.35	35.82 ± 0.16	88.79 ± 0.45	13.64 ± 0.14
Polariser @ 90°	65.38 ± 1.76	124.47 ± 0.77	94.80 ± 1.00	103.26 ± 0.30
Polariser @135°	64.81 ± 0.46	169.22 ± 0.20	91.95 ± 0.95	149.47 ± 0.29
Fluorogold @ 0°	1.36 ± 0.67	113.83 ± 12.57	1.95 ± 0.60	93.99 ± 8.40
Fluorogold @ 90°	2.36 ± 0.34	29.44 ± 4.08	3.51 ± 0.64	176.47 ± 5.14
Fluorogold @ 135°	2.05 ± 0.31	73.73 ± 4.32	2.34 ± 0.44	50.21 ± 5.31

Table 3.4 Calibrated, IP Corrected Results from the Two Modulation Schemes

	Chopper: 4 Hz / Pol. Mod: 20 Hz		*Chopper: 11 Hz / Pol. Mod: 4 Hz*	
Observation	**P (%)**	**χ (°)**	**P (%)**	**χ (°)**
Polariser @ 0°	87.96 ± 0.56	0.00 ± 0.36	88.64 ± 0.46	0.00 ± 0.30
Polariser @ 90°	93.69 ± 1.96	88.26 ± 0.78	94.98 ± 0.55	88.96 ± 0.32
Polariser @135°	91.42 ± 0.77	132.92 ± 0.42	90.87 ± 1.22	135.45 ± 0.54
Fluorogold @ 0°	2.93 ± 0.88	75.48 ± 8.78	2.70 ± 0.33	69.68 ± 3.43
Fluorogold @ 90°	2.61 ± 0.54	178.49 ± 6.11	2.94 ± 0.27	170.32 ± 2.58
Fluorogold @ 135°	3.36 ± 0.72	45.63 ± 6.32	3.30 ± 0.76	40.10 ± 6.59

Table 3.5 Calibrated Results from the SI and CS Modes

	Step and Integrate		*Continuous Spinning*	
Observation	**P (%)**	**χ (°)**	**P (%)**	**χ (°)**
Polariser @ 0°	92.39 ± 0.87	5.03 ± 0.27	90.43 ± 0.32	0.00 ± 0.20
Polariser @ 90°	92.67 ± 0.42	92.21 ± 0.13	97.84 ± 0.37	91.87 ± 0.21
Polariser @135°	92.18 ± 0.31	138.00 ± 0.10	93.20 ± 0.22	135.30 ± 0.17
Fluorogold @ 0°	2.91 ± 0.11	84.87 ± 1.08	2.73 ± 0.21	83.43 ± 2.27
Fluorogold @ 90°	2.91 ± 0.14	174.68 ± 1.40	3.01 ± 0.20	176.02 ± 2.00
Fluorogold @ 135°	2.87 ± 0.08	36.96 ± 0.85	2.79 ± 0.14	38.43 ± 1.54

1) SI Mode

In the SI mode the detector was set to integrate for 2 seconds at 16 different positions of the waveplate. A further 2 seconds were allowed at each integration for detector dead time. The grid observations were repeated through 10 cycles of the waveplate and those of the fluorogold comprised 15 cycles. The IP was estimated from 30 cycles of data. The total integration time used in the SI mode was 320 seconds on the grid measurements (from a total time of 640 seconds) and 480 seconds on the fluorogold measurements (from a total time of 960 seconds). Therefore, the efficiency[16] of this mode is only *50 %*.

2) CS Mode

In comparison, all the CS observations have been derived from data files obtained in 30 seconds (of which only 29 seconds can be fitted) with a sampling rate of 600 Hz. The efficiency of the CS mode measurements can then be estimated as *29/30=97 %*[17].

From these results, it is evident that the CS mode can achieve a similar signal to noise to the SI in a fraction of the time (as little as *3 %* of the time for the fluorogold measurements).

3.3.6 CS Measurements with a Faint Source

Measurements of a faint source were made using the telescope simulator with the two modulation frequencies schemes in both, CS and SI mode. The signal level was greatly reduced by placing a *2 %* neutral density filter at the focal point of the telescope simulator. Table 3.6 lists the results obtained in the two modes. The CS measurements were acquired with a chopper modulation of 11 Hz, a polarisation modulation of 4 Hz and a sampling rate of 100 Hz. The total integration times used were 1800 seconds for the IP and fluorogold measurements and 900 seconds for the grid measurements. Figures 3.10 show a typical trace for one second of CS data for a) the unpolarised and b) the totally polarised cases.

From the measurements given in Table 3.6 it seems likely that the IP was increased by the presence of the filter in the system[18] but the level of detection is poor. In these conditions, the position angle is always a more robust and reliable measurement than the degree of polarisation. The amount by which the source samples are rotated is well tracked in all cases apart from the CS fluorogold measurement at position *90°*.

---

[16] Estimated by dividing the integration time over the total time.
[17] The efficiency is higher the longer the integration, since only one second of data is discarded.
[18] The filter itself is unpolarised but its introduction in the system may give rise to new reflections.

Figures 3.10 **Faint Source CS Data**

a) Unpolarised Source

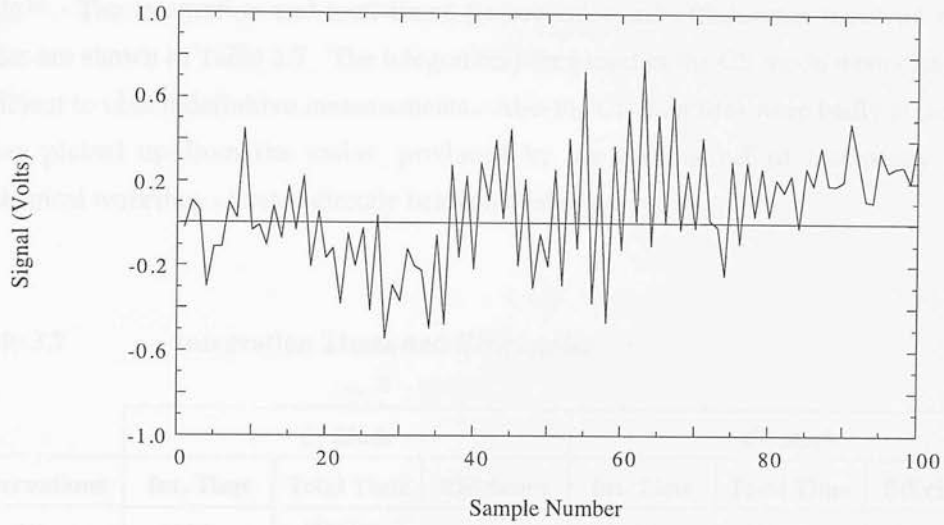

b) Totally Polarised Source

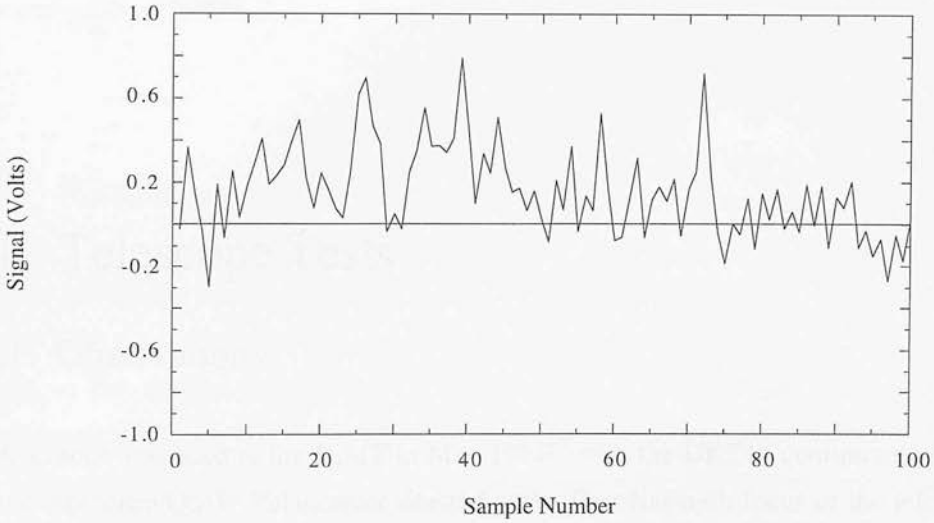

Table 3.6 **Results from the SI and CS Modes with a Faint Source**

	Step and Integrate		*Continuous Spinning*	
Observation	**P (%)**	**χ (°)**	**P (%)**	**χ (°)**
IP	2.07 ± 0.96	77.38 ± 12.10	1.73 ± 2.42	73.75 ± 40.99
Polariser @ 0°	–	–	86.79 ± 4.33	0.00 ± 2.86
Polariser @ 90°	–	–	77.18 ± 9.10	86.39 ± 4.78
Fluorogold @ 0°	3.24 ± 1.03	83.84 ± 1.03	7.78 ± 5.00	84.52 ± 16.91
Fluorogold @ 90°	3.95 ± 1.14	174.30 ± 7.94	1.75 ± 4.42	132.42 ± 28.06

The CS measurements are very noisy (see Figures 3.10) and the signal to noise is very poor but there is a trend of reasonable agreement with the position angles determined in the SI mode[19]. The integration and total times (in seconds) and efficiencies involved in both modes are shown in Table 3.7. The integration times used in the CS mode were clearly not sufficient to obtain definitive measurements. Also the CS data files were badly affected by spikes picked up from the mains, produced by the turning off of machinery in the mechanical workshop situated directly below the laboratory.

Table 3.7 Integration Times and Efficiencies

	SI Mode			*CS Mode*		
Observations	**Int. Time**	**Total Time**	**Efficiency**	**Int. Time**	**Total Time**	**Efficiency**
IP	3200	4480	71 %	1794	1800	99.67 %
Polariser	–	–	–	598	600	99.67 %
Fluorogold	3200	3840	83 %	1794	1800	99.67 %

3.4 Telescope Tests

3.4.1 Observations

The CS mode was tried at the JCMT in May 1994[20] with the UKT14 continuum receiver and the Aberdeen/QMW Polarimeter situated at the East Nasmyth focus of the telescope. The polarimeter module was controlled from the telescope's VAX computer but the signal acquisition was performed on a PC fitted with an ADC card, which sampled and digitised the amplified bolometer signal, the reference from the telescope's chopping secondary mirror and the polarisation modulation reference from the polarimeter rotator module. The sampling rate used in all measurements was 100 Hz. The secondary mirror was set chopping at the default frequency of 7.8125 Hz and the waveplate was rotated at 1 Hz to provide a polarisation modulation of 4 Hz.

---

[19] The results should be similar to the ones obtained with the bright source.

[20] The time available for these test was very limited and most observations were carried out in the afternoon, before the observing shift.

This turned out to be a very unfortunate choice since it makes the frequency of the main spurious spectral component to be centred at 3.8125 Hz (i.e. at the difference between the two modulations), which was virtually superposed on the polarisation component at 4 Hz. This means that the polarised component will be overestimated by an unknown amount[21], with respect to the photometric component, resulting (at least in principle) in a higher degree of polarisation being measured. The telescope was nodded after a 20-second integration to cancel any drifts in the sky thermal background.

Observations were made on Venus (used as a bright unpolarised source) at an elevation of *58°*, to estimate the IP and make observations of *100 %* polarisation by placing a wire grid polariser in front of the polarimeter[22]. Blazar 3C279 was also attempted because it is very bright, highly polarised and has been observed with the JCMT in SI mode on a number of epochs. The number of observations (*nod-pairs*) carried out was 16 for the IP measurements and 20 for 3C279. The beams were not switched during the grid measurements which were repeated 4 times with 30 seconds integrations each. Similar SI measurements were obtained for comparison, using the normal polarimetry data acquisition procedure at the JCMT[23].

3.4.2 Results

The data have been reduced and analysed following the procedures described in § 3.3.4. Figures 3.11 are plots of the raw signal (solid curve) and the model curves fitted (dotted curves) to the source and background parts of the signal[24]. Figure a) shows an IP measurement and b) a wire grid measurement for a one-second integration on Venus. Figure c) is a measurement of Blazar 3C279. The dashed curve is the difference between the fits to the source and background signals (dotted curves), i.e. it corresponds to the signal from the source alone with the background subtracted but not the IP. Nod-pairs have been averaged individually to constitute an *observation*, then all available observations are averaged to obtain a single estimate of the polarisation. Table 3.8 summarises the results obtained (no calibration of the degree of polarisation has been attempted). The 3C279 SI measurement has been corrected for IP but not the CS data.

---

[21] Spectrum analyser traces acquired at the time of the observation would have given the strength of the various components.
[22] These are necessary to calibrate the phase offset introduced in the CS mode (see § 3.3.2).
[23] See Chapters 2 and 4 for details.
[24] The source signal has positive voltage with respect to the background signal.

Figures 3.11 Continuous Spinning Measurements at the JCMT

a) IP Measurement on Venus

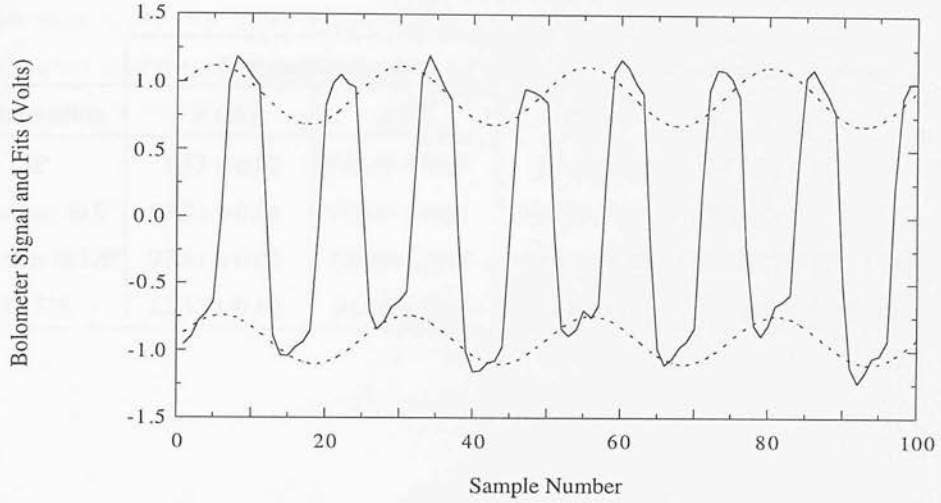

b) 100% Polarisation Measurement

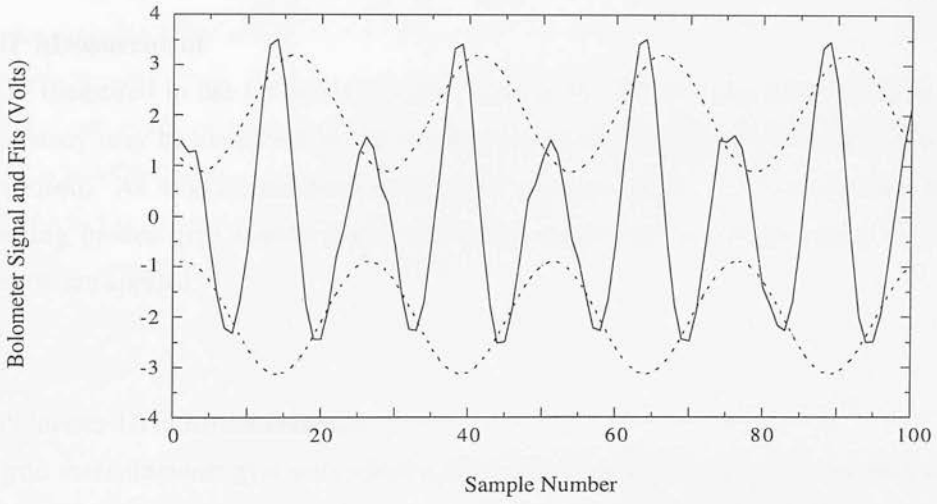

c) 3C279 Measurement

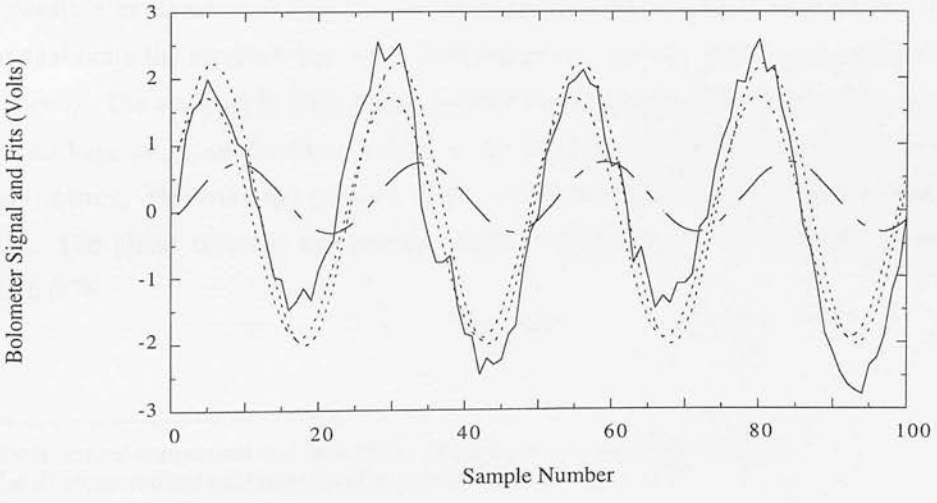

Table 3.8 JCMT Continuous Spinning Observations

	Step and Integrate		*Continuous Spinning*		
Observation	**P (%)**	**χ (°)**	**P (%)**	**$\chi_{measured}$ (°)**	**$\chi_{corrected}$ (°)**
IP	1.53 ± 0.03	165.63 ± 0.63	2.09 ± 0.09	47.39 ± 1.26	159.01 ± 3.05
Polariser @ 0°	97.03 ± 0.06	173.65 ± 0.02	30.23 ± 1.89	10.38 ± 1.79	0.00 ± 3.58
Polariser @120°	97.81 ± 0.05	124.80 ± 0.02	34.50 ± 4.49	129.32 ± 3.70	118.94 ± 4.49
3C279	12.33 ± 0.60	31.15 ± 1.38	7.04 ±12.11	122.84 ± 35.20	50.18 ± 37.00

3.4.3 Discussion

a) IP Measurement

The IP measured in the CS mode is higher than in SI, which is the accepted value. This discrepancy may be explained by the fact that two spectral components close to 4 Hz[25] are superposed. As always, the position angle is a more robust measurement, and the two observing modes give similar results once the corrections for phase offset and source elevation are applied.

b) Polariser Grid Measurements

The grid measurements give only about a third of the expected degree of polarisation. The curves fitted to the source and background parts of the signal are completely *out of phase* (figure b)) while they are *in phase* in the IP and 3C279 measurements (figures a) and c)). One possible explanation is that part of the signal is reflected back up the telescope and down again into the receiver, but with a different phase (perhaps mirror-imaged by multiple reflections). The analyser in front of the receiver window was sufficiently angled to prevent this from happening, so the likely culprit is the back of the wire grid polariser facing the tertiary mirror. However the position angle is correctly tracked as the grid is rotated by *~120°*. The phase offset is the position angle measured with the wire grid at nominal position *0°*[26].

[25] The polarised component at 4 Hz and the difference component at 3.8125 Hz.
[26] The SI measurement estimates that the polariser was placed at *175°*.

c) 3C279 Measurements

The data plotted in figure c) differs from the other plots in that the only modulation appreciable in the raw signal is that due to the rotation of the waveplate, since the chopper modulation (dominant in the Venus observations) is not noticeable. This is because the difference in signal level between the two beams (*source+background*) and (*background*), is large for Venus (with a flux density of 1370 Jy) and much smaller for 3C279 (~10 Jy), i.e. the amplitude of the source signal superposed on the background is 137 times dimmer in the case of 3C279. The fits to the two parts of the signal are in phase. The background in the Venus and 3C279 observations are not the same because the planet was observed around 5 in the evening while the Blazar was observed close to midnight. Their different flux densities also mean that the amplifier gains used were different.

The 3C279 CS measurement was obtained over an integration time of 800 seconds, but does not give even a 1-σ detection. The large error in the CS position angle is due to the poor determination of the degree of polarisation, however the actual position angle derived is realistic once the phase offset and the source elevation have been subtracted. In contrast, the SI measurement is very accurate, and although it was taken over a total observing time of 8448 seconds (with an effective integration time of 5632 seconds), 800 seconds are enough to give a good polarisation estimate in this mode. The most likely reason for failing to get a detection in CS mode, is the inability to subtract the correct background with the available data. The technique used for removing the modulated background works well with computer simulated and laboratory data, and given that the sky background is sampled simultaneously with the source signal, this technique ought to work as well with astronomical data. However, the time taken between telescope nods was perhaps too long (close to 30 seconds[27]) for the sky conditions at the time of the observations. Therefore, the main effects which cannot be adequately corrected for with the available data are due to drifts in the background.

3.4.4 Conclusions

The work presented here provides sufficient evidence to support the claim that the development of a Continuous Spinning polarimetric mode at the JCMT, is a goal worth pursuing as a feasible alternative to the established Step and Integrate mode. It is easily

[27] 20 seconds were spent integrating in each beam, a few seconds were taken by the telescope to nod and some time was needed for communications between the telescope operator and the Nasmyth platform from where the data acquisition PC was run. This is twice as long as in the SI mode.

implemented at the telescope in terms of hardware, and the software data analysis method developed in this work is a reliable way of extracting the polarised signal from the raw data. The main potential benefit of the CS mode is that an estimate of the Stokes parameters can be obtained in a very short time (e.g. once every second). This provides a two-fold improvement in the final detection because it maximises the temporal coherence between the source and background measurements and minimises the amount of data that is thrown away if a spike is detected. These improvements translate into a smaller spread of values of the Stokes parameters obtained from each observing cycle and hence, a given signal to noise can be achieved more quickly. Another important advantage is the greater time efficiency it provides over the SI mode, since the only stoppages necessary during an integration are those used to nod the telescope, reducing by at least a factor 2 the total dead time of the observation. However, this method would need further testing (especially at the telescope) to establish whether it is really workable on faint and/or lowly polarised objects.

Chapter 4

Variability of Blazars: Observations

A systematic programme to monitor the polarisation of a sample of Blazars in the submillimetre is being carried out with the JCMT. Together with the polarimetry, photometric measurements are also made to further characterise the variable behaviour of these sources. Published VLBI observations of their jets have also been obtained from the literature. In this chapter the sample of sources is presented and the Blazar monitoring campaign described.

4.1 Selection Considerations and Source Sample

4.1.1 Selection Criteria

The main criteria adopted in the selection of the source sample are:

- The sources are relatively bright (at least *1 Jy*) in the submillimetre. This enables a usable signal to noise ratio to be achieved in a reasonable time.
- The sample contains a balanced mixture of BL Lac Objects and Highly Polarised Quasars, allowing a statistically significant comparative study between these two classes of objects to be made.
- Most sources are available at the JCMT throughout the year, so that the number of epochs at which they can be observed is maximised. This enables their variability to be characterised.
- In most cases, the sources have been observed with high frequency VLBI. This is essential since the orientation of the jet in the sky must be known in order to estimate

the orientation of the magnetic field relative to it. VLBI polarisation measurements are also available for a number of sources.

- The best known sources have been included, these have been observed at different wavebands throughout the years. These are usually the brightest and more readily available sources like OJ287, 3C273, 3C279, 3C345 and BL Lacertae.

4.1.2 Source Sample

At present, the Blazar polarisation database consists of observations of 10 different BL Lac Objects and 16 Highly Polarised Quasars. At least 5 BL Lacs and 7 Quasars have been observed at 3 or more epochs. Table 4.1 is a list of the objects with acceptable polarimetric detections to date.

Table 4.1 Sample of Sources Observed

BL Lac Objects	
IAU Name	**Other Name**
0235+164	OD160
0735+178	OI158
0829+046	
0851+202	OJ287
1308+326	
1413+134	
1514–241	AP Lib
1749+046	OT081
1823+568	4C56.27
2200+420	BL Lacertae

Highly Polarised Quasars	
IAU Name	**Other Name**
0133+476	DA55
0316+413	3C84
0420–014	
0528+134	
0736+017	OI061
0923+392	4C39.25
1055+018	4C01.28
1226+023	3C273
1253–055	3C279
1335–127	1334–127
1633+382	4C38.41
1641+399	3C345
1741–038	
1921–293	OV–236
2223–052	3C446
2251+158	3C454.3

4.2 Blazars Monitoring Campaign 1991 – 1994

The detector system used is the UKT14 bolometer facility (Duncan *et al.* 1990) with the Aberdeen/QMW Polarimeter (Murray 1991) placed in front of it. Single and two-frequency polarimetry and multi-frequency photometry have been carried out as part of this monitoring programme.

4.2.1 Observation Epochs

Observations have been acquired at the JCMT on seven different epochs between 1991 and 1994. Data on a few sources existed from the polarimeter commissioning runs carried out in September 1989 and June 1990 and these have been incorporated into the database. In the first three epochs (June 1991, January 1992 and February 1992) polarimetry alone was done at 800 and 1100 μm, in the subsequent four epochs (October 1992, February 1993, February 1994 and May 1994) polarimetry was carried out at 1100 μm only, and photometry at 800, 1100 and 2000 μm. Finally, there are some extra four-frequency photometric measurements made with the JCMT taken from a paper by Gear *et al.* (1994) at epochs February 1990, May 1992 and June 1992. Table 4.2 summarises the types of observations carried out at various epochs.

Table 4.2 Observation Epochs and Wavelengths

Epoch	Dates	Polarimetric Wavelengths (μm)	Photometric Wavelengths (μm)
Sep'89	15 — 23 September 1989	800 & 1100	
Feb'90	12 February 1990		800, 1100, 1300 & 2000
Jun'90	28 May — 4 June 1990	800 & 1100	
Jun'91	5 — 9 June 1991	800 & 1100	
Jan'92	4 — 6 January 1992	800 & 1100	
Feb'92	28 February — 1 March 1992	800 & 1100	
May'92	7 May 1992		800, 1100, 1300 & 2000
Jun'92	4 June 1992		800, 1100, 1300 & 2000
Oct'92	24 — 27 October 1992	1100	800, 1100 & 2000
Feb'93	22 — 25 February 1993	1100	800, 1100 & 2000
Feb'94	23 — 25 February 1994	1100	800, 1100 & 2000
May'94	22 — 26 May 1994	1100	800, 1100 & 2000

4.2.2 Photometry

Although extensive continuum photometric measurements of Blazars (including most sources in the sample) are routinely obtained at the JCMT, they are also carried out as part of the polarisation monitoring programme. This is essential in order to relate the total flux density and polarisation at any given epoch, due to the highly variable nature of these sources. The standard photometric mode for UKT14 involves chopping with the secondary mirror and nodding with the telescope to switch the signal and reference beams. The measurements obtained need to be calibrated for atmospheric extinction.

a) Procedure

1) Chopping and Nodding with the JCMT

The secondary mirror can be made to chop between two closely spaced positions on the sky. The default chopping frequency is 7.8125 Hz, well above the typical fluctuations in the thermal sky background and the *1/f* noise spectrum. The chop throw normally used on these sources is 60". The detector aperture used is 65 mm. By chopping with the secondary mirror, two beams are defined on the sky: one containing the source and background (signal beam) and the other containing only the background (reference beam), between which the detector's field of view alternates at the chopping frequency, producing a small AC variation in the detected signal. This signal and the reference from the chopper are fed to a Lock In Amplifier (LIA) where the signal is demodulated, effectively removing the thermal background from the source emission. This enables the amplitude of the AC component (i.e. the signal from the source alone) to be measured.

The local background (from the telescope and surroundings) may not necessarily be the same in the two beams. To account for this effect, the telescope is nodded so that the two beams are interchanged or 'switched'. Therefore, in order to subtract the contribution from the sky background successfully, a *nod-pair* is needed, i.e. a complete detection is carried out by subtracting the signal acquired with the source in each beam in turn. The frequency of nodding will depend on the strength of the source and the atmospheric conditions, but a nod-cycle will typically take between 20 to 40 seconds. Although it is possible to nod faster than this, it may not be advantageous since it takes some 4 seconds for the telescope to nod (during which no data can be acquired) thus reducing the efficiency of the integration.

2) Photometric Measurements of Polarised Sources with the Polarimeter

During a polarimetry run the photometric measurements are taken with the polarimeter placed in front of the receiver. This means that the power that reaches the detector is halved by the presence of the wire grid analyser, since it absorbs *50 %* of the power. The flux density measured may also be affected by the waveplate and analyser combination, given that these sources can be highly polarised. To avoid a situation where, by chance, the waveplate is positioned such that it completely cuts out (or lets through) the polarised component[1], two photometric measurements are performed consecutively at two waveplate positions *45°* apart and averaged. The mean signal level is obtained by averaging these two measurements. A measurement of the total flux density can also be extracted from the polarimetric observations.

b) Calibration

1) Flux Estimation

The flux density measured decreases exponentially with airmass due to the atmospheric extinction (equation (4.1)). The atmospheric extinction coefficient is calculated from measurements of the calibrators carried out at different times throughout the night and at a range of elevations. Planets with small angular sizes are more appropriate for calibrating the signal from point-like objects such as Blazars. In some occasions when no planets were available throughout part of the night, 3C273 (the brightest source in the Blazar sample) has been used to estimate the atmospheric extinction coefficient.

$$f = F\, e^{-\tau a} \tag{4.1}$$

where f is the measured flux
F is the absolute flux (as measured above the atmosphere)
τ is the atmospheric extinction coefficient
a is the airmass at which the measurement is made

For example, from two observations labelled '1' and '2', τ is then given by

$$\tau = \frac{\ln\left(\frac{f_1}{f_2}\right)}{(a_2 - a_1)} \tag{4.2}$$

[1] This depends on the actual position angle of the polarised signal.

For the planets F is well known and hence the flux of a source can be obtained using equation (4.3).

$$F_s = F_p \frac{f_s}{f_p} e^{\tau(a_s - a_p)} \qquad (4.3)$$

where subscripts 's' and 'p' refer to source and planet parameters respectively.

2) *Photometric Uncertainty*

There is a photometric uncertainty involved in the analysis due to changes in atmospheric extinction throughout the night, or due to using planet observations distant in time and/or elevation to calibrate the source signal. This photometric uncertainty is estimated by cross-examining calibrators against each other; for example the flux of calibrator '1' is estimated using observations of calibrator '2' and vice versa. On the best nights this uncertainty is found to be of the order of *5 %* of the flux measured, but more often typical values are around the *10 %* level. On a bad night this can go up to *15 %*, though this is also dependent on the availability of good calibrators throughout the entire night and at a complete range of elevations. Observations of the same source are averaged for each night for the planets and also for each epoch for the Blazars. The uncertainty in the measurements is worked out by adding in quadrature the statistical error from the averages and the photometric error.

3) *Example*

Figure 4.1 shows the typical photometric variability of a Blazar.

Figure 4.1 3C273 Photometric Variability at 1100 μm

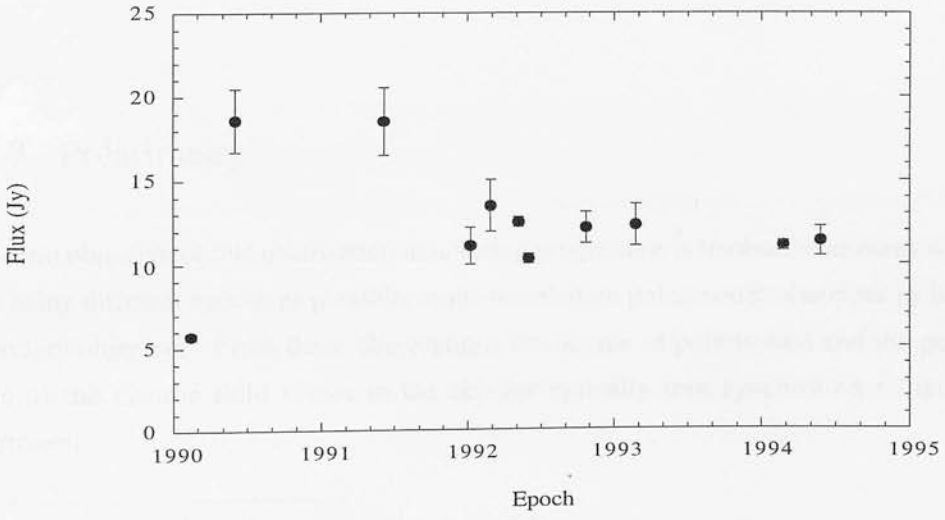

c) Spectral Index

Since October 1992 photometric measurements have been carried out at 800, 1100 and 2000 μm to determine a three-point submillimetre spectral index. The spectral index is estimated by fitting a straight line in log-log space, to the flux density measured at the photometric wavelengths[2]. The fit is weighted by the independent errors in the photometry. For the first three epochs in this programme only two wavelengths were used and the resulting two-point spectral indices have consequently large error bars. The spectral indices taken from Gear *et al.* (1994) are determined from four-frequency measurements. Figure 4.2 illustrates the improvement in the determination of spectral index that comes from increasing the number of photometric frequencies.

Figure 4.2 3C273 Submillimetre Spectral Index

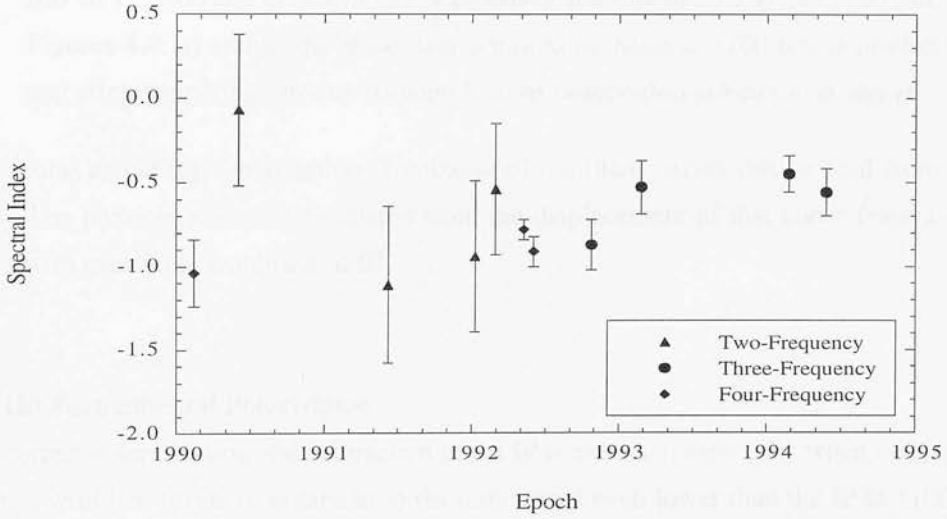

4.2.3 Polarimetry

The main objective of this polarisation monitoring programme is to observe as many sources at as many different epochs as possible, multi-wavelength polarimetric observations being a secondary objective. From these observations the degree of polarisation and the position angle of the electric field vector in the sky for optically thin synchrotron radiation is determined.

---

[2] Synchrotron emission follows a power law (see § 1.3).

a) Observations

The data acquisition and data reduction procedures used during these observations are described and assessed in Chapter 2. All the observations were carried out in the Step and Integrate mode. The number of waveplate positions used up to the February 1993 run was 10; in the two most recent observation runs 16 positions have been used. The typical integration times on each waveplate position in each beam are 8 seconds for the Blazars and 4 seconds for the planets (in good observing conditions). Usually two consecutive full cycles of the waveplate are taken on the sources and a single cycle is used on the planets[3].

Figures 4.3 and 4.4 are typical examples of observations that illustrate the fit to the raw data (normalised by the mean signal level), for three typical Blazars and three planetary observations used to determine the IP.

- Figures 4.3: a) OJ287 (*5 %* polarised and flux of *2 Jy*), b) 3C273 (*2.5 %* polarised and flux of *11.5 Jy*) and c) 3C279 (*15 %* polarised and flux of *13.5 Jy*), at 1100 μm.
- Figures 4.4: a) and b) the same data acquired on Mars at 1100 μm is plotted before and after de-spiking. In c) a 10-point Uranus observation at 800 μm is shown.

The actual percentage polarisation (amplitude of the fitted curve) can be read from the y-axis. The phase can also be estimated from the displacement of this curve from a cosine curve with maximum amplitude at *0°*.

b) The Instrumental Polarisation

The correct determination and subtraction of the IP is essential, especially when dealing with sources with low levels of polarisation (in some cases even lower than the IP at 1100 μm). The procedures used to determine it and the implementation of its subtraction from source observations are described in § 2.3.4.

1) IP Determination

The IP originates mainly at the telescope's wind blind and is known to change slightly with time (in magnitude and position angle) simply due to variations in the tension of the membrane (or its replacement). These changes are more noticeable at 1100 μm because of the greater magnitude of the IP. It is therefore necessary to measure the IP at every epoch in order to calibrate the observations. For the Blazar programme, the correct IP is measured on planets of small angular size which approximate better a point source. Tables 4.3 and 4.4 list the IP measurements obtained at every epoch from 'point-like' and 'extended' planets for the 1100 and 800 μm filters used.

---

[3] With the 10-waveplate positions scheme, each observation usually included 4 waveplate cycles.

Figures 4.3 **Examples of Blazars Observations**

a) OJ287

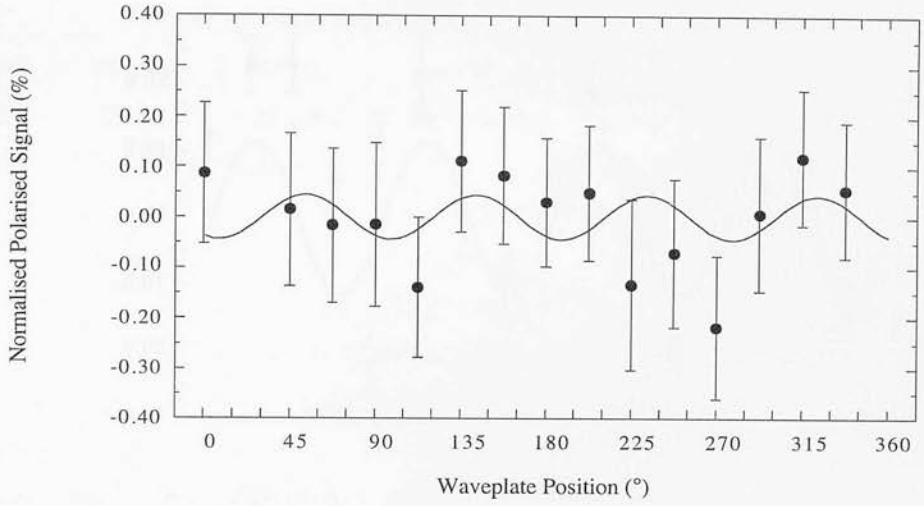

b) 3C273

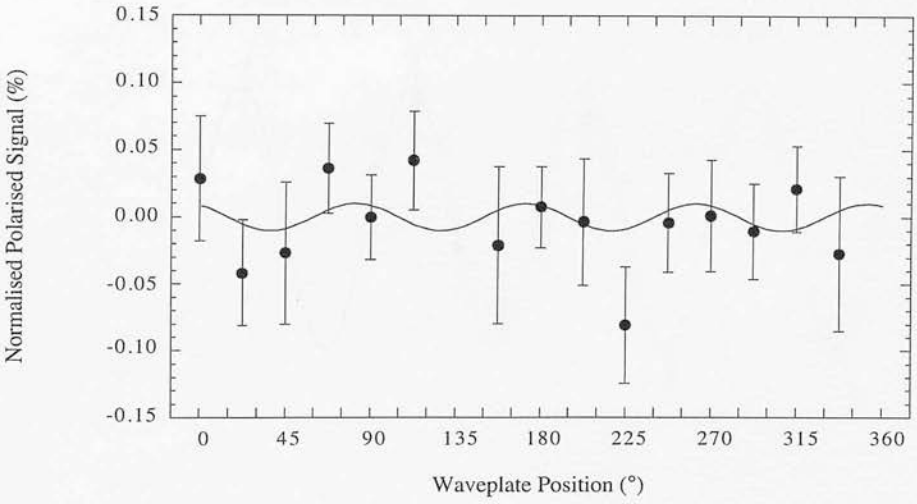

c) 3C279

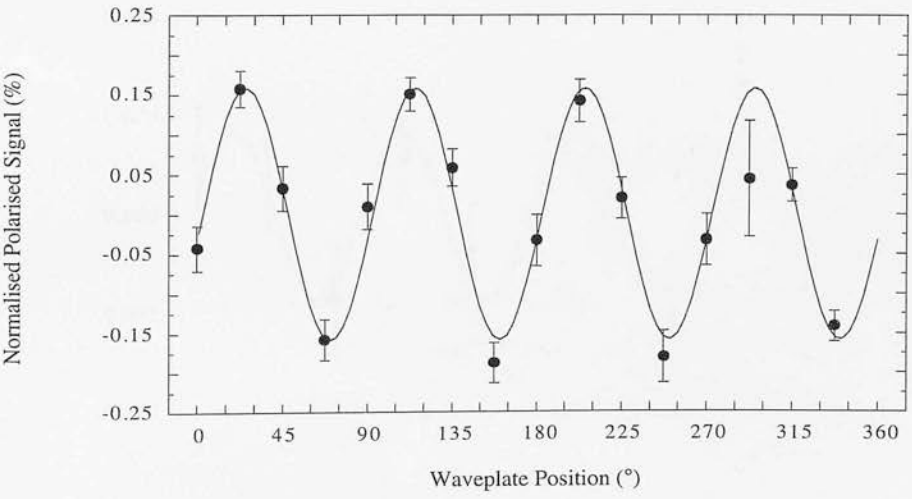

Figures 4.4 **Examples of Planetary Observations**

a) IP on Mars at 1100 μm (16 Positions non-de-spiked)

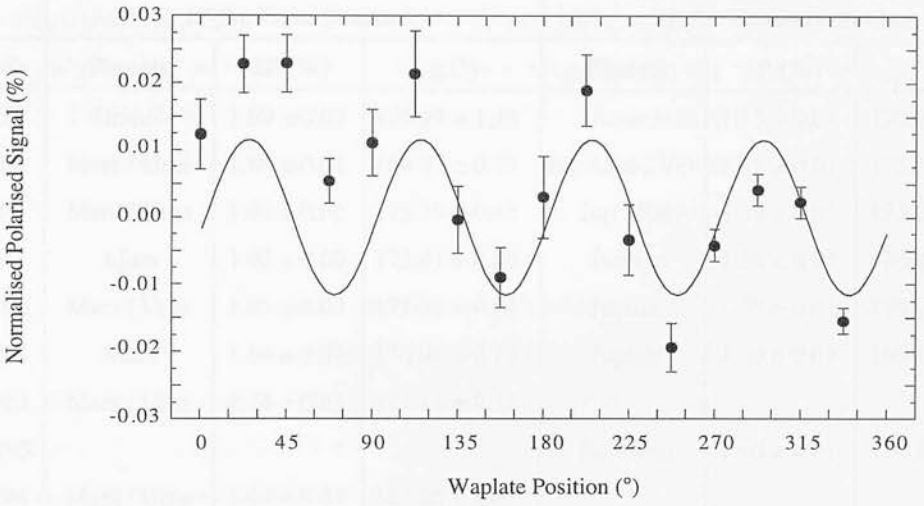

b) IP on Mars at 1100 μm (16 Positions de-spiked)

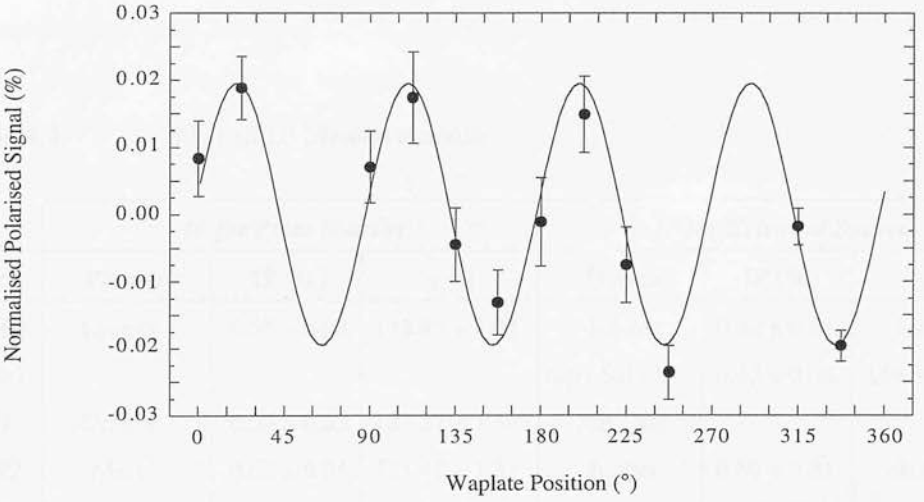

c) IP on Uranus at 800 μm (10 Positions de-spiked)

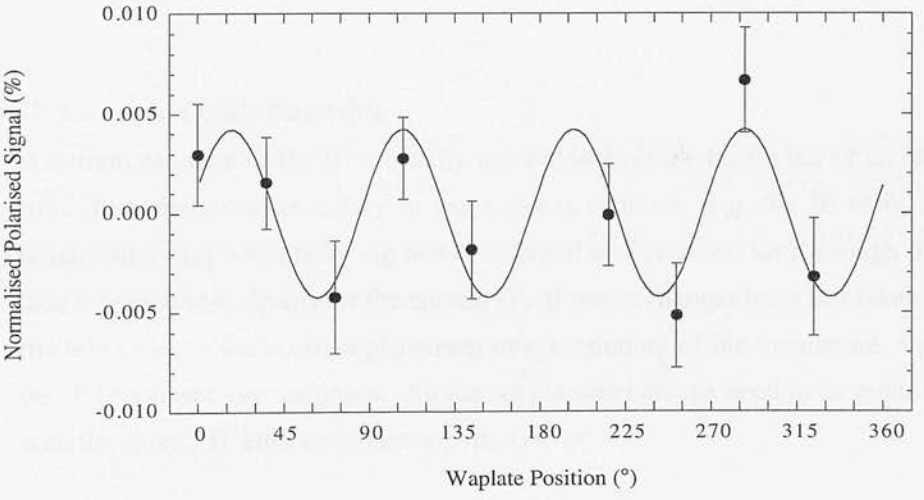

Table 4.3 1100 μm IP Measurements

	IP for Point Sources			*IP for Extended Sources*		
Epoch	**Planets**	**IP (%)**	**χ (°)**	**Planets**	**IP (%)**	**χ (°)**
Sep'89	Uranus	1.69 ± 0.07	175.93 ± 1.13	Jupiter	1.15 ± 0.01	170.48 ± 0.17
Jun'90	Mars / Urns	1.66 ± 0.04	166.97 ± 0.75	Jup / Sat / Ven	1.52 ± 0.01	175.33 ± 0.20
Jun'91	Mars / Urns	1.46 ± 0.02	172.79 ± 0.41	Jup / Sat	1.29 ± 0.01	174.09 ± 0.20
Jan'92	Mars	1.90 ± 0.03	172.61 ± 0.45	Jupiter	1.38 ± 0.01	176.49 ± 0.13
Feb'92	Mars / Urns	1.65 ± 0.04	172.32 ± 0.64	Jupiter	1.35 ± 0.01	176.98 ± 0.10
Oct'92	Mars	1.64 ± 0.01	176.01 ± 0.12	Jupiter	1.26 ± 0.03	169.13 ± 0.67
Feb'93	Mars / Urns	1.74 ± 0.01	173.11 ± 0.13			
Aug'93				Sat / Ven	1.60 ± 0.01	174.34 ± 0.15
Feb'94	Mars / Urns	1.45 ± 0.05	164.85 ± 1.07			
May'94				Jup / Ven	1.68 ± 0.01	168.34 ± 0.24

Table 4.4 800 μm IP Measurements

	IP for Point Sources			*IP for Extended Sources*		
Epoch	**Planets**	**IP (%)**	**χ (°)**	**Planets**	**IP (%)**	**χ (°)**
Sep'89	Uranus	0.55 ± 0.04	178.83 ± 2.08	Jupiter	0.32 ± 0.01	3.27 ± 0.29
Jun'90				Jup / Sat / Ven	0.45 ± 0.02	159.93 ± 1.29
Jun'91	Uranus	0.59 ± 0.03	167.27 ± 1.34	Jup / Sat		
Jan'92	Mars	0.62 ± 0.04	151.48 ± 1.83	Jupiter	0.50 ± 0.01	0.01 ± 0.31
Feb'92	Mars / Urns	0.55 ± 0.05	157.11 ± 2.44	Jupiter	0.34 ± 0.01	170.33 ± 0.39

2) IP Subtraction while Observing

A current estimate of the IP is usually not available at the beginning of an observing run. It is therefore necessary to use a guess estimate (e.g. the IP from a recent polarisation run) when reducing newly acquired observations, until enough planetary data is available to determine the current IP. If major changes have just taken place at the telescope, in particular replacement or retensioning of the membrane, a guess of the IP becomes more uncertain. All the source observations need to be reduced again with the correct IP after the observing run is over.

c) Observing Wavelengths

The Aberdeen/QMW polarimeter is provided with waveplates to carry out measurements with three different UKT14 filters: 450, 800 and 1100 μm. In the earlier epochs of the Blazar programme, polarimetry was done on each source at the wavelengths of 800 and 1100 μm (see Table 4.2). This limited the number of sources that could be covered in a single epoch. Data from these earlier epochs show that in most cases there are no significant differences between the polarisation properties of Blazars at these two wavelengths.

Figures 4.5 illustrate the variability with epoch of the percentage polarisation (a) and b)) and position angle (c) and d)) measured at 1100 μm (a) and c)) and 800 μm (b) and d)) for three typical Blazars. The plots include four-epoch observations of quasar 3C273 and three-epoch observations of quasars 3C279 and 3C454.3. These three sources have different overall polarisation properties, ranging from lowly polarised (3C273) to very highly polarised (3C279).

It was decided to concentrate on single-frequency polarimetry because by observing a greater number of sources the sample begins to be statistically significant. The choice of wavelength for the polarisation measurements was finally 1100 μm. The main advantage at this wavelength is that a good signal to noise is faster to achieve, and also this atmospheric window is less affected by weather conditions. However, the penalty to pay is a level of instrumental polarisation a factor 3 greater than at 800 μm.

d) Detection Criteria

Because of the highly variable nature of these sources the accuracy required (or at least aimed at) in the determination of the polarisation parameters is better than 5σ, to ensure that any variations are due to variability of the objects rather than the uncertainties in the detections. In order to achieve this, a source is targeted with sufficient observing time before it sets. The observations of each source are reduced as soon as they are acquired and the Stokes parameters estimated from all available observations averaged together. The target source is changed when enough signal to noise has been achieved, the source has moved to low elevation or no improvement on the detection seems possible. All observations of a given source obtained on consecutive nights during an observing run are averaged.

Figure 4.6 is a plot in '$q - u$' space of the normalised Stokes parameters obtained for six different Blazars at a particular epoch. These have been averaged for each source resulting in a detection of at least 5σ in every case.

Figures 4.5 **Comparison between the 1100 and 800 μm Polarisation Properties of Blazars**

a) **Variability of Percentage Polarisation at 1100 μm**

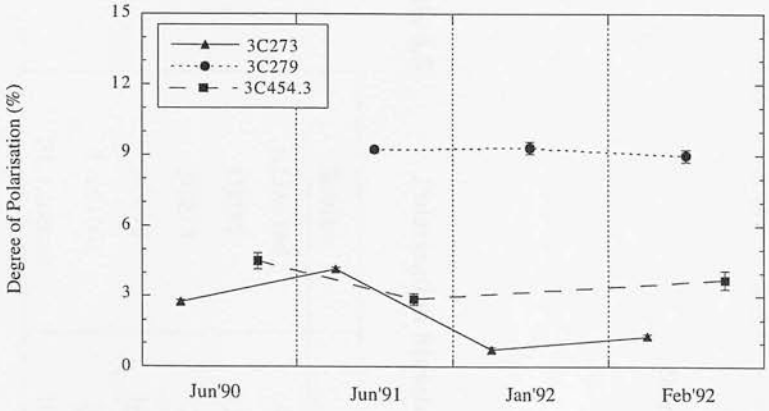

b) **Variability of Percentage Polarisation at 800 μm**

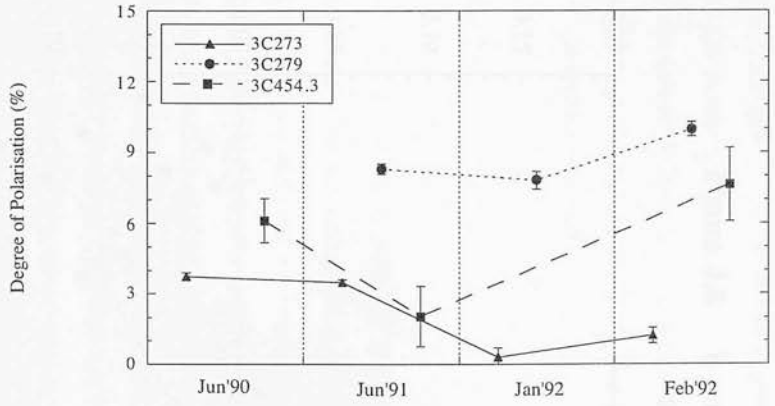

c) **Variability of Position Angle at 1100 μm**

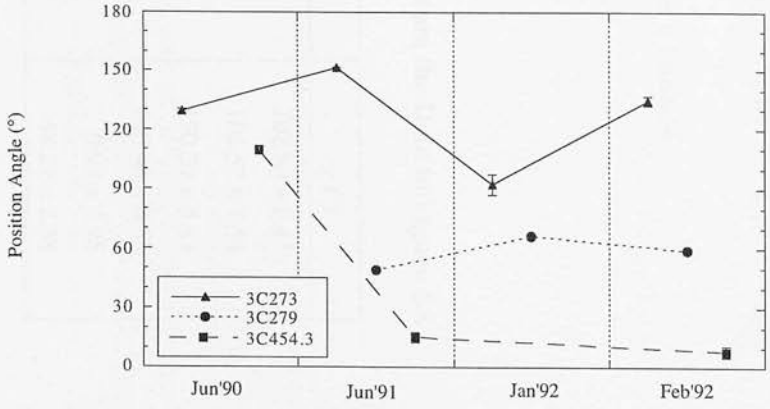

d) **Variability of Position Angle at 800 μm**

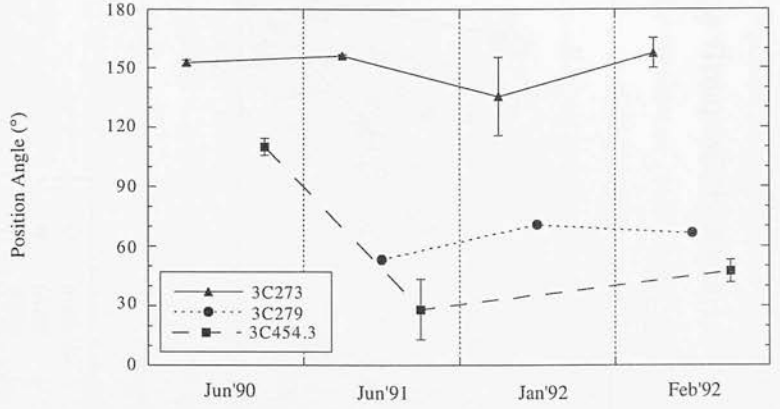

Figure 4.6 q - u Plot for a Group of Six Blazars

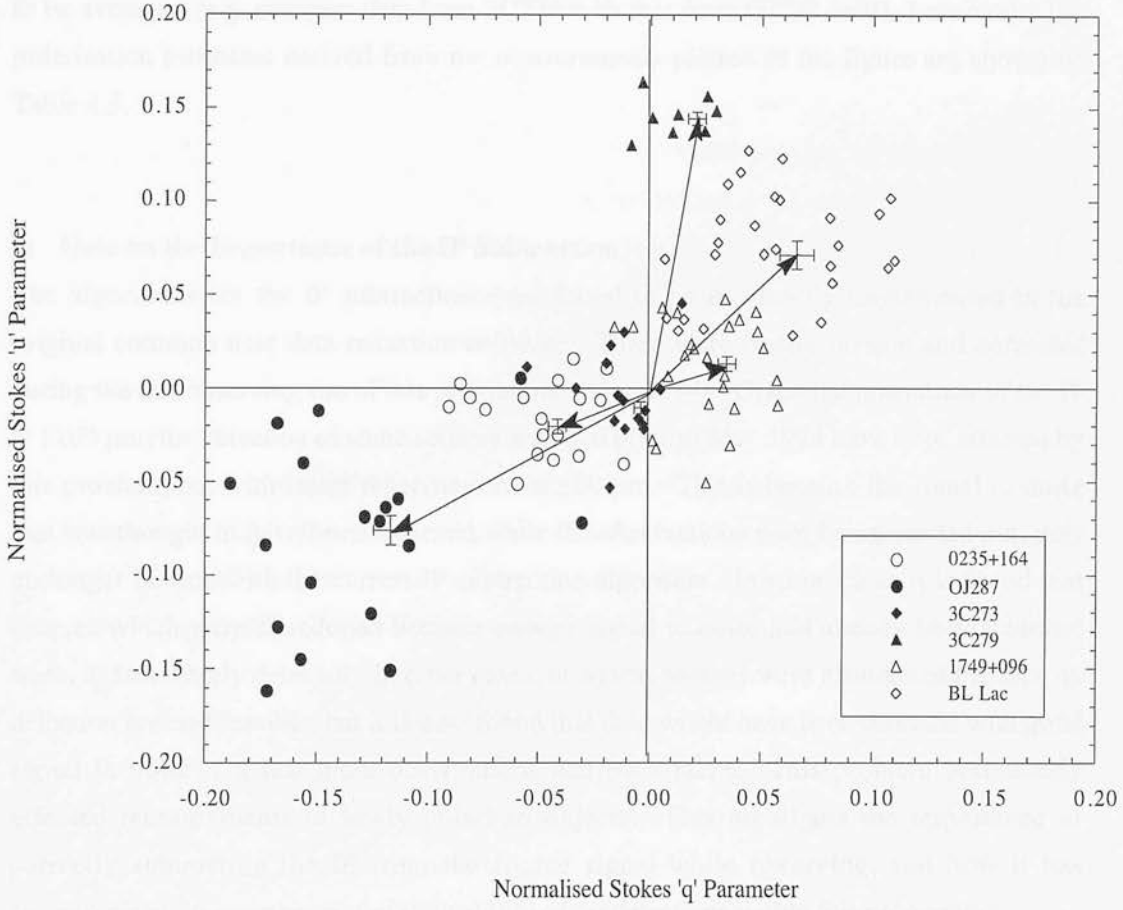

Table 4.5 Polarisation Measurements from the Data in Figure 4.6

Source	P (%)	χ (°)
0235+164	4.63 ± 0.40	102.90 ± 2.45
OJ287	15.09 ± 0.81	104.57 ± 1.54
3C273	2.50 ± 0.52	130.31 ± 5.85
3C279	14.78 ± 0.33	40.40 ± 0.63
1749+096	3.72 ± 0.39	9.97 ± 2.95
BL Lacertae	10.17 ± 0.85	48.22 ± 2.38

A vector from the origin to the average (q, u) pair represents the final measurement of the polarisation: the degree of polarisation is given by the length of the vector, and the angle it makes with the positive q-axis is twice the position angle. This figure also illustrates how the greater the spread in the measurements, the greater the number of observations that need to be averaged (e.g. compare data from 3C279 with that from OJ287 or BL Lacertae). The polarisation estimates derived from the measurements plotted in the figure are shown on Table 4.5.

e) Note on the Importance of the IP Subtraction

The algorithms for the IP subtraction were found to be incorrectly implemented in the original common user data reduction software. These were finally revised and corrected during the last observing run of this programme (May 1994). Given the magnitude of the IP at 1100 μm, the detection of some sources acquired prior to May 1994 have been affected by this problem, but with lesser repercussions at 800 μm. This is because the signal to noise that was thought to have been achieved while the observations were being carried out, may no longer be true with the correct IP subtraction algorithm. In some cases it is found that sources which were abandoned because enough signal to noise had already been achieved were, in fact, barely detected. In other cases, however, sources were abandoned because no detection seemed feasible, but it is now found that they would have been detected with good signal to noise if a few more observations had been taken. This problem particularly affected measurements of lowly polarised objects. This highlights the importance of correctly subtracting the IP from the source signal while observing, and how it has compromised, in some cases, the attainability of 5σ detections within this programme.

4.3 VLBI Observations of Jets

4.3.1 The Need for VLBI Observations

The position angle determined from the polarisation measurements in the submillimetre provides the orientation in the sky of the electric field vector of the electromagnetic wave. The synchrotron origin of the radiation ensures that a magnetic field perpendicular to this direction is responsible for the polarised emission. It is therefore possible to determine the orientation of the magnetic field in the sky from the polarisation measurements. However, in order to test the theoretical models proposed to deal with the energy production and

transport mechanisms in these extragalactic sources, what really needs to be known is the orientation of the magnetic field relative to the flow of the material responsible for the emission, i.e. relative to the structural axis of the jet. This can be obtained from VLBI maps.

4.3.2 The Local Orientation of the VLBI Jet

The jets of Blazars are known to bend at parsec and kiloparsec scales, as it is often seen in VLBI maps (see e.g. Zensus 1992) and there is no evidence to suggest that jets should behave differently at the sub-parsec scales seen in the submillimetre. The higher the frequency at which the VLBI map is taken, the higher is the resolution achieved and the more detail is visible near the most compact regions. The local direction of the jet in this regime does not always coincide with that of the parsec-scale jet. A possible reason for this is that (at least in some sources) VLBI components may be ejected from the cores in different directions at different epochs (see examples in Krichbaum *et al.*1993), although as they move away from the core they tend to follow similar paths (i.e. along the jet). To correctly determine the orientation of the magnetic field with respect to the flow, it is therefore important to know what the *local* orientation of the jet is nearest to the core at (or close to) the epoch at which the polarisation measurement is made. This information is of course not usually available. Allowing for these uncertainties it is still possible to make progress by using the best estimates of the orientation of the VLBI jets. However, for sources far south in the sky there are no VLBI measurements available (e.g. 1921-293).

4.3.3 A Search of the Literature

An exhaustive literature search was carried out for VLBI observations of Blazars published in all the main journals and conference proceedings in the last 10 years. The objective was to collect all the existing measurements of the position angle of the jets of the sources in the sample. The orientations of these jets as used by other authors throughout the years has also been recorded. In many cases this involves their own interpretation (or otherwise) from published VLBI maps, and this is especially true of the most compact sources which are largely unresolved. For those papers which did not include the actual maps used, these were traced back through the references. The results of the literature search are given in Appendix A, including the position angle of the jet, an estimate of its angular distance from the core, the frequency and year of the observation, the reference from which the measurement was taken and some comments relevant to each particular estimate.

High frequency radio observations (43 — 100 GHz) have only become available recently (see e.g. Bääth 1992 and Krichbaum & Witzel 1992) and few (often unconfirmed) images of the most compact regions of the jets of some sources have been obtained. In some cases, these high frequency images indicate a different orientation of the innermost jet from that observed at lower frequency bands. It then becomes necessary to make a choice between using a recent single observation at a more relevant frequency, or a repeated measurement obtained further out in the jet (see for example table for 3C446 in Appendix A). This and the uncertainty involved in the VLBI observations, make the orientation of the magnetic field relative to the local jet the weakest parameter in the database.

4.3.4 Some Observed Practices

In the process of searching the literature some practices were observed that call for some criticism. These were found to be common amongst some authors who have *(not)* searched the literature for VLBI measurements of a large sample of objects. The most objectionable point is the lack of warning about measurements used which are not well determined. All the examples quoted can be found in the tables in Appendix A.

- For a number of sources, the available VLBI maps show a largely unresolved core for which it is pure speculation to quote a jet position angle, yet this is often done, not by the authors of the observation but by other authors, that refer to those maps without letting it be known that the evidence is very weak if not non-existent. For example the measurements on 0420-014 and 1749+076 from reference [26].
- Another worrying practice is that for some sources there really exists only one map made years ago but referred to in many different papers by different authors, thus giving the impression that it is a well determined measurement. An suitable example is that of 1823+568.
- It has also been noticed that certain authors have made it a habit to average the available estimates of a jet's position angle, even if these are somewhat different. For example the measurements of 3C120 and OJ287 in reference [26].
- A shortcut often taken to collect the VLBI position angles of the jets for a number of sources, is to obtain them from a single paper by somebody who has searched the literature before, in this way perpetuating errors of judgement and perhaps ignoring newer and more accurate results. Notice for example the extensive use made of references [27] and [60] in reference [26].

Further examples of these practices can be found in Appendix A.

Chapter 5

Variability of Blazars: Analysis

In this chapter graphical and statistical methods are used to study and compare the properties of the sources in the sample. In the first instance, the database is examined to identify Blazars which exhibit similar polarisation properties, in order to establish basic variability patterns applicable to a number of objects. The objective is to simplify the current picture of chaotic variable behaviour in order to place specific constraints on the theoretical models. Then a comparison is made between observations of BL Lac Objects and Quasars.

5.1 Analytical Approach to the JCMT Database

In this section the main analytical tools and criteria used to collate the database are described. The actual measurements acquired at 1100 μm are tabulated in Appendix B.

5.1.1 The Database Parameters

All sources in the database have been classified as either a BL Lac Object or a Highly Polarised Quasar. The classification has been done according to the most usual conventions (e.g. Burbidge & Hewitt 1992). Their emission is characterised by the four parameters determined from the submillimetre observations :

- F is the 1100 μm flux density in Janskys.
- α is the submillimetre spectral index.
- P is the 1100 μm degree of polarisation in percentages.
- χ is the position angle of the polarisation vector.

The polarisation position angle is perpendicular to the magnetic field, hence its configuration in relation to the structural axis of the jet δ, is obtained from the absolute difference between the measured position angle and that of the VLBI jet in degrees. The convention used throughout is that the magnetic field and the jet are orthogonal at $\delta=0°$ and parallel at $\delta=90°$. When analysing a particular subset of the database involving more than one source, normalised flux (f) is used. Flux measurements are normalised by the lowest value measured for each source, which is the measurement closest to the quiescent state.

5.1.2 Types of Analysis

a) Graphical

The available data from each source or subset of sources is examined graphically by plotting each measured parameter against the other three, in order to look for any correlation between them. These plots are useful to look for overall trends and similarities in the variability of the various objects. Histograms showing the distributions of these parameters are used to indicate the existence (or otherwise) of different populations of objects. The measurements of all sources observed at more than one epoch are graphically represented in the plots in Appendix C.

b) Statistical

Statistical tests have been carried out for each individual source and for subsets of the database. The tests include:

1) Mean and Standard Deviation

The measurements obtained at various epochs on a source are averaged to find the mean and standard deviation of all four measured parameters. This helps characterise the brightness and polarisation levels of each source, the preferred orientation of its magnetic field (if any) and the typical spectral index of the emission. For datasets including more than one source, the means are found from the averaged values of each object, in order to reduce the bias towards those sources with more observations.

2) Kolmogorov-Smirnov Tests

One and two-dimensional Kolmogorov-Smirnov Tests are carried out between datasets for each parameter and combination of parameters. These are useful to

assess statistically the similarities and differences between different classes and groups of sources by establishing whether they could have been drawn from a single population of objects or not. This allows to confirm the correctness and significance of their classification.

3) *Linear Correlations*

Parametric (*Pearson*) and non-parametric (*Spearman rank* and *Kendall* τ) linear correlation tests (e.g. Press *et al.* 1992) are carried out between any two parameters. A real correlation should show in all three tests to similar levels of significance. The sign of any correlation obtained is cross-checked by inspection of the graphical data.

A summary of the main trends in the behaviour of each source for which there are at least two polarisation epochs is given in Table 5.1. This can be used as a rough guide to their variability and it includes the classification of each source, the best estimate for the orientation of the jet close to the core as observed with high frequency VLBI, the number of photometric and polarimetric epochs available, the sign of the correlations between any two parameters measured[1] and the mean value of each parameter over the different epochs.

5.1.3 Source Classification

The Blazars in the sample can be classified according to the overall polarisation properties and variability patterns they exhibit, or according to the type of object (namely BL Lac Object or Quasar).

a) Polarisation Properties

The main features in the polarisation properties of a source can begin to be identified when observed at a number of epochs. This is illustrated by inspection of Figures 5.1, 5.2 and 5.3 (selected from Appendix C) showing the variability of BL Lac Object OJ287 and Quasars 3C273 and 3C279 (all observed in polarimetry at least at 7 different epochs). These include variability plots of a) flux density, b) percentage polarisation, c) the difference between the position angles of the polarisation and the VLBI structural axis and d) the variation of the polarisation with flux density at 1100 μm.

---

[1] In Table 5.1 a '–' sign indicates a negative correlation, a '+' sign a positive correlation and a '0' indicates that the two parameters involved do not appear to be correlated. In some cases, both senses of the correlation are observed to be applicable at different epochs and have been indicated with a '±' sign.

Table 5.1 **Summary of the Observed Porperties of the Sample Sources**

1	*2*	*3*	*4*	*5*	*6*	*7*	*8*	*9*	*10*	*11*	*12*	*13*	*14*	*15*	*16*
Source	**Class**	**Group**	**Jet °**	**nf**	**np**	**P – δ**	**F – δ**	**F – P**	**F – α**	**P – α**	**δ – α**	**F (Jy)**	**α**	**P (%)**	**δ (°)**
0235+164	BL Lac	B	25	5	4	–	+	–	–	+	–	2.20 (0.99)	–0.37 (0.21)	4.92 (1.68)	42.56 (36.85)
0420–014	Quasar	B	90	4	4	–	–	+	+	+		2.78 (1.26)	–0.69 (0.42)	5.04 (0.70)	60.42 (29.65)
0528+134	Quasar	B	44	2	2	–	+	–	+	–	+	2.71 (1.14)	–0.61 (0.12)	3.86 (1.03)	41.39 (55.88)
0735+178	BL Lac	B	73	7	4	–	–	+	0	0	+	1.24 (0.33)	–0.71 (0.45)	6.29 (1.72)	44.55 (34.57)
0736+017	Quasar	B	80	4	2	+	+	+	+	0	0	0.87 (0.27)	–0.54 (0.24)	9.80 (6.21)	24.65 (29.84)
0851+202	BL Lac	A	260	9	7	0	0	±	0	0	0	1.67 (0.48)	–0.61 (0.18)	10.45 (3.21)	28.20 (11.12)
0923+392	Quasar	B	275	4	2	+	–	–	+			1.81 (0.14)	–0.87 (0.24)	4.65 (1.39)	41.49 (17.76)
1226+023	Quasar	C	250	11	8	0	0	+	+	+	0	12.45 (3.62)	–0.71 (0.31)	2.06 (1.09)	65.27 (21.45)
1253–055	Quasar	A	225	10	7	0	0	+	+	0	0	8.31 (2.26)	–0.67 (0.22)	10.47 (2.57)	8.59 (07.71)
1335–127	Quasar	A	135	6	4	0	0	±	+	–	0	2.98 (0.69)	–0.59 (0.27)	5.54 (2.25)	15.20 (02.81)
1641+399	Quasar	C	300	10	7	0	+	–	+	–	0	3.31 (1.47)	–0.69 (0.38)	4.78 (3.37)	64.53 (20.62)
1749+096	BL Lac	B	67	7	3	–	+	–	0	0	0	2.54 (1.38)	–0.56 (0.13)	5.63 (2.55)	36.84 (27.75)
1921–293	Quasar			5	4			±	–	0		6.68 (1.49)	–0.56 (0.09)	9.11 (1.51)	
2200+420	BL Lac	A	200	6	5	0	0	–	+	–	0	1.65 (0.49)	–0.60 (0.57)	9.08 (1.86)	13.08 (15.79)
2223–052	Quasar	B	218	5	2	–	–	+	+			1.96 (1.51)	–0.66 (0.11)	3.01 (1.14)	29.61 (26.97)
2251+158	Quasar	B	295	7	6	–	–	+	+	+	–	4.70 (1.04)	–0.82 (0.58)	4.59 (1.97)	42.45 (29.19)

Column 2 is the *accepted* classification of the source (e.g. Burbridge & Hewitt 1992).
Column 3 is the group assigned according to polarisation properties (§ 5.2).
Column 4 is the orientation of the VLBI jet used in the analysis (see Appendix A).
Columns 5 and 6 are the number of photometric and polarimetric epochs respectively.
Columns 7 to 12 indicate the trend of the correlation between the parameters involved: negative (–), positive (+), both (±) or no correlation (0) (see Appendix D).
Columns 13 to 16 give the mean and standard deviation of flux density F, spectral index α, degree of polarisation P and difference between the position angle and the orientation of the VLBI jet δ.

From these plots variability patterns emerge: for example, 3C279 tends to be highly polarised with a mean polarisation of *10.47 %*, has an unchanging magnetic field perpendicular to the jet, and its flux density and polarisation are strongly correlated (Kendall $\tau = 0.62$ with a significance of *94.91 %*). OJ287 also has a mean polarisation of *10.45 %*, its magnetic field also tends to remain perpendicular to the jet (although the position angle is less stable on this source) and the degree of polarisation and flux density are correlated during some epochs and anticorrelated at others (see later § 5.3). In contrast, the polarisation of Quasar 3C273 has very different characteristics. It always has a very low polarisation level and the magnetic field tends to be parallel to the jet. It is however very bright and the flux and polarisation are highly correlated. These examples illustrate how different types of sources can have similar polarisation properties that can be used to associate them together (see § 5.2), in the hope of simplifying the task of building a general picture against which theoretical models can be assessed (see Chapter 6).

b) Source Type

The classification of these sources as BL Lacs or Highly Polarised Quasars originates primarily from observations carried out at optical wavelengths and pre-dates the advent of the term Blazar, which groups them together. In order to make a statistically significant comparison between the two classes, all available measurements can be considered as independent observations of a BL Lac Object or a Quasar, irrespective of the actual source involved and the epoch of observation. This is in principle a valid and often used approach (e.g. Roberts *et al.* 1990) because of the erratic variability exhibited by these objects. However, it has been observed that the variation of each individual object is usually restricted to a given range of values. This introduces a certain degree of bias towards those sources observed most frequently, which tend to be the brightest and more highly polarised.

5.2 Polarisation Properties of Blazars at 1100 μm

Although the variability of Blazars is a chaotic phenomenom, when a source has been observed at 3 or 4 different epochs, its polarisation properties can begin to be characterised. In this section patterns are identified into which sources with similar polarisation behaviour can be grouped together. These groups are then compared graphically and statistically.

Figures 5.1 Variability of Blazar OJ287 at 1100 μm

a) Flux Density

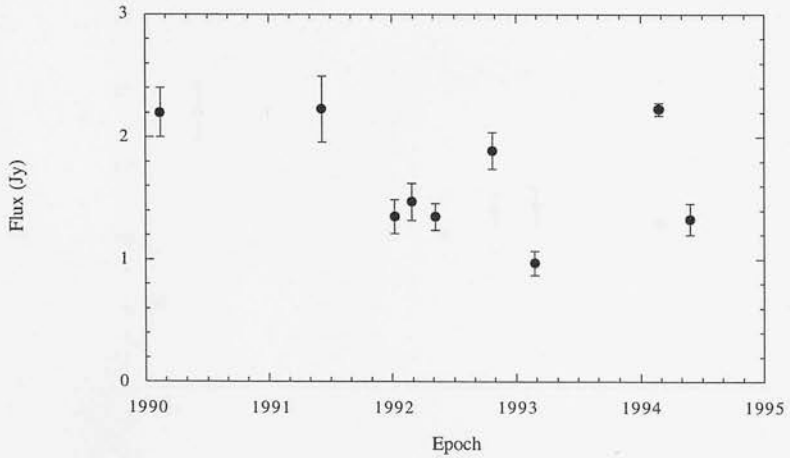

b) Polarisation

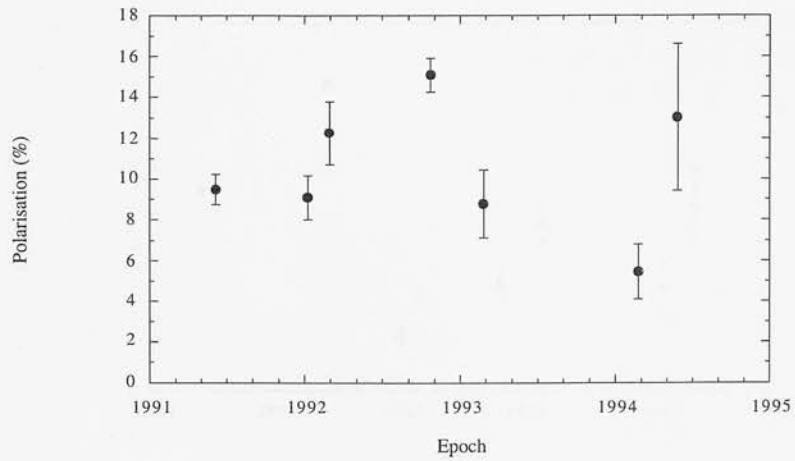

c) Polarisation Variation with Flux Density

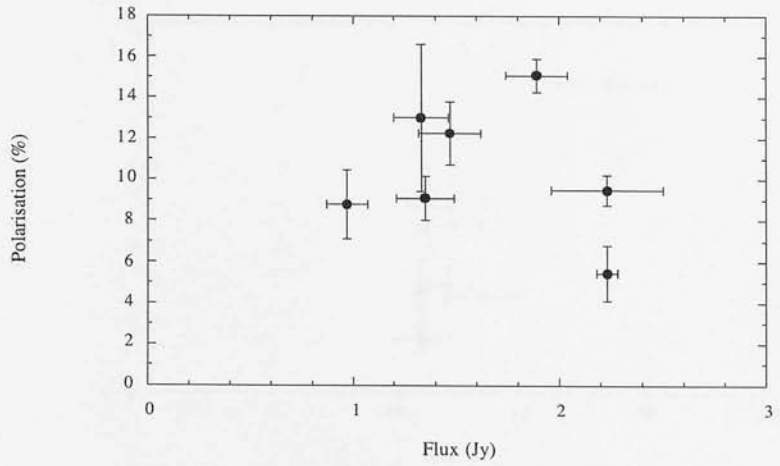

d) Position Angle

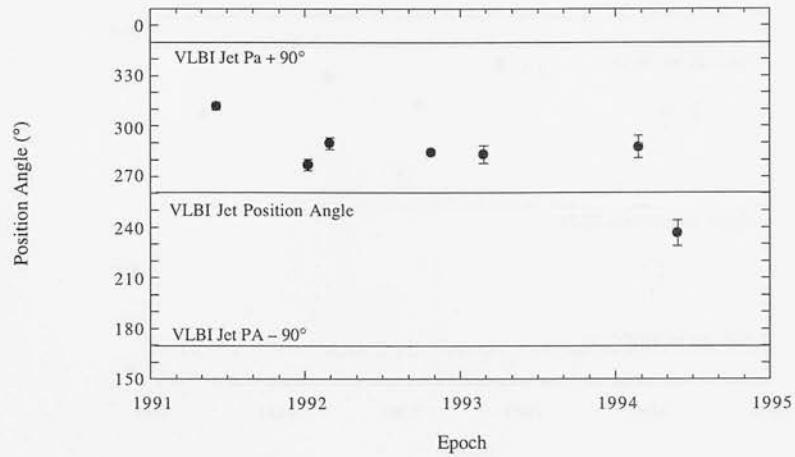

Figures 5.2 **Variability of Blazar 3C273 at 1100 μm**

a) **Flux Density**

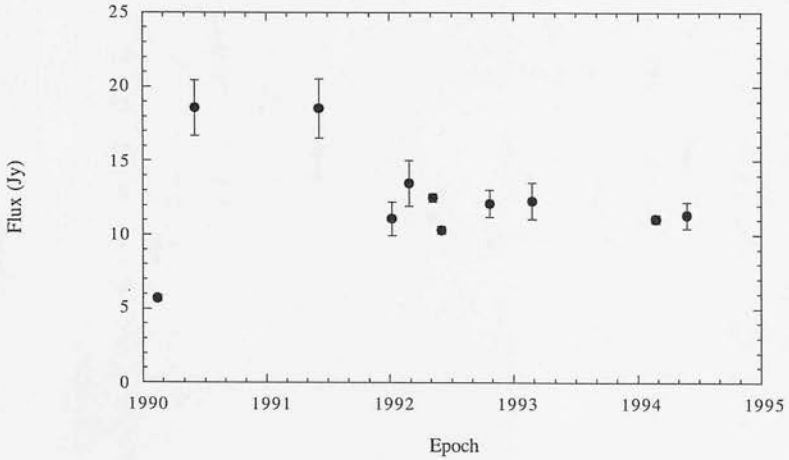

b) **Polarisation**

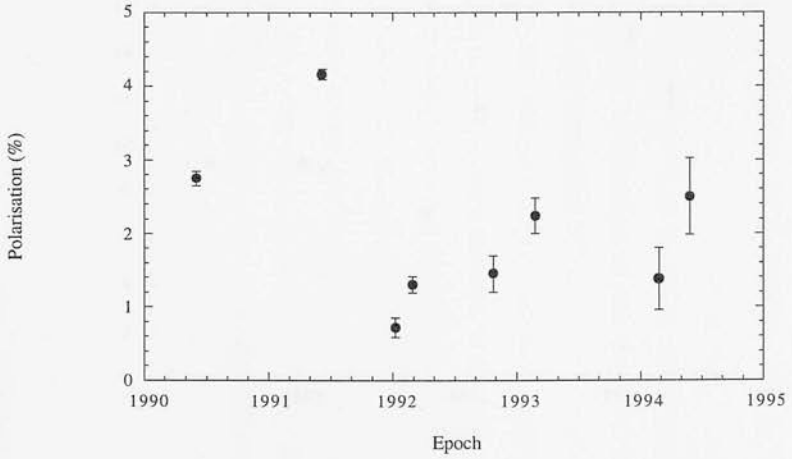

c) **Polarisation Variation with Flux Density**

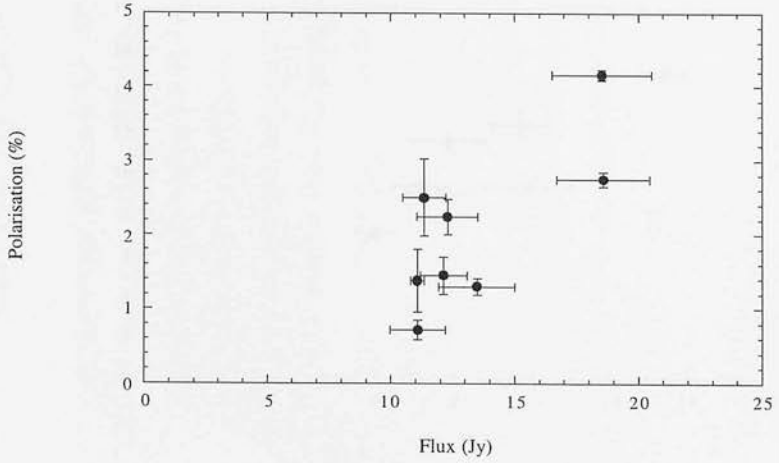

d) **Position Angle**

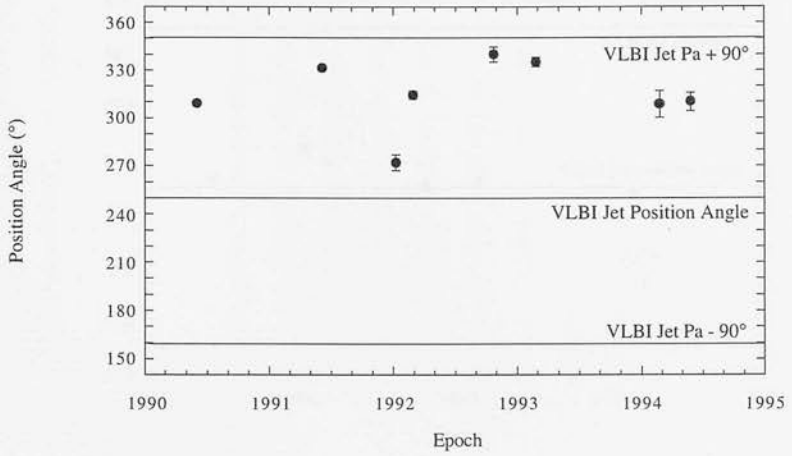

Figures 5.3 Variability of Blazar 3C279 at 1100 μm

a) Flux Density

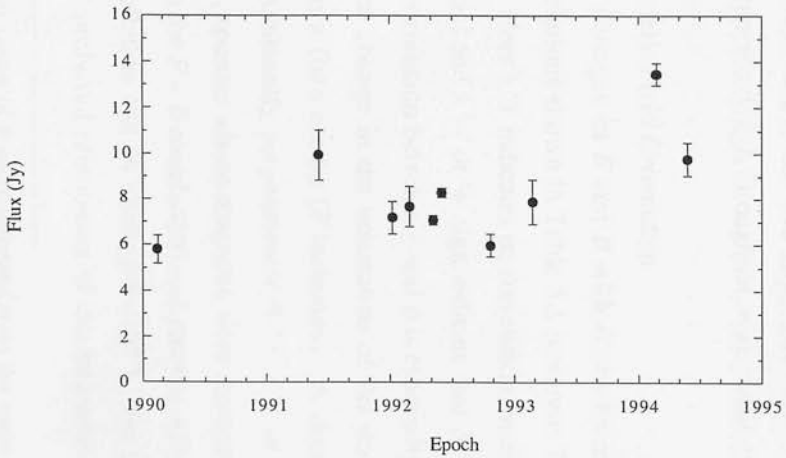

b) Polarisation

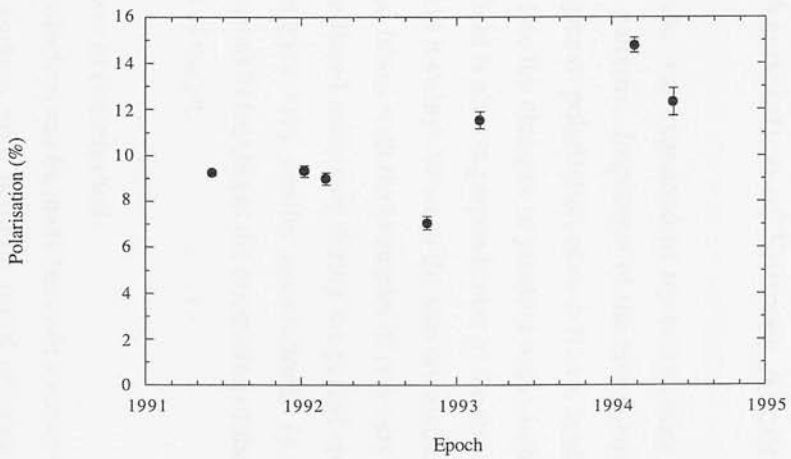

c) Polarisation Variation with Flux Density

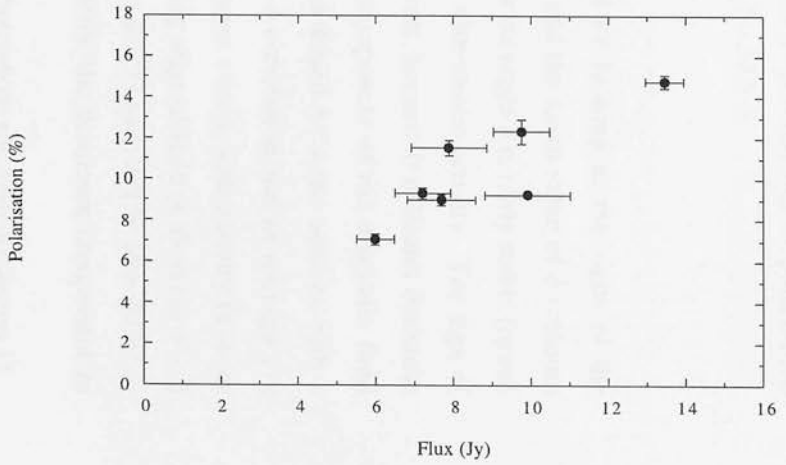

d) Position Angle

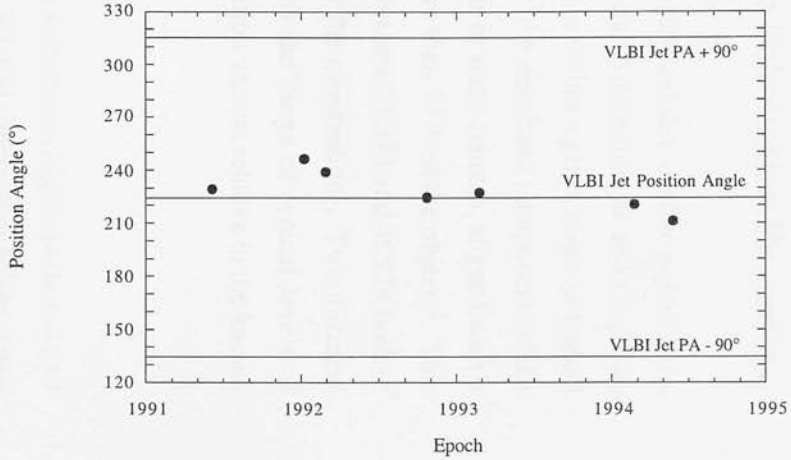

5.2.1 Association of Sources According to Polarisation Properties

The database was examined to try to associate objects that exhibit similar polarisation variability patterns. Inspection of the raw polarisation data (Appendices B and C) shows that the degree of polarisation of each Blazar tends to remain within a given range of typical values. Also, the changes in position angle indicate that the dominant component of the magnetic field is always perpendicular to the structural axis in some sources, aligned with it in others, but it swings between the two orientations in more than *50 %* of the objects[2]. This is illustrated below with the examples of two very bright Quasars, 3C273 and 3C279 both of which have flared massively during the period covered by the observations. Two different approaches give very similar associations: *1)* looking at the range of typical levels of polarisation and *2)* looking at the orientation of the polarisation vectors relative to the known orientation of the jet.

1) Degree of Polarisation

A distinction can be made between sources which on average are highly polarised (*>9 %*), sources with medium mean polarisation (*~5 %*) and those with lower mean polarisation levels (*~3 %*). For example, the flux density in 3C273 has been measured to vary between *11 – 18.5 Jy* while its polarisation ranged between *<1 – 4 %*; likewise, 3C279 has had large flux changes between *6 – 13.5 Jy* but its polarisation has remained high throughout, with values between *7 – 14.8 %*.

2) Magnetic Field Orientation

The changes in F and P with δ can be examined by looking at the signs of the correlations shown in Table 5.1 (columns 7 and 8) and the mean value of δ (column 16). Here a '0' indicates no correlation, meaning that the angle δ is fairly stable (or too erratic) and a '–' or '+' sign indicate that δ changes with source activity. The sign of the correlation between F and δ is especially important, because it indicates the sense of the change in the orientation of the dominant component of the magnetic field when a flare occurs (F increases). A distinction is found between sources with a predominantly perpendicular field (a '0' in the $F - \delta$ correlation and an average $\delta < 30°$), sources whose magnetic field orientation changes widely with activity (a '+' or '–' in the $F - \delta$ correlation) and sources with a roughly aligned field (a '0' in the $F - \delta$ correllation and an average $\delta > 60°$). For example, 3C273 and 3C279 also differ in their preferred orientation of the magnetic field: while the dominant component in

---

2 The mean values of P and δ obtained from the multi-epoch observations are given in columns 15 and 16 on Table 5.1.

3C279 is always perpendicular to the jet, in 3C273 has a strong tendency to be aligned with it (see Figures 5.2 d) and 5.3 d)).

All the sources in the sample for which there are several epochs of observations and VLBI information, can be satisfactorily described according to the criteria outlined above. A most striking result, however, is to find that the two approaches adopted to find polarisation variabitily patterns permit to associate the sources in an identical way. This result enables the sources in the sample to be classified into the following groups for purely analytical purposes:

- ***Group A***: sources which exhibit the highest degrees of polarisation, tend to maintain their polarisation vectors fairly constant (even during large flares) and have their magnetic fields preferentially perpendicular to their jets.
- ***Group B***: sources with more or less intermediate polarisation levels, whose preferred magnetic field orientation can swing between orthogonal congifurations with respect to the structural axis.
- ***Group C***: sources with the lowest degrees of polarisation which have a very strong tendency to keep their magnetic fields roughly aligned with their jets.

The association of each source with the polarisation group which best describes its properties is shown in column 3 of Table 5.1. To ensure that they have all been classified optimally (given the data available) a 1-D Kolmogorov-Smirnov test has been carried out on the polarisation parameters P and δ, between each source and the rest of the sources in its group, and against the other groups. The results of these tests are given in Appendix E. It turns out that a similar ratio of BL Lacs to Quasars is found in groups A and B but in group C there are only Quasars.

5.2.2 Graphical Representation

The measurements carried out at 1100 μm are plotted in Appendix C for each individual source observed more than once. In this section, all the observations recorded in the database are plotted in terms of the photometric and polarisation parameters. No distinction has been made between observations of a given source obtained at different epochs. The error bars are not shown for clarity but all detections are better than 3σ.

a) Photometric Parameters F and α

Significant changes in flux density F indicate the occurrence of flares. Changes in spectral index α characterise the flaring behaviour throughout the frequency range 150 to 375 GHz. Figure 5.4 is a plot of α versus F and it does not indicate any major differences between sources with different polarisation properties, with perhaps the exception of higher fluxes measured in group C sources (probably a consequence of the need for very bright objects to detect low levels of polarisation).

Figure 5.4 Spectral Index vs Flux Density at 1100 μm

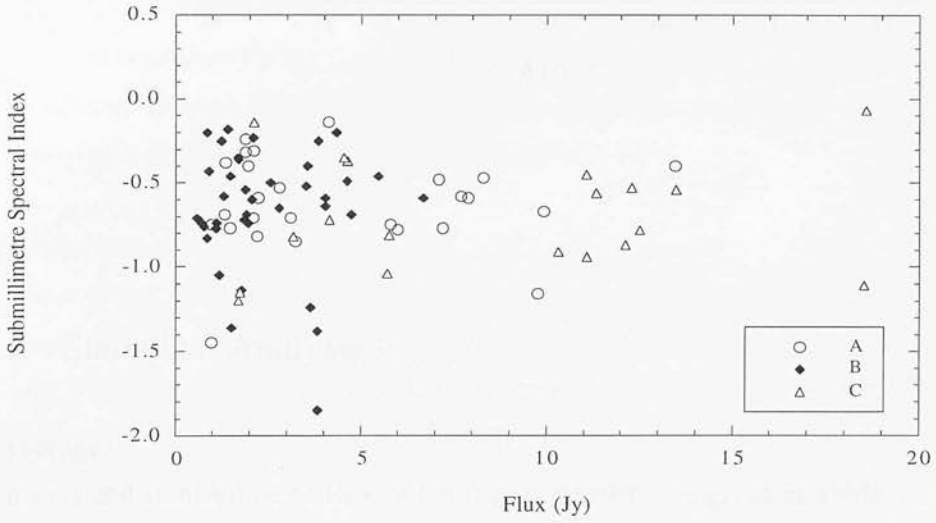

b) Polarisation Parameters P and δ

The percentage polarisation P gives an indication of the degree of ordering of the magnetic field in the emitting region. The difference between the position angle and the structural axis of the VLBI jet δ, gives the direction orthogonal to the magnetic field orientation.

Figure 5.5 clearly shows how the different groups occupy different areas of the plot. It also indicates that when the dominant component of the magnetic field is the one perpendicular to the jet ($\delta=0°$) a higher percentage polarisation is generally measured, and that the polarisation decreases as the dominant component of the magnetic field becomes more aligned with the jet ($\delta=90°$). This observation is a strong indication that all Blazars share the same physical conditions in the most compact regions of their jets.

Figure 5.5 Degree of Polarisation vs Magnetic Field Orientation

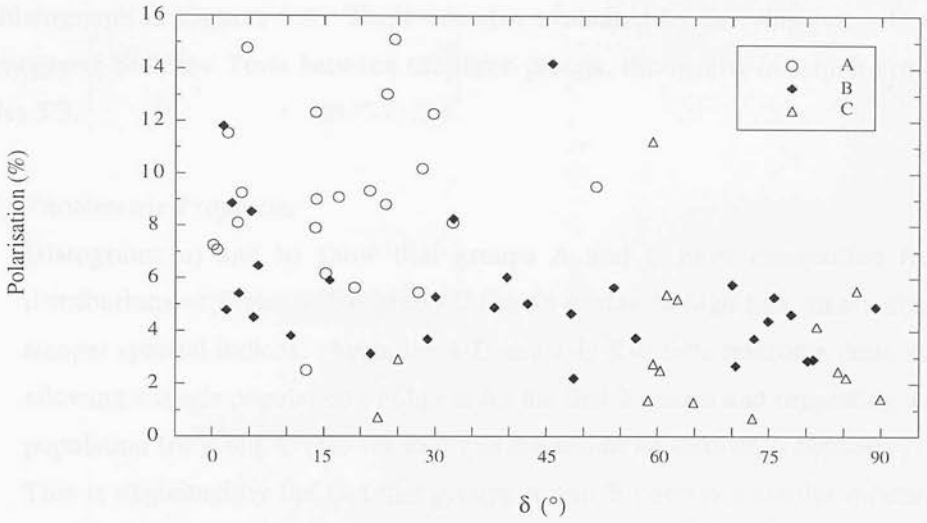

5.2.3 Statistical Analysis

a) Averages

The means and standard deviations of the four parameters are given in Table 5.2 for the three polarisation groups. The mean flux density is highest in group C sources. The spectral index is the same for groups A and B, which contain a mixture of BL Lacs and Quasars, and slightly higher in group C which has lowly polarised Quasars only. This is one way in which the source sample is biased, since low polarisation BL Lacs have not been detected probably due to their intrinsic lower brightness. The mean polarisation parameters P and δ are, however, quite distinct for the three groups, as expected.

Table 5.2 Mean and Standard Deviation

Group	F (Jy)	α	P (%)	δ (°)
A	4.06 (3.30)	–0.63 (0.28)	9.30 (3.06)	16.69 (12.76)
B	2.39 (1.49)	–0.65 (0.36)	5.24 (2.38)	42.40 (28.57)
C	8.10 (5.42)	–0.70 (0.33)	3.33 (2.72)	64.92 (20.31)

b) Frequency Distributions

All the above observations are further reinforced by inspection of the distributions plotted in the histograms in Figures 5.6. These are also evaluated by carrying out 1-D and 2-D Kolmogorov-Smirnov Tests between the three groups, the results of which are listed in Tables 5.3.

1) Photometric Properties

Histograms a) and b) show that groups A and B have compatible frequency distributions of F and α, but group C has an excess of high flux measurements and steeper spectral indices. Again the 1-D and 2-D K-S tests reinforce these results by allowing a single population of objects for the first 2 groups and suggesting a separate population for group C (see for example the results of tests on α between A and B). This is explained by the fact that groups A and B contain a similar mixture of BL Lacs and Quasars, unlike group C which contains only Quasars, and the two classes may have different photometric properties (see § 5.3).

2) Polarisation Properties

Histograms c) and d) in Figures 5.6 clearly show that the three variability groups have very different frequency distributions of P and δ. This is reinforced by the results of the 1-D K-S tests, which show how the three groups are exclusive of each other in terms of their polarisation parameters. The 2-D tests emphasise this result indicating different populations whenever either P or δ is one of the parameters involved. The values of the K-S statistic and the significance levels of the tests involving P and/or δ are especially high in the comparison between groups A and C (opposite extremes). These are slightly lower (and of the same order) between groups A and B and B and C, thus proving the consistency of this classification.

c) Linear Correlations

Linear correlation tests have been carried out between any two parameters for each source individually and for various subsets of data[3]. The number of observations available for each individual object is, in many cases, not sufficient for these tests to be statistically significant. However, the sense of the correlation obtained from these tests can be compared with the graphical information plotted in Appendix C, so they can still be useful in helping to establish any 'trends' present in the variability of most sources.

---

[3] The results obtained are given in Appendix D.

Figures 5.6 Histograms for Polarisation Groups

a) Flux Density (Jy)

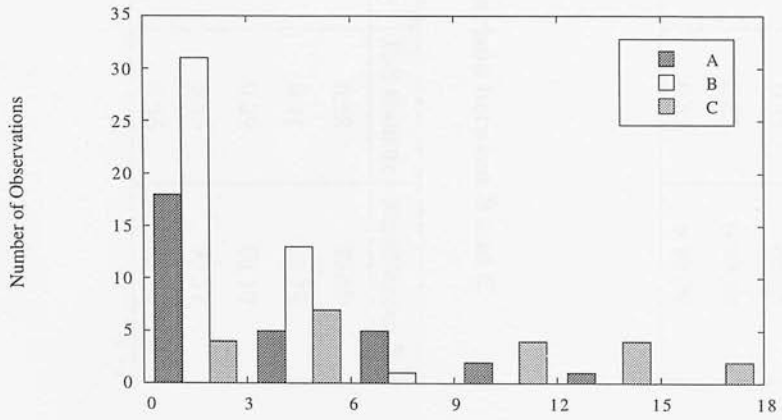

b) Spectral Index

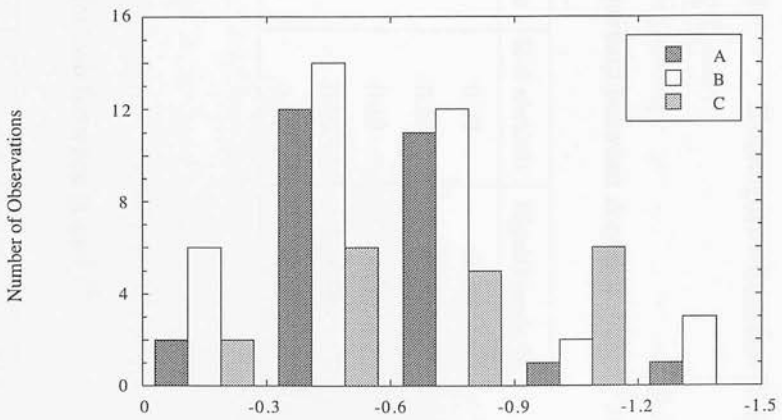

c) Polarisation (%)

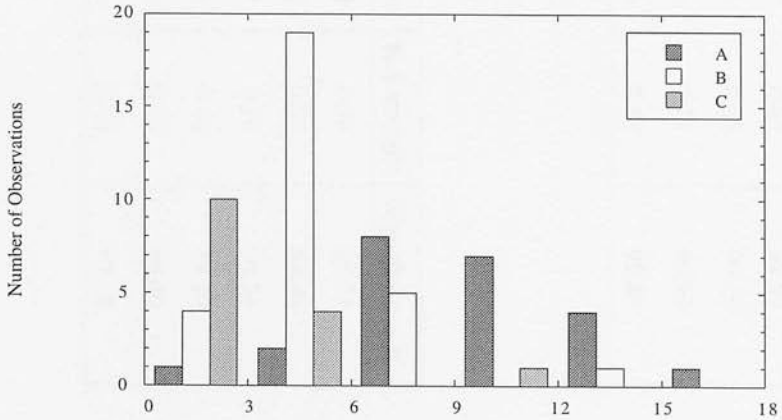

d) Magnetic Field Orientation (°)

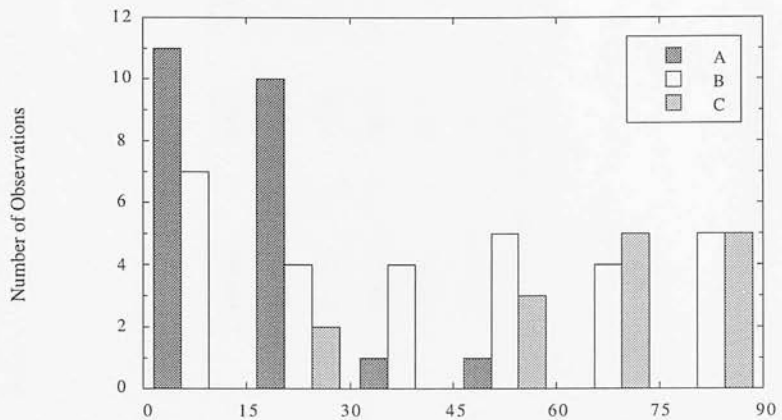

Tables 5.3 Kolmogorov-Smirnov Tests between Polarisation Groups

a) Comparison between A and B

1-Dim	K-S statistic	Significance %
F	0.30	94.20
f	0.29	92.44
α	0.10	0.26
P	0.70	> 99.99
δ	0.58	99.98

2-Dim	K-S statistic	Significance %
$P-\delta$	0.69	> 99.99
$f-\delta$	0.57	99.91
$f-P$	0.66	99.99
$f-\alpha$	0.21	46.78
$P-\alpha$	0.66	99.98
$\delta-\alpha$	0.55	99.64

b) Comparison between A and C

1-Dim	K-S statistic	Significance %
F	0.44	99.06
f	0.46	99.31
α	0.33	84.93
P	0.85	> 99.99
δ	0.87	> 99.99

2-Dim	K-S statistic	Significance %
$P-\delta$	0.91	> 99.99
$f-\delta$	0.78	> 99.99
$f-P$	0.85	> 99.99
$f-\alpha$	0.53	99.46
$P-\alpha$	0.73	99.97
$\delta-\alpha$	0.67	99.89

c) Comparison between B and C

1-Dim	K-S statistic	Significance %
F	0.58	99.99
f	0.41	98.79
α	0.29	80.10
P	0.53	99.57
δ	0.56	99.76

2-Dim	K-S statistic	Significance %
$P-\delta$	0.59	99.77
$f-\delta$	0.63	99.90
$f-P$	0.56	99.54
$f-\alpha$	0.45	98.20
$P-\alpha$	0.57	99.40
$\delta-\alpha$	0.45	95.20

The following are tentative correlations observed between the four measured parameters as summarised in Table 5.1:

1) Flux Density

There is a clear positive correlation between the flux density and the spectral index, which indicates that the continuum emission becomes flatter as the sources flare. The degree of polarisation is also correlated to flux changes but the sense of the correlation varies between sources (see § 5.3).

2) Spectral Index

No specific pattern has been observed between the variation of the spectral index and the polarisation parameters.

3) Degree of Polarisation

There is an overall anticorrelation between the polarisation level and the magnetic field orientation (see Figure 5.5). In general, higher polarisation is observed when the dominant component of the magnetic field is perpendicular to the VLBI jet.

4) Magnetic Field Orientation

Variations in the orientation of the magnetic field, in those sources where it has been observed to change between orthogonal directions, can be related to flux changes. The sense of this correlation is positive in some sources, but negative in others. Figures 5.7 are plots of flux density F versus magnetic field orientation δ for a) sources with a positive correlation and b) sources where this correlation is negative. The results of the Spearman rank-order correlation test between the normalised flux f and δ on these two subgroups of objects emphasises this distinction: sources plotted in figure a) have a correlation coefficient of *0.60* with significance *94.72 %* while sources plotted in figure b) have a correlation coefficient of *–0.55* with significance *98.29 %*. Kolmogorov–Smirnov tests carried out on all measured parameters between these two subgroups did not reveal any other significant differences between them.

One possible explanation for this discrepancy lies in the uncertainty in the determination of the structural position angles of the VLBI jets. In particular, the sources plotted in figure a) have largely unresolved cores (see Appendix A) and the number of VLBI observations is very scarce. Therefore, the fact that the estimates of the VLBI jet position angle used in the analysis is wrong by as much as *90°* has to be considered as an unlikely possibility. If this were indeed the case, the main implication would be that the magnetic field changes from an aligned congiguration to a perpendicular one during flares.

Figures 5.7 Flux Density versus Magnetic Field Orientation

a) Sources with Positive Correlation

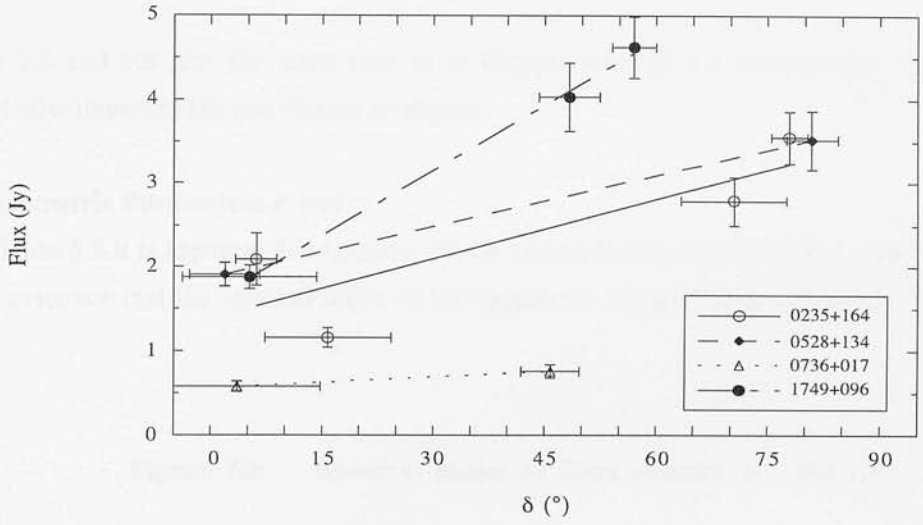

b) Sources with Negative Correlation

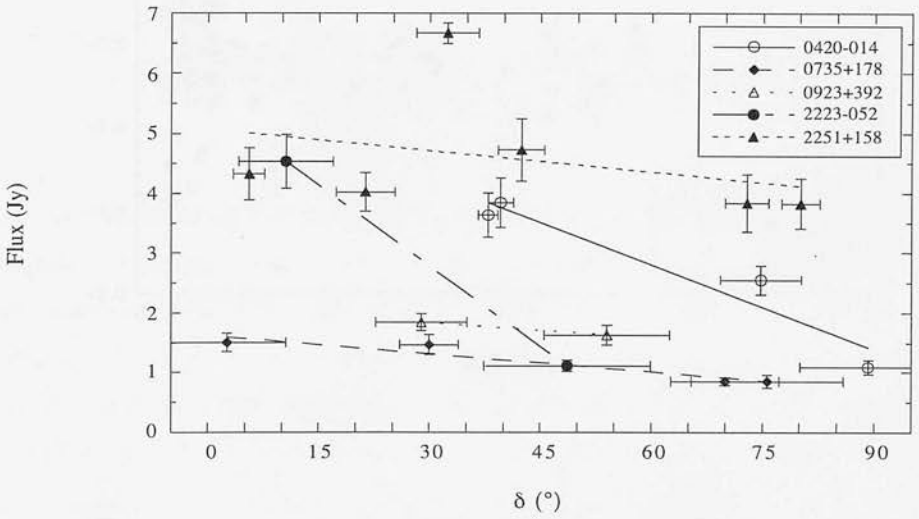

5.3 Polarisation Properties of BL Lacs and Quasars

The analysis of the JCMT database may contribute to establish whether there are significant differences between BL Lac Objects and Quasars, that could be ascribed to their having different parent populations, or if on the contrary, their millimetre properties render them indistinguishable. In this section, the database is analysed in terms of object type.

5.3.1 Graphical Analysis

Figures 5.8 and 5.9 plot the same data as in Figures 5.4 and 5.5 respectively, but the symbols now represent the two classes of objects.

a) Photometric Parameters *F* and α

From Figure 5.8 it is apparent that Quasars can be much brighter than BL Lacs. There may also be evidence that the spectral index of the Quasars is slightly steeper than that of BL Lacs.

Figure 5.8 Spectral Index vs Flux Density at 1100 μm

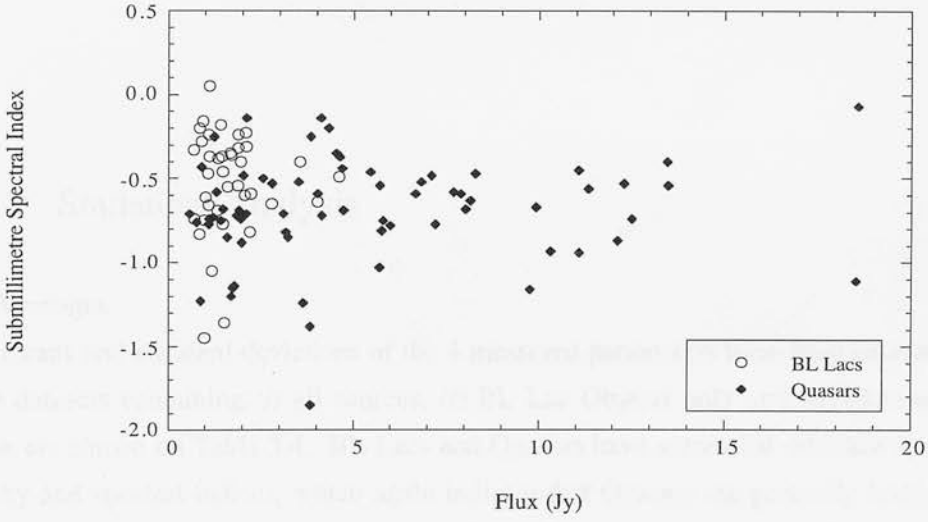

b) Polarisation Parameters *P* and δ

As shown earlier, the degree of polarisation is highest when the magnetic field is orthogonal to the jet. Figure 5.9 indicates that this applies equally to BL Lacs and Quasars. The most noticeable observation is that there are hardly any BL Lacs measurements below the *5 %* polarisation level and few are found with the magnetic field parallel to the jet. A similar plot for BL Lacs can be found in Gabuzda *et al.* (1994b) who observed the cores of this type of source with VLBI polarimetry. In contrast, most Quasar observations have polarisation levels less than *6 %* and a very significant number of them are associated with parallel magnetic fields.

Figure 5.9 Degree of Polarisation vs Magnetic Field Orientation

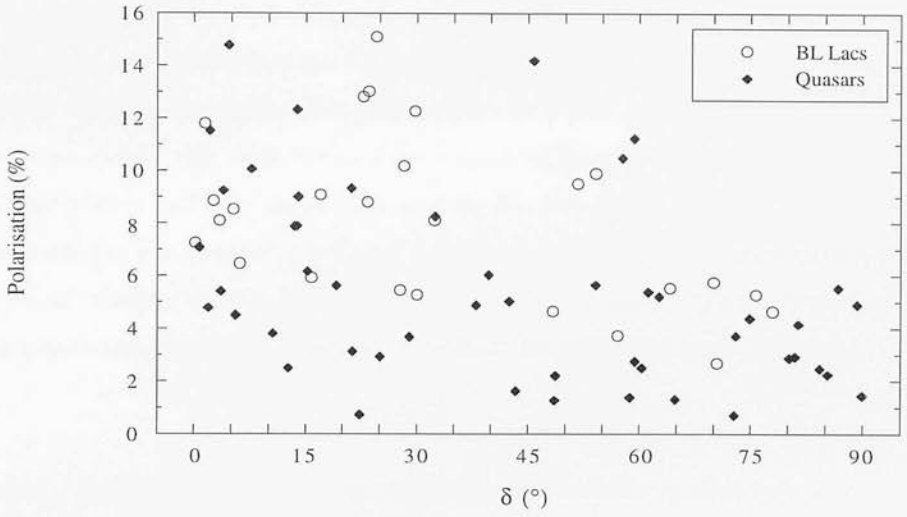

5.3.2 Statistical Analysis

a) Averages

The means and standard deviations of the 4 measured parameters have been calculated for three datasets containing: *i)* all sources, *ii)* BL Lac Objects only and *iii)* Quasars only. These are shown on Table 5.4. BL Lacs and Quasars have somewhat different mean flux density and spectral indices, which again indicate that Quasars are generally brighter and have a steeper sub/millimeter continuum[4]. The polarisation levels and preferred magnetic field orientations do not differ greatly between the two classes.

Table 5.4 Means and Standard Deviation

Dataset	F (Jy)	α	P (%)	δ (°)
All		–0.63 (0.32)	6.36 (3.56)	38.18 (27.82)
BL Lacs	1.61 (0.80)	–0.52 (0.31)	7.59 (3.29)	33.18 (24.94)
Quasars	3.59 (0.85)	–0.69 (0.31)	5.70 (3.56)	41.55 (29.07)

[4] This is especially true close to the 'quiescent state', when the mean $\alpha \sim -0.80$ if only the lowest flux observations of the Quasars with several epochs are used.

Figure 5.9 Degree of Polarisation vs Magnetic Field Orientation

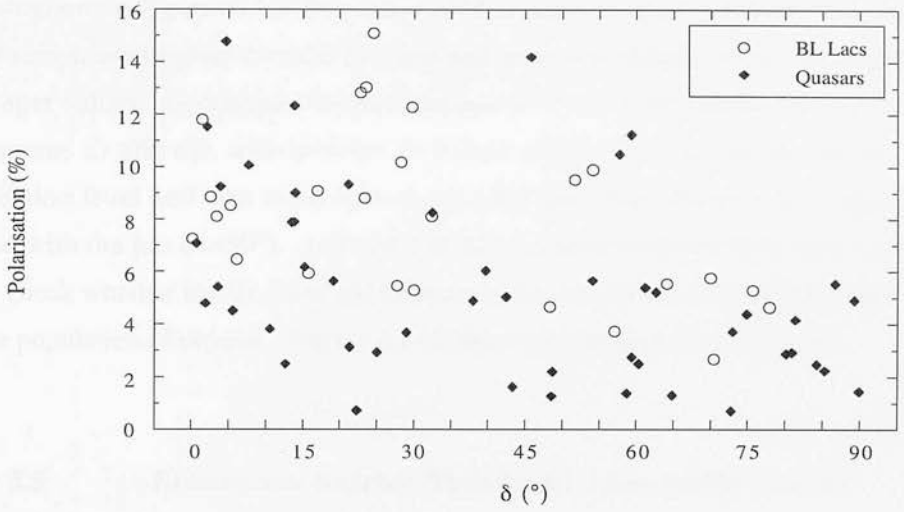

5.3.2 Statistical Analysis

a) Averages

The means and standard deviations of the 4 measured parameters have been calculated for three datasets containing: *i)* all sources, *ii)* BL Lac Objects only and *iii)* Quasars only. These are shown on Table 5.4. BL Lacs and Quasars have somewhat different mean flux density and spectral indices, which again indicate that Quasars are generally brighter and have a steeper sub/millimeter continuum[4]. The polarisation levels and preferred magnetic field orientations do not differ greatly between the two classes.

Table 5.4 Means and Standard Deviation

Dataset	F (Jy)	α	P (%)	δ (°)
All		–0.63 ± 0.32	6.36 ± 3.56	38.18 ± 27.82
BL Lacs	1.61 ± 0.80	–0.52 ± 0.31	7.59 ± 3.29	33.18 ± 24.94
Quasars	3.59 ± 0.85	–0.69 ± 0.31	5.70 ± 3.56	41.55 ± 29.07

4 This is especially true close to the 'quiescent state', when the mean $\alpha \sim -0.80$ if only the lowest flux observations of the Quasars with several epochs are used.

b) Frequency Distributions

The shape of the distributions of the four parameters in BL Lacs and Quasars are shown in the histograms in Figures 5.10. Inspection of histograms a) and b) confirms that the Quasars in this sample are brighter than the BL Lacs and have a distribution of spectral index centred on steeper values. In contrast, the distributions of P and δ are similar for the two classes (histograms c) and d)), with perhaps an excess of Quasar observations below the *3 %* polarisation level and also more Quasar than BL Lac observations with magnetic fields aligned with the jets (δ=*90°*). 1-D and 2-D Kolmogorov-Smirnov tests have been carried out to check whether the BL Lacs and Quasars in the sample could have been drawn from a unique population of objects. The results of these tests are shown on Table 5.5.

Table 5.5 Kolmogorov-Smirnov Tests for BL Lacs against Quasars

1-Dim	K-S statistic	Significance %
F	0.55	> 99.99
f	0.10	11.42
α	0.33	99.32
P	0.31	95.46
δ	0.23	68.64

2-Dim	K-S statistic	Significance %
$P-\delta$	0.40	98.25
$f-\delta$	0.23	59.39
$f-P$	0.31	91.23
$f-\alpha$	0.39	99.60
$P-\alpha$	0.37	95.49
$\delta-\alpha$	0.30	80.56

The relatively small values of the K-S statistic in all the entries in Table 5.5 indicate that the differences between the distributions of the various parameters for the BL Lacs and Quasars must be very mild. A high significance level suggests different populations for BL Lacs and Quasars, while a lower percentage (e.g. <*80 %*) might imply a single population of objects.

1) One-Dimensional K-S Tests

- In terms of flux density F the two classes must have been drawn from different populations (K-S statistic is *0.55* with >*99.99 %* significance), consistent with the fact that Quasars are significantly brighter. However, if normalised flux f is used, this difference disappears (*K-S = 0.10 @ 11.42 %*). This indicates that the flaring variability is comparable in all sources.

- The spectral index α is the main differentiating parameter between the two classes with *K-S = 0.33 @ 99.32 %* significance level.

Figures 5.10 Histograms for BL Lac Objects and Quasars

a) Flux Density (Jy)

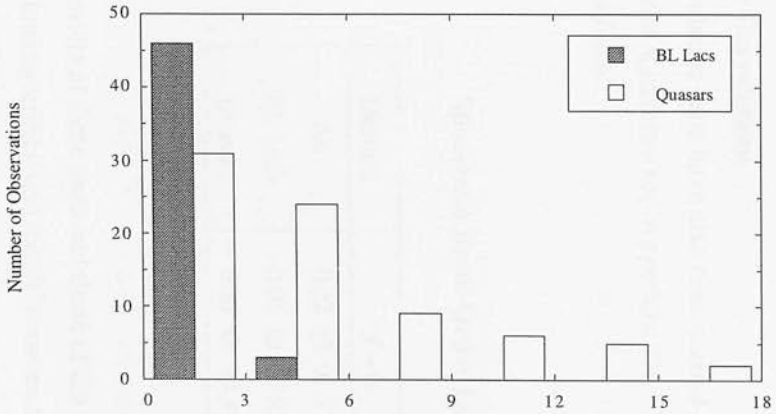

b) Spectral Index

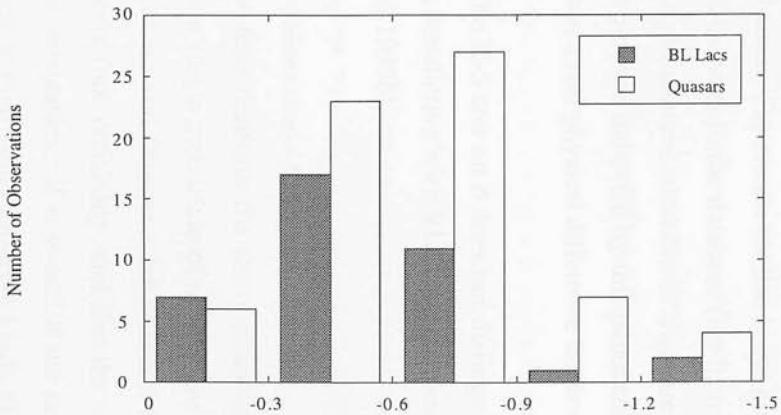

c) Polarisation (%)

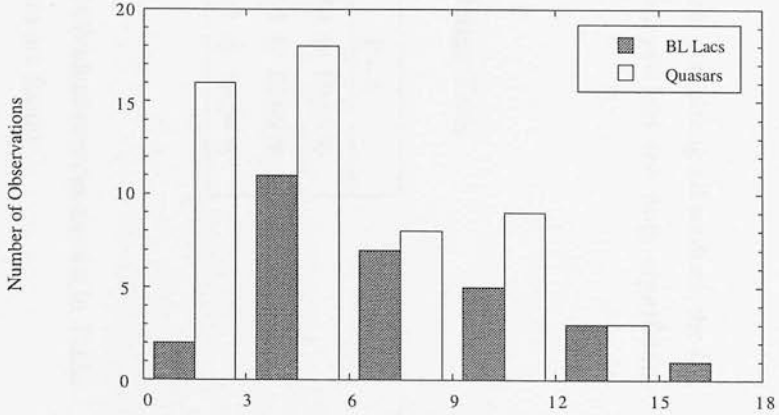

d) Magnetic Field Orientation (°)

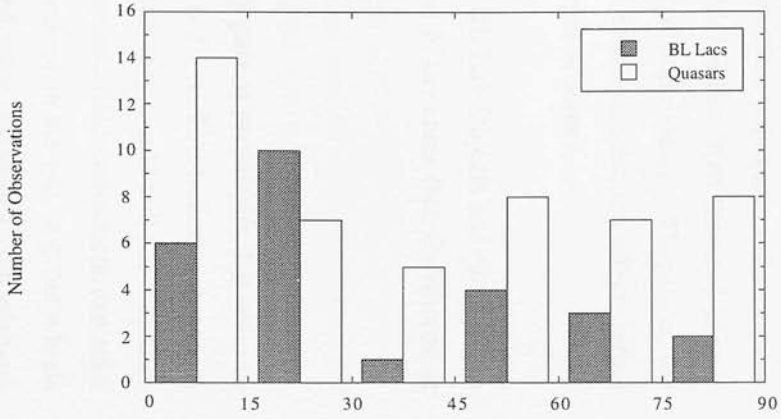

- The percentage polarisation P also indicates a possible difference between the two classes. The reason for this is the greater number of low polarisation observations of Quasars in the database (see histogram c)), which arises from the need of very bright sources in order to measure low levels of polarisation. Therefore, the difference indicated by this parameter could well be due to selection effects rather than a real physical difference between the two types of source.

- The K-S test on δ does not distinguish between BL Lac Objects and Quasars, in contradiction with VLBI polarisation observations of the cores (see Cawthorne *et al.* 1993b).

2) *Two-Dimensional K-S Tests*

These tests reinforce the above results since the only pair of parameters that seem to allow a single population of objects unambiguously is $f - \delta$. This indicates that even if BL Lacs and Quasars were different types of objects they would still show similar intrinsic flux variability, and that the dominant magnetic field component can take either orientation. If α is one of the parameters involved in the test, it gives a high chance of their being different kinds of sources. The same is true of P, but perhaps for the reasons given above.

c) Linear Correlations

Linear correlation tests have also been carried out on datasets containing all sources, the BL Lacs and the Quasars (see Appendix D). Table 5.6 summarises the only significant correlations found.

Table 5.6 Spearman Rank-Order Linear Correlation Tests

Dataset	$f - \alpha$	$P - \delta$
All	0.22 @ 97.87 %	–0.49 @ 99.99 %
BL Lacs	–0.05 @ 25.95 %	–0.50 @ 99.99 %
Quasars	0.33 @ 99.37 %	–0.47 @ 99.94 %

From the results of these tests and those of the analysis of *individual* sources shown in Table 5.1, the following 'correlation trends' between the two classes are found:

1) *Normalised Flux – Spectral Index*

When all the observations are considered there is a hint of a possible correlation between the normalised flux f and the spectral index α ($r=0.22$ with *97.87 %* significance). This vanishes for the BL Lacs alone, but it is somewhat significant for the Quasars ($r=0.33$ @ *99.37 %*), indicating that for these sources the spectral curve tends to become slightly shallower as the flux increases during flares. This discrepancy in the spectral index of the two classes was also indicated in the previous tests and may constitute a possible difference between them.

2) *Polarisation – Magnetic Field Orientation*

A significant anticorrelation is found between the degree of polarisation P and δ and it applies with identical strength ($r\sim0.5$) and to the same level of significance (*~99.99 %*) to both BL Lacs and Quasars. This confirms and quantifies the earlier observations made by inspection of Figure 5.9.

3) *Flux Density – Polarisation*

These two parameters show trends of being either correlated or anticorrelated in all sources (e.g. see Figure 5.2 d) and 5.3 d)). In some cases a correlation of opposite sign is seen at different epochs (e.g. OJ287 see Figure 5.1 d)). From inspection of column 9 in Table 5.1 it can be seen that there is a tendency for the flux density and degree of polarisation to be correlated in Quasars (i.e. both observables increase during flares) and anticorrelated in BL Lacs (i.e. the polarisation drops as the flux increases). In particular,

- F and P are highly correlated in Quasars 3C273, 3C279, 3C454.3. A positive correlation is also observed in BL Lac Object 0735+178 and this is also the trend in most of the 2-epoch Quasars.
- F and P tend to be anticorrelated in BL Lac Objects 0235+164, BL Lacertae and 1749+096 and Quasar 3C345.
- Both types of correlation are clearly seen in BL Lac Object OJ287 and probably in Quasars 1335-127 and 1921-293. The change in the sign of the correlation occurs at an epoch where the flux density was a maximum and the polarisation a minimum.

Examples of these three trends are shown on Figures 5.11, where the percentage polarisation has been plotted against flux for 2 BL Lacs and 2 Quasars, all high polarisation sources. The numeric labels indicate the sequence of observation epochs, so that the sense of the correlation can be followed (no error bars have been included

for clarity). In Table 5.7 are the results from a correlation test performed on these data which clearly indicate the relationship between these two parameters. In the case of OJ287 the sense of the correlation appears to change at epoch '5'. This can be seen both on figure d) and the fact that if all epochs are included, no correlation at all is measured, but when the correlation test is carried out on epochs 1–5 and 5–7 separately, significant correlations of opposite sign are obtained.

Table 5.7 Linear Correlations in Data Plotted in Figures 5.11

Source	Spearman Rank-Correlation	Significance Level (%)
3C279	0.71	92.82
3C454.3	0.94	99.52
BL Lacertae	–0.61	71.52
OJ287 (all epochs)	–0.05	9.16
OJ287 (epochs 1 – 5)	0.70	81.19
OJ287 (epochs 5 – 7)	–0.50	33.33

5.4 Shortcomings of the Present Database

The main factors compromising the validity of the results of the analysis presented here are the quality and quantity of the database. All the polarisation measurements included in the analysis had signal to noise better than 3σ in the worst case. The minimum signal to noise of the photometric measurements is much higher. The amount of data so far gathered is certainly enough to establish an analysis framework into which new observations can be added. As new data is obtained the results shown here will probably be better determined, but the overall pattern seen so far is likely to be preserved. In this section the main limitations of the present database are highlighted.

5.4.1 Bias of the Database

A certain degree of bias is introduced in the data by a number factors:

- There are more observations of Quasars than BL Lacs. This is of course a consequence of the former being brighter and hence easier to detect than the latter.

Figures 5.11 Polarisation and Flux Correlation through Observation Epochs

a) 3C279

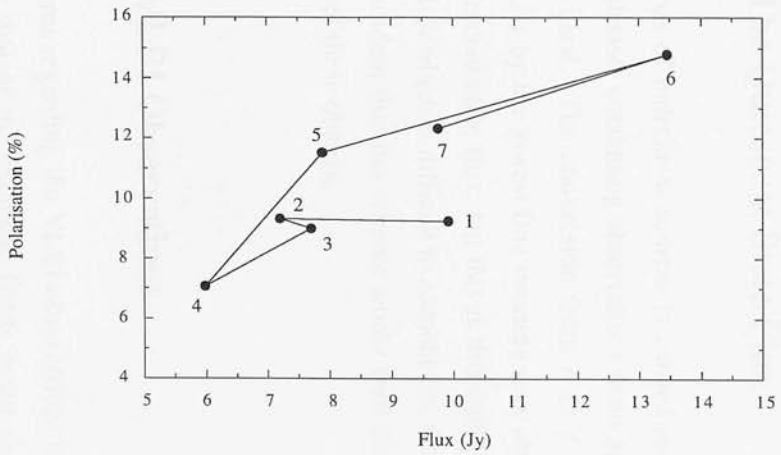

b) 3C454.3

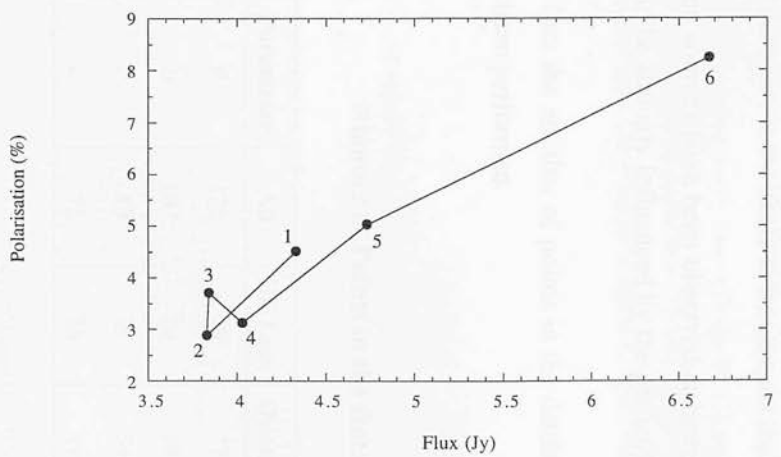

c) BL Lacertae

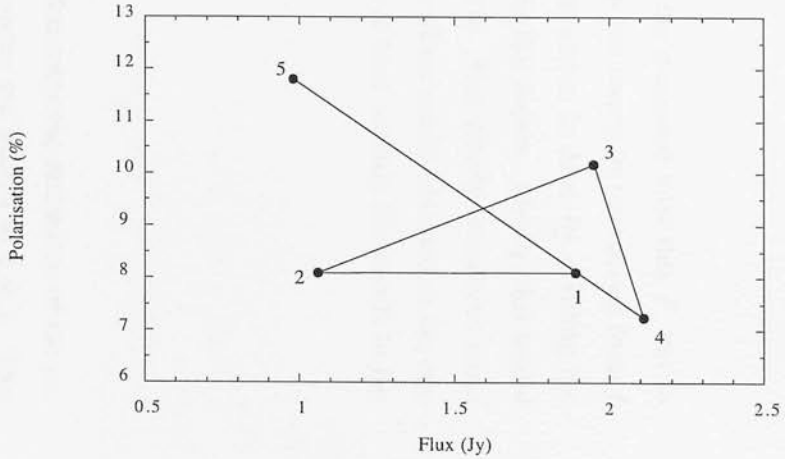

d) OJ287

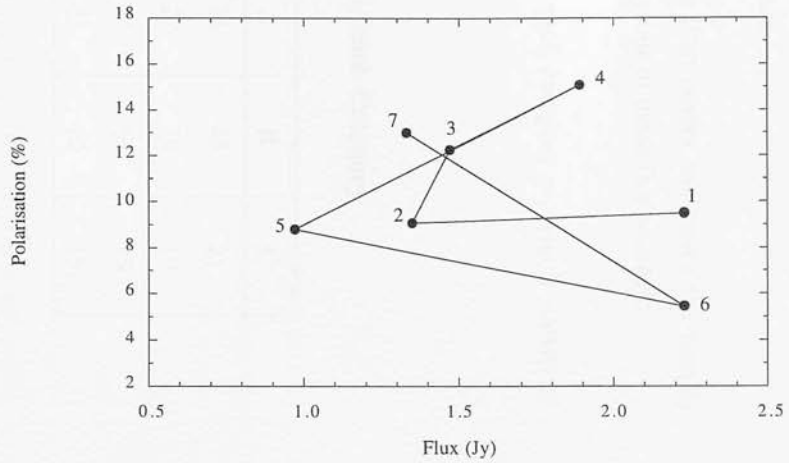

- High polarisation sources are easier to measure and the required signal to noise can be achieved faster. Sources with low polarisation have to be very bright to be detectable and therefore more likely to be Quasars than BL Lacs.
- Some sources have been observed at more epochs than others and hence the results could be strongly influenced by the particular behaviour of these few sources.

Table 5.8 lists the number of points in the database for each category on which statistical tests have been performed.

Table 5.8 Number of Points in the Database for each Category

Parameter	All	BL Lacs	Quasars	A	B	C
F	126	49	77	31	45	21
α	107	39	68	27	38	19
P	83	29	54	23	29	15
δ	75	26	49	23	29	15

5.4.2 The Quiescent State Flux

The analysis of individual sources is carried out using the measured total flux F, but to analyse a dataset containing observations from more than one source its normalised form f has to be used. The conversion from F to f for each source is done by dividing the measured F's by the lowest flux measurement obtained on that source. Ideally, this would be the quiescent state flux, but this is difficult to establish. This clearly introduces some kind of offset which is difficult to account for, but in view of the results obtained so far, one can be confident that the scheme works well enough to at least identify the trends in the behaviour of these objects.

5.4.3 VLBI Observations

The concerns regarding the VLBI observations used to determine the orientaion of the jet, and hence that of the magnetic fields in the sample sources are treated in § 4.3. This

parameter introduces a degree of uncertainty in the results obtained. However, it is unlikely that the data from a majority of sources is badly affected by the use of an incorrect jet position angle. In fact, during the course of the analysis, the jet orientation of a number of sources was changed with the effect of changing their observed properties, but their variability could still be described by one of the basic patterns identified. The results of the statistical tests and the overall shapes of the distributions were not affected as a result of this.

5.4.4 A Statistical Sample

The concerns expressed above about the biasing of the database question the statistical significance of the sample and, therefore, the validity of treating each observation as independent mesurements of 'a Blazar' (ignoring the actual source involved), which is the approach usually adopted. Using single epoch observations of each source would only be statistically significant if the sample contained a very large number of different sources (and ideally as many BL Lacs as Quasars), so that all stages of variability would be likely to have been observed. The best approach would be to work on a sample of reasonable size, with both classes of objects, and observing all sources an equal number of epochs, over a period in time long enough to allow for the occurrence of large flares in at least some sources.

Chapter 6

Variability of Blazars: Discussion

The database presented here is unique in the temporal coverage of the sub-parsec regions of a number of BL Lac Objects and Highly Polarised Quasars and its study can help to discern between physical variability scenarios. In this chapter, the results from the analysis of the database are used to place constrains on the mechanisms likely to be responsible for the observed variability in the emission, within the theoretical framework of the canonical *shock-in-jet* model. A comparison is also made between the properties of BL Lac Objects and Quasars in search of their parent populations.

6.1 Observational Constrains

The observational constrains on the models are mainly set by the sources which have been observed most frequently and whose variability can therefore be best characterised. These include the relation between the changes in polarisation level, magnetic field orientation and flux density.

6.1.1 Range of Polarisation Level

The data shows that the millimetre polarisation of Blazars tends to vary within a range of values typical of each source. The mean polarisation level that results from averaging all the available measurements helps to characterise a source. Highly polarised Blazars tend to have a mean polarisation ~ 9 % and the most lowly polarised objects < 3 %. Most sources, however, have intermediate mean polarisation values of ~ 5 %.

6.1.2 The Polarisation Level and Magnetic Field Orientation Link

In virtually all sources the polarised emission is a maximum when the dominant component of the magnetic field is perpendicular to the structural axis and a minimum when it is parallel, as shown in Figures 5.5 and 5.9[1]. There is a set of sources whose magnetic field orientation remains constant throughout the observation epochs, eventhough changes in flux density and degree of polarisation take place.

a) Sources with High Polarisation and Perpendicular Magnetic Field

They exhibit the highest levels of polarisation and their apparent position angles hardly deviate from alignment with the jet, even during large flares (labelled as Group A in the analysis). Objects that fit this description include OJ287, 3C279, 1335-127 and BL Lacertae (2 BL Lacs and 2 Quasars), all of which have been observed at a number of epochs (see Table 5.1). During the period of observations they have undergone large and frequent changes in flux density and degree of polarisation (all have maximum to minimum flux and polarisation ratios of at least factor 2) but with hardly any changes in position angle. Quasar 1921-293 exhibits similar behaviour, but the orientation of its jet is not known and whether it has a perpendicular magnetic field cannot be established.

b) Sources with Low Polarisation and Parallel Magnetic Field

3C273 and 3C345 are bright Quasars with a strong tendency to be found with their polarisation vectors perpendicular to the jet orientation, indicating a predominantly aligned magnetic field (25° to the jet orientation on average[2]) and, at least in the case of 3C273, lower polarisation levels than any other source measured. Significantly, 3C273 is by far the brightest source in the sample. Their polarisation has been measured at 8 and 7 different epochs respectively, and both sources can be seen recovering from equally massive flares, which more or less coincided with the epoch at which they were first observed (see plots in Appendix C). While the flux of 3C273 drops to a steady level within months, 3C345 takes several years to go back to its pre-flare flux level. If the same physical processes are at play, it would be fair to expect theoretical models to explain how in 3C273 a large flare can evolve and all traces of it vanish in months, while it takes years of steady decline in 3C345. In both sources an epoch of virtually no polarisation has been detected, which in the case of 3C273 it is accompanied by a swing of almost 90° in position angle but not in 3C345. The

---

1 This is also observed in VLBI polarisation measurements (e.g. Gabuzda 1994).
2 This same result is found in VLBI polarisation studies of Quasars (see Roberts *et al.* 1990).

position angle has also been measured nearly $90°$ away from its usual orientation in 3C345, but in this case it cannot be linked to any other feature in the data.

c) Sources with Swinging Magnetic Fields

Most sources in the sample have polarisation vectors that vary between the aligned and the perpendicular orientations and show middle of the range mean polarisation values (~ 5 % on average). Amongst these objects are 0235+164, 0420-014, 0735+178, 1749+096 and 3C454.3 (3 BL Lacs and 2 Quasars), observed at least at 4 epochs. There are another 4 Quasars for which there are only 2-epoch measurements and, although their variability pattern cannot be fully characterised, the fact that the dominant component of the magnetic field does change its orientation can still be established. These sources are 0528+134, 0736+017, 0923+392 and 3C446. In all cases their polarisation vectors are aligned with the jet when the polarisation is a maximum.

6.1.3 Variation of Polarisation with Flux

The variation of the degree of polarisation P with flux density F must also be explained by the theoretical models. It has been observed that this is linked to the class of object rather than the polarisation behaviour of the source. BL Lacs and Quasars tend to differ in the type of correlation between F and P, with a tendency to be positive in Quasars but negative in BL Lacs (see Table 5.1, § 5.3.2 and Appendix D). The main exceptions are 0735+178 in the BL Lacs and 3C345 in the Quasars.

6.1.4 Variation of Magnetic Field Orientation with Flux

For those sources with swinging magnetic fields the correlation between F and the orientation of the dominant magnetic field component δ can be either positive or negative, as shown in Figures 5.7. At minimum flux the dominant magnetic field component is perpendicular to the jet in BL Lacs 0235+164 and 1749+096 and perhaps some 2-epoch Quasars. On the other hand, the perpendicular component of the magnetic field is dominant at maximum flux in BL Lac Object 0735+178 and Quasars 0420-014, 3C454.3 and others observed at only 2 epochs.

6.2 The Shock-in-Jet Model

The *shock-in-jet* model for describing the evolution of flares in Blazars was introduced in § 1.3. In this section, the likely observational effects of a shock propagating at relativistic speeds along a jet lying close to the line of sight are discussed in more detail. This sets the basic scenario against which the observations can be compared and thus allow to assess the adequacy of this model. Other physical factors likely to be at play in these regions are introduced that add complexity to the model but which help to explain more of the observed variability.

6.2.1 The Basic Scenario

The most basic scenario contemplates the formation of a shocked region within the quiescent jet when the source flares. Most of the synchrotron emission is due to relativistic electrons in this region, which is polarised if there is an ordered magnetic field.

a) The Formation and Propagation of Shocks

A plane parallel shock may be created by a prolonged disturbance such as an injection of highly energetic particles from the nucleus of the Blazar into the mouth of the jet. Such a shock may comprise forward and backward fronts moving relativistically along the length of the jet[3]. The reverse shock is closer to the core than the front shock, it moves with a lower bulk Lorentz factor and it travels backward relative to the front shock but forward relative to the observer. In the quiescent state the magnetic field in the jet is likely to have a weak component aligned with the flow due to shear at the edges of the jet or at the back end of shocks. This occurs as the flow mixes with the ambient material outside the jet or behind the shock (Laing 1980 and Marscher *et al.* 1992). The forward shock sweeps undisturbed material compressing it and amplifying the magnetic field component non-aligned with the jet (now parallel to the shock front) by a factor equal to the compression ratio. This is schematically illustrated in Figure 6.1. The ability of the shock wave to change the orientation of the dominant magnetic field component depends on the strength of the shock and on the fraction of the field which is originally random. The electrons swept by the shock front become energised and constitute a region of enhanced emission enclosed between the forward and reverse shocks. Synchrotron emission from this region is Doppler beamed and can be highly polarised if there is a significantly ordered magnetic field.

---

[3] Whether the reverse shock forms or not, depends on the strength and impulse of the initial disturbance (Marscher *et al.* 1992).

Figure 6.1 Magnetic Field Cells Before and After Shock Propagates Through Jet

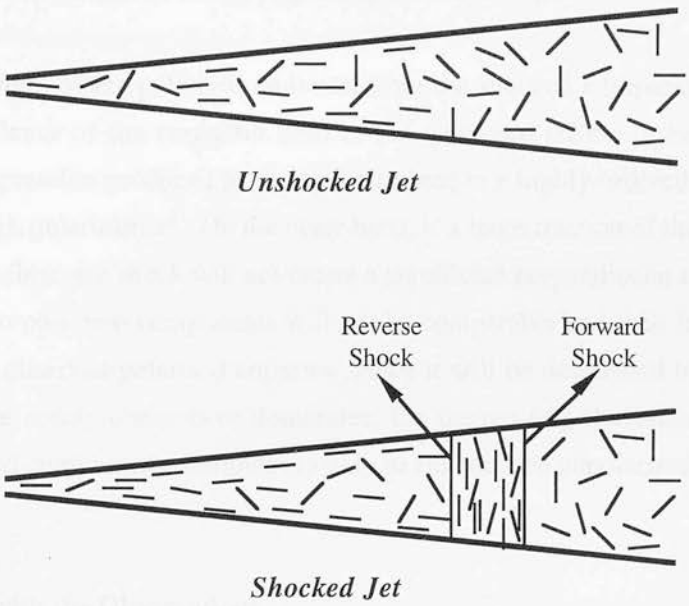

b) Expected Polarisation Variability

Within this simple model the polarisation variability may result from the interaction between two synchrotron components of similar magnitude in polarised flux but with orthogonal polarisation vectors:

- A *steady component* due to the underlying flow of material with its magnetic field preferentially aligned with the jet, because of the flow and/or shear with ambient material at the edges.
- A *shocked component* with magnetic field perpendicular to the jet, produced in a flare and propagating through the jet at relativistic speeds.

In this scenario, the emission observed is the superposition of the steady and shocked components. The polarisation variability might arise from the competition between the orthogonal polarisation vectors from these two regions. In the quiescent state the emission is due to the steady component; when a flare occurs, the degree of polarisation and the total flux density are initially anticorrelated because the flux increases (as the shocked region brightens up) and the polarisation drops (as the orthogonal polarised components become comparable). If the shocked component becomes dominant, after a transition through

virtually zero polarisation (when the polarised components cancel each other out), the polarisation and the flux should be correlated and a $90°$ swing in the position angle should be observed. Small changes in the position angle can also be caused by random walks of the Stokes parameters in the Q – U plane produced by the superposition of polarisation cells with randomly oriented magnetic fields lying along the line of sight.

However, the strength of the polarised emission from the shocked component depends on the level of turbulence of the magnetic field in the quiescent state. If the field is very turbulent, the compression produced by a shock will lead to a highly ordered perpendicular field and hence high polarisation[4]. On the other hand, if a large fraction of the original field is aligned with the flow, the shock will not create a significant perpendicular component. In either case, the two polarised components will *not* be comparable and their interaction will *not* determine the observed polarised emission, since it will be dominated by the stronger component. If the steady component dominates, the degree of polarisation will be low because the shocked component contributes mainly to enhance the unpolarised flux.

c) Comparison with the Observations

Highly polarised sources such as OJ287, 3C279, 1335-127 and BL Lacertae require a highly ordered perpendicular magnetic field, therefore the polarised flux must originate in the shocked component. For the shock to give rise to such an ordered field, the magnetic field in the quiescent state must be quite turbulent, which in turn implies that the component aligned with the jet is weak. Since most of the polarised and unpolarised emission originates in the shocked region, they should always be positively correlated (since the interaction between the polarisation vectors of the steady and the shocked component is negligible) and the position angle should not change significantly from a direction aligned with the jet. However, while these four sources do have steady position angles, the flux density and polarisation are clearly positively correlated only in the case of 3C279. In OJ287 and 1335-127 the correlation changes sign at an epoch of maximum flux, and in BL Lacertae F and P are predominantly anticorrelated. Therefore, the relationship between F and P cannot be ascribed to the interaction between orthogonal synchrotron components because the steady component is only very weakly polarised.

Sources with swinging magnetic fields have somewhat lower levels of polarisation. This means that the magnetic field in the quiescent state is not as turbulent, and hence two comparable orthogonal polarised components may form. BL Lac Object 0735+178 and Quasars 0420-014, 3C454.3 and possibly 0923+392 and 3C446, are in good agreement with

---

[4] Some models need *70 %* of the field to be randomly oriented in order to produce *~5 %* polarisation in the shocked component e.g. Gómez *et al.* 1994a.

the two-component scenario, with correlated F and P, i.e. maximum flux coincides with maximum polarisation and perpendicular magnetic field. Instead, the relationship between F and P in BL Lac Objects 0235+164 and 1749+096 is analogous to that in BL Lacertae (anticorrelated). This can be understood if the steady polarised component is stronger than the shocked component, so that the polarisation drops when the shocked region brightens up. However, this model cannot explain why the magnetic field in these sources (and 2-epoch Quasars 0528+134 and 0736+017) is perpendicular to the jet when the flux is minimum ('quiescent state') and becomes parallel during a flare. One possible explanation would be that the structural position angles of the VLBI jets of these 4 sources (as used in the analysis) are wrong by $\sim 90°$, which upon inspection of Appendix A is not an unlikely proposition, since they have largely unresolved cores in the available VLBI maps.

Finally are the Quasars with low polarisation and a predominantly parallel magnetic field, 3C273 and 3C345. The unchanging polarisation vector during the large flares observed, indicates that there is sufficient alignment of the magnetic field with the flow, to prevent a significant enhancement of the perpendicular component as a shock sweeps through the jet. The polarised emission must then be dominated by the steady parallel component. The observations of 3C345 cover the whole evolution of a flare and show a clear anticorrelation between the flux density and the polarisation (Kendall $\tau = -0.43$ at 82 % significance level). This can be understood within this simple model because as the shocked component lights up, the flux density increases whereas the polarised flux from the steady component remains at a similar level, thus producing the observed drop in the degree of polarisation. In the case of 3C273 the drop in flux density is extremely fast and is accompanied by a total loss of polarisation, which raises the question that if P is correlated with the flux increase produced in the shocked component (Kendall $\tau = 0.43$ at 86 % significance level), why is the dominant component of the magnetic field aligned with the jet?

d) Assessment of the Basic Model

The ability of the *shock-in-jet* model in describing the continuum emission from Blazars was briefly introduced in § 1.3. The following assessment of the basic model deals with its capability to account for the observed polarisation.

1) Successes

- This model explains naturally how the magnetic field can be found to be highly ordered in a direction perpendicular to the jet.
- It provides a physically feasible mechanism for swinging the polarisation vectors through the interactions between orthogonal polarised components.

- It can account for the fact that all sources tend to keep their polarisation levels within a certain range, in terms of the amount of turbulence of the magnetic field in the quiescent state, which determines the degree of ordering of the field in the shocked component:
  - High polarisation is seen if the polarised emission is due to the shocked component (indicated by a perpendicular magnetic field).
  - Middle range polarisation and swinging position angles if both components are comparable.
  - Low polarisation if the polarised emission is due to the steady component (parallel magnetic field).

2) Shortcomings

The main problems with this basic model are not to do with the origin of the various polarisation patterns observed but with their variability. This is especially true of those sources with swinging position angles.

- The interaction between the emission from two orthogonal synchrotron components should result in a large range of polarisation levels, including zero polarisation when they cancel each other out, and this is not observed in any source. However, the frequency of the observations is not sufficient to allow such detailed interaction to be seen.
- The observed correlations between the polarisation and the flux density are not associated with competing polarised components (anticorrelated in the initial stages of the flare but correlated afterwards) but have more to do with the type of object involved.
- When position angle swings are seen, they are not always associated with a change in flux (as expected in a flaring object).
- For the interaction between the two orthogonal polarised components to be possible they must be comparable (in actual Janskys). In the sources with swinging position angles the observed levels of polarisation in the quiescent and flaring states are similar. This implies that during a flare the polarised flux from the shocked component must be of the order of a factor of two greater than that from the steady component, so that their superposition results in a similar degree of polarisation as in the quiescent state, but with orthogonal position angle. This requires a very highly ordered field in the shocked component, which cannot be achieved because the field is already significantly aligned with the jet (i.e. the initial field is not turbulent enough).

6.2.2 Viewing Angle and Relativistic Effects

Intrinsic to the *shock-in-jet* model are the assumptions that the jets of Blazars lie close to the line of sight and that the shocks are relativistic. The characteristics of beamed synchrotron emission are strongly influenced by the viewing angle due to the introduction of relativistic effects. Here, the possible viewing angle configurations are presented and how this might affect the observations discussed.

a) The Viewing Angle

The viewing angle θ is the angle the jet axis makes with the observer's line of sight as shown in Figure 6.2, where ϕ is the jet opening half-angle.

Figure 6.2 Schematic of Viewing Angle θ and Jet Opening Half-angle ϕ

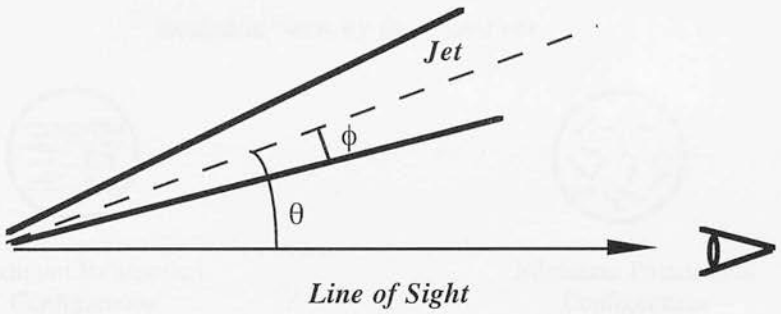

1) Relativistic Effects

- *Relativistic Aberration* is a geometrical effect governed by the Lorentz transformations between the observer's frame and that of the relativistic fluid. A shocked component moving down the jet is seen edge-on at critical viewing angle $\theta_c < sin^{-1}(1/\Gamma)$ and if its magnetic field has any degree of ordering, a maximum in the degree of polarisation is observed (Laing 1980). The magnetic field appears to be random if viewed face-on ($\theta = 0°$).

- *Time Delay Effects* arise because the jet convects divergent flow and hence different fluid lines have different viewing angles and velocities in the observer's frame. Emission from different parts of the jet will have different arrival times at the observer, with the effect of distorting and rotating the appearance of the moving feature (i.e. altering its width and depth). Rotations can cause the alignment of the shocked region with the line of sight, thus enhancing its total and polarised emission.

Figure 6.3 **a) Edge-on and Face-on Shocked Jets**

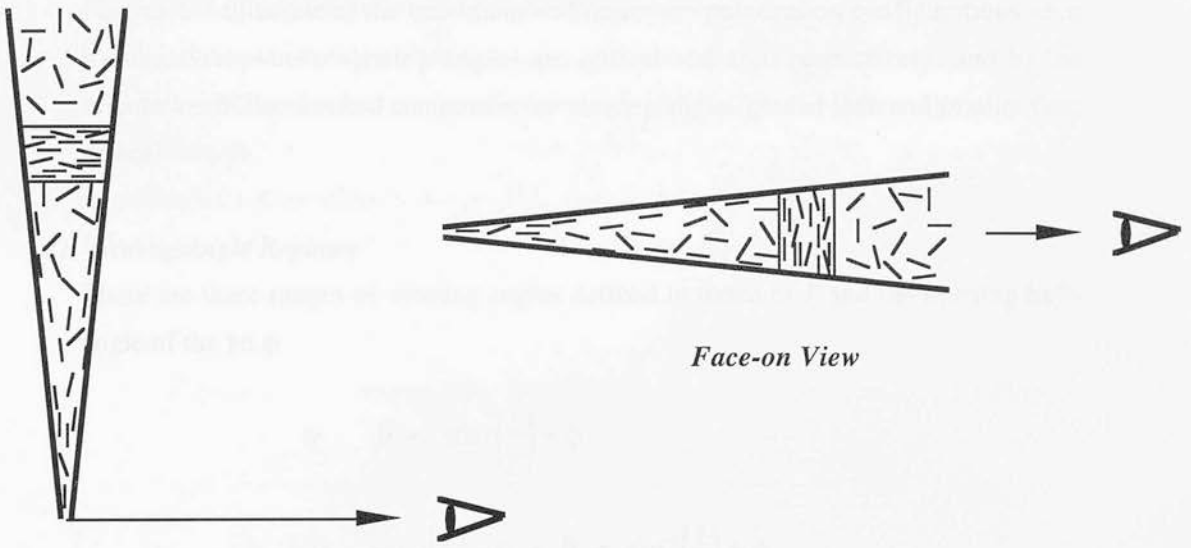

Face-on View

Edge-on View

Emission Seen by the Observer

Maximum Polarisation Configuration

Minimum Polarisation Configuration

b) Viewing Angle of Shocked Jets either side of Critical

$\theta > \theta_C$

$\theta < \theta_C$

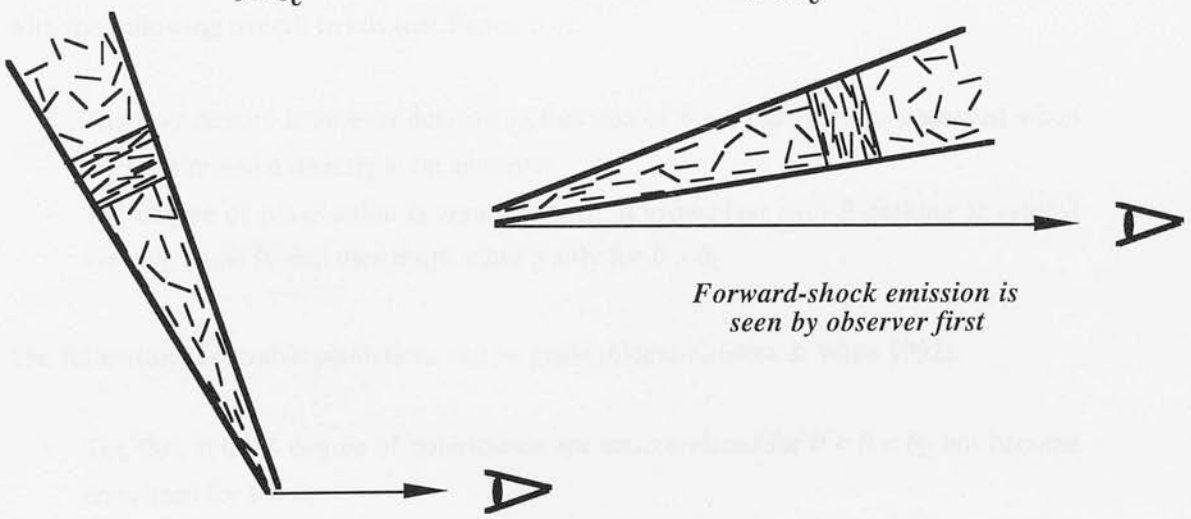

Forward-shock emission is seen by observer first

Reverse-shock emission is seen by observer first

Figures 6.3 illustrate a) the maximum and minimum polarisation configurations seen by observers whose viewing angles are critical and zero respectively, and b) the orientation of the shocked component for viewing angles greater than and smaller than critical.

2) *Viewing Angle Regimes*

There are three ranges of viewing angles defined in terms of Γ and the opening half-angle of the jet ϕ

$$i) \quad \theta < \sin^{-1}\left(\frac{1}{\Gamma}\right) - \phi$$

$$ii) \quad \sin^{-1}\left(\frac{1}{\Gamma}\right) - \phi < \theta < \sin^{-1}\left(\frac{1}{\Gamma}\right) + \phi$$

$$iii) \quad \theta > \sin^{-1}\left(\frac{1}{\Gamma}\right) + \phi$$

In case *i)* the line of sight penetrates first the forward shock and then the reverse shock. In case *ii)* most of the shock is viewed nearly sideways and maximum polarisation and superluminal motion are measured. Finally, in case *iii)* the line of sight first penetrates the reverse shock and then the forward shock (Marscher *et al.* 1992).

b) Observational Implications

The variation of flux density and degree of polarisation with viewing angle is a function of Γ with the following overall trends (see Figure 6.4):

- The flux density is an ever decreasing function of θ. A maximum is observed when the jet is oriented directly at the observer.
- The degree of polarisation is zero at $\theta = 0°$, it grows fast with θ peaking at critical viewing angle θ_C and then drops more gently for $\theta > \theta_C$.

The following observable predictions can be made (Gopal-Krishna & Wiita 1992):

- The flux and the degree of polarisation are anticorrelated for $0 < \theta < \theta_C$ but become correlated for $\theta > \theta_C$.
- For small deviations of the viewing angle around the critical value, the polarisation variability is less pronounced than that of the flux density.

- The effect on the position angle of small changes in θ are also small.
- If BL Lac Objects have smaller viewing angles than the other Blazars, there may well be a statistical preference towards them having anticorrelated flux density and degree of polarisation.
- If relativistic aberration is responsible for changing the viewing angle, a general correlation between position angle variation and flux density can be expected.

Figure 6.4 Variability with Viewing Angle and Lorentz Factor

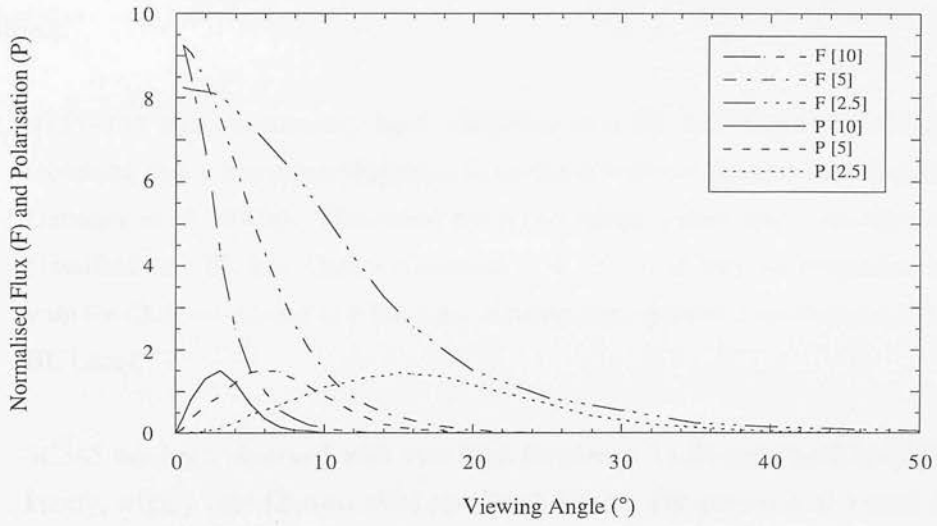

Figure 6.4 is adapted from Gopal-Krishna and Wiita (1992) and shows the variation of flux density F and polarisation P with viewing angle for three values of the Lorentz factor Γ.

c) Comparison with the Observations

This addition to the model provides a new explanation for the sense of the correlation between the flux density F and the polarisation P in terms of the viewing angle. For the three viewing angle regimes:

i) $\theta > \theta_c$

Sources where F and P are highly positively correlated include 3C273, 3C279 and 3C454.3. A positive correlation is also seen in 0420-014, 0735+178 and 3C446 (though they have not been observed at as many epochs). All of these sources are Quasars with the exception of 0735+178.

ii) $\theta < \theta_c$

A clear anticorrelation between F and P is found in 0235+164, 1749+096, BL Lacertae and 3C345, i.e. 3 BL Lac Objects and 1 Quasar.

iii) $\theta \sim \theta_c$

In BL Lac Object OJ287 positive and negative correlation is clearly observed. This may also be the case in Quasars 1335-127 and 1921-293.

If the sense of this correlation is determined by the viewing angle being greater than (+) or less than (–) critical, then an immediate result is that the prediction that BL Lacs would tend to show an anticorrelation is confirmed. The two major sources in disagreement can be qualified:

- 0735+178 has traditionally been classified as a BL Lac Object but evidence is mounting that it has many properties in common with the Quasars (see Chapter 5 and Gabuzda *et al.* 1994a). This could mean two things: either that it has been wrongly classified as a BL Lac Object (Carswell *et al.* 1974) or that the properties it shares with the Quasars are due to it having a viewing angle greater than critical (unlike most BL Lacs).

- 3C345 has been observed with very high frequency VLBI and found to have a very knotty, wiggly core (Zensus 1992 and Bääth 1992). The presence of a bend directed towards the observer could make the viewing angle of the sub-parsec jet more closely aligned with our line of sight (Wardle *et al.* 1994 estimate that the jet lies at 2° from the line of sight). This could explain the variation observed in flux density as the evolution of a flared component passing through a bend.

Sources where the correlation changes sign could be having viewing angles close to critical, so that small changes in the viewing angle can make them cross back and forth between $\theta > \theta_c$ to $\theta < \theta_c$. In particular, OJ287 and 1335-127 have a maximum in flux and a minimum in degree of polarisation at the epoch when the F–P correlation changes sign (e.g. see Figure 5.11 d) for OJ287). A further prediction of this scenario is that the flux density should change significantly, while the polarisation remains similar or changes little for viewing angles that 'hover' around θ_c. This can be checked by looking at Figures 5.1 which show the details of the variability in OJ287. What is found is that the position angle remains exactly the same while the degree of polarisation drops from *8.8 %* to *5.5 %* (with errors of *±1.5 %*) and the flux increases by more than a factor 2 from *< 1 Jy* to *> 2.2 Jy*, in relatively good agreement with the predictions.

Finally, changes in the viewing angle due to relativistic aberration will also change the position angle measured. Since relativistic aberration and Doppler beaming are both a function of the Lorentz factor Γ, the variations in position angle and flux density are expected to be correlated. A large swing in position angle can be due to a significant change in the viewing angle, but in those sources where the polarised emission comes from two distinct areas of the jet with orthogonal magnetic fields (e.g. steady flow and shocked plasma), relativistic aberration can emphasise the emission from one region over the other. This would cause the emission from either synchrotron component to be more Doppler beamed towards the observer at different times, thus explaining the $90°$ swings in position angle. In this scenario, the interaction or superposition of the emission from orthogonal components is no longer required.

6.2.3 Wiggly Jets

Bends are commonly seen in the VLBI images of parsec and kiloparsec-scale jets and have already been reported in the sub-parsec regions of some bright sources (Zensus 1992 and Bääth 1992). They may be produced by the ambient material surrounding the jet or by macroscopic instabilities in the flow (Hardee 1990). A stationary region of enhanced emission is seen if the bend is directed towards the observer, since it increases the thickness of the jet along the line of sight, but flares decay rapidly if the bend is directed away from the observer. A new scenario has been proposed to account for the rapid and chaotic variability of Blazars in terms of the emission from a single shocked synchrotron component, varying due to the presence of small bends or wiggles in the jet. Such wiggles would induce variations in the viewing angle (and hence change the characteristics of the emission) by changing the trajectory followed by the shocked component as it moves down the jet (Gopal-Krishna & Wiita 1992).

Wiggly jets may also be associated with helical magnetic fields. These may arise if, for example, the central engine is a rotating black hole and the magnetic field is attached to it. Helical fields can make the jet orientation change by $90°$ between the parsec and kiloparsec scale (Conway & Murphy 1993).

6.3 BL Lac Objects and Quasars

For years there has been a debate on the parent population of BL Lac Objects and Highly Polarised Quasars. While unifying theories assume that any observable differences between these two classes of objects are no more than an artefact of the observations themselves, like for example a viewing angle effect, there is evidence to suggest that they may indeed be different classes of objects, such as provided by VLBI polarisation measurements in the jets (see § 1.4). The analysis of the JCMT database may contribute to throw some light on this debate, by establishing whether there are significant differences between them that could be ascribed to their having different parent populations or if on the contrary, their submillimetre properties can be understood within the framework of the unifying theories.

6.3.1 Multi-frequency Polarisation Observations

Polarisation observations represent the best way of establishing whether BL Lacs and Quasars originate from a single population of objects, by probing into the properties of the magnetic field. The study of the magnetic field configuration gives information about the morphology of the emitting regions, it can expose the presence and interaction of physical processes such as shocks, shear, turbulence, ..., and it can help characterise the emission and transport mechanisms. In the sub/millimetre, the polarisation properties of BL Lacs and Quasars are mostly indistinguishable (see § 5.3). The following is a summary of the main results obtained from the analysis of the 1100 μm database (*in italics*), compared with the polarisation properties and the magnetic field configuration inferred at different frequencies for BL Lacs and Quasars[5].

- *High levels of polarisation tend to be associated with a magnetic field perpendicular to the jet.*
  This is also clearly seen in VLBI observations of the cores of BL Lacs (Gabuzda *et al.* 1994b). Optical polarisation studies also show alignment between the position angle of highly polarised sources and the jet (Impey *et al.* 1991).

- *All sources tend to maintain their polarisation level within a certain range.*
  This does not seem to be true at optical wavelengths, where the variation in degree of polarisation can be extreme (e.g. see tables in Rusk 1990). More observation epochs are needed to establish whether this is also true of VLBI observations.

---

[5] The optical and radio polarisation properties of Blazars are reviewed in § 1.4.

- *Most low polarisation observations correspond to Quasars.*
  This is also true of VLBI polarisation measurements (Roberts *et al.* 1990). The reason for this could be that a large signal is required to detect low polarisation and low polarisation BL Lacs may not be bright enough for current receivers.

- *The magnetic field in some sources keeps a preferred orientation while in others it can swing between orthogonal directions.*
  Position angle swings of up to $90°$ have often been reported at the other wavelengths (e.g. Aller *et al.* 1994), but not the fact that some sources tend to keep their magnetic field orientation largely unchanged.

- *The cores of BL Lacs and Quasars have a bimodal distribution of preferred magnetic field orientation.*
  This is also observed in VLBI measurements of BL Lacs (see Figure 1.9 a)) but it is not so clear in the Quasars. The distributions peak at the perpendicular and aligned configurations, although more Quasars than BL Lacs are found with magnetic fields parallel to the jet (Figure 5.10 d)). This may also be attributed to the fact that low polarisation BL Lacs have not been readily detected yet. However, in the optical this distribution is clearly one-sided towards the perpendicular magnetic field configuration (Figure 1.10), although Impey (1987) suggests that there is a smaller peak at $90°$.

Another two important results obtained by combining 1100 μm polarisation and photometric data are:

- *Quasars are generally brighter and have steeper sub/millimetre spectral indices than BL Lac Objects.*

- *The flux density and percentage polarisation tend to be correlated in the emission from Quasars but anticorrelated in BL Lacs.*

The polarisation properties of Blazars at optically thin frequencies (optical to submillimetre) are generally in good agreement. This is true of the variability observed, the distribution of preferred magnetic field orientation and the association between high polarisation and perpendicular fields. The radio polarisation from the jets, however, seems to agree broadly in the case of BL Lacs but not so in Quasars. The main difference is that the magnetic field in the jets of Quasars are predominantly parallel to the structural axis.

6.3.2 The Parent Population

The similarities in the polarisation properties of both classes of object indicate that the same physical phenomena are responsible for the polarised emission and its variability, which are well approximated by the description provided by the *shock-in-jet* model. However, BL Lac Objects and Quasars have traditionally been associated with different types of galaxies. There are therefore two competing scenarios: one that tries to prove that the differences between the two classes are due to them having different parent populations, and a second scenario that proposes a unique population of objects and seeks to explain their observed differences in terms of observational effects.

a) FR I and FR II Galaxies

The tendency in the literature has been to associate BL Lac Objects and Highly Polarised Quasars with different morphological types of extended radio sources, and in particular FR I and FR II galaxies respectively (Fanaroff & Riley 1974 and e.g. Wardle *et al.* 1984, Impey *et al.* 1991). FR I galaxies have lower power and are brightest close to their nuclei, whereas the more powerful FR II sources are brightest at their extremities. They also seem to differ in the type of galactic environment they are imbedded in, the FR IIs requiring a less luminous host galaxy (Laing 1993), and have different magnetic field structures (Bridle & Perley 1984). In a recent paper, Falcke *et al.* (1995) suggest that the difference between FR I and FR II galaxies may be due to morphological characteristics of the tori surrounding the central engine, rather than the engine itself.

In this scenario, both BL Lacs and Quasars would be lying with their jets closely aligned to our line of sight giving rise to the 'Blazar phenomenon', which enhances the similarities of their emission while making their differences harder to observe. *A Blazar* would then be a manifestation of some physical process rather than a type of object.

Most of the evidence in favour of this scenario is provided by multi-frequency photometric measurements and radio polarisation observations:

- BL Lacs usually have lower emission-line luminosities, extended radio power and redshift than Quasars, and their properties lie in the ranges typical of FR I and FR II galaxies respectively. However, Kollgaard *et al.* (1992) report observations of BL Lacs with FR II characteristics.

- The spectral index of HPQs has been measured to be steeper than that of BL Lacs at *x*–ray and optical frequencies (Impey *et al.* 1991 and references therein) and in the sub/millimetre (Gear *et al.* 1994 and § 5.3).

- Generally, lower superluminal speeds are inferred in BL Lacs (Gabuzda *et al.* 1994b).

- The radio polarisation level from the unresolved cores is lower in Quasars than BL Lacs (Roberts *et al.* 1990 and § 5.3).

- In the outer jets, Quasars tend to have magnetic fields aligned with the structural axis while in BL Lacs it is perpendicular (Cawthorne *et al.* 1993b).

There are no significant differences between the two types of object in the polarisation measurements at 1100 μm, which show that Quasars can be as highly polarised as BL Lacs. However, the presence of an external emission-line region in the Quasars (absent in the BL Lacs) would contain ionised gas that could introduce Faraday depolarisation near the core, thus reducing the more optically thick radio polarisation. Low polarisation is much harder to measure with significant signal to noise and this might explain the scarcity of VLBI measurements of the cores of Quasars (see Figure 1.2 a)). Shear between the jet flow and the ambient gas can align the magnetic field with the jet axis in Quasars, leading to a higher ordering of the field and therefore a higher degree of polarisation further from the core, as the VLBI observations seem to indicate (Cawthorne *et al.* 1993b).

The 1100 μm photometric data indicates that Quasars are generally brighter than BL Lacs. The excess of low polarisation Quasar observations can be understood in terms of their intrinsic higher brightness enabling the detection. Also, given the correlation between the level of polarisation and magnetic field orientation (see Table 5.6), this would explain the greater number of observations with aligned magnetic fields in Quasars.

Quasars also seem to have steeper spectral indices than BL Lacs. Gear *et al.* (1994) have investigated the observed difference in radio–submillimetre spectral indices betwen the two classes and discussed the implications on the parent populations. They concluded that this difference can be attibuted to the characteristics of the magnetic field in the underlying jets of BL Lacs and Quasars, which will be different if their parent populations are indeed FR I and FR II galaxies respectively. However, the present 1100 μm polarisation database does not indicate any significant differences between the two classes in terms of magnetic field structure near the cores (see Figure 5.10 d)). Therefore selection effects cannot be ruled out as a likely reason for the discrepancy in spectral index.

b) The Unifying Theories

In the Blazar context, a unifying theory proposes a single parent population for both BL Lac Objects and Highly Polarised Quasars, on the grounds that their similarities far outweigh their differences. In contrast with the above scenario, instead of looking for specific observational evidence that separates the two classes, unifying theories propose physical mechanisms that can give rise to these observational differences under probable observing conditions. For example, Gopal-Krishna & Wiita (1993) believe that the lower superluminal speeds of BL Lacs, the weakness of their emission lines in the optical and the different magnetic field configuration in the jets of BL Lacs and Quasars (as inferred from VLBI observations), could all be caused by relativistic aberration effects due to the jets of BL Lacs lying closer to the line of sight than those of Quasars. In a previous paper by the same authors (see § 6.2.2), they make observable predictions regarding the variability of the total and polarised emission from Blazars within the framework of the *shock-in-jet* model, which are closely matched by the results from the analysis of the JCMT database. In particular, these show that there is a trend for BL Lacs to have anticorrelated polarisation and flux density, while these parameters are usually correlated in Quasars. If the interpretation of this observation in terms of BL Lacs having viewing angles closer to the line of sight than Quasars (discussed in § 6.2.2[6]) is correct, it would provide strong support for the unifying theories. However, the possibility of the two types of objects being viewed within different ranges of the viewing angle is contested by modelling results of Hughes *et al.* (1989b) and Ghisellini *et al.* (1993). At present, the number of observations of BL Lac Objects is too scarce to establish unambiguously that the flux and polarisation are usually anticorrelated in these sources. Further measurements, especially of those sources already observed at a number of epochs, would confirm or refute this possibility.

6 The jets of BL Lacs would be lying within the critical viewing angle with respect to the line of sight, while for the Quasars the viewing angle would be greater than critical.

Chapter 7

Summary and Future Prospects

In this chapter, the main contributions to performing and understanding of polarisation measurements with the JCMT presented in this thesis and the results of the monitoring campaign of Blazars are summarised. The future prospects of submillimetre polarimetry and its application to the study of Blazars are reviewed.

7.1 Summary

7.1.1 Submillimetre Polarimetry with the JCMT

The methodology for carrying out polarisation measurements with the JCMT has been investigated in three main areas: observation modes, data acquisition schemes and data reduction techniques.

a) Observation Modes

The Step and Integrate (SI) mode of observation has been proven and implemented at the telescope, but it is not necessarily the most efficient, since it requires a number of photometric measurements to obtain an estimate of the polarisation. The Continuous Spinning (CS) mode is easy to implement in hardware but it complicates greatly the recovery of the signal due to the modulation of the background. Its advantages are the speed with which a full polarisation measurement can be carried out (thus avoiding the chance of being affected by large sky fluctuations) and its overall efficiency, since the integration is only stopped while the telescope is nodding.

The work presented in Chapter 3 shows that the software approach adopted for the recovery of a strong but lowly polarised signal acquired in CS mode, is capable of achieving similar signal to noise detections as the SI mode but in a fraction of the time. Preliminary tests done on the telescope indicate that the CS mode of observation could be implemented in the future, although its capability for detecting a weakly polarised signal in a strong noisy background still has to be unambiguously demonstrated.

b) Data Acquisition Schemes

The original data acquisition scheme implemented at the telescope (Murray 1991) has been extended from 10 to 16 waveplate positions in the SI mode. This allows the $cos(4\theta)$ symmetry of the waveplate-modulated polarised signal to be exploited, so that different data reduction algorithms can be implemented. The Stokes parameters can now be estimated from either 4, 8 or 16 waveplate positions and the observations can be de-spiked. Photometric measurements with the polarimeter in place are now performed at two positions of the waveplate $45°$ apart and averaged.

c) Data Reduction Algorithms

A new suite of software routines have been written to reduce the polarimetry data acquired with the JCMT. The main innovations include:

- Estimation of the Stokes parameters by least squares fitting of a number of waveplate positions with or without de-spiking of the data, or by direct subtraction of (Q, U) photometric measurements obtained $45°$ apart.
- Estimation of the independent uncertainties in the Stokes parameters from the fit.
- Integrated plotting facility to display the raw data and fit.
- Statistical analysis of all observations of the same source in terms of the distributions of the three Stokes parameters (Kolmogorov - Smirnov test).
- Standard and/or error weighted average of all available estimates of the normalised Stokes parameters.
- Elevation tracking information, fitted and averaged Stokes parameters and polarisation estimates are all written to log files.

During the development of this software package problems with the original data reduction programme available to the common user were identified and correct algorithms for IP subtraction implemented.

7.1.2 Submillimetre Polarimetry of Blazars

The first systematic monitoring campaign of the sub/millimetre polarisation of Blazars is described in this thesis. It is found that there are no significant differences between the 800 μm and 1100 μm polarisation properties of these sources, and that they can all be described by one of three characteristic variability patterns. This allows one to constrain theoretical models so that only the overall patterns observed need to be explained, rather than the peculiarities exhibited by each source. The photometric and polarimetric properties of BL Lacs and Quasars have also been compared.

a) Polarisation Properties of Blazars

The graphical and statistical analysis performed on the database shows that there is a link between the orientation of the magnetic field and the level of polarisation near the cores of Blazars. In many sources the magnetic field remains virtually unchanged even during periods of great activity, being either perpendicular to or aligned with the structural axis. In other sources however, the orientation of the magnetic field changes readily between the two configurations. It is found that the polarisation level is highest in those objects with perpendicular fields, with a mean percentage polarisation > 9 %; if the field is parallel to the jet, the sources tend to be lowly polarised, < 3 % on average. Sources with swinging magnetic fields tend to have a mean polarisation of ~ 5 %. Changes in the degree of polarisation can also be linked to changes in the total intensity, however the relationship between these two parameters is not the same in all sources. In some objects the polarisation and flux density are clearly positively correlated, while they are mainly or partially anticorrelated in others.

b) The Shock-in-Jet Model

Most of the properties of the emission of Blazars derived from these observations can be understood within the *shock-in-jet* model. This model provides a natural explanation for the creation and propagation of shocks and the origin of polarised synchrotron emission. In the first instance, the observed variability was investigated in terms of the interaction between orthogonal synchrotron components: one always present in the underlying jet with a weakly aligned magnetic field, and a second shocked component responsible for the stronger flared emission, having an associated magnetic field perpendicular to the jet. Although this basic scenario can explain most of the observed behaviour it does not provide a full explanation for all the properties observed, like for example:

- In most sources, 90° swings in position angle during powerful flares accompanied by near *0 %* polarisation measurements when the position angle reverses are not seen, as would be expected if there was a cancellation of the polarised fluxes from the two components.
- The origin of the rapid and chaotic variability features of the emission.
- The relation between the changes in the polarisation and the flux density.

Adding further complexity to the model by considering the relativistic effects introduced by the small viewing angle between the jet and our line of sight allows most of these features to be explained, still within the framework of the *shock-in-jet* model. Relativistic aberration between the observer's and the fluid frames of reference can greatly enhance the observational effects of small changes in the viewing angle, perhaps induced by small deviations in the trajectory of the shock as it moves down the jet. In this scenario, the expected variation of the total intensity and the polarisation is closely matched by the observations. Other features such as the relation between changes in flux density and position angle have also been observed.

c) BL Lacs and Quasars

The photometric and the polarisation properties of these two classes of objects observed at 1100 μm have been compared. It is found that Quasars are generally brighter and the number of accessible sources largely exceeds that of BL Lac Objects. Their submillimetre spectral index is also somewhat steeper. These two factors may indicate fundamental differences between the two classes, perhaps associated with an external line-emitting region surrounding the cores of Quasars and/or different magnetic field structures. This would seem to agree with the view that BL Lacs and flat spectrum radio Quasars have different parent populations, the most likely candidates being FRI and FRII galaxies respectively.

However, in terms of their submillimetre polarisation they seem indistinguishable, both in polarisation level and variability of the position angle. Very low polarisation is never detected in BL Lacs; the most likely reason for this is their intrinsic lower brightness. No differences are found between the preferred orientation of the magnetic field in the two classes, contrary to reported VLBI observations obtained further out in the jets. Finally, there is a trend for the flux density and percentage polarisation to be correlated in the emission from Quasars but perhaps anticorrelated in the case of the BL Lacs. This result comes from the examination of each source individually and, if confirmed, could imply that the BL Lac – Quasar dichotomy is only a viewing angle effect, which would be an important boost for the unifying theories of extragalactic radio sources.

7.2 Future Prospects

The field of submillimetre polarimetry is relatively new (only 10 years have past since the first real detection) and there is great scope for improvement on the instrumental side and new science to be done. In relation to the JCMT, the advent of SCUBA[1] and its polarimeter will provide unprecedented sensitivity. This will allow measurements to be made much faster than it is possible today, thus facilitating the task of monitoring variable sources such as Blazars.

7.2.1 Instrumental

Up to now, single and dual channel polarimeters have been the norm, but most of the new receiver systems being developed for sub/millimetre telescopes will use array detectors which can be exploited in polarimetry. These instruments require new observing modes, sophisticated optical components such as achromatic waveplates (Murray *et al.* 1995) and complicated data reduction schemes.

a) Array Polarimeters: SCUBA

The group at the University of Chicago have pioneered the development of array polarimeters in the submillimetre. They have successfully operated a pair of 32 bolometer arrays in a dual channel polarimeter working at 100 μm (Platt *et al.* 1991) and a 7 bolometer array polarimeter is currently being used at the CSO[2] working at a wavelength of 450 μm (Schleuning *et al.* 1995). SCUBA is soon to be commissioned at the JCMT and it is designed to operate in mapping mode at two submillimetre frequencies (450 and 850 μm) simultaneously, with 91 and 37 channel arrays respectively, and is fitted with single photometric pixels at a number of other wavelengths. Like its predecessor UKT14, SCUBA will be provided with an add-on polarimeter. With the sensitivity enhancement expected to be achieved per pixel (at least a factor 10 greater than the current single channel continuum receiver), there will be a manifold increase in the number of polarised sources that will be detectable and a very significant reduction in the integration time required to perform a measurement.

---

1 Submillimetre Common-User Bolometer Array (Gear & Cunningham 1990).
2 The Caltech Submillimetre Observatory at Mauna Kea, Hawaii.

b) Continuous Spinning Mode

The SI mode has been universally used in rotating half-waveplate polarimeters but the CS mode is being considered for some of the new systems (Schleuning 1995 – private communication) and may yet prove to be a feasible alternative at the JCMT. In the development of the CS mode the next step is to successfully measure a lowly polarised signal immersed in a larger amplitude background. A new digital data acquisition system is now available that can be used to obtain data in a systematic way, by using the passage of the waveplate datum to trigger the acquisition of a number of samples. This will simplify the analysis of the data significantly and make it more flexible than it has been in the past, since samples are acquired at the same waveplate positions in each revolution. It also enables some data reduction algorithms to be performed in real time which will reduce immensely the size of the raw data files. This new system will be tried in the laboratory at QMW and if successful, it should be considered for test trials at the telescope, either with the current system or during the commissioning of the SCUBA polarimeter.

7.2.2 Observational

The available Blazar databases are growing all the time, with measurements taken at wavelengths from γ-rays to radio, including the newest astronomical windows in the submillimetre and VLBI techniques. In the near future submillimetre VLBI polarimetry could be a reality and might be capable of probing further into the cores of Blazars.

a) The Need for a Monitoring Programme

The variable nature of Blazars require that their emission is sampled frequently. The *resolution* of the variability observed depends on the periodicity of the observations and, given that rapid chaotic variability is a feature of all Blazars, a concerted monitoring programme is the only way forward. The work presented in this thesis shows that the overall properties of the polarised emission of individual Blazars are not entirely chaotic; instead the variability exhibited by most sources can begin to be characterised after being observed at a number of epochs, especially if flares have occurred. Monitoring a source can show whether it tends to be always highly polarised or not, giving an indication as to the characteristic degree of ordering of the magnetic field, or its entanglement due to turbulence in the jet. It can also show if there is a preferred orientation of the dominant component of the magnetic field with respect to the structural jet, or whether it changes between the parallel and perpendicular configurations. If it does, one can establish if these position angle swings are related to flux increases and in what way. Also the correlation (or otherwise) between the flux density and the polarisation may give important information

about the alignment of the jets with our line of sight. This knowledge helps to constrain the theoretical models and cannot be obtained from single or few-epoch observations. In fact, in order to understand the Blazar phenomenon, frequent monitoring of a few selected sources may yield more useful information than infrequent observations on many sources. However, in order to study the relation between BL Lac Objects and Quasars, a statistically significant sample of both types of object is required.

b) Simultaneous Multi-frequency Observations

The optical and centimetre observations discussed in § 1.4 and the millimetre observations presented in Chapter 5 show that the behaviour observed at different frequencies can be different, although the emission is almost certainly coming from the same region. The benefits of carrying out these observations simultaneously are enormous, since they can yield information not only about the physical processes involved, but also about the way the radiation interacts with the surrounding medium (a frequency dependent effect), because this mainly affects the emission at the optically thick frequencies. Multi-frequency monitoring will lead to finally understanding whether the differences observed between BL Lacs and Quasars are intrinsic to the nature of these objects or arise due to observational effects.

7.2.3 Theoretical

Theoretical modelling of Blazars and extragalactic sources in general can only advance at the pace of the observations needed to have their predictions either confirmed or refuted. All models need to be able to account for the polarised emission and its characteristics. This is perhaps why the *shock-in-jet* models have been the most successful. The number of 'free parameters' introduced in most models keeps increasing as they become more complicated, by including morphological defects such as bends or helical magnetic fields (Conway & Murphy 1993), relativistic aberration and time delay effects (Gómez *et al.* 1994b). This implies that more assumptions need to be made (when solving the relevant equations) about the strength of the magnetic field, its likely orientation before and after a flare, the degree of turbulence in the flow, the Doppler factor, the opening angle of the jet, the viewing angle, etc. Clearly, assigning values to all these variables must be done with care and with a knowledge of what is likely to be true in these sources, and this can only come about as a result of extensive observations. New observations will set better ranges for the values these parameters can have, thus setting constraints which will allow one to discriminate between the various models.

Bibliography

Aller, M. F., Aller, H. D. & Hughes, P.A.: 1992, *Astrophys. J.* **399**, 16

Aller, H. D., Hughes, P.A. & Aller, M. F.: 1994, *Compact Extragalactic Radio Sources*, Zensus, J. A. & Kellerman, K. I., eds, National Radio Astronomy Observatory, Greenbank, 223

Angel, J. R. P. & Stockman, H. S.: 1980, *Ann. Rev. Astron. Astrophys.* **8**, 321

Bääth, L. B.: 1992, *Variability of Blazars*, Valtaoja, E. & Valtonen, M., eds, Cambridge University Press, 196

Ballard, K. R., Mead, A. R. G., Brand, P. W. J. L. & Hough, J. H.: 1990, *Mon. Not. Roy. Astron. Soc.* **243**, 640

Begelman, M. C., Blandford, R. D. & Rees, M. J.: 1984, *Rev. Mod. Phys.* **56**, 255

Björnsson, C. -I.: 1992, *Variability of Blazars*, Valtaoja, E. & Valtonen, M., eds, Cambridge University Press, 264

Blandford, R. D. & Königl, A.: 1979, *Astrophys. J.* **232**, 34

Blandford, R. D. & Rees, M. J.: 1978, *Pittsburgh Conference on BL Lac Objects*, Wolfe, M. A., edt., University of Pittsburgh, p.238

Bowers, R. L. & Deeming, T.: 1984, *Astrophysics II: Interstellar Matter and Galaxies*, Jones & Bartlett Publishers

Bridle, A. H.: 1984, *Astron. J.* **305**, 109

Bridle, A. H. & Perley, R. A.: 1984, *Ann. Rev. Astron. Astrophys.* **22**, 319

Brindle, C., Hough, J. H., Bailley, J. A., Axon, D. J. *et al.* : 1985, *Mon. Not. Roy. Astron. Soc.* **214**, 619

Burbridge, G. & Hewitt, A.: 1992, *Variability of Blazars*, Valtaoja, E. & Valtonen, M., eds, Cambridge University Press, 4

Carswell, R. F., Strittmatter, P. A., Williams, R. E., Kinman, T. D. & Serkowski, K.: 1974, *Astrophys. J. Letters* **190**, L101

Cawthorne, T. V., Wardle, J. F. C., Roberts, D. H., Gabuzda, D. C. & Brown, L. F.: 1993a, *Astrophys. J.* **416**, 496

Cawthorne, T. V., Wardle, J. F. C., Roberts, D. H. & Gabuzda, D. C.: 1993b, *Astrophys. J.* **416**, 519

Clarke, D. & Stewart, B. G.: 1986, *Vistas in Astronomy* **29**, 27

Clemens, D. P., Leach, R. W., Barvainis, R. & Kane, B. D.: 1990, Pub. Astron. Soc. Pac. **102**, 1064

Conway, J. E. & Murphy, D. W.: 1993, *Astrophys. J.* **411**, 89

Cudlip, W., Furniss, I., King, K. J. & Jennings, R. E.: 1982, *Mon. Not. Roy. Astron. Soc.* **200**, 1169

Duncan, D. W., Robson, E. I., Ade, P. A. R., Griffin, M. J. & Sandell, G.: 1990, *Mon. Not. Roy. Astron. Soc.* **243**, 126

Falcke, H., Gopal-Krishna & Biermann, P.: 1995, *Astron. Astrophys.* **298**, 395

Fanaroff, B. & Riley, J. M.: 1974, *Mon. Not. Roy. Astron. Soc.* **167**, 31P

Gabuzda, D. C., Cawthorne, T. V., Roberts, D. H. & Wardle, J. F. C.: 1992, *Astrophys. J.* **388**, 40

Gabuzda, D. C., Wardle, J. F. C., Roberts, D. H., Aller, M. F. & Aller, H. D.: 1994a, *Astrophys. J.* **435**, 128

Gabuzda, D. C., Mullan, C. M., Cawthorne, T. V., Wardle, J. F. C. & Roberts, D. H.: 1994b, *Astrophys. J.* **435**, 140

Gabuzda, D. C. & Sitko, M. L.: 1994, *Astron. J.* **107**, 884

Gabuzda, D. C.: 1994, *Compact Extragalactic Radio Sources*, Zensus, J. A. & Kellerman, K. I., eds, National Radio Astronomy Observatory, Greenbank, 211

Gear, W. K.: 1988, *Millimetre and Submillimetre Astronomy,* Wolstencroft, R. & Burton, W., eds, Kluwer Academic Publishers, 307

Gear, W. K. & Cunningham, C. R.: 1990, ESA SP-314, 353

Gear, W. K.: 1991, *Nature* **349**, 676

Gear, W. K., Stevens, J. A., Hughes, H. D., Litchfield, S. J., Robson, E. I., Teräsanta, H., Valtaoja, E., Steppe, H., Aller, M. F., Aller, H. D.: 1994, *Mon. Not. Roy. Astron. Soc.* **267**, 167

Ghisellini, G., Padovani, P., Celotti, A. & Maraschi, L.: 1993, *Astrophys. J.* **407**, 65

Gómez, J. L., Alberdi, A. & Marcaide, J. M.: 1994a, *Astron. Astrophys.* **284**, 51

Gómez, J. L., Alberdi, A., Marcaide, J. M., Marscher, A. P. & Travis, J. P.: 1994b, *Astron. Astrophys.* **292**, 33

Gopal-Krishna & Wiita, P.: 1992, *Astron. Astrophys.* **259**, 109

Gopal-Krishna & Wiita, P.: 1993, *Nature* **363**, 142

Hardee, P. E. : 1990, *Parsec-Scale Radio Jets,* Zensus *et al.*, eds, Cambridge University Press, 267

Hecht, E.: 1987, *Optics* (2nd Edition), Addison Wesley

Hildebrand, R. H., Dragovan, M. & Novak, G.: 1984, *Astrophys. J.* **284**, L51

Holmes, P. A., Brand, P. W. J. L., Impey, C. D., Williams, P. M. *et al.*: 1984, *Mon. Not. Roy. Astron. Soc.* **210**, 497

Hughes, P. A., Aller, H. D. & Aller, M. F.: 1985, *Astrophys. J.* **298**, 301

Hughes, P. A., Aller, H. D. & Aller, M. F.: 1989a, *Astrophys. J.* **341**, 54

Hughes, P. A., Aller, H. D. & Aller, M. F.: 1989b, *Astrophys. J.* **341**, 68

Impey, C. D.: 1987, *Superluminal Radio Sources*, Zensus, A. & Pearson, T., eds, Cambridge University Press, 233

Impey, C. D., Lawrence, C. R. & Tapia, S.: 1991, *Astrophys. J.* **375**, 46

Kollgard, R. I., Roberts, D. H., Wardle, J. F. C. & Gabuzda, D. C.: 1992, *Astron. J.* **104**, 687

Königl, A.: 1987, *Extragalactic Magnetic Fields*, Asseo, E. & Sol, H., eds, North-Holland, Amsterdam, 271

Krichbaum, T. P. & Witzel, A.: 1992, *Variability of Blazars*, Valtaoja, E. & Valtonen, M., eds, Cambridge University Press, 205

Krichbaum, T. P., Witzel, A., Graham, D. A., Standke, K. J., Schwartz, R., Lochner, O., Schalinski, C. J., Greve, A., Steppe, H., Brunswig, W., Butin., G., Hein, H., Navarro, S., Peñalver, J., Grewing, M., Booth, R. S., Colomer, F. & Rönnäng, B. O.: 1993, *Astron. Astrophys.* **275**, 375

Laing, R. A.: 1980, *Mon. Not. Roy. Astron. Soc.* **193**, 439

Laing, R. A.: 1993, *Astrophysical Jets*, Burgarella, Livio, O"Dea, eds, Space Telescope Science Institute Symp. Series, Cambridge University Press, 95

Longair, M. S.: 1981, *High Energy Astrophysics* (1st Edition), Cambridge University Press

Marscher, A. & Gear, W. K.: 1985, *Astrophys. J.* **298**, 114

Marscher, A., Gear, W. K. & Travis, J. P.: 1992, *Variability of Blazars*, Valtaoja, E. & Valtonen, M., eds, Cambridge University Press, 85

Mead, A. R. G., Ballard, K. R., Brand, P. W. J. L., Hough, J. H., Bailey, J. A. & Brindle, C.: 1990, *Astron. Astrophys. Suppl. Ser.* **83**, 183

Miller, H. R., Carini, M. T., Noble, J. C., Webb, J. R. & Wiita, P. J.: 1992, *Variability of Blazars*, Valtaoja, E. & Valtonen, M., eds, Cambridge University Press, 320

Moore, R. L., McGraw, J. T., Angel, J. R. P., *et al.*: 1982, *Astrophys. J.* **260**, 415

Murray, A. G.: 1991, *Ph. D. Thesis*, University of Aberdeen

Murray, A. G., Flett, A. M., Murray, G. & Ade, P. A. R.: 1992, *Infrared Physics*, **33**, 113

Murray, A. G., Ade, P. A. R. & Griffin, M. J.: 1995, *Proc. Polarimetry of the Interstellar Medium*, Rensselaer Polytechnic Institute, Troy, NY (in Press)

Ostriker, J. P. & Vietri, M.: 1985, *Nature* **318**, 446

Ostriker, J. P.: 1989, *BL Lac Objects*, Maraschi, L., Maccacaro, T. & Ulrich, M., eds, Springer-Verlag, 420

Pacholczyk, A. G.: 1970, *Radio Astrophysics*, San Francisco: W. H. Freeman and Company

Perley, R. A.: 1987, *Extragalactic Magnetic Fields*, Asseo, E. & Sol, H., eds, North-Holland, Amsterdam, 255

Platt, S. R., Hildebrand, R. H., Pernic, R. J., Davidson, J. A. & Novak, G.:: 1991, *Pub. Astron. Soc. Pacific* **103**, 1193

Press, W. H., Teukolsky, S. A., Vetterling, W. T. & Flannery, B. P.: 1992, *Numerical Recipes in C 2nd Edition*, Cambridge University Press

Roberts, D. H., Wardle, J. F. C., Brown, L. F., Gabuzda, D. C. & Cawthorne, T. V.: 1990, *Parsec-Scale Radio Jets,* Zensus *et al.*, eds, Cambridge University Press, 110

Robson, E. I., Gear, W. K., Clegg, P. E., Smith, M. G., Ade, P. A. R., Griffin, M. J., Nolt, I. G. & Howard, R. J.: 1983, *Nature* **305**, 194

Rusk, R. & Seaquist, E. R.: 1985, *Astron. J.* **90**, 30

Rusk, R.: 1988, *The Impact of VLBI on Astrophysics and Geophysics,* Reid et al., eds, IAU *Symp.* **129**, 161

Rusk, R.: 1990, *J. Roy. Astron. Soc. Can.* **84**, 199

Saikia, D. J. & Salter, C. J.: 1988, *Ann. Rev. Astron. Astrophys.* **26**, 93

Schleuning, D. A., Dowell, C. D. & Platt, S. R.: 1995, *Proc. Polarimetry of the Interstellar Medium*, Rensselaer Polytechnic Institute, Troy, NY (in Press)

Simmons, J. F. L. & Stewart, B. G.: 1985, *Astron. Astrophys.* **142**, 100

Telervich, R., Tenorio-Tagle, G., Franco, J. & Melnick, J.: 1992, *Mon. Not. Roy. Astron. Soc.* **225**, 713

Wardle, J. F. C. & Kronberg, P. P.: 1974, *Astrophys. J.* **194**, 249

Wardle, J. F. C., Moore, R. L. & Angel, J. R. P.: 1984, *Astrophys. J.* **279**, 83

Wardle, J. F. C., Cawthorne, T. V., Roberts, D. H. & Brown, L. F.: 1994, *Astrophys. J.* **437**, 122

Wiita, P. J., Miller, H. R., Gupta, N. & Chakrabarti, K.: 1992, *Variability of Blazars*, Valtaoja, E. & Valtonen, M., eds, Cambridge University Press, 311

Wills, B. J.: 1989, *BL Lac Objects*, Maraschi, L., Maccacaro, T. & Ulrich, M., eds, Springer-Verlag, 109

Zensus, J. A.: 1992, *Variability of Blazars*, Valtaoja, E. & Valtonen, M., eds, Cambridge University Press, 187

Appendix A

VLBI Observations of Blazar Jets

0133+473 DA 55 OC 457

PA (°)	*r (mas)*	*GHz*	*Year*	*Refs.*	*Comments*
125 - 170			1985	[60]	From 1978 map in [49]
303	3	5	1988	[49]	Elongation of core along 123° + 180°
305			1992	[26]	From [49] gets 125°, I add 180°
305	1.3		1993	[15]	
305	**1.3**				

0235+164 OD 160

PA (°)	*r (mas)*	*GHz*	*Year*	*Refs.*	*Comments*
210	0.5	22	1984	[28]	Weak component
0 - 50	≤ 5	5	1984	[4]	Three epochs, three orientations
0 - 45			1985	[60]	
20			1987	[27]	
45	1.8	5	1988	[20]	Weak evidence
?	≤ 5	5	1989	[24]	North-East extension mentioned
26			1990	[61]	Different references than in [60]
?	≤ 5	5	1992	[25]	Four epochs maps, very compact
20			1992	[26]	From [60] and [27]
25	**≤ 5**				

0316+413 3C84 NGC 1275

PA (°)	*r (mas)*	*GHz*	*Year*	*Refs.*	*Comments*
210	1.5	22	1983	[56]	B component
225	≤ 1	89	1983	[57]	This angle quoted in [5]
12			1987	[27]	
210	3	22	1989	[40]	Complex, rotating components
225	0.1	100	1990	[5]	Confirms [57]
170			1990	[61]	From Martin'83
200 - 220	≤ 0.5	43	1990	[30]	
202	≤ 0.03	100	1992	[7]	Direction of strongest components
190 - 220	≤ 0.5	43	1992	[32]	
220	≤ 0.5	43	1992	[33], [72]	Refs [30], [32], [33] & [72] same data
12			1992	[26]	From [27]
12 / 354			1992	[3]	From Rusk's Ph D Thesis cf. [61]
200 - 220	≤ 0.5	43	1993	[35]	Jet along 160 - 180 towards 2 mas
210 - 225	≤ 0.7	22	1993	[67]	Jet turns to 180°
210	**≤ 0.5**				

0420-014

PA (°)	*r (mas)*	*GHz*	*Year*	*Refs.*	*Comments*
?	≤ 2	5	1992	[71]	Very compact, perhaps North-South
90			1992	[26]	From map in [71]
90	**≤ 2**				

0430+052 3C120

PA (°)	*r (mas)*	*GHz*	*Year*	*Refs.*	*Comments*
250			1985	[60]	From Benson'84
243			1987	[27]	Quotes 63° I add 180°
260	≤ 20	5	1987	[52]	1.66 GHz map also similar result
264	≤ 3	5	1988	[68]	
265	~ 5	1.7	1988	[9]	All 5 GHz components blended together
250			1989	[36]	From Walker'82
250			1990	[61]	From Smith'86
257			1992	[26]	From [60] & [68]
265	**≤ 3**				

0528+134

PA (°)	*r (mas)*	*GHz*	*Year*	*Refs.*	*Comments*
220	0.75	8.4	1990	[16]	Similar result at 2.3 GHz
44	≤ 0.5	23	1993	[76]	Similar @ 8.3 GHz. 180° from [16]
44	**≤ 0.5**				

0735+178 OI 158

PA (°)	*r (mas)*	*GHz*	*Year*	*Refs.*	*Comments*
~ 70	≤ 5	5	1984	[4]	Orientation is North-East
45 - 90			1985	[60]	From [4]
45			1987	[27]	
72	≤ 5	5	1988	[68]	
67	≤ 5	5	1989	[22]	From a 1982 map
59			1990	[61]	Quotes 6 references. Eror ± 20°
25	1.2	22	1991	[6]	
70	≤ 5	22	1991	[6]	
73	0.37	22	1991	[75]	Refs. [6] & [75] use same data
65			1992	[26]	From references up to 1989
73	**≤ 0.5**				

0736+017 OI 061

PA (°)	*r (mas)*	*GHz*	*Year*	*Refs.*	*Comments*
90	6	1.7	1984-86	[59], [46]	Unresolved at 1.4 GHz. Two epochs maps
72			1985	[60]	Orientation of 13 mas source from [59]
82			1990	[61]	From references up to 1987
80	**~ 6**				

0851+202 OJ 287

PA (°)	*r (mas)*	*GHz*	*Year*	*Refs.*	*Comments*
90			1987	[27]	
245	≤ 1.3	5	1987-88	[58], [68]	Two epochs result
260	≤ 1	5	1989	[21]	Third epoch added to [58] & [68]
245			1990	[61]	Using earlier data than [21]
265	~ 3	2.3	1990	[16]	Unresolved at 8.4 GHz
240	≤ 0.07	100	1992	[7]	Weak component but agrees with [35]
252		5	1992	[26]	From [68] and [21]
232	0.9	43	1993	[35]	Error of ± 20° Single measurement
260	**≤ 1**				

0923+392 4C 39.25

PA (°)	*r (mas)*	*GHz*	*Year*	*Refs.*	*Comments*
75	4 asc	0.408	1982	[12]	Quotes a mas double at 95°
270			1987	[27]	
277	1.9	5	1988	[49]	Claim that [12] is 245°
277			1990	[61]	From Moore'84
285			1992	[26]	From references after 1987
277			1992	[3]	From Rudnick'83
282	2.6	23	1993	[1]	Several epochs and frequencies
272	2.2	43	1993	[2]	Core still invisible, unresolved
279	≤ 2	1.7	1994	[73]	Rotating jet, angle is for nearest, core position unknown
275	**~ 2**				

1055+018 4C 01.28

PA (°)	*r (mas)*	*GHz*	*Year*	*Refs.*	*Comments*
40	4	1.7	1984-86	[59], [46]	NW compt. PA 303° at 8 mas, same flux
305			1992	[26]	From O'Dea'88
305	**4**				

1156+295

PA (°)	*r (mas)*	*GHz*	*Year*	*Refs.*	*Comments*
20	≤ 1	1.7 - 2.2	1990	[38]	mas jet bends from 20° to 70°
22			1992	[26]	From McHardy
20	**~ 1**				

1226+023 3C 273

PA (°)	*r (mas)*	*GHz*	*Year*	*Refs.*	*Comments*
245	≤ 20	10.7	1985	[66]	Jet turns to 223° further out
233	≤ 2	10.7	1985	[10]	Turns to 245° at 6 mas
230			1987	[27]	Quotes 50° I add 180°
232	≤ 2	10.7	1987	[17]	Confirms results in [10]
222	acs		1989	[62]	Optical jet orientation
250			1989	[36]	From [17]
245			1990	[61]	From references up to 1987
232	≤ 2.5	22	1990	[74]	Covers 0.5 - 2.5 mas, error ± 3°
257	≤ 0.5	43	1990	[30]	Average of two components, error ± 12°
250	≤ 0.25	100	1990	[5]	PA range is 240° - 260°
260	0.2	43	1990	[31]	Jet bends to 245° at 0.8 mas
270	0.25	43	1992	[33]	PA ranges: ~270° mas to ~220 optical
243			1992	[26]	From pre-1987 references
250	**0.25**				

1253-055 3C 279

PA (°)	*r (mas)*	*GHz*	*Year*	*Refs.*	*Comments*
230			1987	[27]	Quotes 50° I add 180°
206	acs	1.7 - 5	1987	[52]	One compt. at 215°, no mas structure
225	≤ 1.5	5, 11, 22	1989	[66]	Several epochs maps
225			1990	[61]	From references up to 1981
227			1992	[26]	From pre-1987 references
225	≤ 0.2	100	1992	[7], [8]	mas jet ≤ 5° away from acs jet
225	~ 1	11, 22	1993	[13]	PA is 245° wrt core at ~-20°, hence 225°
225	**≤ 0.2**				

1308+326

PA (°)	*r (mas)*	*GHz*	*Year*	*Refs.*	*Comments*
10 / 330			1985	[60]	From Zensus'84
280	4	5	1990	[44]	From [25]
350			1990	[61]	From Angel'80 with error ± 30°
314	0.7	5	1992	[25]	296° at 1.6 mas & 274° at 3.9 mas
330			1992	[26]	From [60]
314	**0.7**				

1335-127 1334-127

PA (°)	*r (mas)*	*GHz*	*Year*	*Refs.*	*Comments*
345		VLA	1982	[50]	Jet to 6.5 acs East of core
135	≤ 1.5	5	1992	[71]	Estimate, very compact no structure visible
135	**≤ 1.5**				

1514-241 AP Lib

PA (°)	*r (mas)*	*GHz*	*Year*	*Refs.*	*Comments*
120	200	VLA	1982	[50]	VLA at 4885 & 1465 MHz
120	**200**				

1633+382 4C 38.41

PA (°)	*r (mas)*	*GHz*	*Year*	*Refs.*	*Comments*
295	2	5	1988	[49]	Good fit to a 1979 map
296			1990	[61]	From Moore'84
295			1992	[3]	From Rudnick'83
296		VLBI	1993	[18]	From Pearson'93, VLA PA at 168°
315	1.3	5	1993	[14]	North-West component
265	2.2	5	1993	[14]	South-West component
315	**1.3**				

1641+399 3C 345

PA (°)	*r (mas)*	*GHz*	*Year*	*Refs.*	*Comments*
230	≤ 1	22.2	1983	[56]	Different orientation than at 10.7 GHz
225	~ 0.4	22.2	1984	[43]	New epochs added from [56]
225	≤ 25	1.7	1986	[41]	Arcsec scale orientation at 330°
225	≤ 0.4	2.3 - 89	1986	[11]	C4 bends to 274°, C5 appears at 270°
230	0.3	10.7	1987	[52]	From Biretta'83
285			1988	[68]	Average PA for the jet
319	2 acs	5	1989	[29]	VLA. Two further knots at 327°
235	≤ 0.5	8.3	1989	[64], [65]	C6 & C4 similar PA, C5 towards 262°
286			1990	[61]	From references up to 1986
246	~ 0.1	43	1990	[30]	C6 emerges, C5 @ 280°-240°, C4 as [11]
310	~ 0.1	100	1990	[5], [54]	Quotes 22 GHz obs. with PA 225°
250	≤ 0.1	43, 100	1992	[42]	PA for injection of electrons using data from Krichbaum and Bääth
305	≤ 0.1		1992	[8], [7]	New compt.(s) observed in two epochs
230	~ 0.4	100	1992	[55]	PA is 315° at 50 mas
300	~ 0.5	1.7	1992-93	[33], [34] [35], [53]	PA for C7. Other compts. seen at: C6 @250°, C5 @270° C4 @230°
225		43	1992	[26]	From Hardee'88
230			1992	[3]	From Rudnick'83
299	3 acs	5	1993	[14]	VLA map for jet. PA for C4 is 270°
300	**≤ 0.1**				

1749+096 OT 081

PA (°)	*r (mas)*	*GHz*	*Year*	*Refs.*	*Comments*
13	0.8	5	1988	[20]	From Dec'81 data
19			1989	[23]	From Cohen'88
13			1990	[61]	Error of ± 20°. From refs. up to 1987
?	~ 1	5	1992	[71]	Quotes East orientation from [23]
67			1992	[26]	Uses map in [71]
67	**~ 1**				

1823+568 4C 56.27

PA (°)	*r (mas)*	*GHz*	*Year*	*Refs.*	*Comments*
197	1.35	5	1988	[49]	Map from Dec'79
197	≤ 3	5	1989-92	[23], [24] [25]	Map from Oct'84
197		5	1990	[44]	From [49] & [24]
197			1992	[3]	From Wrobel'88, but not true
195	≤ 2	5	1993	[14]	Same map as [23], [24] & [25]
197	**≤ 2**				

1921-293 OV -236

PA (°)	*r (mas)*	*GHz*	*Year*	*Refs.*	*Comments*
25			1990	[61]	Error ± 20°. From Smith'87

2200+420 BL Lac

PA (°)	*r (mas)*	*GHz*	*Year*	*Refs.*	*Comments*
183			1987	[27]	Quotes 3° I add 180°
180	≤ 4	5	1988	[49]	
184	~ 2	5	1989-93	[23], [24] [37], [14]	Map from 1984
188			1990	[61]	From Smith'87. Error ± 10°
190	~ 2	5, 10, 6	1990	[44], [45]	VLBI at 2, 3 epochs. Error ± 5°
190			1992	[26]	From [44] & [45]
201	≤ 1.5	100	1992	[7], [8]	Highest resolution image
200	**≤ 1.5**				

2223-052 3C 446

PA (°)	*r (mas)*	*GHz*	*Year*	*Refs.*	*Comments*
100	250	1.66	1985	[63]	
112			1987	[27]	
100			1990	[61]	From references up to 1987. Eror ± 5°
95	3.5	5	1990	[70]	
113	50	1.6, 5	1992	[19]	Jet turns through 43° to 70° at 320 mas
100			1992	[26]	From [27] and [60]
218	0.1	100	1993	[8], [37]	Higher resolution than 5 GHz
218	**0.1**				

2230+114 CTA 102

PA (°)	*r (mas)*	*GHz*	*Year*	*Refs.*	*Comments*
140	1.6 asc	VLA	1982	[50]	VLA at 4885 & 1465 MHz
146			1987	[27]	
157	≤ 3	5	1989	[69], [70]	15 mas tail along 140°
146			1990	[61]	From references up to 1986
155			1992	[26]	From [27]
155	**≤ 3**				

2251+158 3C 454.3

PA (°)	*r (mas)*	*GHz*	*Year*	*Refs.*	*Comments*
295	10	5	1984	[47]	Arcsec jet along 312°
300	12	1.7	1984	[59]	
130			1987	[27]	
295	~ 1	5, 10.7	1987	[48]	PA at 20 mas along 307°
12			1988	[68]	
295			1990	[61]	From refs. up to 1987
295			1992	[26]	From [60]
295	**~ 1**				

References

[1] Alberdi, A., Marcaide, J. M., Marscher, A. P., Zhang, Y. F., Elósegui, P., Gómez, J. L. & Shaffer, D. B.: 1993, *Astrophys. J.* **402**, 160

[2] Alberdi, A., Krichbaum, T. P., Marcaide, J. M., Witzel, A., Graham, D. A., Inoue, M., Morimoto, M., Booth, R. S., Rönnäng, B. O., Colomer, F., Rogers, A. E. E., Zensus, J. A., Readhead, A. C. S., Lawrence, C. R., Vermeulen, R., Bartel, N., Shapiro, I. I. & Burke, B.F.: 1993, *Astron. Astrophys.* **271**, 93

[3] Aller, M. F., Aller, H. D. & Hughes, P. A.: 1992, *Astrophys. J.* **399**, 16

[4] Bääth, L. B.: 1984, *VLBI and Compact Radio Sources*, Fanti *et al.*, eds, IAU *Symp.* **110**, p. 127

[5] Bääth, L. B.: 1990, *Parsec-Scale Radio Jets*, Zensus *et al.*, eds, Cambridge University Press, p. 91

[6] Bääth, L. B. & Zhang, F. J.: 1991, *Astron. Astrophys.* **243**, 328

[7] Bääth, L. B., Rogers, A. E. E., Inoue, M., Padin, S., Wright, M. C. H., Zensus, A., Kus, A. J., Backer, D. C., Booth, R. S., Carlstrom, J. E., Dickman, R. L., Emerson, D. T., Hirabayashi, H., Hodges, M. W., Kobayashi, H., Lamb, J., Moran, J. M., Morimoto, M., Plambeck, R. L., Predmore, C. R., Rönnäng, B. O. & Woody, D: 1992, *Astron. Astrophys.* **257**, 31

[8] Bääth, L. B.: 1992, *Variability of Blazars*, Valtaoja, E. & Valtonen, M., eds, Cambridge University Press, p. 196

[9] Benson, J. M., Walker, R. C., Unwin, S. C., Muxlow, T. W. B., Wilkinson, P. N., Booth, R. S., Pilbratt, G. & Simon, R. S.:1988, *Astrophys. J.* **334**, 560

[10] Biretta, J. A., Cohen, M. H., Hardebeck, H. E., Kaufmann, P., Abraham, Z., Perfetto, A. A., Scalise, E., Schaad, R. E. & Silva, P. M.: 1985, *Astrophys. J.* **292**, L5

[11] Biretta, J. A., Moore, R. L. & Cohen, M. H.:1986, *Astrophys. J.* **308**, 93

[12] Browne, I. W. A., Orr, M. J. L., Davis, R. J., Foley, A., Muxlow, T. W. B. & Thomasson, P: 1982, *Mont. Not. Roy. Astron. Soc.* **198**, 673

[13] Carrara, E. A., Abraham, Z., Unwin, S. C. & Zensus, J. A.: 1993, *Astron. Astrophys.* **279**, 83

[14] Cawthorne, T. V., Wardle, J. F. C., Roberts, D. H., Gabuzda, D. C. & Brown, L. F.: 1993, *Astrophys. J.* **416**, 496

[15] Cawthorne, T. V., Wardle, J. F. C., Roberts, D. H. & Gabuzda, D. C.: 1993, *Astrophys. J.* **416**, 519

[16] Charlot, P.: 1990, *Astron. Astrophys.* **229**, 51

[17] Cohen, M. H., Zensus, J. A., Biretta, J. A., Comoretto, G., Kaufmann, P. & Abraham, Z.: 1987, *Astrophys. J.* **315**, L89

[18] Conway, J. E. & Murphy, D. W.: 1993, *Astrophys. J.* **411**, 89

[19] Fejes, I., Porcas, R. W. & Akujor, C. E.: 1992, *Astron. Astrophys.* **257**, 459

[20] Gabuzda, D. C., Roberts, D. H., Wardle, J. F. C. & Brown, L. F.: 1988, *The Impact of VLBI on Astrophysics and Geophysics,* Reid *et al.*, eds, IAU *Symp.* **129**, p. 167

[21] Gabuzda, D. C., Wardle, J. F. C. & Roberts, D. H.: 1989, *Astrophys. J.* **336**, L59

[22] Gabuzda, D. C., Wardle, J. F. C. & Roberts, D. H.: 1989, *Astrophys. J.* **338**, 743

[23] Gabuzda, D. C., Cawthorne, T. V., Roberts, D. H. & Wardle, J. F. C.: 1989, *BL Lac Objects,* Maraschi *et al.*, eds, Springer-Verlag, p. 22

[24] Gabuzda, D. C., Cawthorne, T. V., Roberts, D. H. & Wardle, J. F. C.: 1989, *Astrophys. J.* **347**, 701

[25] Gabuzda, D. C., Cawthorne, T. V., Roberts, D. H. & Wardle, J. F. C.: 1992, *Astrophys. J.* **388**, 40

[26] Hughes, P. A., Aller, H. D. & Aller, M. F.: 1992, *Astrophys. J.* **396**, 469

[27] Impey, C. D.: 1987, *Superluminal Radio Sources*, Zensus, A. & Pearson, T., eds, Cambridge University Press, p. 233

[28] Jones, D. L., Davis, M. M. & Unwin, S. C.: 1984, *VLBI and Compact Radio Sources*, Fanti *et al.*, eds, IAU *Symp.* **110**, p. 47

[29] Kollgaad, R. I., Wardle, J. F. C. & Roberts, D. H.: 1989, *Astron. J.* **97**, 1550

[30] Krichbaum, T. P.: 1990, *Parsec-Scale Radio Jets,* Zensus *et al.*, eds, Cambridge University Press, p. 83

[31] Krichbaum, T. P., Booth, R. S., Kus, A. J., Rönnäng, B. O., Witzel, A., Graham, D. A., Pauliny-Toth, I. I. K., Quirrenbach, A., Hummel, C. A., Alberdi, A., Zensus, J. A., Johnston, K. J., Spencer, J. H., Rogers, A. E. E., Lawrence, C. R., Readhead, A. C., Hirabayashi, H., Inoue, M., Morimoto, M., Dhawan, V., Bartel, N., Shapiro, I. I., Burke, B. F. & Marcaide, J. M.: 1990, *Astron. Astrophys.* **237**, 3

[32] Krichbaum, T. P., Witzel, A., Graham, D. A., Alef, W., Pauliny-Toth, I. I. K., Hummel, C. A., Quirrenbach, A., Inoue, M., Hirabayashi, H., Morimoto, M., Rogers, A. E. E., Zensus, J. A., Readhead, A. C., Booth, R. S., Rönnäng, B. O., Kus, A. J., Johnston, K. J., Spencer, J. H., Burke, B. F., Dhawan, V., Bartel, N., Shapiro, I. I., Alberdi, A. & Marcaide, J. M.: 1992, *Astron. Astrophys.* **260**, 33

[33] Krichbaum, T. P. & Witzel, A.: 1992, *Variability of Blazars*, Valtaoja, E. & Valtonen, M., eds, Cambridge University Press, p. 205

[34] Krichbaum, T. P., Witzel, A., Graham, D. A. & Zensus, J. A.: 1992, *Physics of Active Galactic Nuclei,* Duschl, W. J. & Wagner, S. J., eds, Springer-Verlag, p. 574

[35] Krichbaum, T. P., Witzel, A., Graham, D. A., Standke, K. J., Schwartz, R., Lochner, O., Schalinski, C. J., Greve, A., Steppe, H., Brunswig, W., Butin., G., Hein, H., Navarro, S., Peñalver, J., Grewing, M., Booth, R. S., Colomer, F. & Rönnäng, B. O.: 1993, *Astron. Astrophys.* **275**, 375

[36] Kuril'chik, V. N. & Ashimbaeva, N. T.: 1989, *Sov. Astron.* **33**, 286

[37] Lerner, M. S., Bääth, L. B., Inoue, M., Padin, S., Rogers, A. E. E., Wright, M. C. H., Zensus, J. A., Backer, D. C., Booth, R. S., Carlstrom, J. E., Emerson, D. T., Hirabayashi, H., Hodges, M. W., Jewell, P., Kobayashi, H., Kus, A. J., Moran, J. M., Morimoto, M., Plambeck, R. L., Rantakyrö, F. T. & Woody, D. P.: 1993, *Astron. Astrophys.* **280**, 117

[38] McHardy, I. M., Marscher, A. P., Gear, W. K., Muxlow, T., Lehto, H. J. & Abraham, R. G.: 1990, *Mont. Not. Roy. Astron. Soc.* **246**, 305

[39] McHardy, I. M., Merrifield, M. R., Abraham, R. G. & Crawford, C. S.: 1994, *Mont. Not. Roy. Astron. Soc.* **268**, 681

[40] Marr, J. M., Backer, D. C. & Wright, M. C. H.: 1990, *Parsec-Scale Radio Jets,* Zensus *et al.*, eds, Cambridge University Press, p. 78

[41] Matveenko, L. I., Pauliny-Toth, I. I. K., Sherwood, W. A., Bääth, L. B. & Kus, A.: 1986, *Sov. Astron. Lett.* **12**, 63

[42] Matveenko, L. I., Graham, D. A., Pauliny-Toth, I. I. K., Sherwood, W. A., Bääth, L. B. & Kus, A.: 1992, *Sov. Astron. Lett.* **18**, 379

[43] Moore, R. L., Biretta, J. A., Readhead, A. C. S. & Bääth, L. B.: 1984, *VLBI and Compact Radio Sources*, Fanti *et al.*, eds, IAU *Symp.* **110**, p. 109

[44] Mutel, R. L.: 1990, *Parsec-Scale Radio Jets,* Zensus *et al.*, eds, Cambridge University Press, p. 98

[45] Mutel, R. L., Phillips, R. B., Su, B. & Bucciferro, R. R.: 1990, *Astrophys. J.* **352**, 81

[46] Padrielli, L., Romney, J. D., Bartel, N., Fanti, R., Ficarra, A., Mantovani, F., Matveenko, L., Nicolson, G.D. & Weiler, K.W.: 1986, *Astron. Astrophys.* **165**, 53

[47] Pauliny-Toth, I. I. K., Porcas, R. W., Zensus, J. A. & Kellermann, K. I.: 1984, *VLBI and Compact Radio Sources*, Fanti *et al.*, eds, IAU *Symp.* **110**, p. 149

[48] Pauliny-Toth, I. I. K., Porcas, R. W., Zensus, J. A., Kellermann, K. I., Wu, S. Y., Nicolson, G. D. & Mantovani, F.: 1987, *Nature* **328**, 778

[49] Pearson, T. J. & Readhead, A. C. S.: 1988, *Astrophys. J.* **328**, 114

[50] Perley, R. A.: 1982, *Astron. J.* **87**, 859

[51] Perlman, E. S. & Stocke, J. T.: 1994, *Astron. J.* **108**, 56

[52] Pilbratt, G., Booth, R. S. & Porcas, R. W.: 1987, *Astron. Astrophys.* **173**, 12

[53] Qian, S., Witzel, A., Krichbaum, T. P., Quirrenbach, A. & Zensus, J. A.: 1993, *Chin. Astron. Astrophys.* **17**, 150

[54] Rantakyrö, F. & Bääth, L. B.: 1990, *Nordic-Baltic Astronomy Meeting on Astrophysical Processes and Structures in the Universe*, Kiselman & Lagerkvist (eds), Sweden, p. 253

[55] Rantakyrö, F., Bääth, L. B., Pauliny-Toth, I. I. K., Matveenko, L. I. & Unwin, S. C.: 1992, *Astron. Astrophys.* **259**, 8

[56] Readhead, A. C. S., Hough, D. H., Ewing, M. S., Walker, R. C. & Romney, J. D.: 1983, *Astrophys. J.* **265**, 107

[57] Readhead, A. C. S., Masson, C. R., Moffet, A. T., Pearson, T. J., Seielstad, G. A., Woody, D. P., Backer, D. C., Plambeck, R. L., Welch, W. J., Wright, M. C. H., Rogers, A. E. E., Webber, J. C., Shapiro, I. I., Moran, J. M., Goldsmith, P. F., Predmore, C. R., Bääth, L. B. & Rönnäng, B.: 1983, *Nature* **303**, 504

[58] Roberts, D. H., Gabuzda, D. C. & Wardle, J. F. C.:1987, *Astrophys. J.* **323**, 536

[59] Romney, J. D., Padrielli, L., Bartel, N., Weiler, K.W., Ficarra, A., Mantovani, F., Bääth, L. B., Kogan, L., Matveenko, L., Moiseev, I. G. & Nicolson, G.D.: 1984, *Astron. Astrophys.* **135**, 289

[60] Rusk, R. & Seaquist, E. R.: 1985, *Astron. J.* **90**, 30

[61] Rusk, R.: 1990, *J. Roy. Astron. Soc. Can.* **84**, 199

[62] Scarrott, S. M. & Rolph, C. D.: 1989, *Mont. Not. Roy. Astron. Soc.* **238**, 349

[63] Simon, R. S., Johnston, K. J. & Spencer, J. H.: 1985, *Astrophys. J.* **290**, 66

[64] Tang, G., Rönnäng, B. O. & Bääth, L. B.: 1989, *Astron. Astrophys.* **216**, 31

[65] Tang, G., Bartel, N., Ratner, M. I., Shapiro, I. I., Bääth, L. B. & Rönnäng, B. O.: 1990, *Parsec-Scale Radio Jets,* Zensus *et al.*, eds, Cambridge University Press, p. 32

[66] Unwin, S. C., Cohen, M. H., Biretta, J. A., Hodges, M. W., & Zensus, J. A.: 1989, *Astrophys. J.* **340**, 117

[67] Venturi, T., Readhead, A. C. S., Marr, J. M. & Backer, D. C.: 1993, *Astrophys. J.* **411**, 552

[68] Wardle, J. F. C. & Roberts, D. H.: 1988, *The Impact of VLBI on Astrophysics and Geophysics,* Reid *et al.*, eds, IAU *Symp.* **129**, p. 143

[69] Wehrle, A. E. & Cohen, M. H.: 1989, *Astrophys. J.* **346**, L69

[70] Wehrle, A. E., Cohen, M. H. & Unwin, S. C.: 1990, *Parsec-Scale Radio Jets,* Zensus *et al.*, eds, Cambridge University Press, p. 49

[71] Wehrle, A. E., Cohen, M. H., Unwin, S. C., Aller, H. D., Aller, M. F. & Nicolson, G.: 1992, *Astrophys. J.* **391**, 589

[72] Witzel, A.: 1992, *Physics of Active Galactic Nuclei,* Duschl, W. J. & Wagner, S. J., eds, Springer-Verlag, p. 484

[73] Wu, S.-Y., Pauliny-Toth, I. I. K. & Porcas, R. W.: 1994, *Chin. Astron. Astrophys.* **18**, 20

[74] Zensus, J. A., Unwin, S. C., Cohen, M. H., Biretta, J. A.: 1990, *Astron. J.* **100**, 1777

[75] Zhang, F. J. & Bääth, L. B.: 1991, *Mont. Not. Roy. Astron. Soc.* **248**, 566

[76] Zhang, Y. F., Marscher, A. P., Aller, H. D., Aller, M. F., Terasäsanta, H. & Valtaoja, E.: 1994, *Astrophys. J.* **432**, 91

Appendix B

Blazar Database at 1100 μm

0133+476

Epoch	*F (Jy)*	±	α	±	*P (%)*	±	χ (°)	±
1993.15	1.47	0.15	-0.68	0.16	10.48	1.76	2.68	4.75

0235+164

Epoch	*F (Jy)*	±	α	±	*P (%)*	±	χ (°)	±
1990.12	1.41	0.20	-0.18	0.01				
1992.02	1.16	0.12			5.91	1.84	9.23	8.52
1992.16	2.09	0.31	-0.23	0.49	6.46	0.63	31.11	2.79
1992.81	3.55	0.31	-0.40	0.15	4.63	0.40	102.90	2.45
1993.15	2.79	0.29	-0.65	0.20	2.68	0.68	95.47	7.09

0316+413

Epoch	*F (Jy)*	±	α	±	*P (%)*	±	χ (°)	±
1992.02	2.32	0.23			1.62	0.63	73.31	10.43
1992.81	1.98	0.15	-0.88	0.15	1.26	0.63	78.56	12.84

0420-014

Epoch	*F (Jy)*	±	α	±	*P (%)*	±	χ (°)	±
1992.02	3.64	0.37	-1.24	0.45	4.88	0.22	52.05	1.32
1992.16	3.85	0.42	-0.25	0.38	6.02	0.36	50.35	1.73
1992.81	2.55	0.24	-0.50	0.15	4.37	0.84	15.19	5.38
1993.15	1.09	0.12	-0.77	0.15	4.89	1.65	179.25	9.16

0528+134

Epoch	*F (Jy)*	±	α	±	*P (%)*	±	χ (°)	±
1992.81	1.91	0.14	-0.69	0.18	4.79	0.80	45.88	4.72
1993.15	3.52	0.35	-0.52	0.15	2.92	0.35	124.90	3.44

0735+178

Epoch	*F (Jy)*	±	α	±	*P (%)*	±	χ (°)	±
1990.12	1.70	0.20	-0.36	0.18				
1992.02	1.51	0.15	-1.36	0.45	8.84	2.56	70.41	7.98
1992.16	1.47	0.17	-0.46	0.40	5.28	0.73	103.00	3.94
1992.35	1.18	0.03	-1.05	0.19				
1992.81	0.85	0.07	-0.20	0.17	5.75	1.52	3.03	7.32
1993.15	0.85	0.11	-0.83	0.18	5.27	2.02	177.37	10.24
1994.15	1.14	0.03						

0736+017

Epoch	*F (Jy)*	±	α	±	*P (%)*	±	χ (°)	±
1990.12	0.90	0.10	-0.43	0.13				
1992.35	1.23	0.03	-0.25	0.14				
1992.81	0.58	0.06	-0.71	0.17	5.41	2.31	76.45	11.25
1993.15	0.76	0.08	-0.76	0.21	14.19	1.95	34.25	3.90

0829+046

Epoch	*F (Jy)*	±	α	±	*P (%)*	±	χ (°)	±
1990.12	1.10	0.10						
1992.81	0.93	0.07	-0.16	0.19	4.94	1.71	45.86	9.36
1993.15	1.44	0.18	-0.37	0.16	2.87	1.21	39.63	11.16

0851+202

Epoch	*F (Jy)*	±	α	±	*P (%)*	±	χ (°)	±
1990.12	2.20	0.20	-0.82	0.18				
1991.43	2.23	0.27	-0.59	0.50	9.49	0.74	131.71	2.23
1992.02	1.35	0.14			9.08	1.07	96.90	3.34
1992.16	1.47	0.15	-0.77	0.36	12.26	1.54	109.73	3.58
1992.35	1.35	0.11	-0.38	0.18				
1992.81	1.89	0.15	-0.32	0.24	15.09	0.81	104.57	1.54
1993.15	0.97	0.10	-0.75	0.19	8.79	1.66	103.28	5.32
1994.15	2.23	0.05	-0.59	0.14	5.45	1.35	107.70	6.88
1994.40	1.33	0.13	-0.69	0.15	13.02	3.58	56.49	7.60

0923+392

Epoch	*F (Jy)*	±	α	±	*P (%)*	±	χ (°)	±
1992.02	1.63	0.16			5.64	1.75	149.05	8.49
1992.35	1.96	0.19	-0.74	0.16				
1992.81	1.85	0.14	-0.72	0.18	3.67	0.81	123.94	6.17
1994.40	1.78	0.14	-1.14	0.21				

1055+018

Epoch	*F (Jy)*	±	α	±	*P (%)*	±	χ (°)	±
1992.35	2.02	0.05	-0.48	0.10				
1993.15	1.59	0.17	-0.85	0.16	10.06	1.39	117.35	3.93

1226+023

Epoch	*F (Jy)*	±	α	±	*P (%)*	±	χ (°)	±
1990.12	5.70	0.20	-1.04	0.20				
1990.42	18.58	1.88	-0.07	0.45	2.75	0.10	129.36	1.07
1991.43	18.53	2.01	-1.11	0.47	4.16	0.07	151.36	0.51
1992.02	11.08	1.11	-0.94	0.45	0.72	0.13	92.29	5.08
1992.16	13.48	1.54	-0.54	0.39	1.30	0.11	134.82	2.37
1992.35	12.50	0.30	-0.78	0.06				
1992.42	10.31	0.26	-0.91	0.09				
1992.81	12.12	0.94	-0.87	0.15	1.45	0.25	160.06	4.84
1993.15	12.29	1.24	-0.53	0.16	2.24	0.24	155.32	3.06
1994.15	11.07	0.28	-0.45	0.11	1.38	0.42	128.73	8.36
1994.40	11.34	0.87	-0.56	0.14	2.50	0.52	130.31	5.85

1253-055

Epoch	*F (Jy)*	±	α	±	*P (%)*	±	χ (°)	±
1990.12	5.80	0.60	-0.75	0.13				
1991.43	9.92	1.10	-0.67	0.47	9.24	0.11	48.89	0.34
1992.02	7.21	0.72	-0.77	0.44	9.32	0.26	66.13	0.79
1992.16	7.70	0.88	-0.58	0.39	8.99	0.27	58.94	0.88
1992.35	7.10	0.19	-0.48	0.10				
1992.42	8.29	0.19	-0.47	0.04				
1992.81	5.99	0.49	-0.78	0.16	7.07	0.28	44.34	1.12
1993.15	7.89	0.97	-0.59	0.16	11.53	0.36	47.08	0.88
1994.15	13.46	0.49	-0.40	0.12	14.78	0.33	40.40	0.63
1994.40	9.76	0.73	-1.16	0.12	12.33	0.60	31.15	1.38

1308+326

Epoch	*F (Jy)*	±	α	±	*P (%)*	±	χ (°)	±
1990.12	1.00	0.10	-0.61	0.27				
1992.35	1.09	0.03	-0.66	0.04				
1993.15	1.00	0.10			9.88	2.44	8.10	6.86

1335-127

Epoch	*F (Jy)*	±	α	±	*P (%)*	±	χ (°)	±
1990.12	2.10	0.20	-0.71	0.12				
1992.42	2.80	0.07	-0.53	0.05				
1992.81	2.50	0.23			5.62	0.61	115.89	3.08
1993.15	3.10	0.32	-0.71	0.17	6.16	0.68	119.77	3.16
1994.15	4.12	0.11	-0.14	0.12	2.49	0.71	122.34	7.81
1994.40	3.23	0.25	-0.85	0.12	7.89	2.25	121.18	7.86

1413+135

Epoch	*F (Jy)*	±	α	±	*P (%)*	±	χ (°)	±
1990.12	1.60	0.20	-0.55	0.19				
1992.02	1.59	0.16			3.70	1.08	33.14	8.03
1992.42	0.69	0.01	-0.33	0.08				

1514-241

Epoch	*F (Jy)*	±	α	±	*P (%)*	±	χ (°)	±
1990.12	0.90	0.10	-0.28	0.21				
1992.35	1.10	0.03	-0.24	0.12				
1992.42	1.11	0.03	-0.37	0.11				
1993.15	1.11	0.12	0.05	0.24	5.51	1.64	4.13	8.16

1633+382

Epoch	*F (Jy)*	±	α	±	*P (%)*	±	χ (°)	±
1993.15	0.87	0.09	-1.23	0.19	7.88	2.71	148.47	9.31

1641+399

Epoch	*F (Jy)*	±	α	±	*P (%)*	±	χ (°)	±
1990.12	1.70	0.20	-1.20	0.18				
1990.42	1.61	0.17						
1991.43	5.76	0.65	-0.81	0.48	5.53	0.24	26.68	1.27
1992.02	4.63	0.46	-0.37	0.48	0.71	0.38	47.26	13.58
1992.16	4.54	0.53	-0.35	0.40	2.47	0.35	35.79	4.06
1992.42	4.15	0.19	-0.72	0.04				
1992.81	3.68	0.31			5.19	0.46	57.37	2.52
1993.15	3.17	0.35	-0.82	0.16	2.93	0.97	95.01	9.02
1994.15	2.11	0.06	-0.14	0.14	5.38	1.29	58.83	6.67
1994.40	1.74	0.13	-1.15	0.17	11.23	2.90	60.71	7.16

1741-038

Epoch	*F (Jy)*	±	α	±	*P (%)*	±	χ (°)	±
1992.35	1.42	0.04	-0.75	0.09				
1992.42	1.21	0.03	-0.73	0.14				
1993.15	1.16	0.13			4.59	1.59	125.68	9.38

1749+096

Epoch	*F (Jy)*	±	α	±	*P (%)*	±	χ (°)	±
1990.12	0.71	0.07	-0.74	0.26				
1992.35	1.68	0.04	-0.35	0.09				
1992.42	2.06	0.06	-0.60	0.18				
1992.81	4.62	0.36	-0.49	0.19	3.72	0.39	9.97	2.95
1993.15	4.03	0.41	-0.64	0.17	4.65	0.67	18.70	4.06
1994.15	2.81	0.10						
1994.40	1.88	0.14	-0.54	0.15	8.53	2.84	61.80	9.04

1823+568

Epoch	*F (Jy)*	±	α	±	*P (%)*	±	χ (°)	±
1990.12	1.08	0.03	-0.47	0.14				
1992.81	1.10	0.09			12.81	1.28	39.73	2.86

1921-293

Epoch	*F (Jy)*	±	α	±	*P (%)*	±	χ (°)	±
1991.43	4.70	0.58	-0.44	0.51	9.51	0.33	99.61	0.99
1992.35	6.83	0.19	-0.52	0.08				
1993.15	5.71	0.67	-0.54	0.16	9.68	0.56	124.93	1.64
1994.15	8.15	0.17	-0.63	0.12	6.91	0.99	149.98	4.05
1994.40	8.02	0.61	-0.68	0.12	10.35	1.76	133.50	4.80

2200+420

Epoch	*F (Jy)*	±	α	±	*P (%)*	±	χ (°)	±
1991.43	1.89	0.22			8.10	0.65	23.36	2.30
1992.02	1.06	0.11			8.09	1.22	167.70	4.26
1992.35	1.89	0.05	-0.24	0.07				
1992.81	1.95	0.16	-0.40	0.15	10.17	0.85	48.22	2.38
1993.15	2.11	0.22	-0.31	0.16	7.24	1.30	20.10	5.08
1994.15	0.98	0.04	-1.45	0.17	11.80	3.55	18.57	8.26

2223-052

Epoch	*F (Jy)*	±	α	±	*P (%)*	±	χ (°)	±
1990.42	4.54	0.45			3.81	0.88	27.46	6.42
1991.43	2.04	0.26						
1992.35	1.30	0.03	-0.58	0.04				
1992.81	1.11	0.10	-0.74	0.16	2.20	0.94	169.32	11.26
1994.15	0.81	0.02						

2251+158

Epoch	*F (Jy)*	±	α	±	*P (%)*	±	χ (°)	±
1990.42	4.33	0.44	-0.20	0.46	4.51	0.34	109.46	2.12
1991.43	3.83	0.42	-1.38	0.47	2.88	0.26	15.13	2.55
1992.16	3.84	0.48	-1.85	0.42	3.71	0.38	7.94	2.93
1992.35	5.46	0.14	-0.46	0.11				
1992.81	4.03	0.32	-0.59	0.16	3.13	0.44	136.30	3.98
1993.15	4.73	0.52	-0.69	0.16	5.03	0.56	157.42	3.15
1994.15	6.67	0.17	-0.59	0.11	8.25	1.23	82.62	4.21

Appendix C

Graphical Representation of the 1100 μm Database

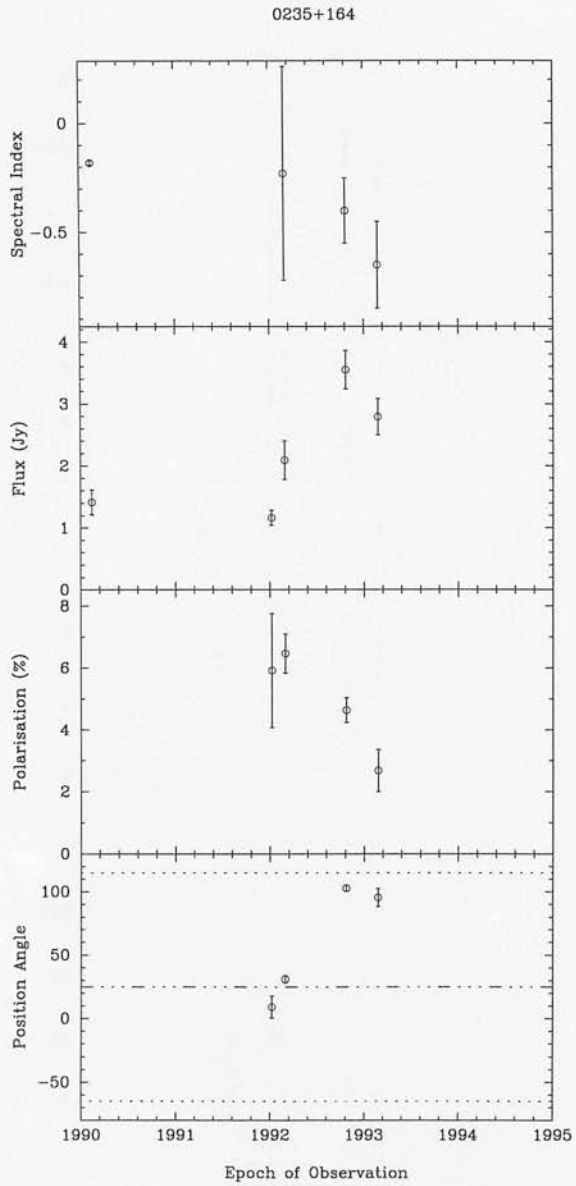
0235+164
Spectral Index
Flux (Jy)
Polarisation (%)
Position Angle
Epoch of Observation

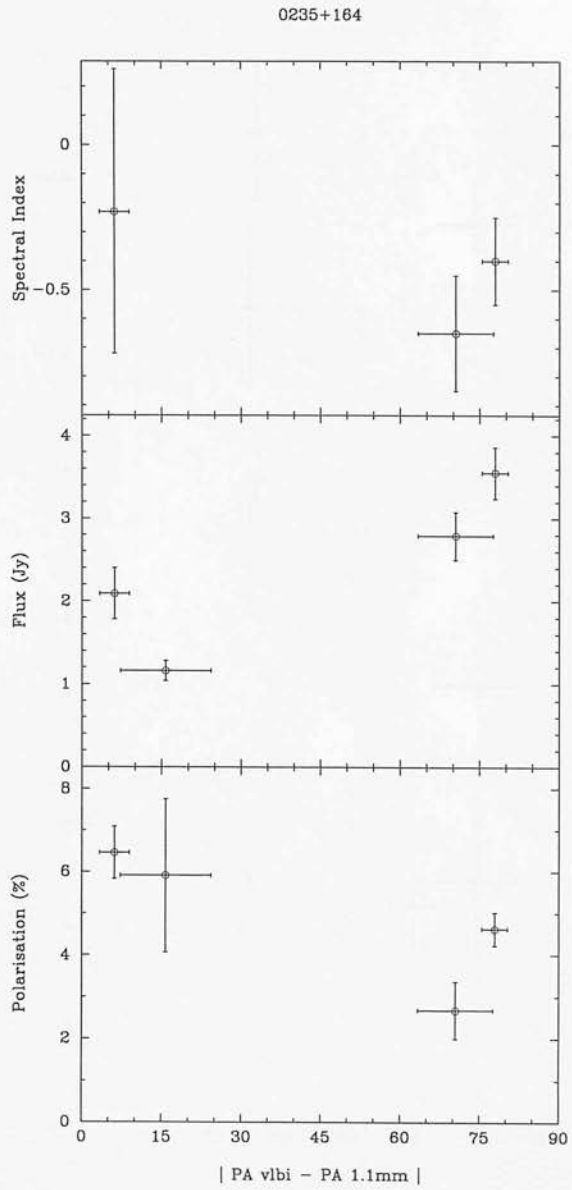
0235+164
Spectral Index
Flux (Jy)
Polarisation (%)
| PA vlbi − PA 1.1mm |

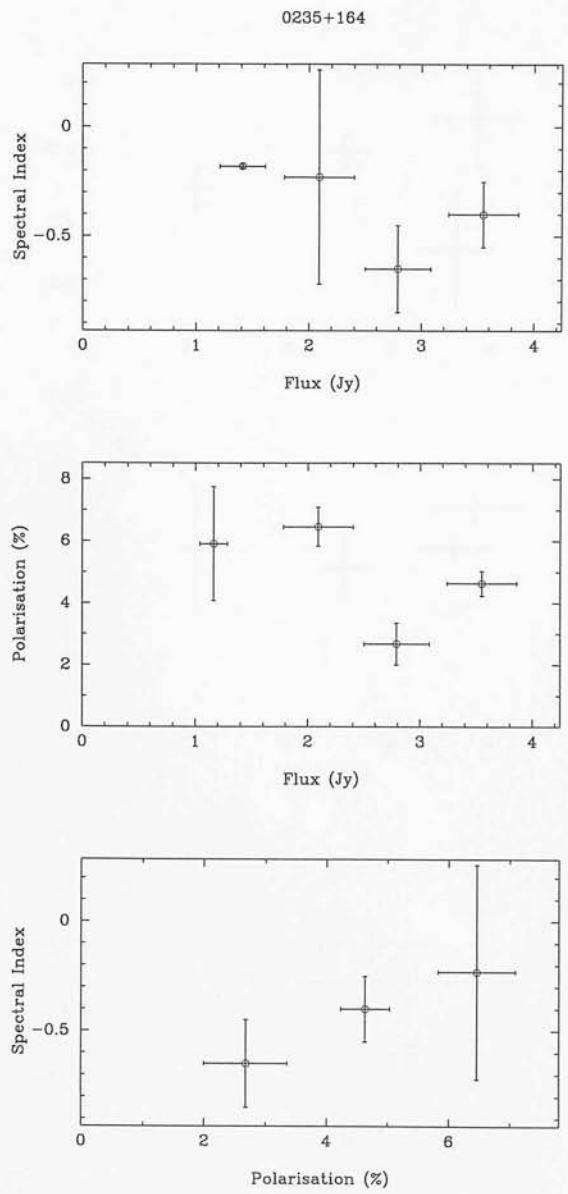
0235+164
Spectral Index
Flux (Jy)
Polarisation (%)
Flux (Jy)
Spectral Index
Polarisation (%)

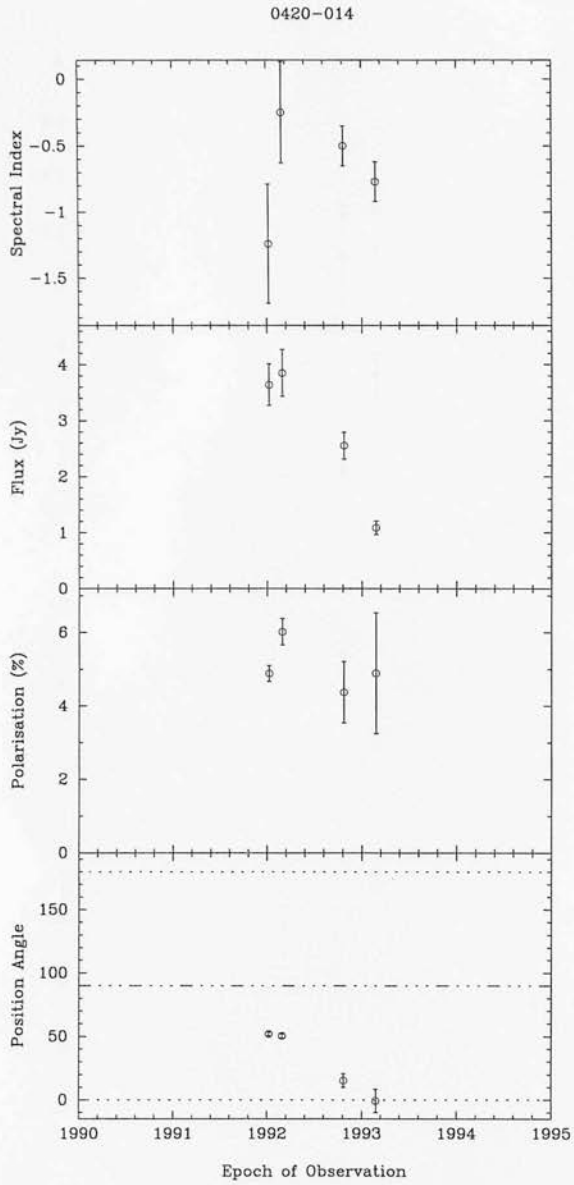
0420−014
Spectral Index
Flux (Jy)
Polarisation (%)
Position Angle
1990
1991
1992
1993
1994
1995
Epoch of Observation

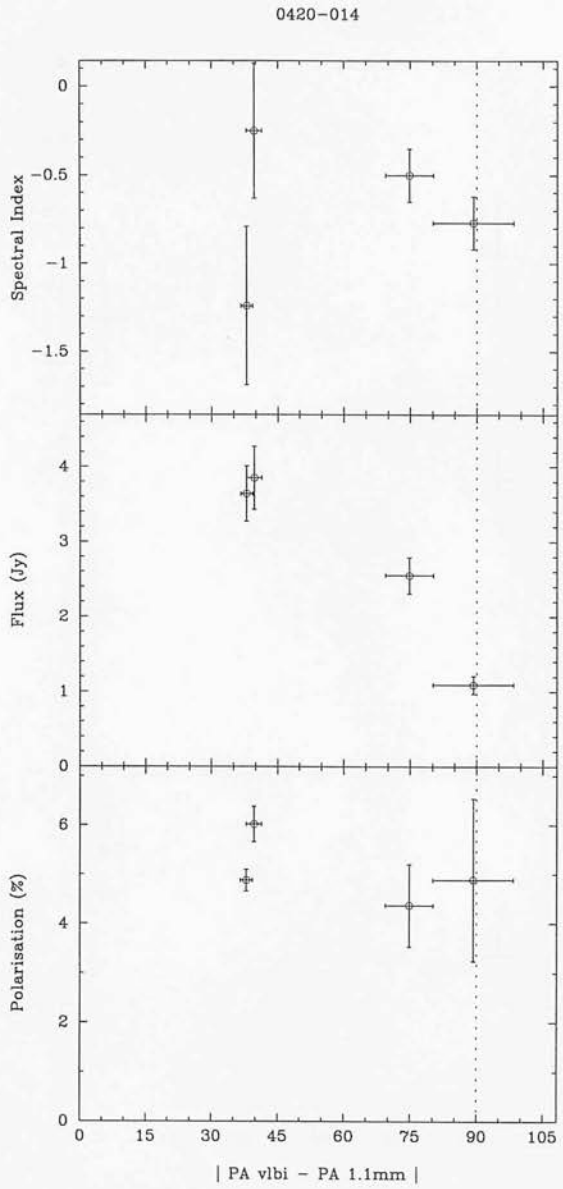
0420−014
Spectral Index
Flux (Jy)
Polarisation (%)
| PA vlbi − PA 1.1mm |

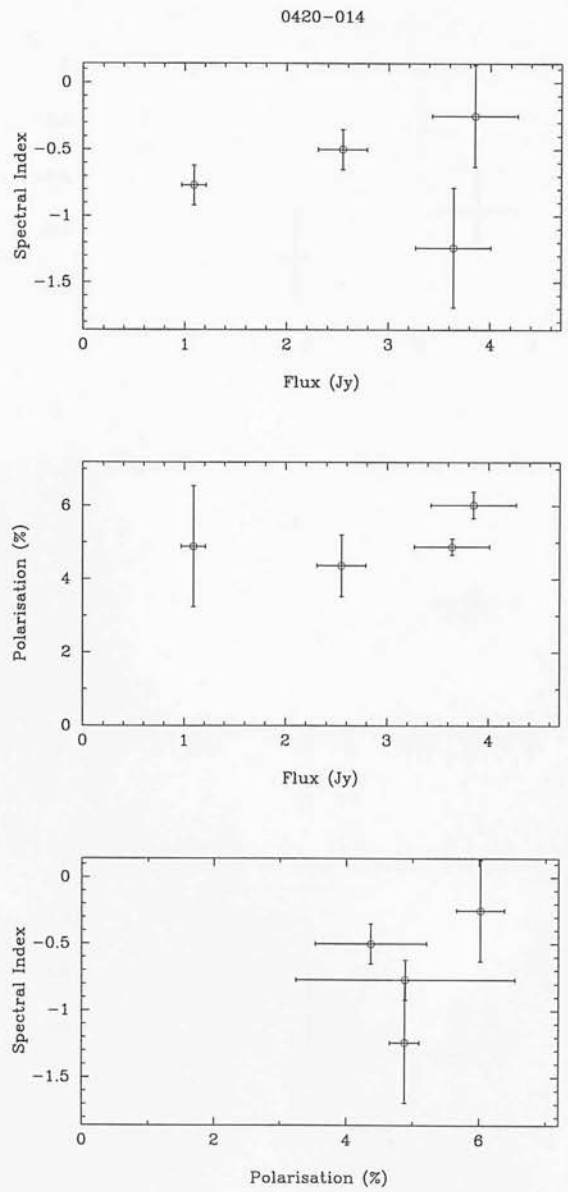
0420−014
Spectral Index
Flux (Jy)
Polarisation (%)
Flux (Jy)
Spectral Index
Polarisation (%)

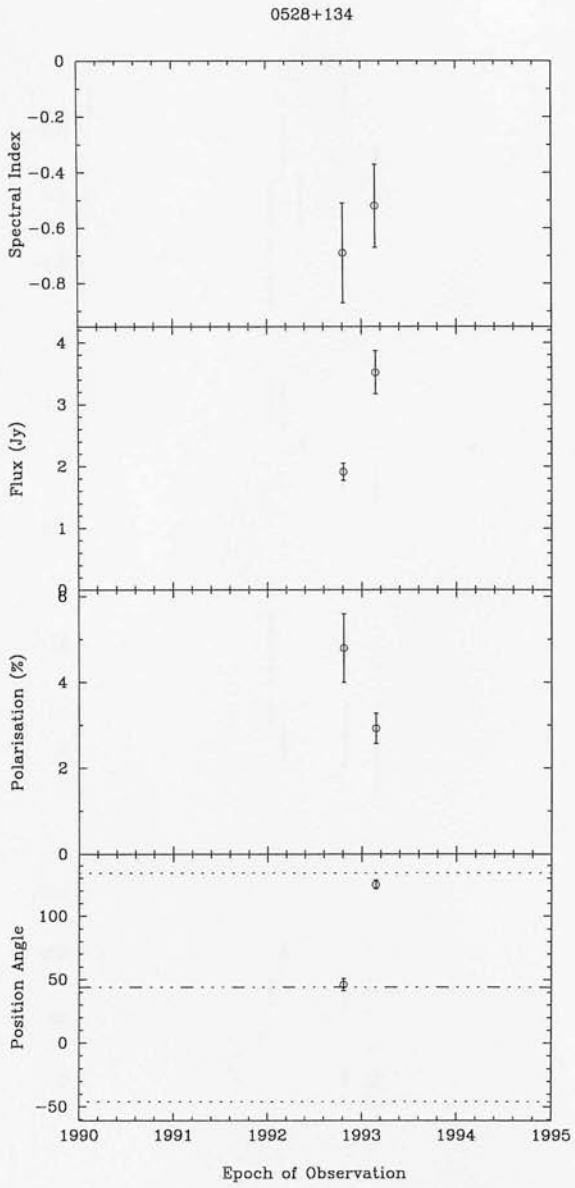
0528+134
Spectral Index
Flux (Jy)
Polarisation (%)
Position Angle
Epoch of Observation

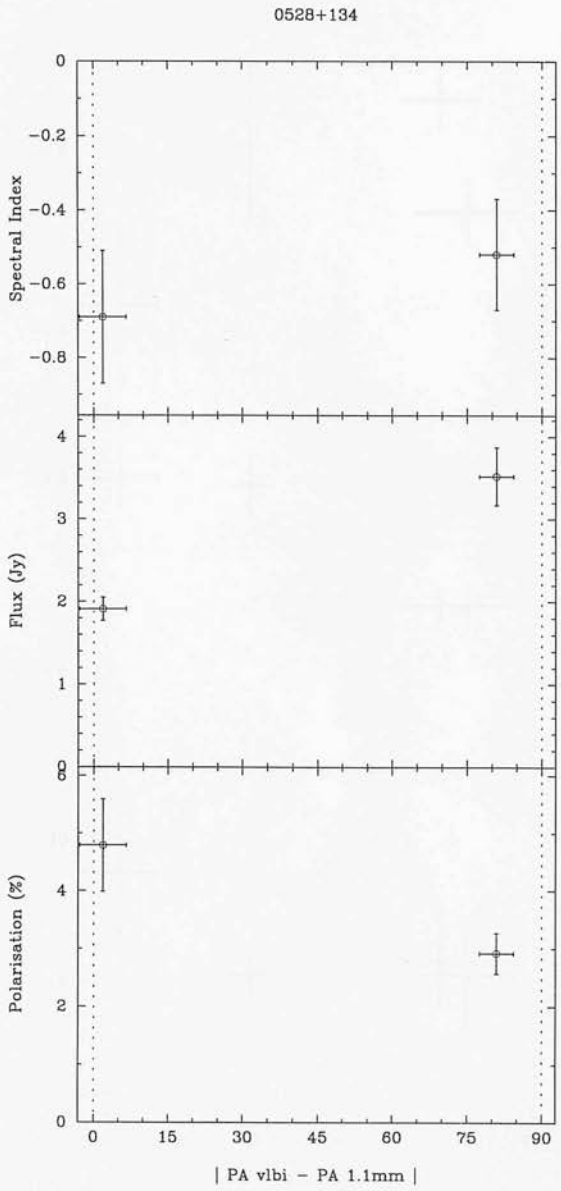
0528+134
Spectral Index
Flux (Jy)
Polarisation (%)
| PA vlbi − PA 1.1mm |

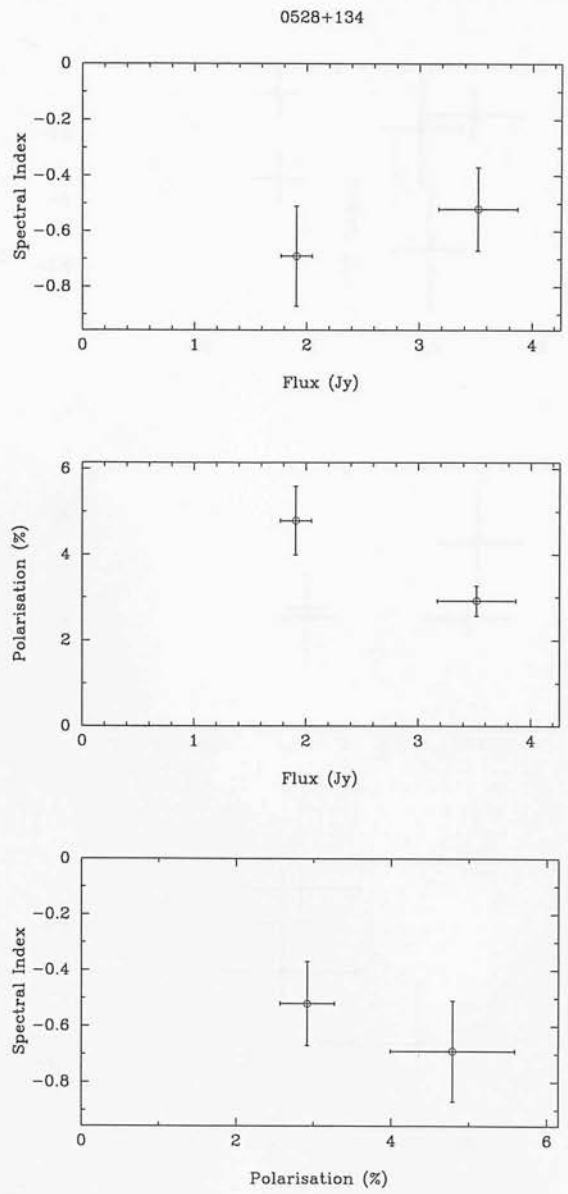
0528+134
Spectral Index
Flux (Jy)
Polarisation (%)
Flux (Jy)
Spectral Index
Polarisation (%)

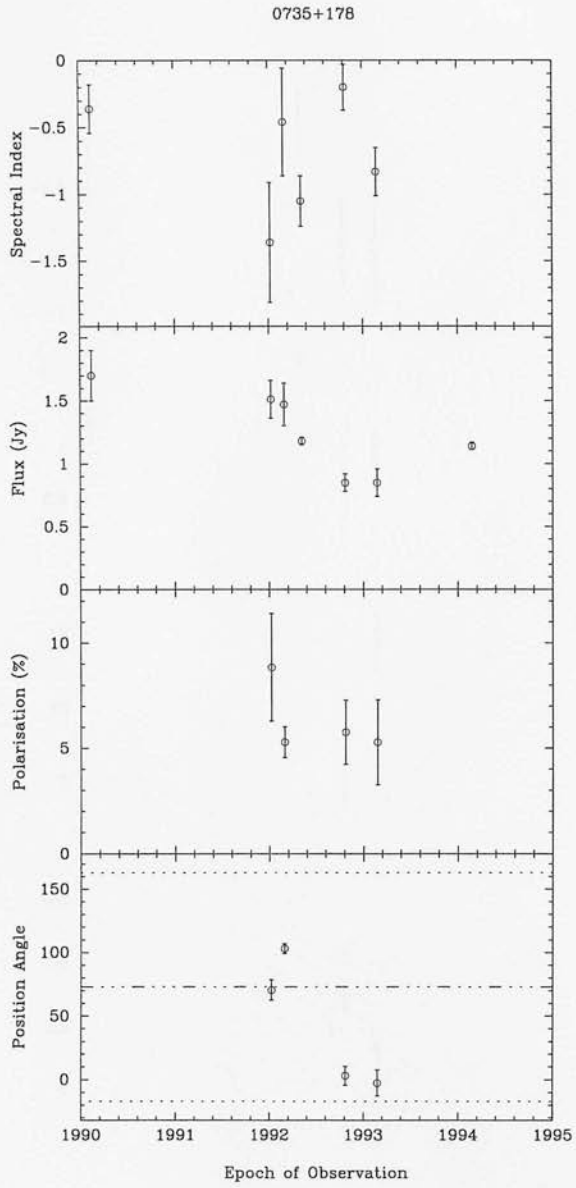
0735+178
Spectral Index
Flux (Jy)
Polarisation (%)
Position Angle
Epoch of Observation

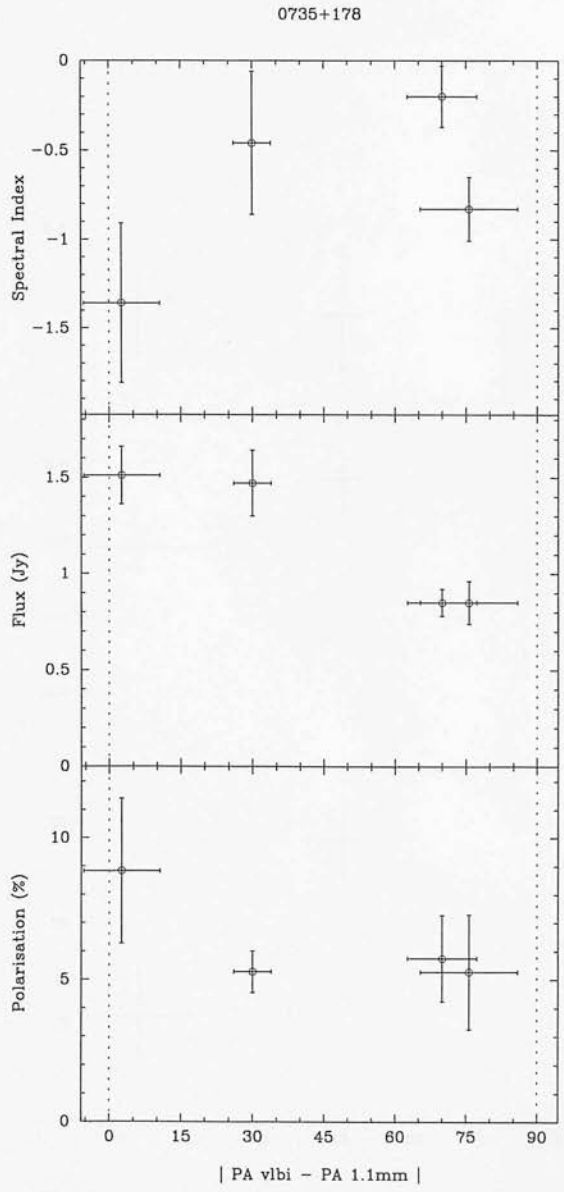
0735+178
Spectral Index
Flux (Jy)
Polarisation (%)
| PA vlbi − PA 1.1mm |

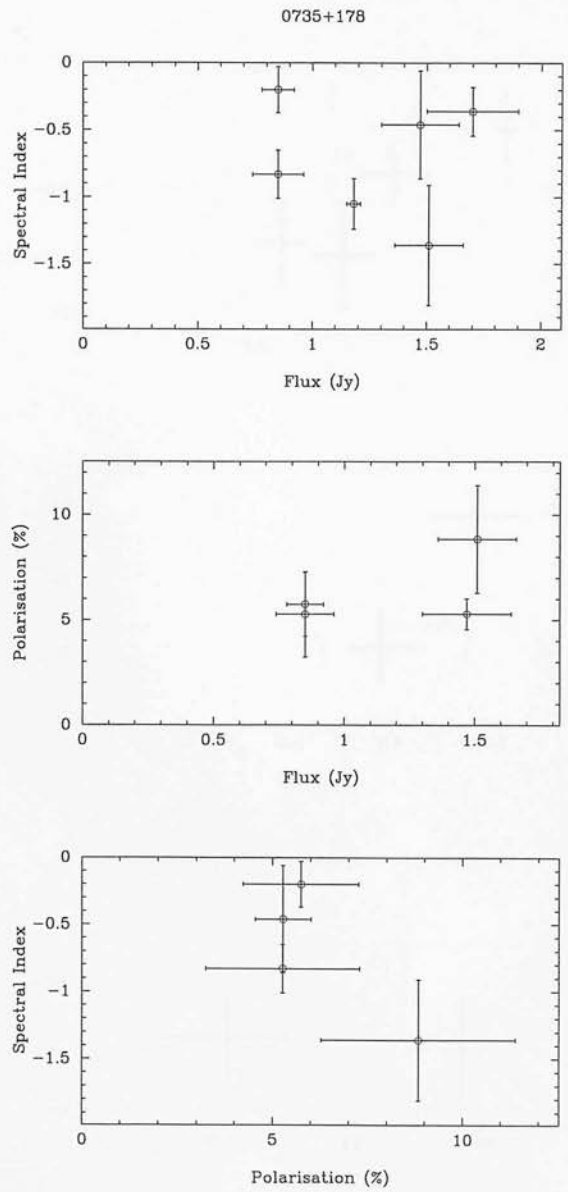
0735+178
Spectral Index
Flux (Jy)
Polarisation (%)
Flux (Jy)
Spectral Index
Polarisation (%)

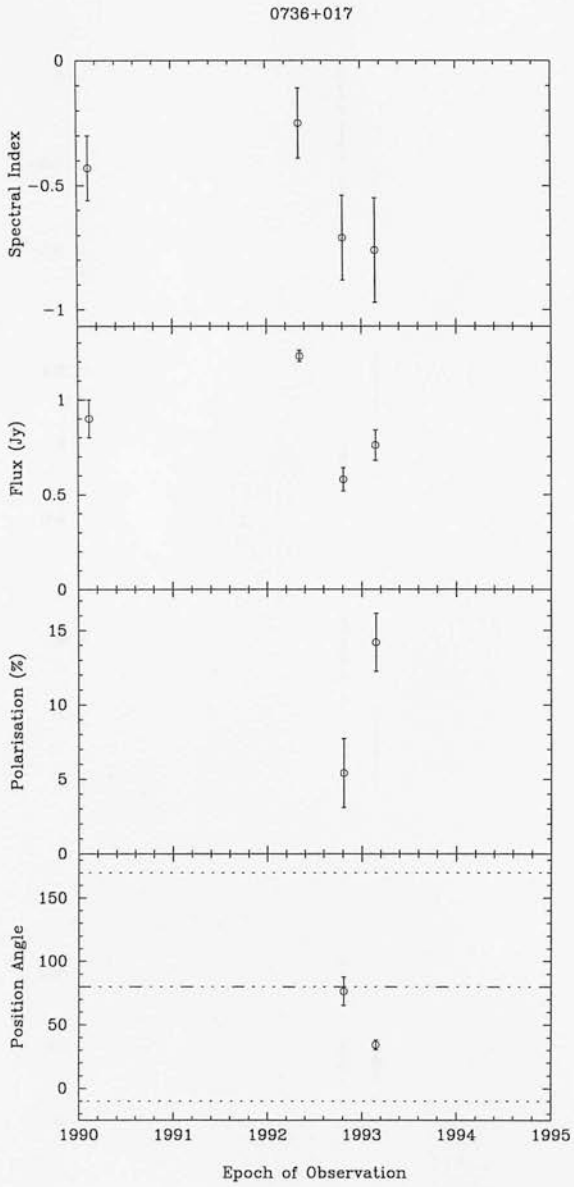
0736+017
Spectral Index
Flux (Jy)
Polarisation (%)
Position Angle
Epoch of Observation

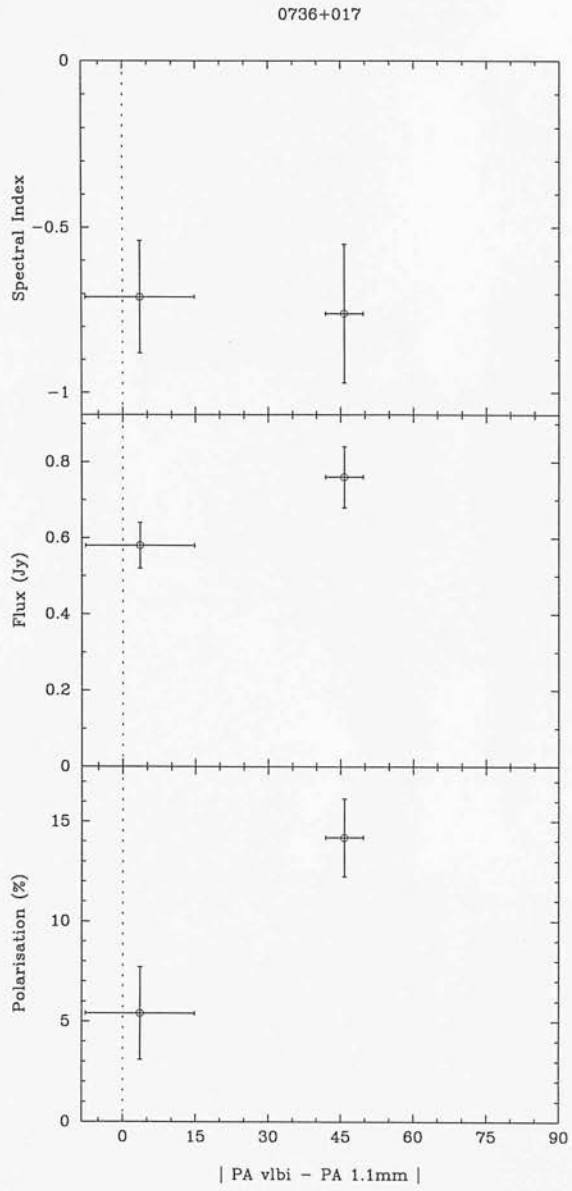
0736+017
Spectral Index
Flux (Jy)
Polarisation (%)
| PA vlbi − PA 1.1mm |

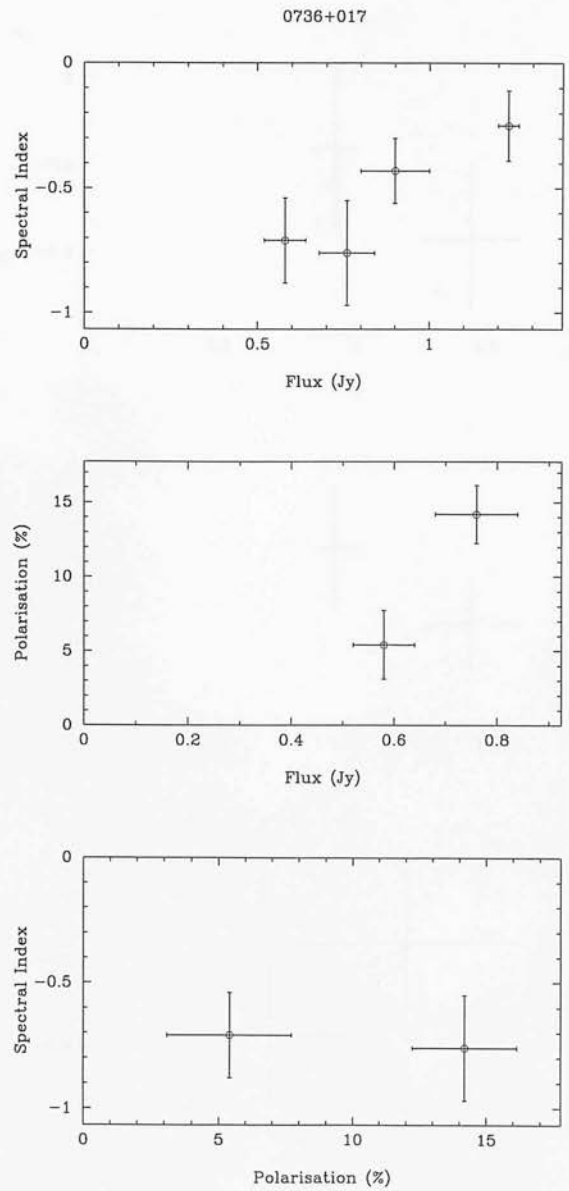
0736+017
Spectral Index
Flux (Jy)
Polarisation (%)
Flux (Jy)
Spectral Index
Polarisation (%)

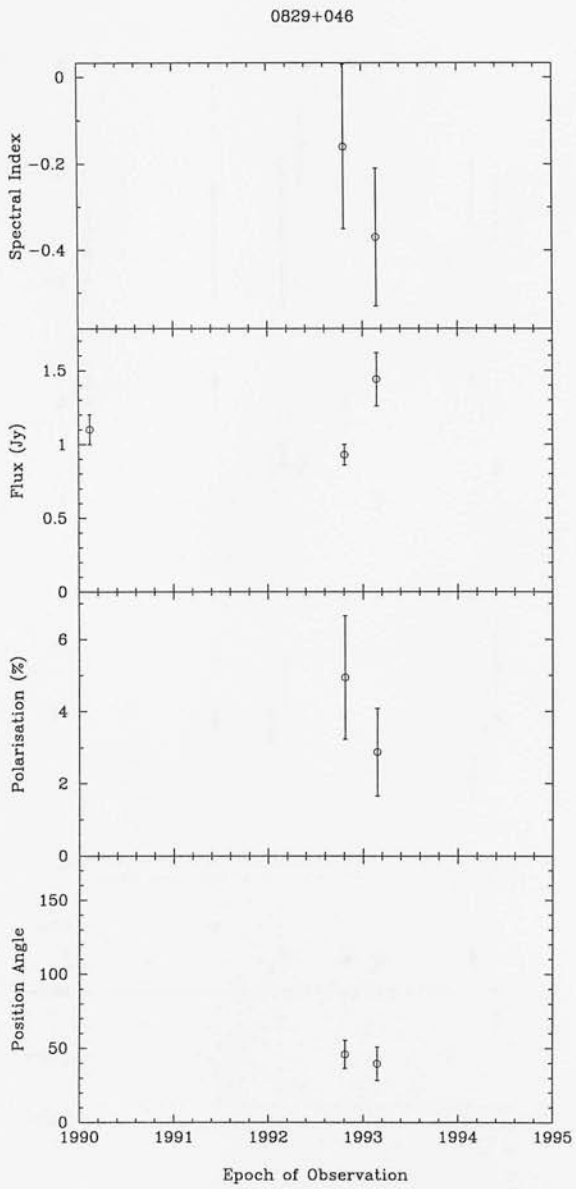
0829+046
Spectral Index
Flux (Jy)
Polarisation (%)
Position Angle
Epoch of Observation
1990
1991
1992
1993
1994
1995

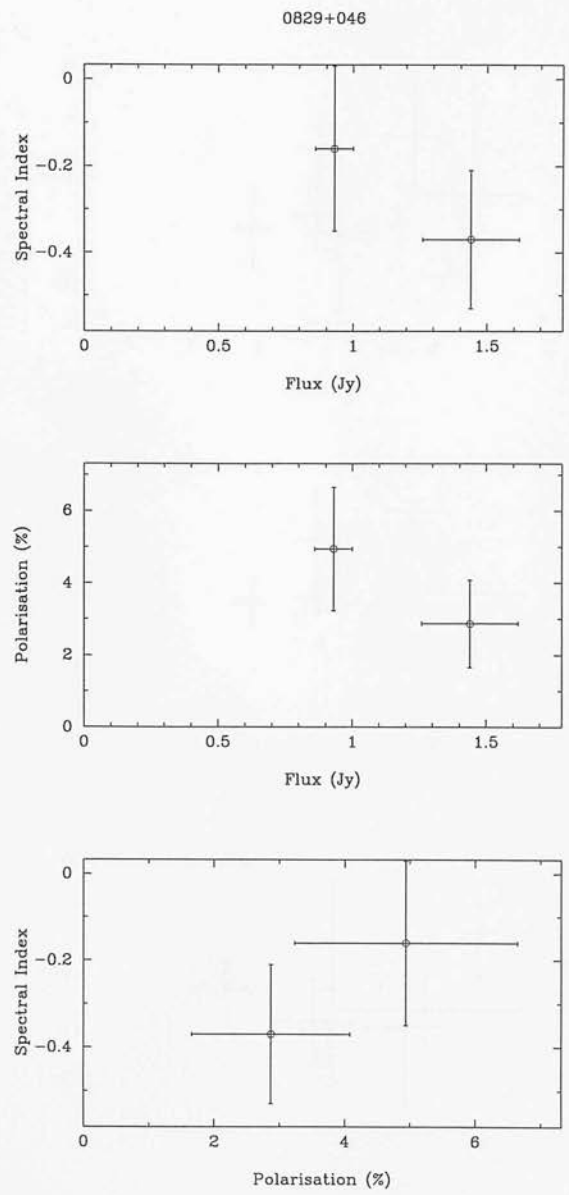
0829+046
Spectral Index
Flux (Jy)
Polarisation (%)
Spectral Index
Flux (Jy)
Spectral Index
Polarisation (%)

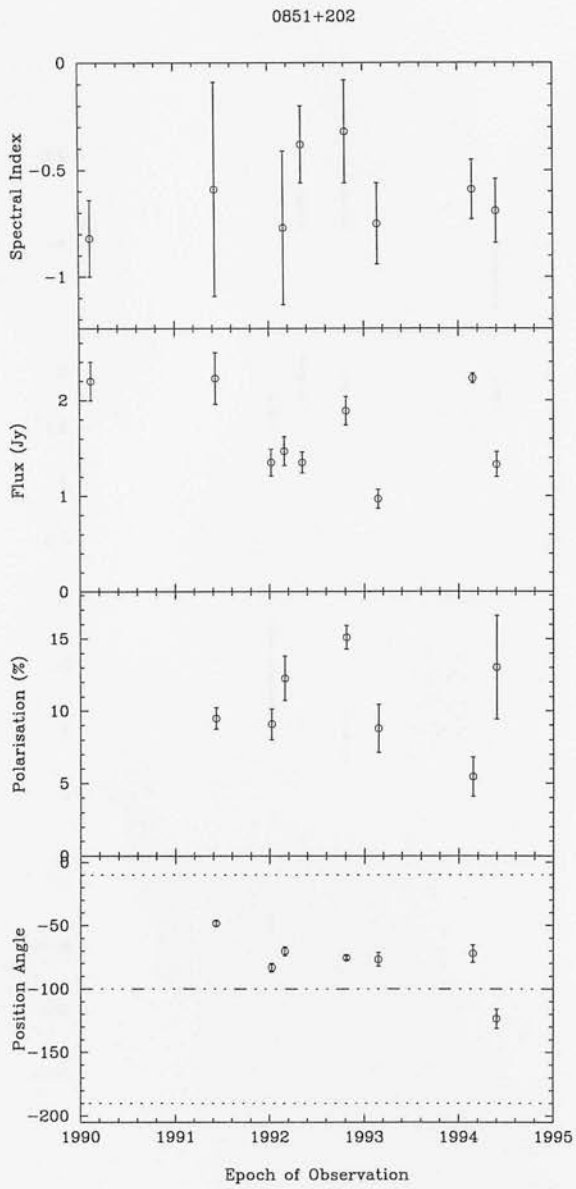
0851+202
Spectral Index
Flux (Jy)
Polarisation (%)
Position Angle
Epoch of Observation

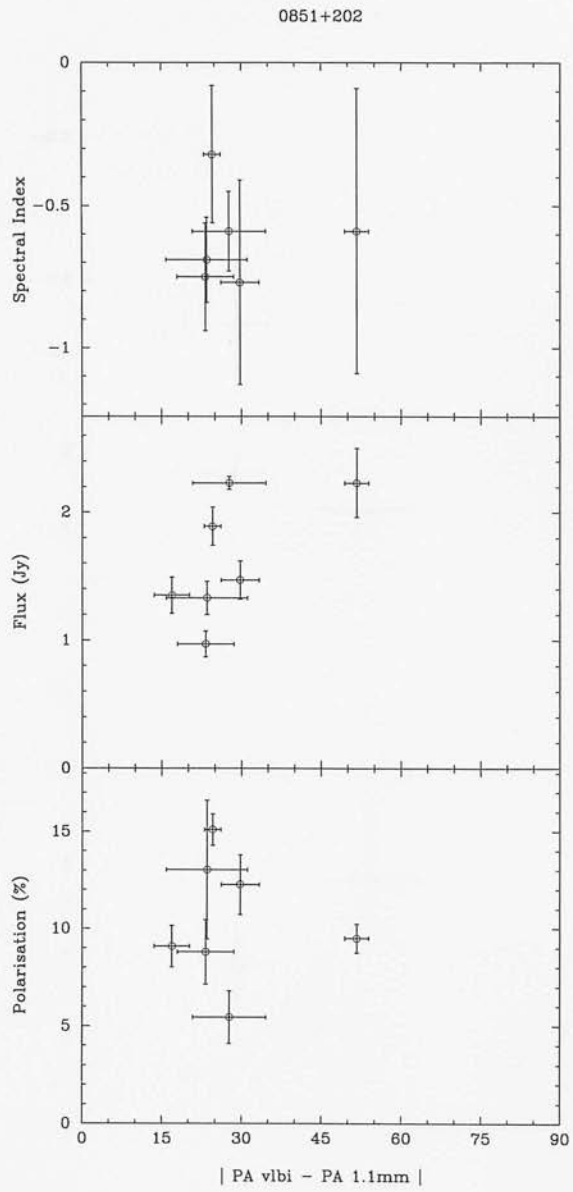
0851+202
Spectral Index
Flux (Jy)
Polarisation (%)
| PA vlbi − PA 1.1mm |

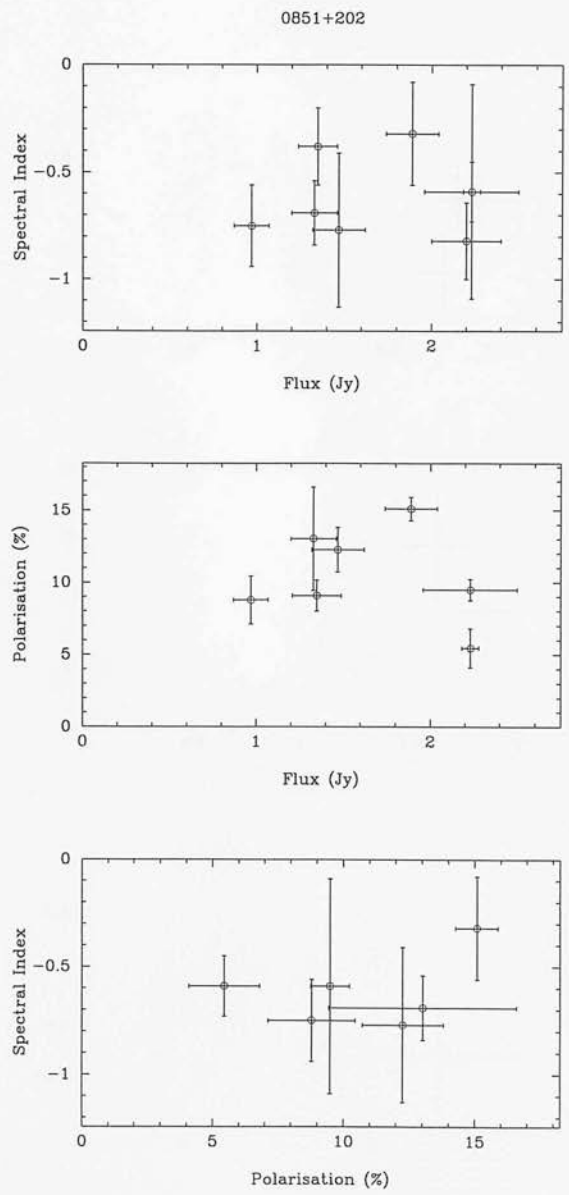
0851+202
Spectral Index
Flux (Jy)
Polarisation (%)
Flux (Jy)
Spectral Index
Polarisation (%)

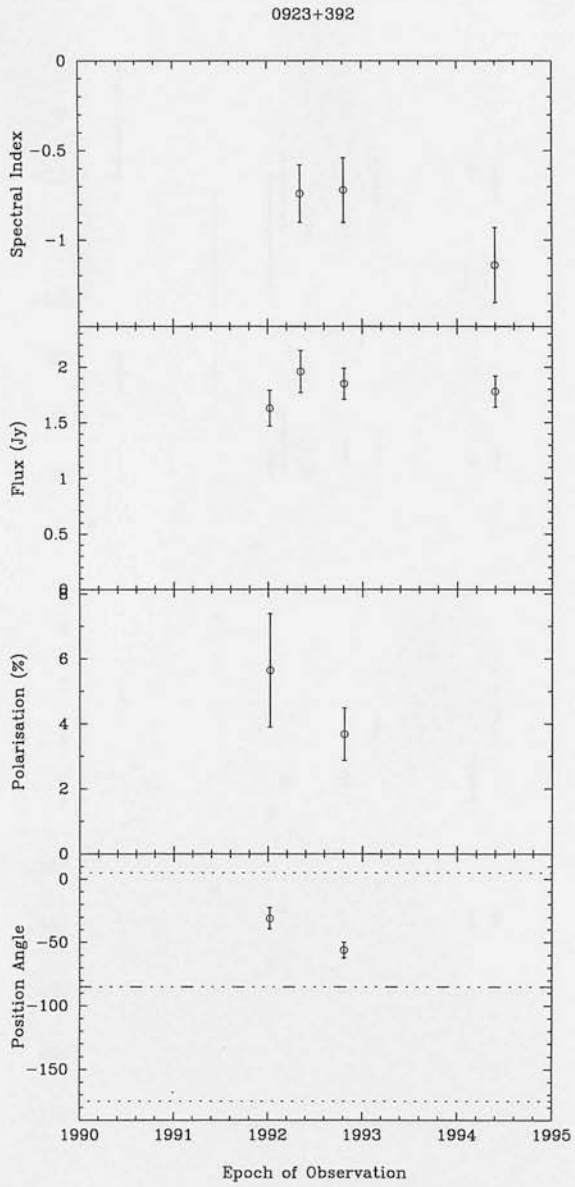
0923+392
Spectral Index
Flux (Jy)
Polarisation (%)
Position Angle
Epoch of Observation

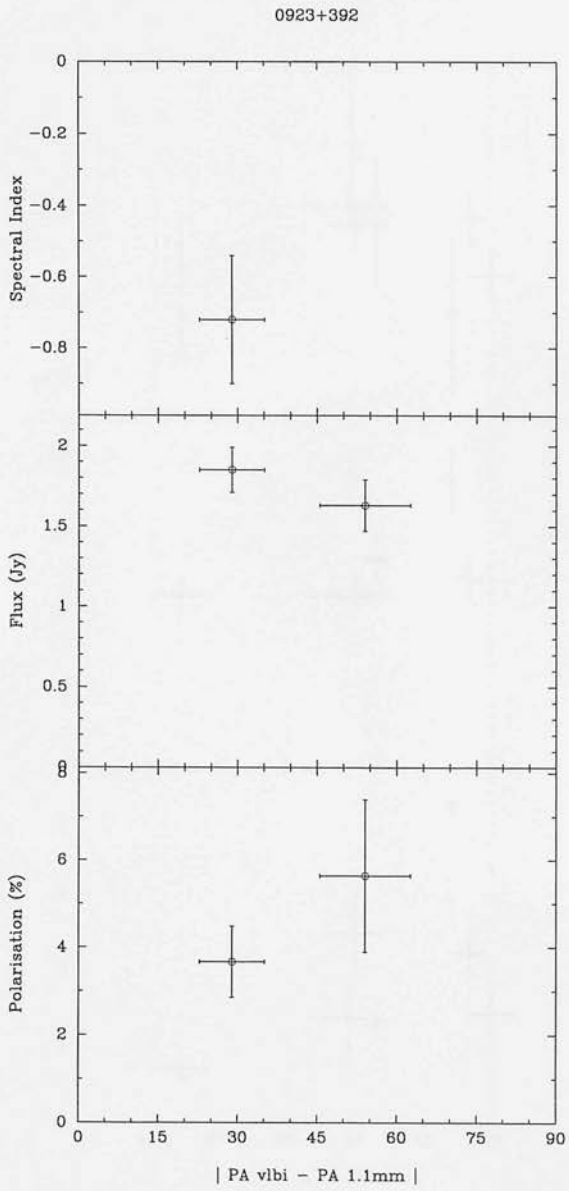
0923+392
Spectral Index
Flux (Jy)
Polarisation (%)
| PA vlbi − PA 1.1mm |

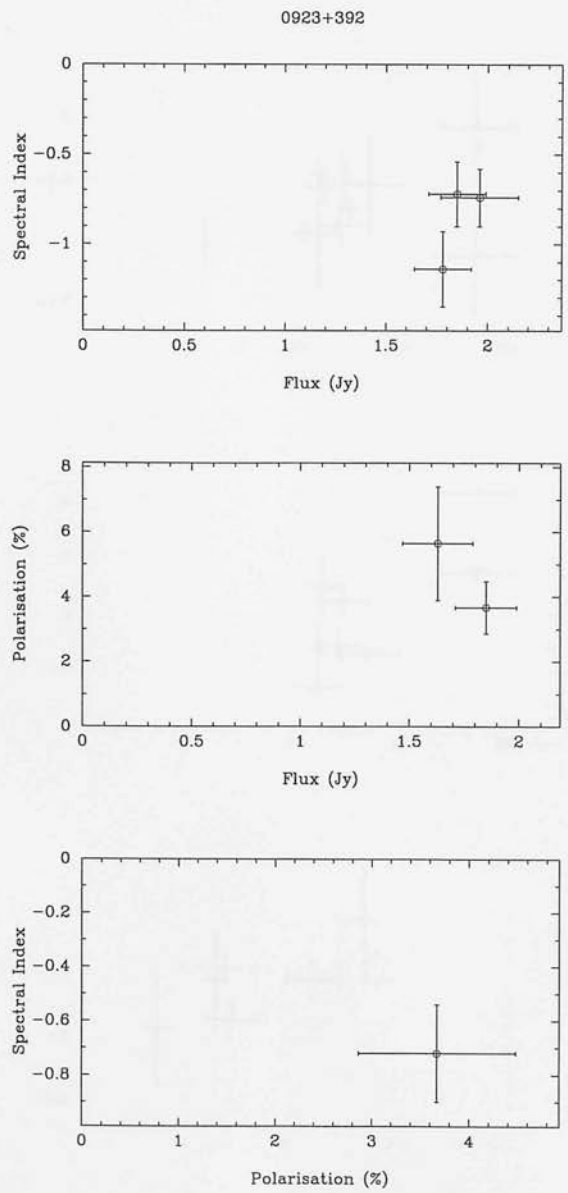
0923+392
Spectral Index
Flux (Jy)
Polarisation (%)
Flux (Jy)
Spectral Index
Polarisation (%)

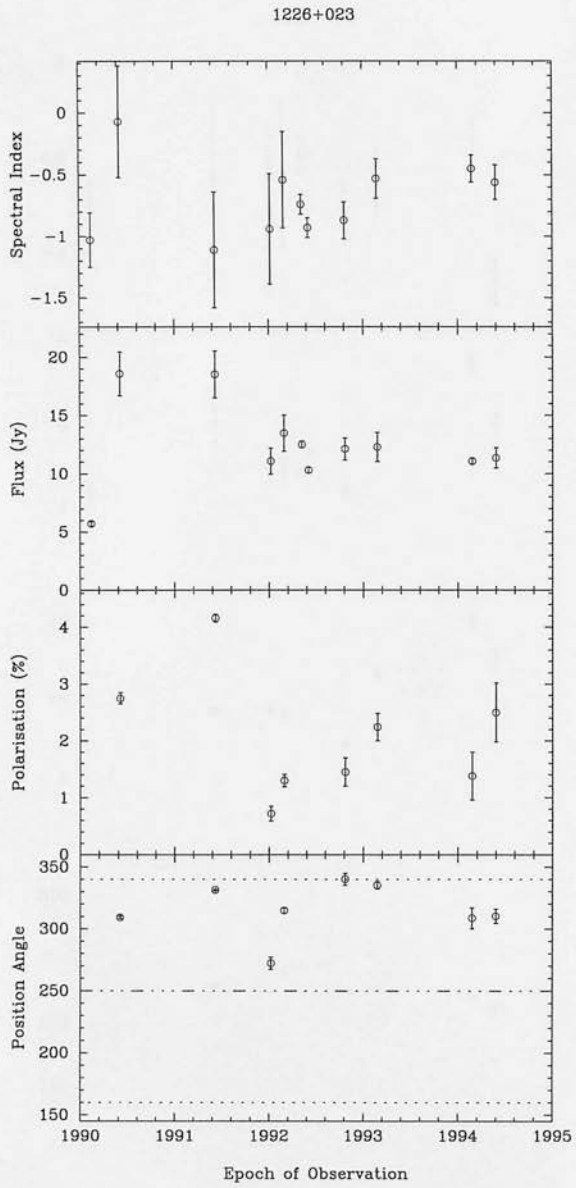
1226+023
Spectral Index
Flux (Jy)
Polarisation (%)
Position Angle
Epoch of Observation

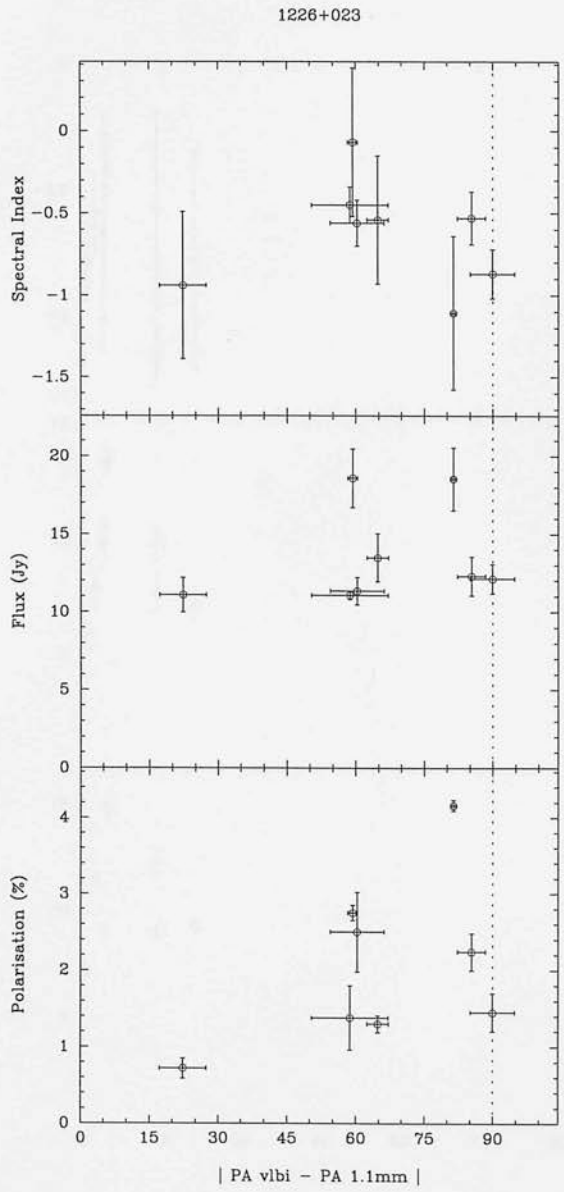
1226+023
Spectral Index
Flux (Jy)
Polarisation (%)
| PA vlbi − PA 1.1mm |

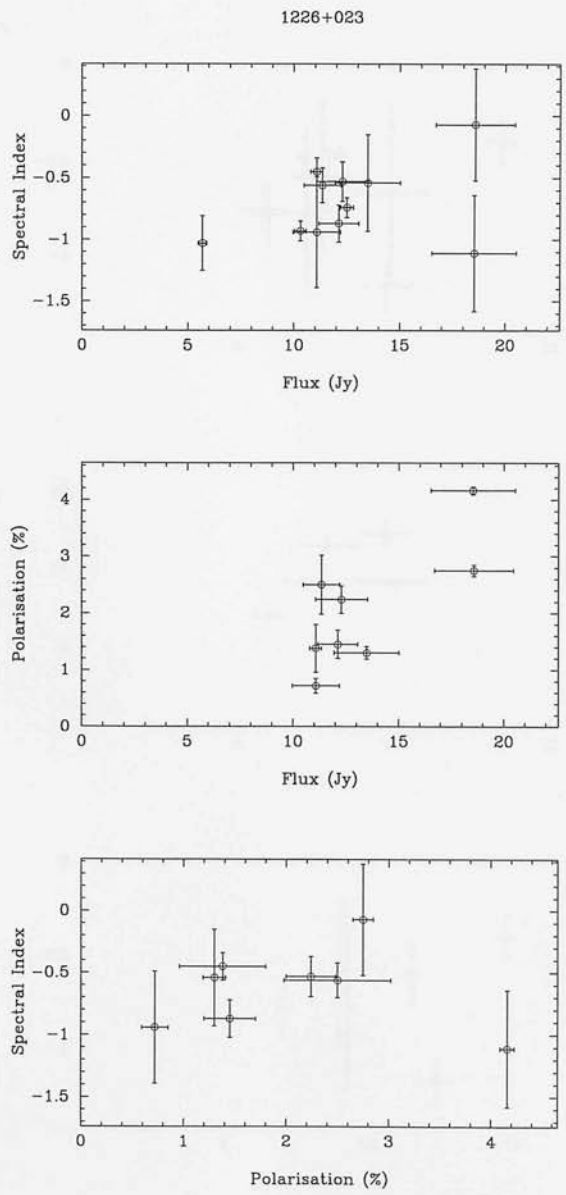
1226+023
Spectral Index
Flux (Jy)
Polarisation (%)
Flux (Jy)
Spectral Index
Polarisation (%)

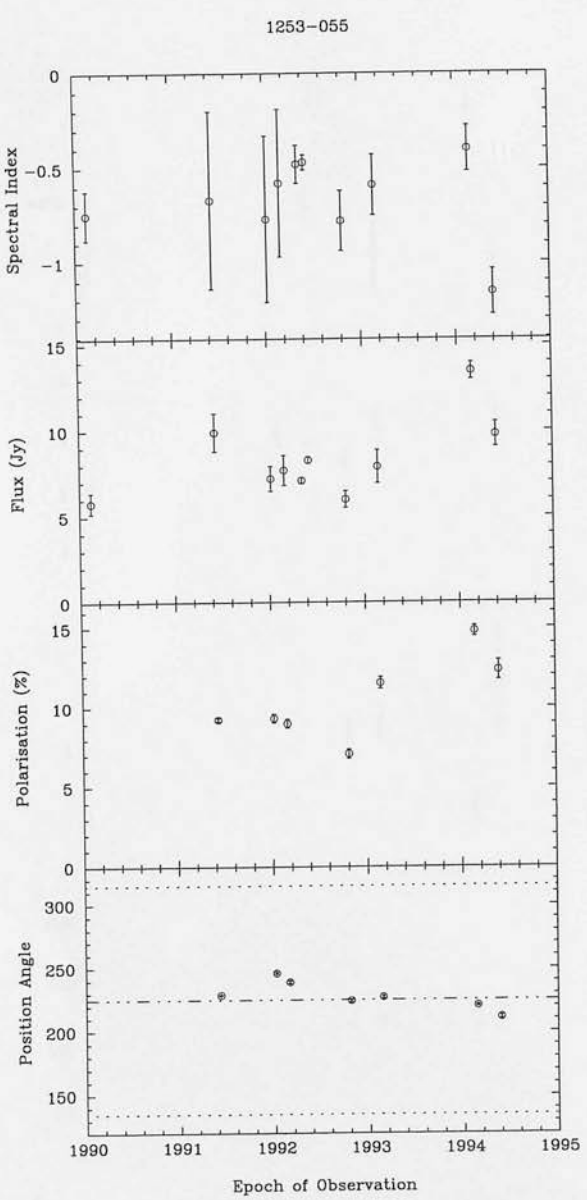
1253−055
Spectral Index
Flux (Jy)
Polarisation (%)
Position Angle
Epoch of Observation

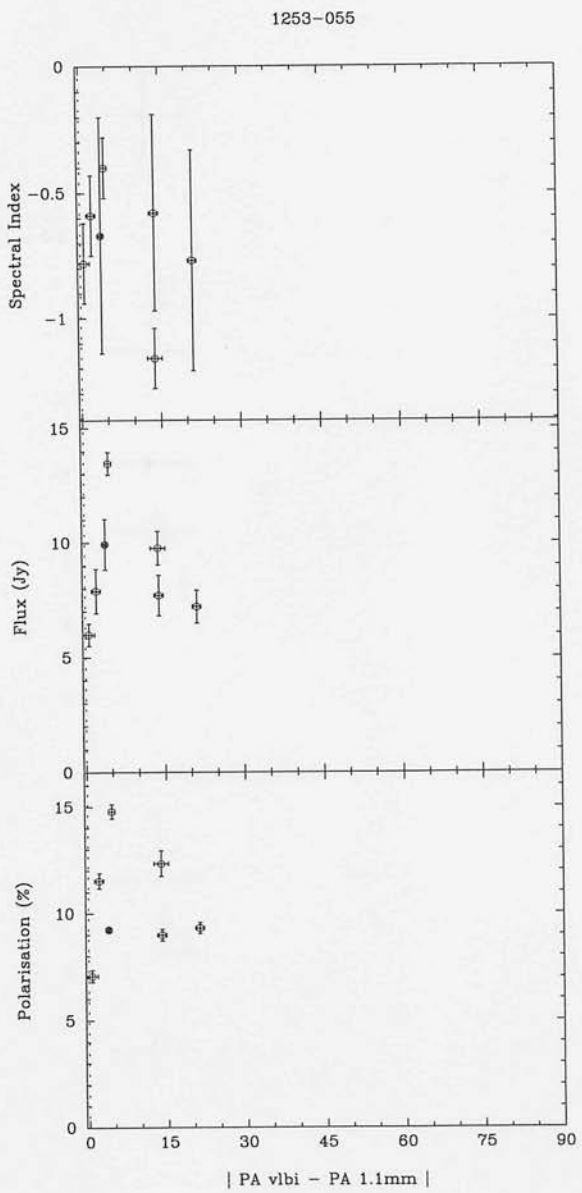
1253−055
Spectral Index
Flux (Jy)
Polarisation (%)
| PA vlbi − PA 1.1mm |

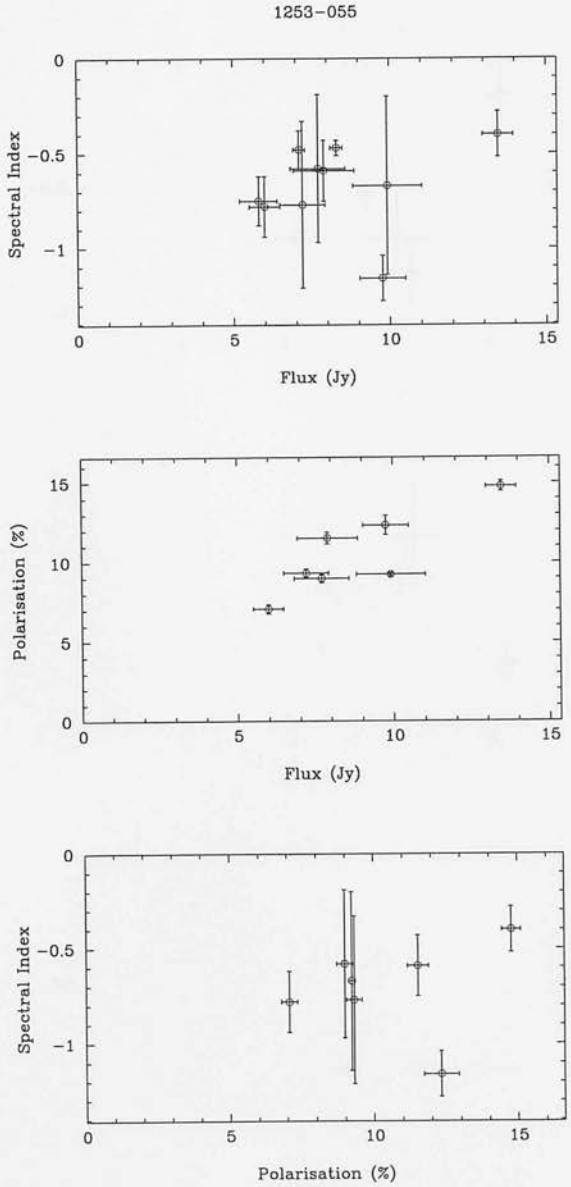
1253−055
Spectral Index
Flux (Jy)
Polarisation (%)
Flux (Jy)
Spectral Index
Polarisation (%)

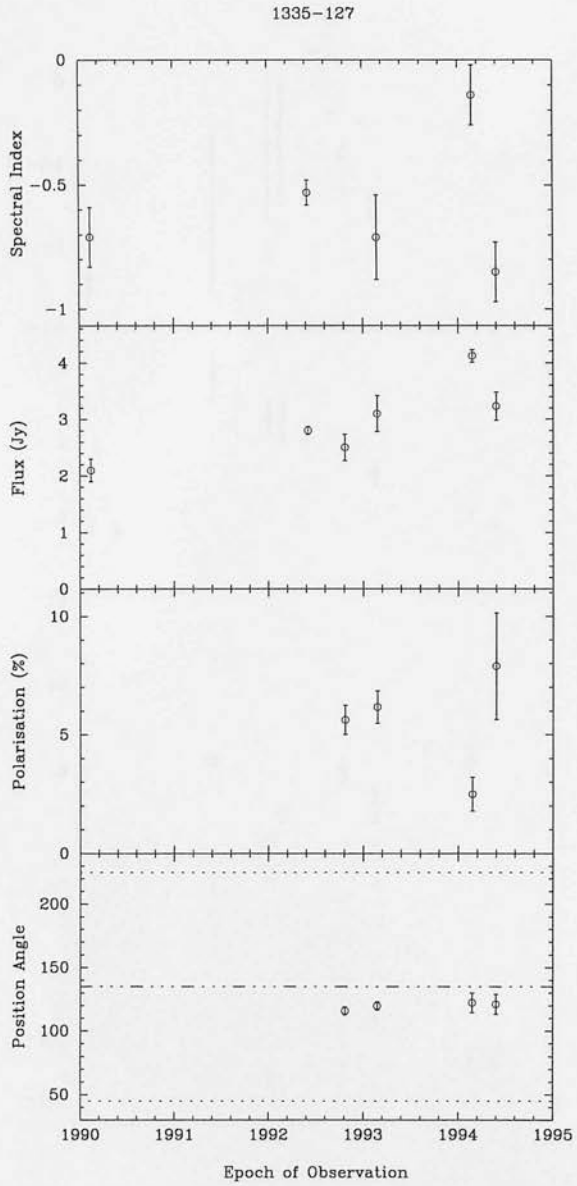
1335−127
Spectral Index
Flux (Jy)
Polarisation (%)
Position Angle
Epoch of Observation

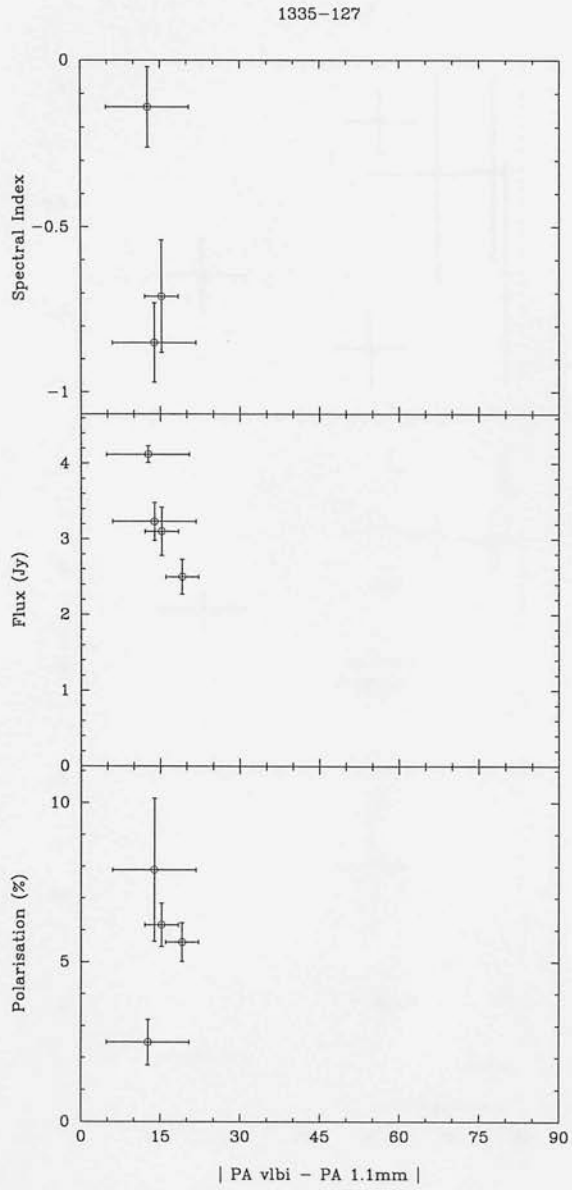
1335−127
Spectral Index
Flux (Jy)
Polarisation (%)
| PA vlbi − PA 1.1mm |

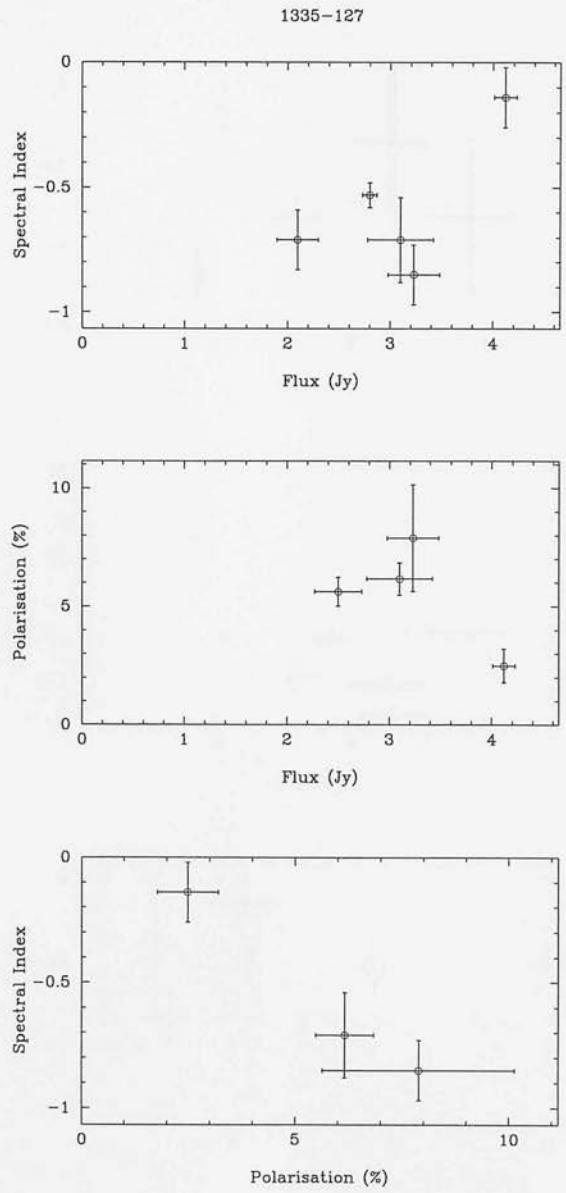
1335−127
Spectral Index
Flux (Jy)
Polarisation (%)
Flux (Jy)
Spectral Index
Polarisation (%)

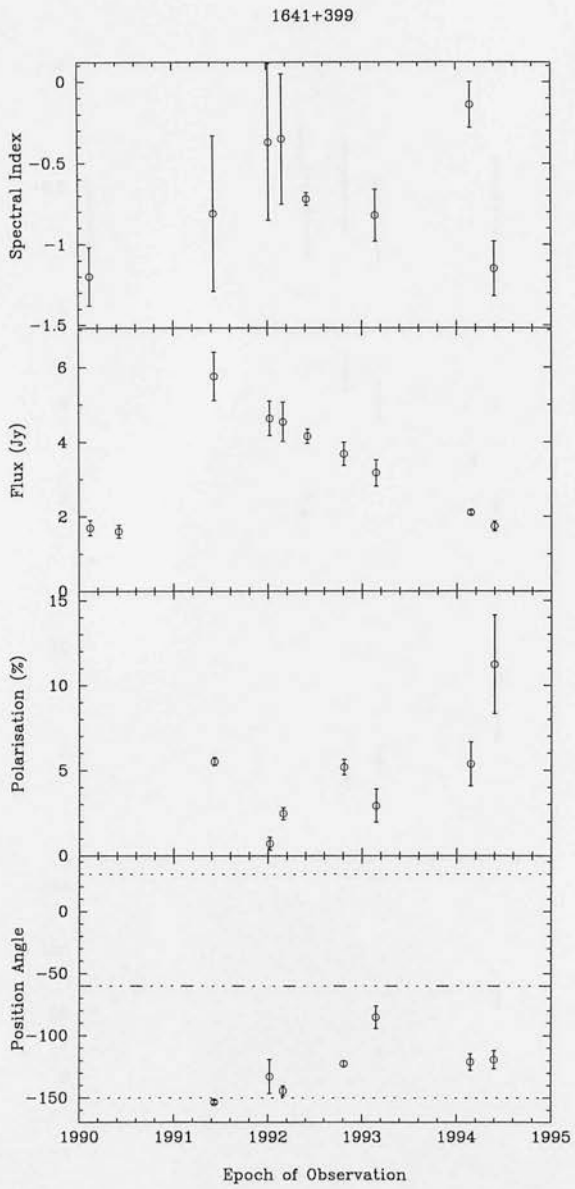
1641+399
Spectral Index
Flux (Jy)
Polarisation (%)
Position Angle
Epoch of Observation

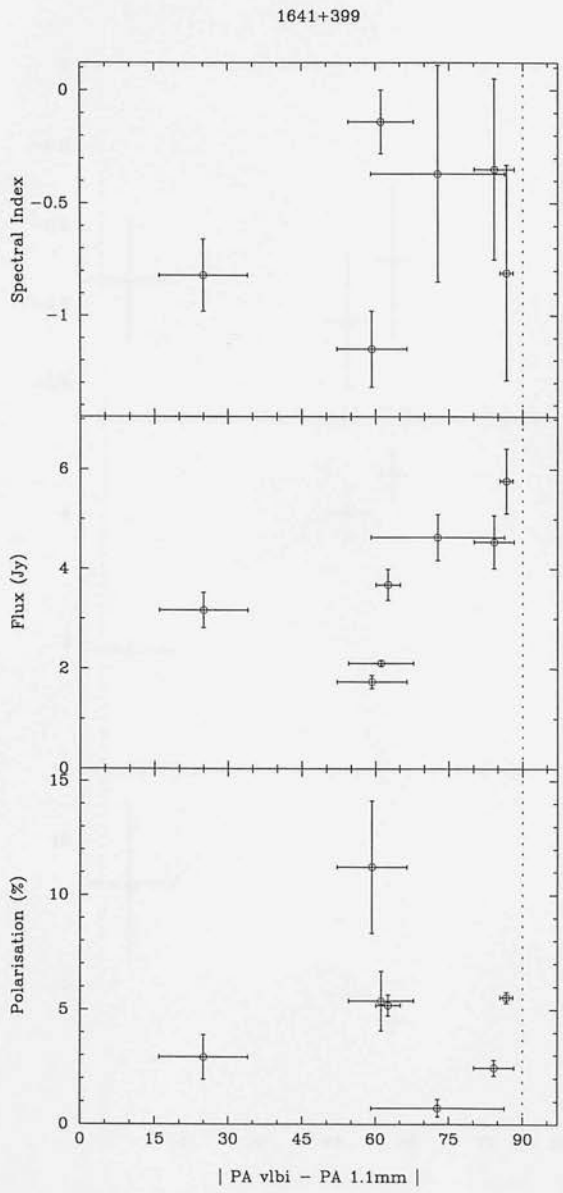
1641+399
Spectral Index
Flux (Jy)
Polarisation (%)
| PA vlbi − PA 1.1mm |

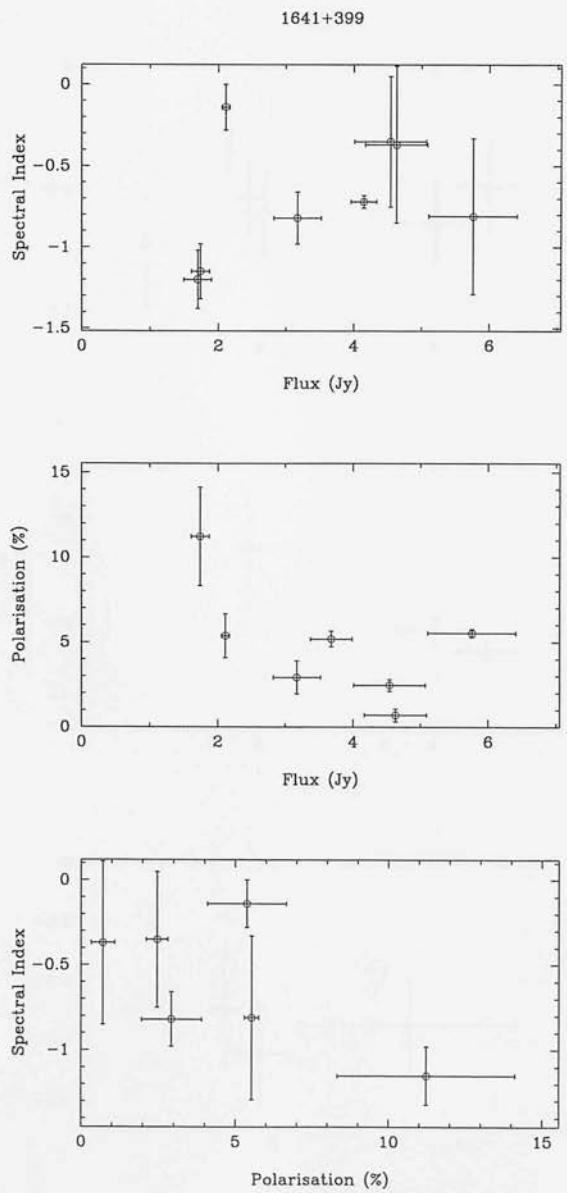
1641+399
Spectral Index
Flux (Jy)
Polarisation (%)
Flux (Jy)
Spectral Index
Polarisation (%)

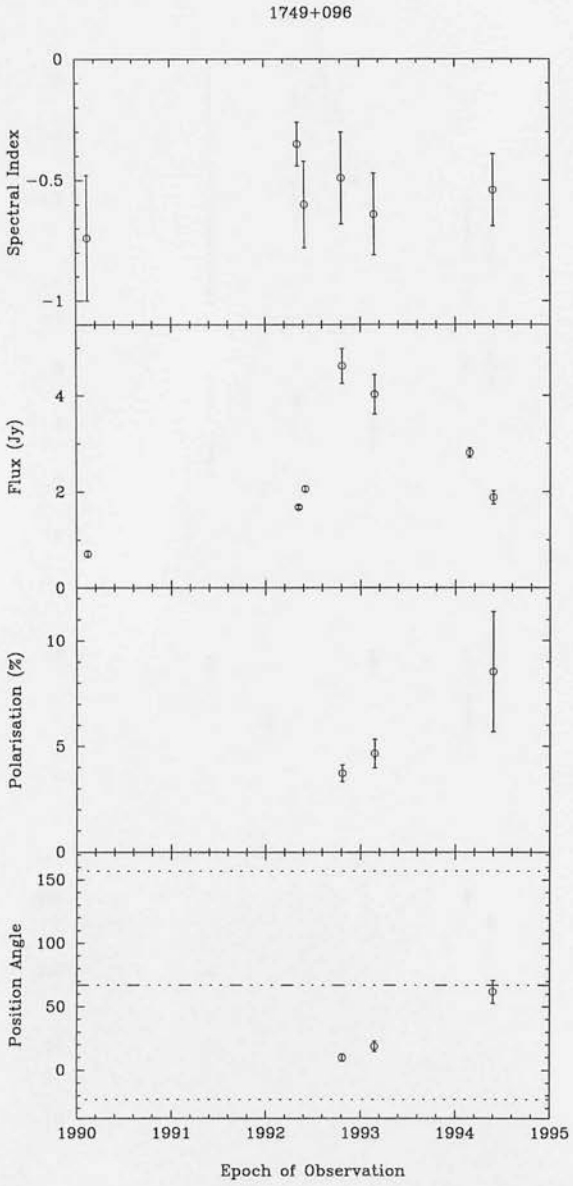
1749+096
Spectral Index
Flux (Jy)
Polarisation (%)
Position Angle
Epoch of Observation

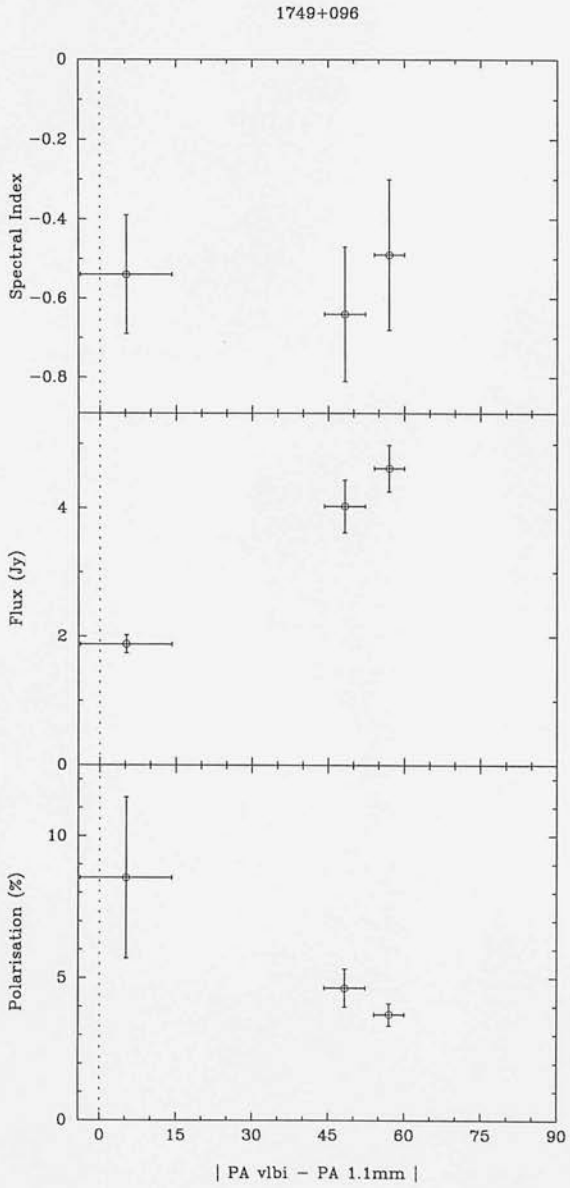
1749+096
Spectral Index
Flux (Jy)
Polarisation (%)
| PA vlbi − PA 1.1mm |

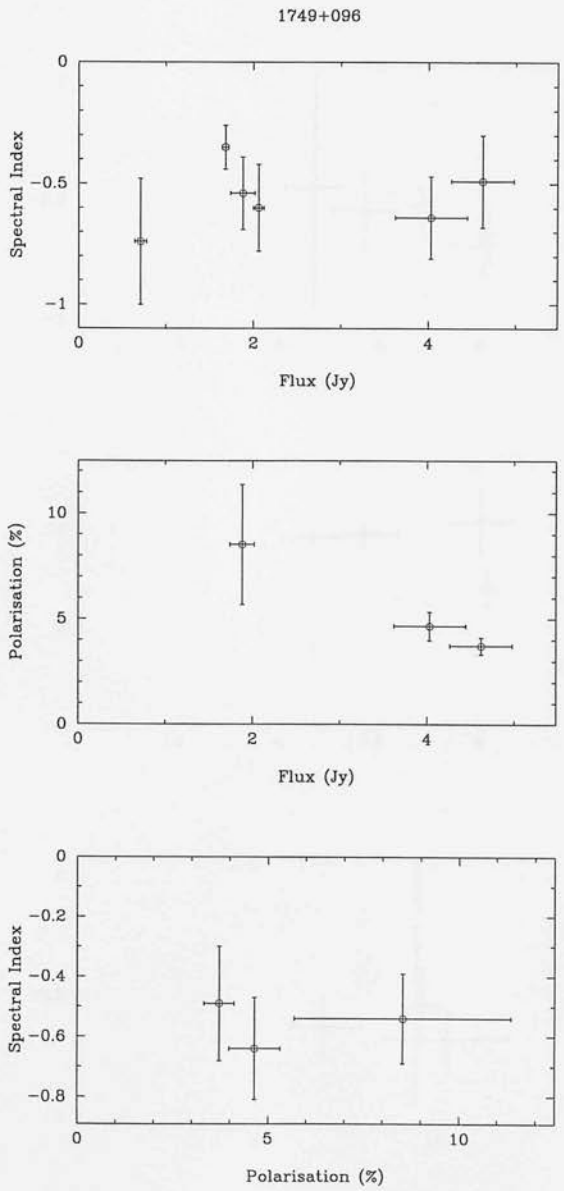
1749+096
Spectral Index
Flux (Jy)
Polarisation (%)
Flux (Jy)
Spectral Index
Polarisation (%)

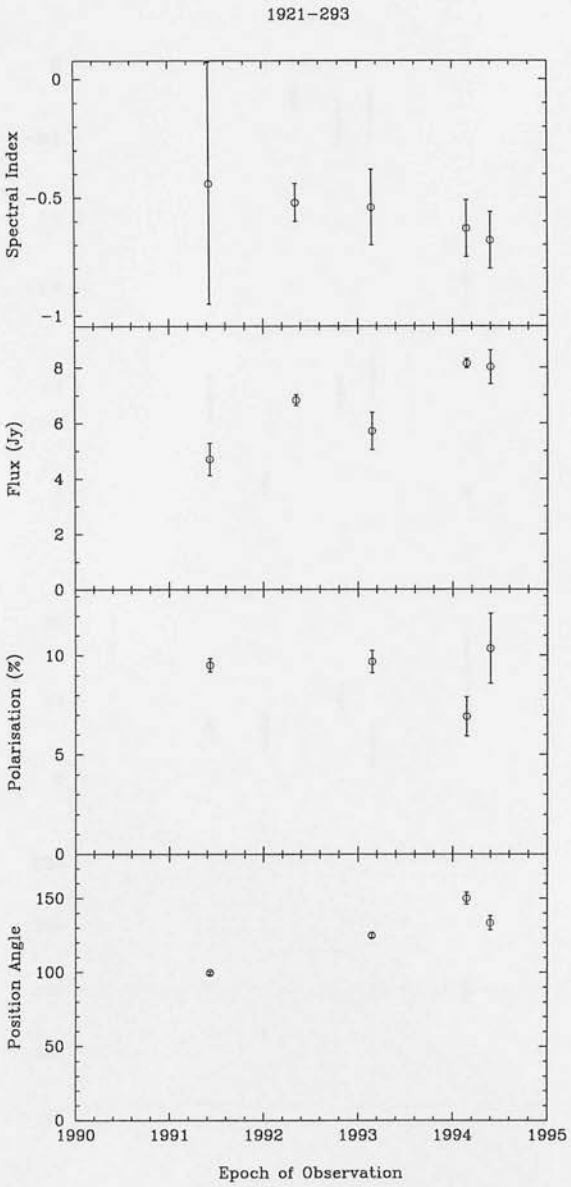
1921−293
Spectral Index
Flux (Jy)
Polarisation (%)
Position Angle
Epoch of Observation

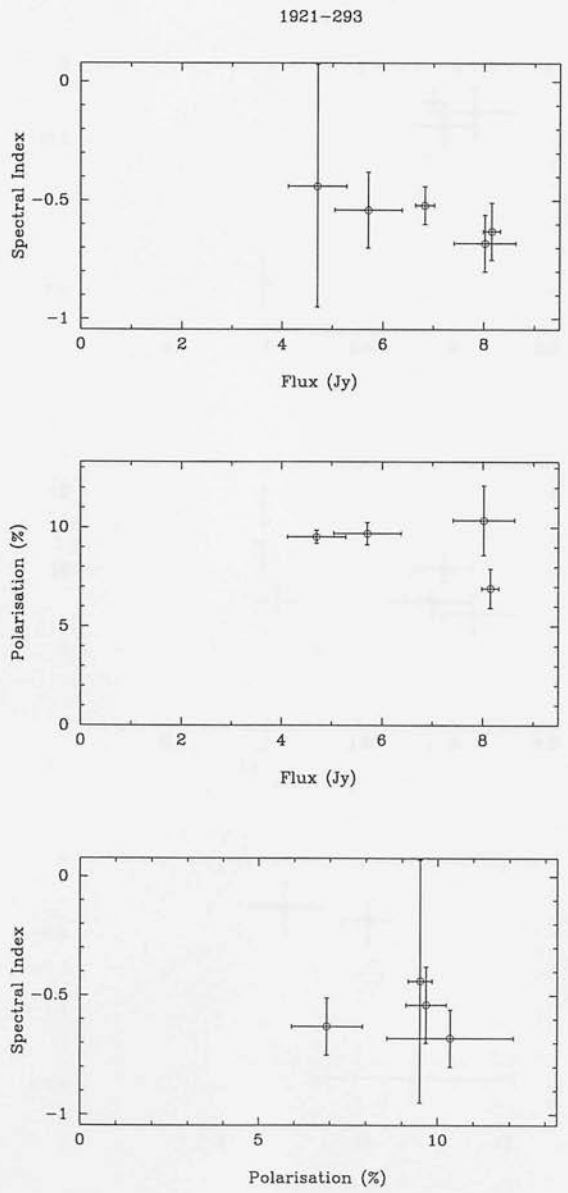
1921−293
Spectral Index
Flux (Jy)
Polarisation (%)
Flux (Jy)
Spectral Index
Polarisation (%)

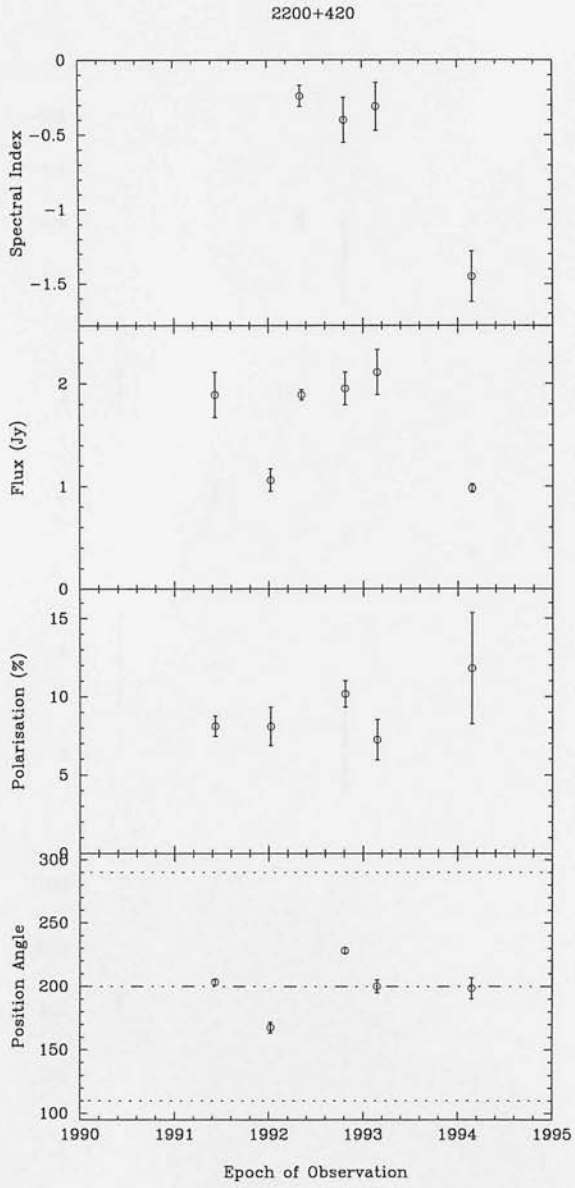
2200+420
Spectral Index
Flux (Jy)
Polarisation (%)
Position Angle
Epoch of Observation

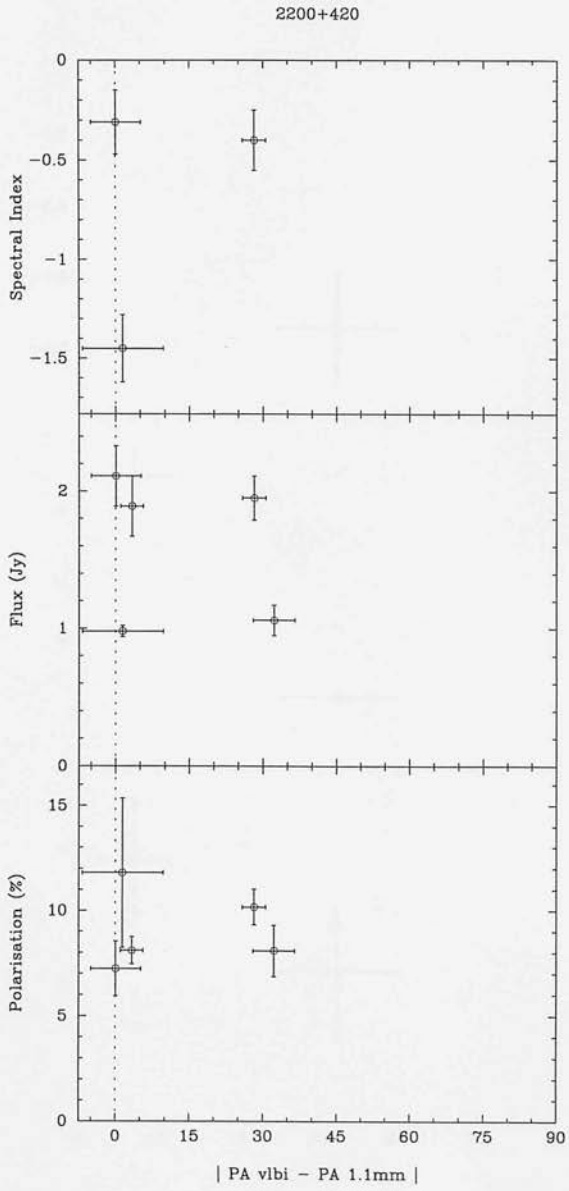
2200+420
Spectral Index
Flux (Jy)
Polarisation (%)
| PA vlbi − PA 1.1mm |

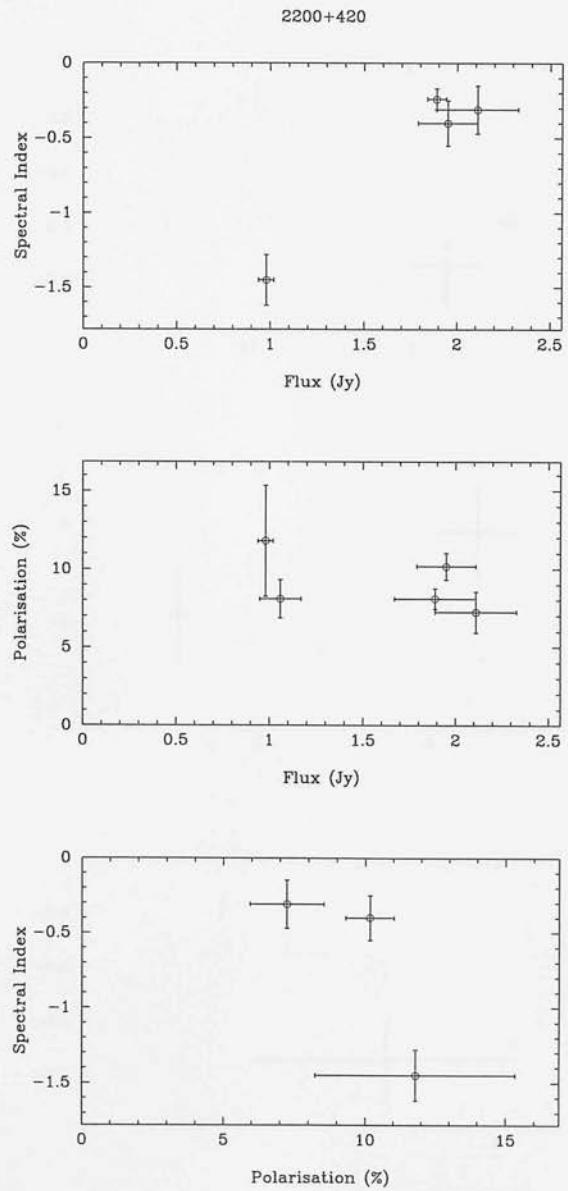
2200+420
Spectral Index
Flux (Jy)
Polarisation (%)
Flux (Jy)
Spectral Index
Polarisation (%)

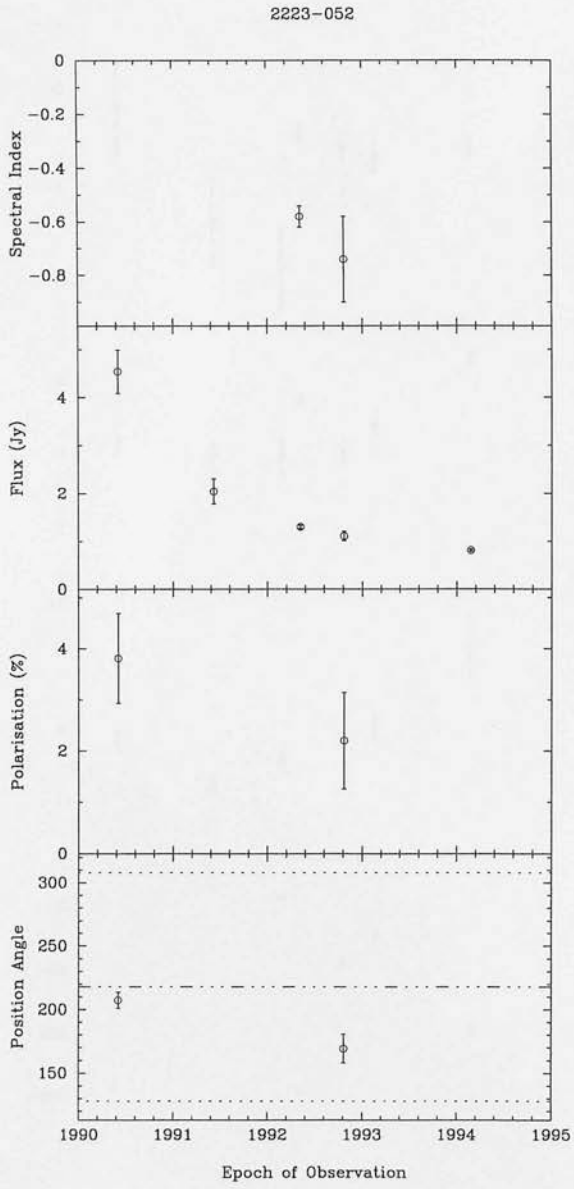
2223−052
Spectral Index
Flux (Jy)
Polarisation (%)
Position Angle
Epoch of Observation

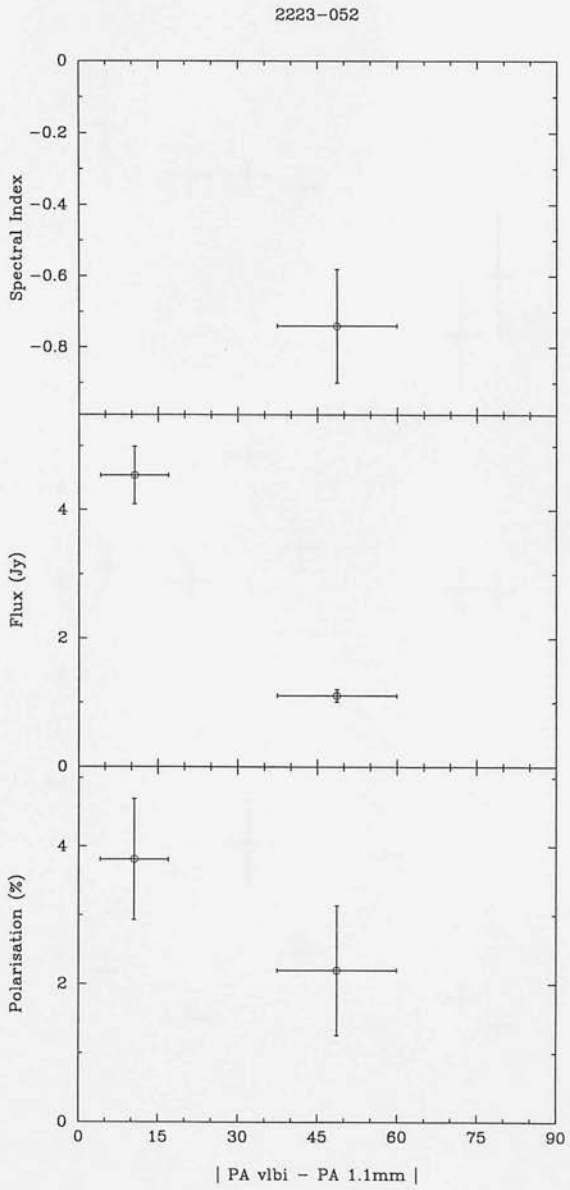
2223−052
Spectral Index
Flux (Jy)
Polarisation (%)
| PA vlbi − PA 1.1mm |

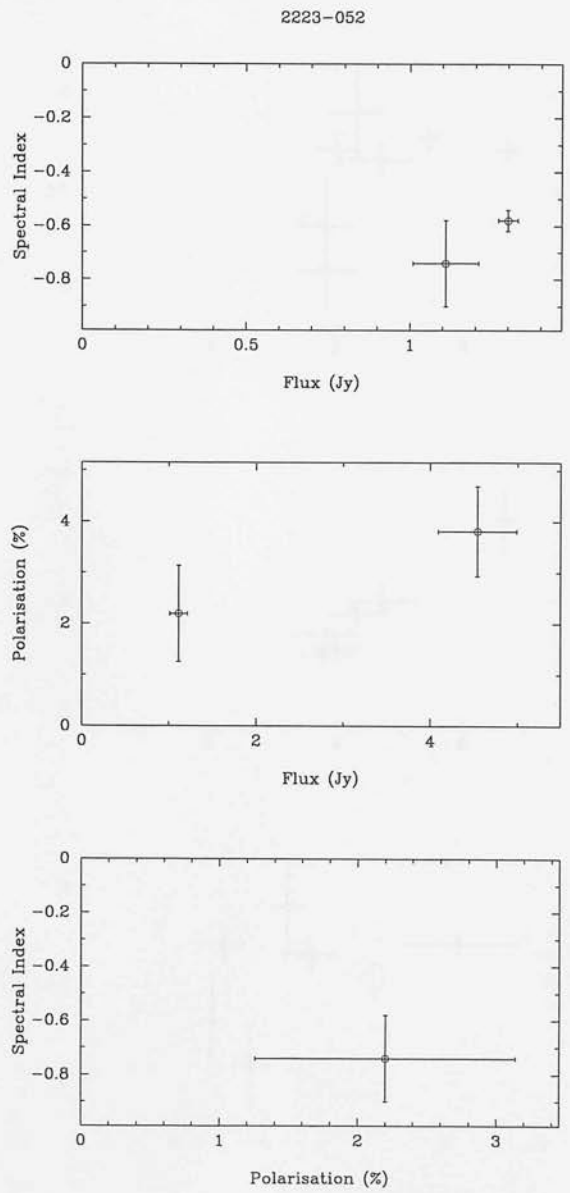
2223−052
Spectral Index
Flux (Jy)
Polarisation (%)
Flux (Jy)
Spectral Index
Polarisation (%)

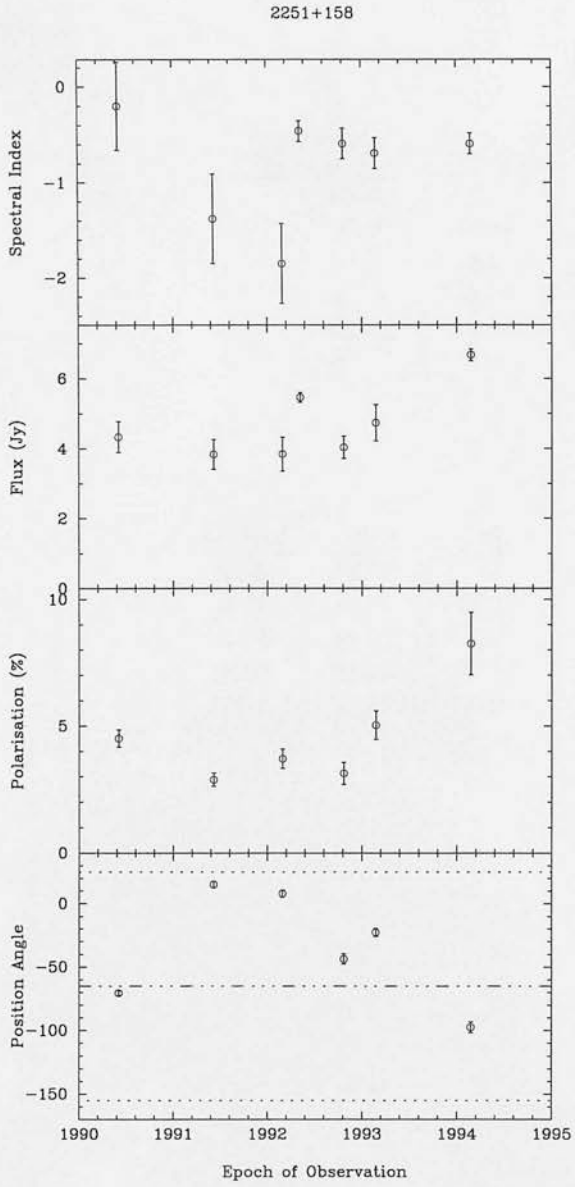
2251+158
Spectral Index
Flux (Jy)
Polarisation (%)
Position Angle
Epoch of Observation

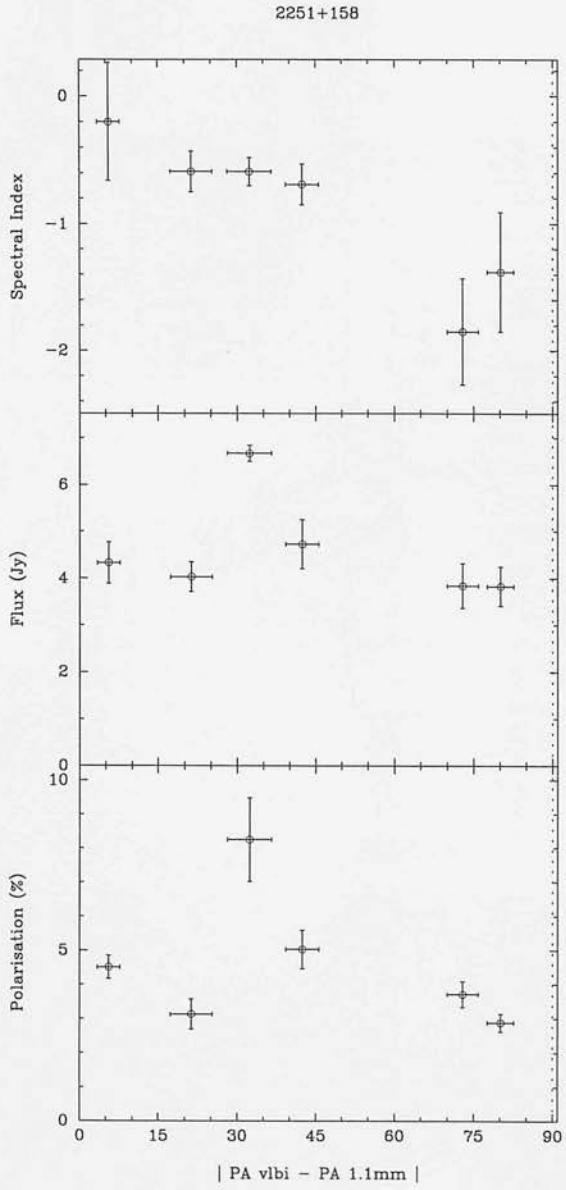
2251+158
Spectral Index
Flux (Jy)
Polarisation (%)
| PA vlbi − PA 1.1mm |

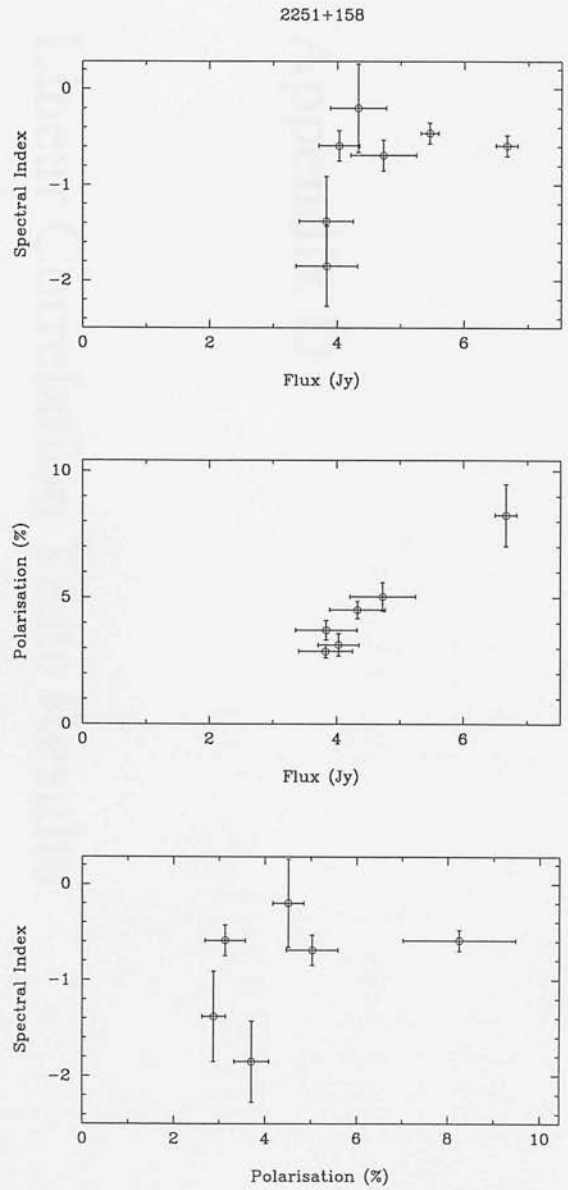
2251+158
Spectral Index
Flux (Jy)
Polarisation (%)
Flux (Jy)
Spectral Index
Polarisation (%)

Appendix D

Linear Correlation Tests Results

All Sources

Corrln.	*Kendal*	*%*	*Spear.*	*%*	*Pearson*	*%*
$\delta - f$	0.09	72.66	0.13	75.00	0.19	90.30
$\delta - P$	-0.32	100.00	-0.49	100.00	-0.47	100.00
$\delta - \alpha$	0.06	52.30	0.07	39.22	0.03	17.30
$f - \alpha$	-0.04	48.06	-0.06	46.74	-0.04	33.84
$f - P$	-0.19	98.82	-0.27	98.81	-0.19	91.43
$P - \alpha$	-0.08	67.50	-0.12	67.39	-0.11	65.15

BL LACs

Corrln.	*Kendal*	*%*	*Spear.*	*%*	*Pearson*	*%*
$\delta - f$	0.03	15.82	0.06	22.99	0.26	80.43
$\delta - P$	-0.33	98.16	-0.50	99.00	-0.48	98.76
$\delta - \alpha$	0.13	56.63	0.18	54.42	0.34	85.94
$f - \alpha$	-0.02	16.39	-0.03	15.86	0.02	10.17
$f - P$	-0.17	80.01	-0.25	80.84	-0.35	93.59
$P - \alpha$	-0.18	75.44	-0.24	72.52	-0.33	86.64

Quasars

Corrln.	*Kendal*	*%*	*Spear.*	*%*	*Pearson*	*%*
$\delta - f$	0.05	38.91	0.09	48.21	0.15	69.38
$\delta - P$	-0.31	99.86	-0.47	99.94	-0.44	99.84
$\delta - \alpha$	0.02	14.51	0.01	4.24	-0.07	36.30
$f - \alpha$	0.09	74.71	0.15	79.12	0.11	64.08
$f - P$	-0.06	47.90	-0.11	58.77	-0.07	38.65
$P - \alpha$	-0.07	50.25	-0.12	58.08	-0.08	42.65

Group A

Corrln.	*Kendal*	*%*	*Spear.*	*%*	*Pearson*	*%*
$\delta - f$	0.02	10.55	0.09	30.53	0.16	53.34
$\delta - P$	0.11	52.42	0.16	52.88	0.04	12.89
$\delta - \alpha$	0.07	33.00	0.08	24.45	0.14	43.33
$f - \alpha$	0.28	95.67	0.41	96.67	0.44	97.92
$f - P$	0.07	34.78	0.08	29.53	0.04	14.20
$P - \alpha$	-0.05	22.36	-0.08	25.54	-0.23	64.98

Group B

Corrln.	*Kendal*	*%*	*Spear.*	*%*	*Pearson*	*%*
$\delta - f$	0.01	3.10	-0.02	7.66	-0.01	3.21
$\delta - P$	-0.28	96.75	-0.41	97.34	-0.30	88.35
$\delta - \alpha$	-0.10	52.14	-0.13	46.55	-0.17	58.20
$f - \alpha$	0.24	96.90	0.36	97.51	0.18	73.22
$f - P$	-0.06	35.92	-0.08	30.83	-0.12	45.55
$P - \alpha$	0.09	46.48	0.13	45.77	0.04	15.82

Group C

Corrln.	*Kendal*	*%*	*Spear.*	*%*	*Pearson*	*%*
$\delta - f\partial$	0.39	95.75	0.58	97.72	0.44	89.66
$\delta - P$	-0.03	11.80	0.02	5.04	0.06	16.41
$\delta - \alpha$	0.03	13.05	0.09	22.92	0.10	25.92
$f - \alpha$	0.35	96.10	0.44	94.30	0.36	86.63
$f - P$	-0.03	11.80	-0.04	12.05	-0.30	73.04
$P - \alpha$	-0.14	52.33	-0.20	51.67	-0.37	80.65

0235+164

Corrln.	*Kendal*	*%*	*Spear.*	*%*	*Pearson*	*%*
$\delta - F$	0.67	82.58	0.80	80.00	0.85	85.35
$\delta - P$	-0.67	82.58	-0.80	80.00	-0.84	83.75
$\delta - \alpha$	-0.33	39.85	-0.50	33.33	-0.75	53.69
$F - \alpha$	-0.67	82.58	-0.80	80.00	-0.64	64.35
$F - P$	-0.33	50.31	-0.60	60.00	-0.57	56.81
$P - \alpha$	1.00	88.28	1.00	100.00	1.00	94.19

0420-014

Corrln.	*Kendal*	*%*	*Spear.*	*%*	*Pearson*	*%*
$\delta - F$	-0.67	82.58	-0.80	80.00	-0.96	96.19
$\delta - P$	0.00	0.00	0.00	0.00	-0.57	57.28
$\delta - \alpha$	0.00	0.00	0.20	20.00	0.11	11.18
$F - \alpha$	0.33	50.31	0.40	40.00	0.06	5.56
$F - P$	0.33	50.31	0.40	40.00	0.50	49.89
$P - \alpha$	0.33	50.31	0.40	40.00	0.46	45.59

0735+178

Corrln.	*Kendal*	*%*	*Spear.*	*%*	*Pearson*	*%*
$\delta - F$	-0.91	93.72	-0.95	94.87	-0.96	95.72
$\delta - P$	-0.67	82.58	-0.80	80.00	-0.77	77.31
$\delta - \alpha$	0.33	50.31	0.40	40.00	0.63	63.00
$F - \alpha$	-0.14	30.27	-0.17	25.83	-0.11	16.55
$F - P$	0.55	73.57	0.63	63.25	0.56	55.77
$P - \alpha$	0.00	0.00	-0.20	20.00	-0.80	79.56

0851+202

Corrln.	*Kendal*	*%*	*Spear.*	*%*	*Pearson*	*%*
$\delta - F$	0.59	93.52	0.76	95.11	0.63	87.07
$\delta - P$	0.05	11.94	0.14	24.01	-0.11	17.75
$\delta - \alpha$	0.14	30.27	0.14	21.59	0.04	5.35
$F - \alpha$	0.11	29.97	0.16	28.89	0.09	17.69
$F - P$	0.00	0.00	-0.05	9.16	-0.21	34.59
$P - \alpha$	0.14	30.27	0.20	30.02	0.34	49.30

1226+023

Corrln.	*Kendal*	*%*	*Spear.*	*%*	*Pearson*	*%*
$\delta - F$	0.21	54.21	0.40	68.01	0.26	46.27
$\delta - P$	0.21	54.21	0.36	61.49	0.48	77.07
$\delta - \alpha$	-0.14	37.93	-0.21	38.97	-0.06	12.11
$F - \alpha$	0.27	75.71	0.32	65.97	0.37	73.72
$F - P$	0.43	86.24	0.62	89.83	0.77	97.40
$P - \alpha$	0.07	19.54	0.02	4.46	-0.08	15.05

1253-055

Corrln.	*Kendal*	*%*	*Spear.*	*%*	*Pearson*	*%*
$\delta - F$	-0.05	11.94	0.00	0.00	-0.14	24.23
$\delta - P$	0.14	34.77	0.21	35.55	-0.03	5.57
$\delta - \alpha$	0.05	11.94	0.07	12.10	-0.37	58.60
$F - \alpha$	0.24	67.48	0.35	67.18	0.21	43.38
$F - P$	0.62	94.91	0.71	92.87	0.86	98.61
$P - \alpha$	0.14	34.77	0.21	35.55	0.19	31.39

1335-127

Corrln.	*Kendal*	*%*	*Spear.*	*%*	*Pearson*	*%*
$\delta - F$	-1.00	95.85	-1.00	100.00	-0.91	90.88
$\delta - P$	0.00	0.00	0.20	20.00	0.25	25.49
$\delta - \alpha$	-0.33	39.85	-0.50	33.33	-0.72	51.18
$F - \alpha$	0.11	20.37	0.21	25.94	0.66	77.00
$F - P$	0.00	0.00	-0.20	20.00	-0.63	63.15
$P - \alpha$	-1.00	88.28	-1.00	100.00	-0.99	91.61

1641+399

Corrln.	*Kendal*	*%*	*Spear.*	*%*	*Pearson*	*%*
$\delta - F$	0.71	97.57	0.86	98.63	0.60	84.29
$\delta - P$	-0.14	34.77	-0.18	29.83	-0.06	10.46
$\delta - \alpha$	0.20	42.70	0.43	60.35	0.28	41.55
$F - \alpha$	0.36	78.40	0.48	76.71	0.35	60.50
$F - P$	-0.43	82.35	-0.43	66.26	-0.58	82.53
$P - \alpha$	-0.33	65.24	-0.49	67.13	-0.65	83.66

1749+096

Corrln.	*Kendal*	*%*	*Spear.*	*%*	*Pearson*	*%*
$\delta - F$	1.00	88.28	1.00	100.00	1.00	96.94
$\delta - P$	-1.00	88.28	-1.00	100.00	-1.00	98.39
$\delta - \alpha$	0.33	39.85	0.50	33.33	-0.03	2.05
$F - \alpha$	0.07	14.90	0.20	29.60	0.18	26.70
$F - P$	-1.00	88.28	-1.00	100.00	-1.00	98.55
$P - \alpha$	-0.33	39.85	-0.50	33.33	0.01	0.44

1921-293

Corrln.	*Kendal*	*%*	*Spear.*	*%*	*Pearson*	*%*
$\delta - F$						
$\delta - P$						
$\delta - \alpha$						
$F - \alpha$	-0.60	85.84	-0.80	89.59	-0.92	97.14
$F - P$	0.00	0.00	-0.20	20.00	-0.38	37.51
$P - \alpha$	-0.33	50.31	-0.40	40.00	0.14	13.50

2200+420

Corrln.	*Kendal*	*%*	*Spear.*	*%*	*Pearson*	*%*
$\delta - F$	-0.20	37.58	-0.30	37.62	-0.22	27.30
$\delta - P$	0.00	0.00	0.10	12.71	-0.01	0.87
$\delta - \alpha$	-0.33	39.85	-0.50	33.33	0.40	26.14
$F - \alpha$	0.33	50.31	0.40	40.00	0.97	97.27
$F - P$	-0.40	67.28	-0.60	71.52	-0.50	60.88
$P - \alpha$	-1.00	88.28	-1.00	100.00	-0.82	60.81

2251+158

Corrln.	*Kendal*	*%*	*Spear.*	*%*	*Pearson*	*%*
$\delta - F$	-0.47	81.15	-0.54	73.43	-0.32	46.73
$\delta - P$	-0.33	65.24	-0.37	53.15	-0.33	47.41
$\delta - \alpha$	-0.83	98.04	-0.93	99.23	-0.93	99.25
$F - \alpha$	0.39	78.17	0.58	82.46	0.47	71.77
$F - P$	0.87	98.54	0.94	99.52	0.98	99.95
$P - \alpha$	0.28	56.33	0.38	53.85	0.40	56.23

Appendix E

Kolmogorov-Smirnov Tests Results

1-dimensional Kolmogorov-Smirnov Tests between Individual Sources and Polarisation Groups A, B, C.

	Polarisation						*Magnetic Field Orientation*					
	A		B		C		A		B		C	
Source	**K–S**	**%**	**K–S**	**%**	**K–S**	**%**	**K–S**	**%**	**K–S**	**%**	**K–S**	**%**
0235+164	0.83	99.26	0.28	10.14	0.58	86.25	0.50	74.34	0.33	22.44	0.50	72.91
0316+413	1.00	98.44	1.00	98.51	0.71	81.19	1.00	98.44	0.67	77.37	0.88	95.02
0420–014	0.87	99.60	0.30	15.82	0.79	98.62	0.46	64.04	0.43	58.00	0.89	99.67
0528+134	0.96	97.64	0.60	65.63	0.63	70.46	0.50	42.10	0.50	42.44	0.50	41.22
0735+178	0.62	91.43	0.65	93.90	0.84	99.31	0.66	94.58	0.28	10.14	0.39	43.75
0736+017	0.46	30.72	0.68	79.06	0.89	95.66	0.46	30.72	0.44	26.75	0.89	95.66
0851+202	0.36	53.28	0.78	99.92	0.89	99.98	0.75	99.65	0.45	84.82	0.89	99.98
0923+392	0.87	94.90	0.34	5.94	0.68	78.75	0.87	94.90	0.40	17.00	0.84	93.29
1226+023	0.96	100.00	0.84	99.99	0.42	70.43	0.88	99.99	0.62	99.02	0.19	1.22
1253–055	0.42	72.21	0.85	99.98	0.95	100.00	0.54	92.99	0.67	99.31	1.00	100.00
1335–127	0.84	99.31	0.42	53.81	0.70	95.89	0.47	66.83	0.67	95.15	1.00	99.93
1641+399	0.77	99.87	0.32	45.81	0.57	93.19	0.86	99.98	0.60	97.90	0.21	2.86
1749+096	0.62	84.60	0.29	5.93	0.68	90.31	0.62	84.60	0.33	14.48	0.84	97.96
1921–293	0.40	47.94	0.85	99.54	0.95	99.85	–	–	–	–	–	–
2200+420	0.28	13.34	0.85	99.85	0.95	99.96	0.49	78.25	0.56	90.65	0.89	99.89
2223–052	0.96	97.64	0.74	86.41	0.41	18.38	1.00	98.44	0.74	86.41	0.65	72.62
2251+158	0.79	99.80	0.43	72.90	0.63	97.13	0.62	97.28	0.21	3.58	0.53	88.58

The columns labelled 'K-S' contain the statistic obtained from the test and the adjacent columns labelled '%' their significance. A low K-S statistic and low significance indicate good agreement between the P and δ parameters of the source and those described by groups A, B and C.